

Geosynchronous Orbit Determination Using Space Surveillance Network Observations and Improved Radiative Force Modeling

by

Richard Harry Lyon

B.S., Astronautical Engineering
United States Air Force Academy, 2002

SUBMITTED TO THE DEPARTMENT OF AERONAUTICS AND ASTRONAUTICS
IN PARTIAL FULFILLMENT OF THE REQUIREMENTS FOR THE DEGREE OF

MASTER OF SCIENCE IN AERONAUTICS AND ASTRONAUTICS
AT THE
MASSACHUSETTS INSTITUTE OF TECHNOLOGY

JUNE 2004

© 2004 Massachusetts Institute of Technology. All rights reserved.

Signature of Author: _____
Department of Aeronautics and Astronautics
May 14, 2004

Certified by: _____
Dr. Paul J. Cefola
Technical Staff, the MIT Lincoln Laboratory
Lecturer, Department of Aeronautics and Astronautics
Thesis Supervisor

Accepted by: _____
Edward M. Greitzer
H.N. Slater Professor of Aeronautics and Astronautics
Chair, Committee on Graduate Students

Report Documentation Page

Form Approved
OMB No. 0704-0188

Public reporting burden for the collection of information is estimated to average 1 hour per response, including the time for reviewing instructions, searching existing data sources, gathering and maintaining the data needed, and completing and reviewing the collection of information. Send comments regarding this burden estimate or any other aspect of this collection of information, including suggestions for reducing this burden, to Washington Headquarters Services, Directorate for Information Operations and Reports, 1215 Jefferson Davis Highway, Suite 1204, Arlington VA 22202-4302. Respondents should be aware that notwithstanding any other provision of law, no person shall be subject to a penalty for failing to comply with a collection of information if it does not display a currently valid OMB control number.

1. REPORT DATE 15 JUL 2004	2. REPORT TYPE N/A	3. DATES COVERED -		
4. TITLE AND SUBTITLE Geosynchronous Orbit Determination Using Space Surveillance Network Observations and Improved Radiative Force Modeling		5a. CONTRACT NUMBER		
		5b. GRANT NUMBER		
		5c. PROGRAM ELEMENT NUMBER		
6. AUTHOR(S)		5d. PROJECT NUMBER		
		5e. TASK NUMBER		
		5f. WORK UNIT NUMBER		
7. PERFORMING ORGANIZATION NAME(S) AND ADDRESS(ES) Massachusetts Institute Of Technology		8. PERFORMING ORGANIZATION REPORT NUMBER		
9. SPONSORING/MONITORING AGENCY NAME(S) AND ADDRESS(ES)		10. SPONSOR/MONITOR'S ACRONYM(S)		
		11. SPONSOR/MONITOR'S REPORT NUMBER(S)		
12. DISTRIBUTION/AVAILABILITY STATEMENT Approved for public release, distribution unlimited				
13. SUPPLEMENTARY NOTES The original document contains color images.				
14. ABSTRACT				
15. SUBJECT TERMS				
16. SECURITY CLASSIFICATION OF:			17. LIMITATION OF ABSTRACT	
a. REPORT unclassified	b. ABSTRACT unclassified	c. THIS PAGE unclassified	UU	18. NUMBER OF PAGES 375
				19a. NAME OF RESPONSIBLE PERSON

[This page intentionally left blank.]

Geosynchronous Orbit Determination Using Space Surveillance Network Observations and Improved Radiative Force Modeling

by

Richard Harry Lyon

Submitted to the Department of Aeronautics and Astronautics on May 14, 2004
in Partial Fulfillment of the Requirements for the Degree of
Master of Science in Aeronautics and Astronautics

ABSTRACT

Correct modeling of the space environment, including radiative forces, is an important aspect of space situational awareness for geostationary (GEO) spacecraft. Solar radiation pressure has traditionally been modeled using a rotationally-invariant sphere with uniform optical properties. This study is intended to improve orbit determination accuracy for 3-axis stabilized GEO spacecraft via an improved radiative force model. The macro-model approach, developed earlier at NASA GSFC for the Tracking and Data Relay Satellites (TDRSS), models the spacecraft area and reflectivity properties using an assembly of flat plates to represent the spacecraft components. This ‘box-wing’ approach has been adapted for the UNIX version of the Goddard Trajectory Determination System (GTDS) at the MIT/Lincoln Laboratory. This thesis presents background and mathematical development of the macro-model approach. This thesis also describes software development and testing, including incorporation of a one-panel spacecraft model along with the full macro-model. A model for Earth albedo and Earth infrared radiation and related software development is also described. Additionally, this thesis gives details about the TDRSS macro-model, and explains the development of a macro-model for the NASA Geosynchronous Operational Environmental Satellites (GOES) I-M spacecraft. Results of simulated data testing using the improved radiative force models are presented. The real data testing detailed in this thesis is an investigation into improving GEO orbit determination using the new force models along with observation data from the Space Surveillance Network (SSN). For the TDRSS spacecraft, HANDS optical observations are used in conjunction with the SSN data. NOAA ranging observations are included in some of the tests for the GOES-10 spacecraft. The space-based visible (SBV) observation model has also been incorporated into GTDS, and SBV observations are included in the orbit determination testing. The tests combine the various types of observation data, and implement various observations corrections and biases. The results of this thesis give a better understanding of the process of determining precise orbits for GEO spacecraft with the box-wing model and SSN observations.

Thesis Supervisor: Dr. Paul J. Cefola
Title: Technical Staff, the MIT Lincoln Laboratory
Lecturer, Department of Aeronautics and Astronautics

DISCLAIMERS

The views expressed in this article are those of the author and do not reflect the official policy or position of the United States Air Force, Department of Defense, or the U.S. Government.

This work was sponsored by the National Oceanic and Atmospheric Administration under Air Force Contract F19628-00-C-0002. "Opinions, interpretations, conclusions, and recommendations are those of the author and are not necessarily endorsed by the United States Government."

This material is based upon work supported under a National Science Foundation Graduate Research Fellowship. "Any opinions, findings, conclusions or recommendations expressed in this publication are those of the author and do not necessarily reflect the views of the National Science Foundation."

Acknowledgements

I would like to take this opportunity to thank the people who have helped me over the past two years and made this thesis possible.

First, I would like to thank my thesis advisor, Dr. Paul Cefola, for his guidance and support over the past two years. It has been an honor to work with such a distinguished professional who has contributed so much to the field. You have taught me a lot, not only about astrodynamics; but also about management, leadership, and life.

Second, I would like to thank Mr. Zach Folcik of MIT/Lincoln Laboratory for all of his hard work on this orbit determination study, and for teaching me to use UNIX, FORTRAN, and GTDS. Thank you for your constant help and work toward getting real data results and understanding the process for doing precision GEO orbit determination with GTDS.

At MIT/Lincoln Laboratory, I would also like to acknowledge my other coworkers, especially Eric Phelps, Bob Flanagan, Rick Abbot, Lori Thornton, Carl Toews, Denis Durand, Anthea Coster, and Susan Shulman, for their expertise and help on this project; Armand Lagasse, Jim Apicella, and Sherry Robarge for computer support; Bonnie Tuohy, Lisa Lombardo, Karen Fraser, Nancy Meehan, Kathy Fellows, and Nancy Alusow for administrative and travel support; and the Lincoln management, including Peter Blankenship, Greg Berthiaume, Sid Sridharan, Mark Czerwinski, and Forrest Hunsberger, for their support.

I would also like to thank several people from the Draper Laboratory for their help on this project: Ron Proulx for providing the DSST Standalone and his astrodynamics expertise, Rick Metzinger for his help with reflectivity coefficients, and Dave Carter for his advice on document editors. I would also like to thank Luke Sauter for his friendship over the years and throughout our many classes and workouts together.

I also want to thank Ed Miller and Sandy Ashton at NOAA for their support of this project and for coordinating GOES observation data and testing, Ed Harvie and the GOES Flight Ops team for providing the GOES solar torque model, and Mike Wong of Space Systems/Loral for providing data to construct the GOES macro-model.

I would like to thank the people from NASA Goddard Space Flight Center, especially Scott Luthcke and Dave Rowlands, for their work on the TDRSS macro-model and for making the GEODYN source code available to this study. Thanks also to Mahima Kaushik and Ann Nicholson at AI Solutions, and Holly Offerman at Swales Aerospace for providing TDRS maneuver information and element sets to this study.

I would like to gratefully acknowledge Dr. Chris Sabol of AFRL/AMOS for providing his HANDS observation data and his expertise in orbit determination and GTDS to this study.

I would like to thank Dr. Ken Chan at the Aerospace Corporation for providing his excellent work on solar radiation pressure and for discussing the project with me.

I would like to thank Dr. T.S. Kelso at Analytical Graphics, Inc., for his help in providing SATCAT analysis.

I would also like to acknowledge the many astrodynamics professionals that I have met at the AAS/AIAA Astrodynamics Specialist and Spaceflight Mechanics Conferences, including Dave Vallado, Sal Alfano, Tom Eller, John Draim, Kim Luu, and Jim Wright, for sharing their expertise and experiences with me.

I would like to acknowledge my professors at MIT, especially Dr. Battin for his excellent courses in astrodynamics and Dr. Vander Velde for his courses in controls; Dr. Martinez-Sanchez, for being my academic advisor; and Marie Stuppard, for administrative support in the Aero/Astro department.

I would like to thank Lt Lynch, my program manager at AFIT, for her support and for arranging TDYs. I would also like to thank the cadre at AFROTC Det 365, especially TSgt Meno for his help with Personnel issues and Col Rojko for his support in securing my PRK waiver and ENJJPT slot.

I would like to thank the National Science Foundation for their support through the Graduate Research Fellowship Program.

I would like to thank the MIT/Lincoln Laboratory for their support through the Military Officer Research Assistant Program.

I would like to thank my family for all they have done for me, including my new family, for making me feel so welcome. I would especially like to thank my wife for always being there with support and love throughout our first year of marriage, and let Baby X know that we can't wait for their arrival.

Most importantly, I would like to thank God for the many blessings in my life.

Table of Contents

Chapter 1	Introduction	23
1.1	Radiative Force Modeling	27
1.2	Orbit Determination Using Space Surveillance Network Observations	32
1.2.1	U.S. Space Surveillance Network (SSN) Overview	32
1.2.2	MIT/Lincoln Laboratory's GEA CRDA.....	34
1.2.3	AFRL/AMOS High Accuracy Network Determination System	37
1.2.4	Russian Space Surveillance Center (SSC).....	38
1.2.5	European Space Surveillance.....	40
1.3	Previous Work on Improved Radiative Force Modeling.....	40
1.3.1	Ron Proulx' One-panel Model.....	40
1.3.2	Ken Chan's Two-plate Model and Work on Complex Spacecraft Structures	41
1.3.3	Kay Pechenick's TDRS Solar Radiation Pressure Model	42
1.3.4	Scott Luthcke et al.'s TOPEX/POSEIDON and TDRSS Macro-models	43
1.3.5	Ed Harvie et al.'s GOES Solar Radiation Torque Model	45
1.4	Outline of Thesis.....	46
Chapter 2	Mathematical Background in Orbit Propagation and Observations Models	51
2.1	Keplerian (Two-body) Motion.....	51
2.2	Orbital Elements	53
2.2.1	Integrals of the Two-body Problem	54
2.2.1.1	Specific Angular Momentum Vector.....	54
2.2.1.2	Specific Mechanical Energy	55
2.2.1.3	Eccentricity Vector	56
2.2.1.4	Parameter and Vis-viva Integral	57
2.2.1.5	Equation of Orbit and Kepler's First Law	58
2.2.1.6	Period and Mean Motion (Kepler's Second and Third Laws)...	59
2.2.2	Keplerian Elements.....	60

2.2.2.1	True, Eccentric, and Mean Anomalies.....	63
2.2.2.2	Keplerian Elements from Position and Velocity	66
2.2.2.3	Position and Velocity from the Keplerian Elements.....	67
2.2.3	Delaunay Variables.....	68
2.2.3.1	Delaunay Variables from Position and Velocity	70
2.2.3.2	Position and Velocity from the Delaunay Variables.....	71
2.2.4	Equinoctial Elements	72
2.2.4.1	Equinoctial Elements from Position and Velocity.....	75
2.2.4.2	Position and Velocity from the Equinoctial Elements.....	77
2.2.5	Poincaré Variables	79
2.2.5.1	Poincaré Variables from Position and Velocity.....	80
2.2.5.2	Position and Velocity from the Poincaré Variables.....	82
2.3	Reference Frames	83
2.3.1	Geocentric Equatorial Coordinate System (IJK)	85
2.3.2	Earth-Centered Earth-Fixed Coordinate System (ECEF).....	87
2.3.3	Coordinate Transformations	87
2.3.3.1	Precession	87
2.3.3.2	Nutation.....	88
2.3.3.3	Sidereal Time	89
2.3.3.4	Polar Motion	91
2.3.3.5	Coordinate Transformation Summary	92
2.3.4	NORAD True Equator/Mean Equinox (TEME) Coordinate System .	92
2.3.5	Topocentric Coordinate Systems	93
2.3.6	Spacecraft Body-Fixed Coordinate System (SBF).....	94
2.4	Special Perturbations, General Perturbations, and Semi-analytical Methods	97
2.4.1	Special Perturbations (Cowell Method).....	97
2.4.1.1	Numerical Integration Techniques.....	98
2.4.2	Variation of Parameters (VOP).....	99
2.4.2.1	Gaussian VOP	102
2.4.2.2	Lagrangian VOP (Lagrange Planetary Equations)	104
2.4.2.3	Hamiltonian VOP.....	107
2.4.3	General Perturbations from VOP.....	109

2.4.4	Semi-analytical Techniques	112
2.4.5	Generalized Method of Averaging.....	113
2.4.6	The Draper Semi-analytical Satellite Theory (DSST)	116
2.5	Observations Models	124
2.5.1	Space-Based Visible Observations Model.....	124
2.5.1.1	Partial Derivatives of the SBV Data Type in GTDS.	126
2.5.2	Observations Corrections.....	129
2.5.2.1	Light-time Correction	129
2.5.2.2	SBV Light-time Correction.....	129
2.5.2.3	Ionospheric Refraction Correction.....	131
2.5.2.4	Measurement Bias Estimation	132
Chapter 3	Solar Radiation Pressure Force Modeling.....	133
3.1	Introduction.....	133
3.2	Spherical Spacecraft Model	133
3.3	Macro-model Approach.....	134
3.3.1	Absorption.....	136
3.3.2	Specular Reflection.....	137
3.3.3	Diffuse Reflection.....	138
3.3.4	Total Differential Force on a Surface Area Element	140
3.4	Macro-model Force Acting on a Flat Plate.....	140
3.5	One-panel Spacecraft Model (Alternate Parameterization).....	141
3.6	Macro-model Force Acting on a Sphere.....	143
3.7	Macro-model Force Acting on a Cylinder.....	145
3.8	Earth Albedo and Earth Infrared Radiation Pressure Model	148
3.9	“Default” Reflectivity Value Analysis	154
Chapter 4	Solar Radiation Pressure Variational Equations.....	157
4.1	Introduction to Statistical Orbit Determination	157
4.1.1	Gauss’ Method of Least Squares	158
4.1.2	Nonlinear Least Squares	159
4.1.3	Calculating the Partial Derivative Matrix	161

4.2	Cowell Theory and Associated Variational Equations	162
4.3	Semi-analytical Satellite Theory and Averaged Partial Generator	165
4.4	Macro-model (Box-wing) Partial Derivatives	168
4.4.1	Cowell Variational Equations	168
4.4.2	Averaged Equations of Motion Variational Equations	170
4.5	One-panel Model (Alternate Parameterization) Partial Derivatives....	171
4.5.1	Cowell Variational Equations (Alternate Parameterization)	172
4.5.2	Averaged Equations of Motion Variational Equations (Alt Parameterization)	173
4.6	Partial Derivatives With Respect to Position.....	174
4.6.1	Spherical Model Position Partial Derivatives	175
4.6.2	Macro-model Position Partial Derivatives.....	177
Chapter 5	Macro-model Specifications	181
5.1	TDRSS Macro-model	181
5.2	GOES Macro-model	184
Chapter 6	Tools and Software	191
6.1	UNIX GTDS	191
6.1.1	Status of UNIX GTDS at Lincoln.....	192
6.2	Implementation of External Subroutines	193
6.2.1	Introduction.....	193
6.2.2	'Middle-ware' Approach	193
6.2.3	New GTDS Input Keywords.....	194
6.3	DSST Standalone Subroutine Incorporation.....	198
6.3.1	DSST Standalone Spherical Solar Radiation Pressure Model	198
6.3.2	One-panel Solar Radiation Pressure Model.....	201
6.4	GEODYN Subroutine Incorporation	202
6.4.1	GEODYN Box-wing Solar Radiation Pressure Model.....	202
6.4.2	GEODYN Earth Albedo and Earth Infrared Radiation Pressure Model	205
6.5	Differential Correction Implementation	209
6.5.1	Cowell D.C. Implementation	211

6.5.2	Semi-analytical Satellite Theory (DSST) D.C. Implementation	213
6.6	Kalman Filter Implementation.....	215
6.7	Implementation of the Space-Based Visible Observations Model	216
Chapter 7	Simulated Data Results	221
7.1	Regression Test Results	221
7.2	Macro-model Acceleration Profiles.....	223
7.2.1	TDRSS Macro-model Acceleration Profiles	223
7.2.2	GOES Macro-model Acceleration Profiles	230
7.3	Short-periodic Orbital Element Behavior Testing.....	234
7.4	Mean Element Evolution Testing	238
7.4.1	One-year Mean Element Propagation Runs.....	238
7.4.2	Short-periodic Coefficient Testing	242
7.5	Single Panel Default Reflectivity Test Results.....	242
7.6	Differential Correction Test Results	243
7.6.1	PCE Runs	244
7.6.2	DATASIM Runs	247
Chapter 8	Real Data Processing Results	249
8.1	TDRSS Test Cases.....	249
8.1.1	SSN with HANDS Optical Data.....	249
8.1.2	Kalman Filter Cases Processing TDRSS Data.....	251
8.2	GOES Test Cases.....	263
8.2.1	SSN with NOAA Ranging Data	263
8.2.2	SSN with NOAA Ranging Data and SBV Observation Data.....	269
8.2.3	Kalman Filter Cases Processing GOES Data.....	270
Chapter 9	Conclusions	283
9.1	Modeling Enhancements in the Orbit Determination Software.....	283
9.2	Macro-model Analysis.....	284
9.3	Geosynchronous Orbit Determination	286
Chapter 10	Future Work	289

10.1	Conical Shadow Model.....	289
10.2	Spacecraft Thermal Imbalance Model.....	290
10.3	Earth Radiation Pressure Variational Equations.....	290
10.4	Attitude Estimation	291
10.5	Kalman Filter Implementation.....	291
10.6	SOLVE Mathematics.....	292
10.7	Macro-model Development for Other Spacecraft	292
Appendix A Element Propagation Results		295
A.1	Short-periodic Element Results	295
A.2	One Year Mean Element Propagation	302
A.2.1	March 2003 – March 2004 (Vernal Equinox).....	302
A.2.2	June 2003 – June 2004 (Summer Solstice).....	305
Appendix B Description of Modified/New GTDS Subroutines		309
B.1	GTDS Subroutines for Improved Force Models.....	309
B.1.1	Existing GTDS Subroutines Modified.....	310
B.1.2	New GTDS Subroutines Created	312
B.1.3	Subroutines Incorporated from the DSST Standalone Orbit Propagator	313
B.1.4	Subroutines Incorporated from the GEODYN Orbit Determination System.....	314
B.2	GTDS Subroutines for SBV Observations Model.....	315
B.2.1	Existing GTDS Subroutines Modified.....	315
B.2.2	New GTDS Subroutines Created	317
B.3	GTDS Developmental History.....	317
B.4	Concurrent Versions System (CVS) at MIT/LL.....	320
Appendix C GTDS Input Keyword Descriptions		321
Appendix D Example GTDS Input Data Files		337
D.1	EPHEM Runs.....	337
D.2	PCE Runs.....	339

D.3	DATASIM Runs	342
D.4	Real Data DC Runs	346
D.5	Real Data ESKF Runs.....	350
Appendix E One-panel Aerodynamic Force Model		357
E.1	Introduction.....	357
E.2	Mathematical Specification	358
E.3	Software Development	361
E.3.1	Force Model Implementation.....	361
E.3.2	Differential Correction Implementation	363
E.4	Simulated Data Results	365
E.5	Real Data Processing Results	366
References		369

[This page intentionally left blank.]

List of Figures

Figure 1-1 – Classification of Geostationary (GEO) Space Objects	24
Figure 1-2 – Radiative Forces Acting on a Spacecraft	28
Figure 1-3 – Solar Radiation Pressure Acting on a Spherical Spacecraft Model	30
Figure 1-4 – Space Surveillance Network (SSN) Sensor Locations.....	33
Figure 1-5 – GMWS Orbit Accuracy for TDRS-4 Using Various Data Sources.....	36
Figure 2-1 – Keplerian Orbital Elements.....	62
Figure 2-2 – Orbital Anomalies for Elliptic Motion.....	64
Figure 2-3 – Equinoctial Coordinate Frame	73
Figure 2-4 – Precession and Nutation Effects.....	86
Figure 2-5 – Precession Angles	88
Figure 2-6 – Nutation Angles, the Equation of the Equinoxes, and Relationship Between True (TOD), Mean (MOD), and Uniform (TEME) Equinoxes of Date	89
Figure 2-7 – Greenwich Sidereal Time (θ_{GST}) and Greenwich Hour Angle (GHA).....	90
Figure 2-8 – Spacecraft Body-Fixed (SBF) Coordinate System	95
Figure 2-9 – Solar Array (SA) Coordinate Frame	96
Figure 3-1 – Absorption.....	134
Figure 3-2 – Specular Reflection	135
Figure 3-3 – Diffuse Reflection	135
Figure 3-4 – Perfect Specular Reflection.....	137
Figure 3-5 – Near-perfect Specular Reflection.....	137
Figure 3-6 – Geometry of Hemispherical Interception of Radiant Flux from a Lambertian Surface	139
Figure 3-7 – Solar Radiation Pressure Acting on a Flat Plate	141
Figure 3-8 – Spherical Spacecraft Hemisphere Illuminated by the Sun.....	143
Figure 3-9 – Right Circular Cylinder Illuminated by the Sun	145

Figure 5-1 – TDRS-05 Spacecraft Graphic	181
Figure 5-2 – Spacecraft Body-Fixed (SBF) Coordinate Frame for the TDRS-05 S/C... ..	182
Figure 5-3 – GOES I-M Spacecraft Graphic	185
Figure 5-4 – Spacecraft Body-Fixed (SBF) Coordinate Frame for the GOES I-M S/C.	186
Figure 6-1 – UNIX GTDS Input Keyword Structure	194
Figure 6-2 – Software Design Tree for Incorporation of DSST Standalone Solar Radiation Pressure Model Subroutines into GTDS	200
Figure 6-3 – Software Design Tree for Incorporation of GEODYN Solar Radiation Pressure Model Subroutines into GTDS	205
Figure 6-4 – Software Design Tree for Incorporation of GEODYN Earth Radiation Pressure Model (Earth Albedo and Earth IR) Subroutines into GTDS	209
Figure 6-5 – Software Design Tree for GTDS Differential Correction Program	211
Figure 6-6 – Software Design Tree for GTDS Cowell Theory DC	212
Figure 6-7 – Software Design Tree for GTDS Semi-analytical Satellite Theory DC	214
Figure 7-1 – UNIX GTDS TDRS Macro-model Solar Radiation Acceleration Profile at β' = 22.5	226
Figure 7-2 – GEODYN TDRS Solar Radiation Acceleration Difference Profile at $\beta' =$ 23.4.....	226
Figure 7-3 – UNIX GTDS TDRS Macro-model - Spherical Acceleration Diff. Profile at $\beta' = 22.5$	227
Figure 7-4 – GEODYN TDRS Macro-model - Spherical Acceleration Difference Profile at $\beta' = 23.4$	227
Figure 7-5 – UNIX GTDS TDRS Macro-model Solar Radiation Acceleration Profile for $\beta' = 0^\circ$	229
Figure 7-6 – UNIX GTDS TDRS Macro-model - Spherical Acceleration Difference Profile for $\beta' = 0^\circ$	229
Figure 7-7 – UNIX GTDS GOES Macro-model Solar Radiation Acceleration Profile at $\beta' = 22.5^\circ$	231
Figure 7-8 – UNIX GTDS GOES Macro-model-Spherical Acceleration Difference Profile at $\beta' = 22.5^\circ$	231

Figure 7-9 – UNIX GTDS GOES Macro-model Solar Radiation Acceleration Profile for $\beta' = 0^\circ$	233
Figure 7-10 – UNIX GTDS GOES Macro-model-Spherical Acceleration Difference Profile for $\beta' = 0^\circ$	233
Figure 7-11 – Box-wing – Spherical Difference in a and e	235
Figure 7-12 – Box-wing – Spherical Difference in i and Ω	236
Figure 7-13 – Box-wing – Spherical Difference in ω and v	237
Figure 7-14 – Box-wing – Spherical Difference in h (Jun 03 – Jun 04 Case).....	240
Figure 7-15 – Box-wing – Spherical Difference in h (Sep 03 – Sep 04 Case).....	240
Figure 7-16 – Box-wing – Spherical Difference in k (Jun 03 – Jun 04 Case).....	241
Figure 7-17 – Box-wing – Spherical Difference in k (Sep 03 – Sep 04 Case).....	241
Figure 8-1 – Mean Keplerian Elements vs Time using Only HANDS Data with Spherical Model (ESKF).....	254
Figure 8-2 – Mean Equinoctial Elements vs Time using Only HANDS Data with Spherical Model (ESKF).....	255
Figure 8-3 – Mean Keplerian Elements vs Time using Only HANDS Data with Box-wing Model (ESKF).....	256
Figure 8-4 – Mean Equinoctial Elements vs Time using Only HANDS Data with Box-wing Model (ESKF).....	257
Figure 8-5 – HANDS Azimuth and Elevation Residuals vs Time using Only HANDS Data with Spherical Model (ESKF).....	258
Figure 8-6 – HANDS Azimuth and Elevation Residuals vs Time using Only HANDS Data with Box-wing Model (ESKF).....	259
Figure 8-7 – HANDS Azimuth and Elevation Residuals vs Time using SSN and HANDS Data with Spherical Model (ESKF).....	261
Figure 8-8 – HANDS Azimuth and Elevation Residuals vs Time using SSN and HANDS Data with Box-wing Model (ESKF).....	262
Figure 8-9– GOES Station 6 Range Residuals Using SSN Obs and NOAA Ranging Data – Semi-analytical Satellite Theory Fit (DC)	266
Figure 8-10–GOES Station 6 Range Residuals Using SSN Obs and NOAA Ranging Data – Cowell Theory Fit (DC).....	266

Figure 8-11– GOES Station 6 Range Residuals Using SSN Obs and Thinned/Deweighted NOAA Ranging Data, Spherical Range Bias (DC)	267
Figure 8-12 – GOES Station 6 Range Residuals Using SSN Obs and Thinned/Deweighted NOAA Ranging Data, Spherical/Macro-model Range Biases (DC)	267
Figure 8-13 - GOES Station 6 Range Residuals Using SSN Obs and Thinned/Deweighted NOAA Ranging Data, Equal % Obs Accepted (DC).....	268
Figure 8-14 – Mean Keplerian Elements vs Time using Only NOAA Ranging Data with Spherical Model (ESKF).....	272
Figure 8-15 – Mean Equinoctial Elements vs Time using Only NOAA Ranging Data with Spherical Model (ESKF).....	273
Figure 8-16 – Mean Keplerian Elements vs Time using Only NOAA Ranging Data with Box-wing Model (ESKF).....	274
Figure 8-17 – Mean Equinoctial Elements vs Time using Only NOAA Ranging Data with Box-wing Model (ESKF).....	275
Figure 8-18 – GOES Station 6 Range Residuals vs Time using Only NOAA Ranging Data with Spherical Model (ESKF)	276
Figure 8-19 – GOES Station 6 Range Residuals vs Time using Only NOAA Ranging Data with Box-wing Model (ESKF)	276
Figure 8-20 – Mean Keplerian Elements vs Time using SSN and NOAA Ranging Data with Spherical Model (ESKF).....	278
Figure 8-21 – Mean Equinoctial Elements vs Time using SSN and NOAA Ranging Data with Spherical Model (ESKF).....	279
Figure 8-22 – Mean Keplerian Elements vs Time using SSN and NOAA Ranging Data with Box-wing Model (ESKF).....	280
Figure 8-23 – Mean Equinoctial Elements vs Time using SSN and NOAA Ranging Data with Box-wing Model (ESKF).....	281
Figure 8-24 – GOES Station 6 Range Residuals vs Time using SSN and NOAA Ranging Data with Spherical Model (ESKF)	282
Figure 8-25 – GOES Station 6 Range Residuals vs Time using SSN and NOAA Ranging Data with Box-wing Model (ESKF)	282
Figure A-1 – Box-wing – Spherical Difference in a and e (Summer Solstice Case).....	296
Figure A-2 – Box-wing – Spherical Difference in i and Ω (Summer Solstice Case).....	297

Figure A-3 – Box-wing – Spherical Difference in ω and v (Summer Solstice Case).....	298
Figure A-4 – Box-wing – Spherical Difference in a and e (Autumnal Equinox Case) ..	299
Figure A-5 – Box-wing – Spherical Difference in i and Ω (Autumnal Equinox Case)..	300
Figure A-6 – Box-wing – Spherical Difference in ω and v (Autumnal Equinox Case) .	301
Figure A-7 – One-year Mean Element Plot of a (Vernal Equinox).....	302
Figure A-8 – One-year Mean Element Plots of h and k (Vernal Equinox)	303
Figure A-9 – One-year Mean Element Plots of p and q (Vernal Equinox)	304
Figure A-10 – One-year Mean Element Plot of a (Summer Solstice)	305
Figure A-11 – One-year Mean Element Plots of h and k (Summer Solstice).....	306
Figure A-12 – One-year Mean Element Plots of p and q (Summer Solstice).....	307
Figure B-1 – GTDS Initial Developmental History Diagram.....	318
Figure B-2 – Draper and MIT/LL R&D GTDS Developmental History	319
Figure D-1 - EPHEM Input Data File with Spherical Model	337
Figure D-2 – EPHEM Input Data File with One-panel Model.....	338
Figure D-3 – EPHEM Input Data File with Macro-model (Single-Panel Case)	338
Figure D-4 - EPHEM Input Data File with Albedo Model	339
Figure D-5 – PCE Input Data File for “Default” Reflectivity Test Case.....	340
Figure D-6 – PCE Input Data File with 2-plate Macro-model Test Case.....	341
Figure D-7 – Cowell DATASIM Input Data File using TDRS-05 Macro-model.....	344
Figure D-8 – Cowell DC Input Data File for DATASIM Case using TDRS-05 Macro- model.....	345
Figure D-9 – Real Data Input Data File for GOES-10 using Spherical Model	347
Figure D-10 – Real Data Input Data File for TDRS-05 using Macro-model	350
Figure D-11 – Real Data ESKF Input Data File for GOES-10 using Spherical Model .	352
Figure D-12 – Real Data ESKF Input Data File for TDRS-05 using Macro-model	356
Figure E-1 – Flat Plate Aerodynamic Force Model.....	359

Figure E-2 – Software Design Tree for Incorporation of DSST Standalone One-panel
Drag Model Subroutines into GTDS 362

Figure E-3 – Software Design Tree for GTDS One-panel Drag Model DSST DC..... 364

Figure E-4 – Semimajor Axis and Eccentricity Behavior Using the Spherical Model .. 367

Figure E-5 – Semimajor Axis and Eccentricity Behavior Using the One-panel Model. 368

List of Tables

Table 1-1 – Approximate Number of GEO Space Objects in SATCAT	25
Table 5-1 – TDRS-05 Macro-model Plate Specifications	183
Table 5-2 – 20-plate GOES Macro-model Plate Specifications	188
Table 5-3 – 15-plate GOES Macro-model Plate Specifications	189
Table 6-1 – Summary and Classification of New GTDS Input Keywords.....	195
Table 7-1 – Initial Orbital Elements for SSFLA Orbit [Ref 78].....	221
Table 7-2 – Regression Test Results for 90-day DSST Orbit Generator Run	222
Table 7-3 – Regression Test Results for ESKF Processing Astra 1K Observations	222
Table 7-4 – Single Plate Model Default Values (To Replicate Spherical $C_R = 1.2$)	242
Table 7-5 – DSST Differential Correction Run Results (SSFLA Orbit Case)	245
Table 7-6 – DSST Differential Correction Run Results (GEO Orbit Case).....	245
Table 7-7 – Cowell Differential Correction Run Results (SSFLA Orbit Case)	246
Table 7-8 – Cowell Differential Correction Run Results (GEO Orbit Case)	247
Table 8-1 – TDRS-5 Results, Processing SSN and HANDS Data	251
Table 8-2 – GOES-10 Results of Including SBV Observations	269
Table 8-3 – GOES-10 Results of Using Observations Corrections and Biases.....	270
Table B-1 - Summary of Improved Force Model GTDS Subroutines.....	309
Table B-2 - Summary of SBV Obs Model GTDS Subroutines	315

[This page intentionally left blank.]

Chapter 1 Introduction

On January 11, 2001, the Commission to Assess United States National Space Security Management and Organization, chaired by the Honorable Donald H. Rumsfeld, submitted their report, concluding, "...that the security and well being of the United States, its allies and friends depend on the nation's ability to operate in space." [Ref 1, pp vii].

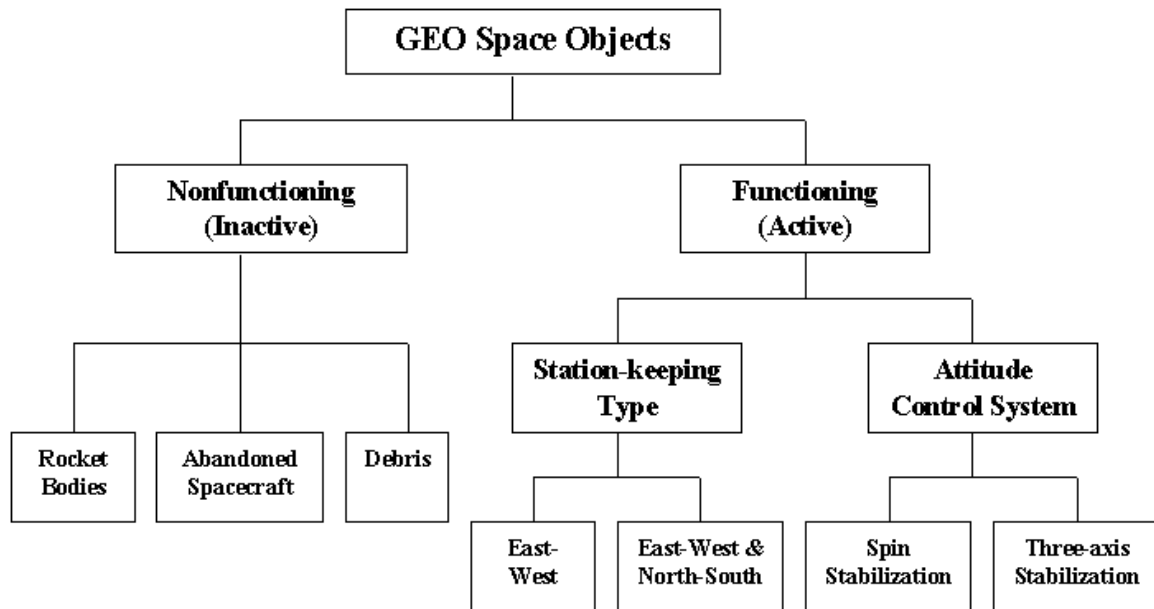
Space situational awareness was identified as one of the U.S. objectives for space, and includes, "...tracking and identifying many thousands of objects in space..." [Ref 1, pp 31]. The commission's report included the following comments regarding space situational awareness:

"An improved space surveillance network is needed to reduce the chance of collision between satellites, the Space Shuttle or the International Space Station and the thousands of pieces of space debris orbiting the earth. It will also have to track objects deeper in space, such as asteroids or spacecraft. And to reduce the possibility of surprise by hostile actors, it will have to monitor space activity. The evolution of technology and the character of this problem argue for placing elements of the surveillance network in space, including both electro-optical and radar systems." [Ref 1, pp 31]

These comments clearly argue for improvements in the hardware (radar and optical sensors) that make up the space surveillance network. Most specifically, they call for space-based space surveillance sensors. In a more subtle way, these comments also call for improvements in the orbit determination software that processes the observation data from the space surveillance network.

Space situational awareness is dependent on understanding the space environment where it is not already well-known. Current areas of research relative to the space environment include improved modeling of the atmospheric density variations and improved modeling of the solar radiation pressure and the other sources of radiative forces. The technology generated from this research enables the achievement of better knowledge of spacecraft orbits, which results in the end product of better space situational awareness.

Geostationary (GEO) space objects are a high-interest group of space objects for both commercial and military applications. These space objects can be classified according to the chart shown in Figure 1-1:



Source – Dr. Vasily S. Yurasov, et al. [Ref 2, pp 122]

Figure 1-1 – Classification of Geostationary (GEO) Space Objects

Approximate numbers of GEO space objects in the various classifications were graciously provided by Dr. T.S. Kelso of AGI’s Center for Space Standards and Innovation [Ref 3]. Kelso filtered the March 4, 2004 SATCAT to arrive at a catalog of

objects that are in GEO orbit or pass through the operational GEO regime [Ref 3]. His filtering process involved eliminating all decayed objects, eliminating all objects outside earth orbit, eliminating all objects with no elements available, eliminating all objects with apogees less than 34,786 km altitude (~ GEO - 1,000 km), eliminating all objects with perigees greater than 36,786 km altitude (~ GEO + 1,000 km), and eliminating all objects with inclinations greater than 17 degrees [Ref 3]. The resulting catalog included a total of 960 GEO space objects, as shown in Table 1-1 [Ref 3].

Table 1-1 – Approximate Number of GEO Space Objects in SATCAT

Source – Dr. T.S. Kelso [Ref 3]

GEO Space Object Category	Number of Objects
Payloads (Active and Inactive)	645
Rocket Bodies	234
Debris	81
TOTAL	960

The majority of modern active GEO spacecraft are of the three-axis stabilized type. For example, eight of the nine major spacecraft bus types currently in operation by commercial telecommunication satellite companies are three-axis stabilized (the other is spin-stabilized) [Ref 4]. The operators of GEO spacecraft typically seek to keep a set of instruments oriented toward the Earth (nadir-pointing). At the same time, the solar panels of these spacecraft are typically sun-tracking, so that they generate the maximum amount of power possible for the spacecraft. As a result, three-axis stabilized spacecraft typically have complex structures and complex attitude control systems [Ref 4].

Most operators of GEO spacecraft also seek to maintain their position within the geostationary belt to ensure their desired coverage of the Earth. This results in the need for numerous station-keeping maneuvers, both East-West and North-South. Many

spacecraft complete these maneuvers by firing chemical thrusters; however, increasing numbers of modern spacecraft are using electric propulsion for station keeping maneuvers, including the Xenon Ion Propulsion System (XIPS) used on the Boeing 702 spacecraft [Refs 4 - 6].

The complex nature of three-axis stabilized GEO spacecraft means that orbit determination for these spacecraft is not a simple task. Orbit determination is difficult in several ways. The complex geometry and structure of these spacecraft make it difficult to model the spacecraft-dependent perturbations. The complex attitude-control systems and frequent station-keeping maneuvers result in numerous discrete events that are difficult to model. The space environment itself is complicated to model, especially during eclipse season when geostationary spacecraft experience numerous umbra and penumbra transitions.

It is clear that a multitude of tools and technologies are needed to move forward and gain better space situational awareness of GEO spacecraft:

- Improved spacecraft models that deal with the complex spacecraft geometry and attitude.
- Recursive filter/smoothers that can deal with frequent discrete events such as attitude control or station-keeping maneuvers. The filter portion of the problem has been researched and documented in theses by previous MIT graduate students, including SM theses by Steve Taylor and Elaine Wagner [Refs 7, 8], and Bob Herklotz' Ph.D. thesis [Ref 9].

- Improved models of the space environment, including solar radiation pressure, models of the Earth's shadow (including umbra and penumbra regions), Earth radiation pressure effects, and spacecraft thermal imbalance.

This study focuses on addressing the first and part of the third items in the above list, by improving orbit determination via an improved model for the radiative forces on the spacecraft. The improved model takes into account the actual geometry and surface properties of spacecraft, as opposed to the traditional method of modeling the spacecraft as a uniform sphere. The model includes solar radiation pressure and Earth radiation pressure effects, but uses a cylindrical Earth shadow model (umbra only) and neglects thermal imbalance. This study seeks to use this improved radiative force modeling, along with a combination of space surveillance network observation data, optical observation data, and owner/operator ranging data, for precision orbit determination of 3-axis stabilized geostationary spacecraft.

1.1 Radiative Force Modeling

Radiative force creates a perturbing acceleration on spacecraft in orbit and includes the force due to all of the electromagnetic radiation incident to or emitted by a spacecraft. *Direct solar radiation* is the primary source of radiation that spacecraft experience, and includes all of the electromagnetic waves emitted by the Sun incident to the spacecraft. *Earth albedo* is the solar radiation incident to the Earth that is reflected back into space by the Earth's atmosphere. Both direct solar radiation and Earth albedo are primarily in the visible region of the electromagnetic spectrum. The incident radiation that is not reflected is absorbed by the Earth and reradiated back into space in the infrared spectrum as heat. This radiation is called *Earth infrared* radiation. *Thermal*

emission occurs due to the thermal imbalance between the spacecraft and the ambient space environment. This radiation is also in the infrared spectrum. Figure 1-2 shows the various sources of radiative force acting on a spacecraft.

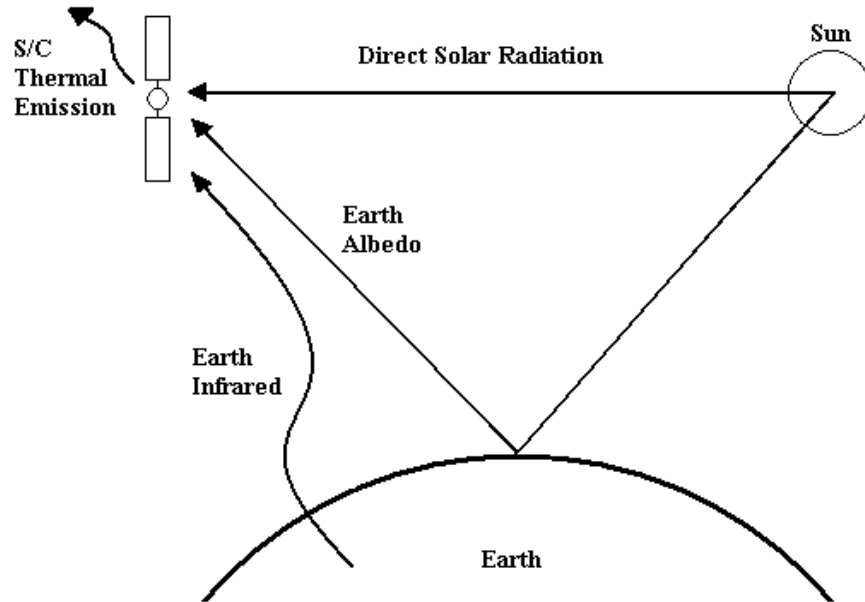


Figure 1-2 – Radiative Forces Acting on a Spacecraft

Direct solar radiation is the dominant source of electromagnetic radiation on spacecraft. *Solar radiation pressure* is the force per unit area acting on a surface due to the change in momentum of the incident solar radiation. Solar radiation pressure creates a significant perturbing acceleration for spacecraft in orbit at high altitudes. Specifically, solar radiation pressure creates the predominant perturbing acceleration above approximately 800 km altitude [Ref 10, pp 518].

The mean solar energy flux over all wavelengths is proportional to the inverse square of the distance from the sun [Ref 11, pp 130]. The mean solar energy flux at 1 AU is also called the *solar radiation constant* or simply *solar flux*. Its value is approximately [Ref 10, pp 518; Ref 11, pp 130]:

$$\Phi_{SR} = 1353 \frac{W}{m^2} \quad (1.1)$$

Wertz gives a more precise time-varying value for the solar flux, and accounts for the variation over a year, where D is the phase of the year measured from Earth aphelion (approximately July 4) [Ref 11, pp 130]:

$$\Phi_{SR} = \frac{1353}{1.0004 + 0.0334 \cos D} \frac{W}{m^2} \quad (1.2)$$

To determine the pressure, or amount of momentum imparted, we use the relativistic energy-momentum relationship, with c being the speed of light [Ref 12, pp 70]:

$$E^2 = p^2 c^2 + m^2 c^4 \quad (1.3)$$

For electromagnetic radiation, since the mass of a photon is zero in all reference frames, Eq (1.3) reduces to [Ref 12]:

$$E = pc \quad (1.4a)$$

which can be rearranged to obtain:

$$p = \frac{E}{c} \quad (1.4b)$$

This allows us to solve for the solar radiation pressure, which is equivalent to the change in momentum or force per unit area [Ref 10, pp 518]:

$$p_{SR} = \frac{\Phi_{SR}}{c} = \frac{1353 \frac{W}{m^2}}{3 \times 10^8 \frac{m}{s}} = 4.51 \times 10^{-6} \frac{W}{m^3} = 4.51 \times 10^{-6} \frac{N}{m^2} \quad (1.5)$$

The force acting on a spacecraft due to solar radiation pressure is traditionally modeled using a spherical model of the spacecraft for orbit determination applications. This so-called ‘‘cannonball’’ approach treats the spacecraft as a rotationally invariant

sphere with uniform thermo-optical properties over the entire surface. An average cross-sectional area projected toward the sun, A , is determined (or guessed) for the spacecraft, as is the average reflectivity, C_R , of the spacecraft. The force due to solar radiation pressure can then be defined by:

$$\mathbf{F} = -p_{SR} A C_R \hat{\mathbf{s}} = -\frac{\Phi_{SR} A}{c} C_R \hat{\mathbf{s}} \quad (1.6)$$

where:

- \mathbf{F} = force due to solar radiation pressure on the sphere, N
- Φ_{SR} = solar flux, W/m^2
- A = projected surface area of the spacecraft, m^2
- c = speed of light, m/s
- C_R = spacecraft reflectivity coefficient
- $\hat{\mathbf{s}}$ = spacecraft - to - sun unit vector

Similar expressions can be used to model other radiative forces, with the difference being the value of the radiation flux and the direction of the force. The projected cross-sectional area and reflectivity coefficient used in the spherical model for solar radiation force are correct only if the spacecraft is truly a uniform sphere; otherwise, these values represent average values over the spacecraft's orbit and thus do not accurately model the solar radiation force. Additionally, with the spherical model, the solar radiation force is modeled as acting only in the direction opposite the spacecraft-to-sun vector, as shown in Figure 1-3.

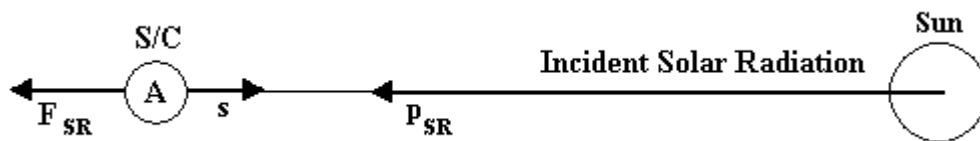


Figure 1-3 – Solar Radiation Pressure Acting on a Spherical Spacecraft Model

The approach used in this thesis is to model the force due to solar radiation pressure using a macro-model that more accurately characterizes the spacecraft. The

macro-model breaks the spacecraft up into an assembly of simple geometric plates, each with its own orientation, cross-sectional area, and thermo-optical properties. The macro-model approach thus accounts for the changing cross-sectional area of the spacecraft projected toward the sun due to the geometrically complex shape and 3-axis stabilized attitude of typical geostationary spacecraft. Additionally, the macro-model accounts for the varying reflectivity of the spacecraft due to the non-homogeneity of the spacecraft thermo-optical properties. Finally, the macro-model accounts for the fact that the solar radiation force can act in directions other than opposite the spacecraft-to-sun vector due to the actual geometry of the spacecraft.

There are some limitations of the macro-model approach used in this thesis. It does not take into account any self-shadowing effects, which occur when part of the spacecraft structure causes shadowing of other portions of the spacecraft. Additionally, the macro-model does not consider any secondary reflection effects, which refer to radiation reflected by one part of the spacecraft that then becomes incident radiation on another spacecraft structure. The macro-model approach also makes the assumption that the thermo-optical properties are homogeneous over each particular plate in the model. More precise micro-model approaches or finite element analysis, using computer programs such as TRASYS or SINDA [Refs 13, 14], can provide greater modeling precision by further resolving each plate into smaller surface elements, but suffer greater computational expense as a result.

1.2 Orbit Determination Using Space Surveillance Network

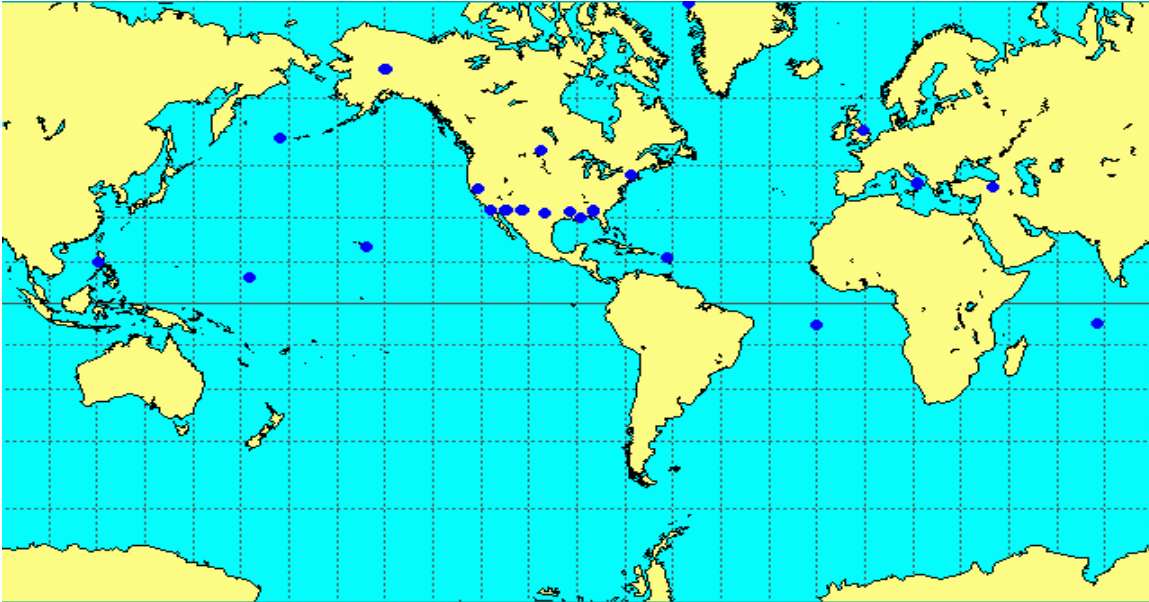
Observations

1.2.1 U.S. Space Surveillance Network (SSN) Overview

The U.S. Space Surveillance Network (SSN) is a worldwide network of sensors whose primary mission is to monitor the population of artificial satellites in orbit about the Earth [Refs 15 – 19]. Locations of SSN sensors are shown in Figure 1-4 [Ref 19]. The SSN is capable of producing a total of up to 80,000 observations per day from three primary types of sensors [Ref 19]:

- Conventional radars
- Phased-array radars
- Optical sensors

Conventional radars include both tracking and immobile antennae [Ref 19]. Millstone Hill radar (MHR), in Westford, Massachusetts, and ALTAIR, on Kwajalein Atoll, Marshall Islands, are examples of tracking antennae that contribute to the SSN. The NAVSPASUR system is a series of three transmitting and six receiving radars spanning the continental United States, and is one of the more interesting conventional radars in the SSN [Ref 19]. The NAVSPASUR system creates a fence of electromagnetic energy along the 32nd and 33rd parallel capable of detecting objects that pass through it up to 25,000 km altitude [Ref 20].



Source: Dr. T.S. Kelso [Ref 19]

Figure 1-4 – Space Surveillance Network (SSN) Sensor Locations

Phased-array radars do not have any moving mechanical parts. Instead, they are made up of thousands of small elements that are phased to electronically steer the antennae [Ref 19]. As a result, phased-array radars are capable of tracking over a dozen objects simultaneously and scan large volumes of space [Ref 19]. An example of a SSN phased-array radar is the AN/FPS-85 radar located at Eglin AFB, Florida [Ref 19].

The optical sensors in the SSN are known as the Ground-based Electro-Optical Deep Space Surveillance, or GEODSS, system [Ref 19]. Each GEODSS site combines two 40-inch primary telescopes and one 15-inch auxiliary telescope, and uses charge-coupled devices (CCDs) to electronically image spacecraft tracks [Ref 19]. Computer processing then removes the stars and other background light sources to produce the observations [Ref 19]. Examples of GEODSS sites include Haleakala Crater on Maui, Hawaii, and Diego Garcia in the Indian Ocean.

One of the more interesting optical sensors in the SSN is the Space Based Visible (SBV) telescope [Refs 15, 16]. The SBV sensor became operational in October 2000,

and is incorporated on the Midcourse Space Experiment (MSX) satellite [Ref 15]. As such, the SBV has visibility of the entire geosynchronous belt [Ref 15]. Additionally, the wide field of view of the SBV allows for efficient search operations and simultaneous multiple detections of resident space objects (RSO) [Ref 15].

1.2.2 MIT/Lincoln Laboratory's GEA CRDA

MIT/Lincoln Laboratory operates the Millstone Hill radar (MHR) as well as the SBV telescope which, as mentioned previously, provides complete coverage of the geosynchronous belt. With this unique capability, MIT/Lincoln Laboratory became involved in a Geosynchronous Encounter Analysis Cooperative Research and Development Agreement (GEA CRDA) with a number of owner/operators of geostationary spacecraft [Ref 21]. The purpose of this CRDA is to monitor close approach distances of drifting space objects with the active CRDA partner spacecraft, as well as close approach distances of other active spacecraft that can be a potential threat to the CRDA partner spacecraft [Ref 21].

As part of the GEA CRDA, MIT/Lincoln Laboratory developed the Geosynchronous Monitoring and Warning System (GMWS) to provide automated estimates of future encounters with CRDS partner spacecraft and to generate alerts of close approaches if necessary [Ref 21]. GMWS uses the MIT Lincoln Laboratory special perturbations orbit determination program DYNAMO [Ref 22]. The DYNAMO theory is used to predict close approach distances by propagating orbits out 60 days [Ref 21]. GMWS then generates WATCHES approximately 60 days in advance of a possible encounter, and WARNINGS 15 days before the encounter [Ref 21]. The WATCH and WARNING period provides time to MIT/Lincoln Laboratory and the CRDA partner to

obtain additional tracking information to improve the accuracy of the orbits, as well as an opportunity for the CRDA partner to consider any avoidance maneuvers [Ref 21].

Inputs to the GMWS orbit determination system include the following [Ref 21]:

- Millstone Hill radar (MHR) data (range, azimuth, elevation, and range-rate)
- Ground-based Electro-Optical Deep Space Surveillance (GEODSS) optical data
- Space-based visible (SBV) optical data
- Other Space Surveillance Network (SSN) observations as available
- CRDA owner/operator range and range-rate data

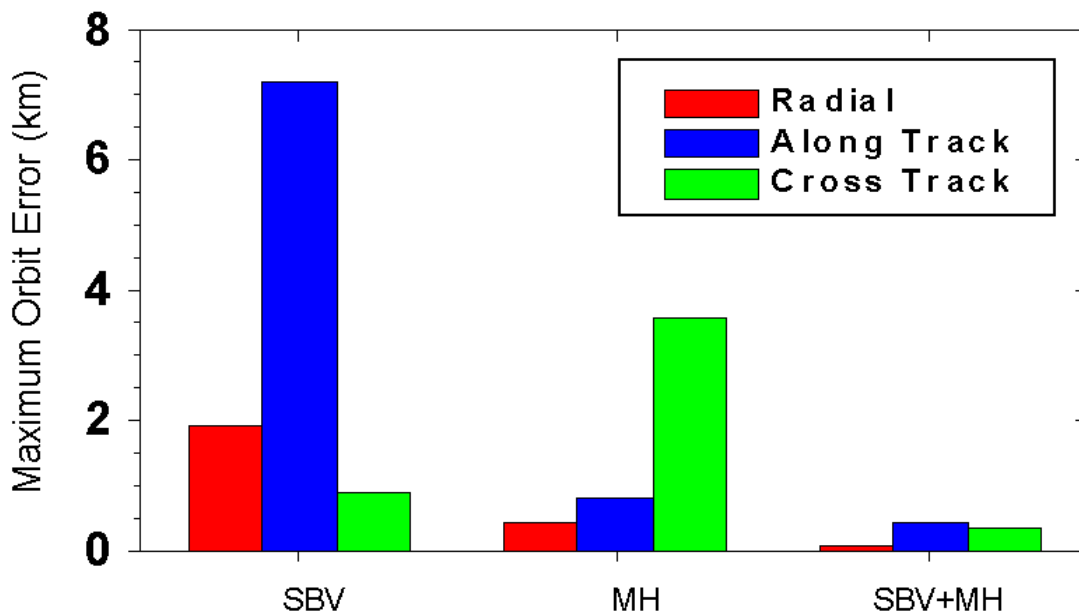
Orbit accuracy for the GMWS system is important so that an accurate estimate can be given of the error in the predicted close approach distances [Ref 21]. There are four methods used to measure geosynchronous orbit accuracy with GMWS [Ref 21]:

- Using an external reference orbit
- Overlap testing, which compares orbits with a small percentage of the fit span in common
- Examining data residuals from the orbit fits for systematic errors
- Monitoring solve-for parameters in the orbit estimation for validity

Some of the accuracy and performance testing that has been conducted using GMWS includes studies of the proper mixture of tracking data to improve orbit accuracy. Examples of such testing were conducted in late 1997 through early 1998 and involved combining MHR data with CRDA partner ranging data [Ref 21]. The orbit accuracy was determined using overlap testing, and it was found that the overlap error improved from 1272 m using only MHR data to 64 meters using MHR and CRDA partner ranging data

[Ref 21]. It is important to note that range biases were estimated and removed from the CRDA owner/operator ranging data, a process that is necessary when combining these data with other SSN observations [Ref 21].

Another orbit accuracy test was conducted in 1997 using the TDRS-4 spacecraft, with orbit accuracy determined by comparison to NASA high-accuracy reference orbits [Ref 21]. The test compared the orbit error over a long arc fit span of 30 days using only SBV data, only MHR data, and finally a combination of SBV and MHR data [Ref 21]. As Figure 1-5 shows, a 1 km error could be obtained with a mixture of the two data sources [Ref 21].



Source – Dr. Rick Abbot, et al. [Ref 21]

Figure 1-5 – GMWS Orbit Accuracy for TDRS-4 Using Various Data Sources

Additional analysis is performed at MIT/Lincoln Laboratory with the UNIX version of the Goddard Trajectory Determination System (GTDS). Details about the status of this system at MIT/Lincoln Laboratory and information about recent problems that have been studied using UNIX GTDS can be found in Chapter 6.1.1 of this thesis.

1.2.3 AFRL/AMOS High Accuracy Network Determination System

Dr. Chris Sabol and his colleagues at Air Force Maui Optical and Supercomputing Site (AMOS) have experience in precision geosynchronous orbit determination using the High Accuracy Network Determination System, or HANDS [Ref 23]. The HANDS program consists of a network of Raven-class telescopes that are used to autonomously track spacecraft and provide high-accuracy optical observations [Ref 23]. These telescopes are built with a philosophy of using commercially available products, which results in flexible systems and reduced costs [Ref 24]. The telescopes in the HANDS program have a subarcsecond metric data accuracy requirement [Ref 23]. Simulation studies by Sabol et al., have shown that geosynchronous orbit determination using a combination of the high-accuracy angular observation data with ranging data from other sensors generates much more accurate orbits than those generated using only the ranging data [Refs 18, 25].

In cooperation with the Air Force Center for Research Support (CERES), Sabol et al. have completed initial real data processing with the HANDS system [Ref 23]. One test case involved the TDRS-5 spacecraft, with the orbits generated at AMOS using only HANDS angles data [Ref 23]. The orbit determination system used was the Ops GTDS Differential Correction program, and the orbit solutions were compared to reference orbits generated by NASA/Goddard Space Flight Center (GSFC) [Ref 23]. Sabol found that Ops GTDS has difficulty converging to a solution using right ascension and declination data, so the observation pairs had to be converted to azimuth and elevation [Ref 23]. Additionally, the observation preprocessing included light time correction, which is discussed in Chapter 2.5.2 of this thesis [Ref 23]. Initial results for TDRS-5

produced an overall orbit position error of about 300 meters [Ref 23]. Sabol then solved for and removed biases in the optical data, and was able to improve the orbit accuracy to the 200 meter level [Ref 23].

The second test case run in Sabol's study involved the DSCS-3 spacecraft. In this case, the accuracy of the orbits generated was determined using abutment checks, which measure orbit accuracy by comparing adjoining fit spans in a similar manner to overlap testing [Ref 23]. The initial orbit determination was completed by CERES using only Air Force Satellite Control Network (AFSCN) observation data [Ref 23]. (The AFSCN is separate from the SSN; the AFSCN is part of the space support mission, while the SSN is part of the space control mission.) Sabol then determined the DSCS-3 orbit using only HANDS angle measurements with the range biases removed [Ref 23]. Finally, Sabol combined the HANDS angles data with the AFSCN data to determine the DSCS-3 orbit [Ref 23]. The abutment checks improved from 775 meters to 200 meters to 130 meters, respectively, for the three cases described [Ref 23].

1.2.4 Russian Space Surveillance Center (SSC)

The Russian Space Surveillance Center (SSC) began cataloging GEO spacecraft in the 1980s [Ref 26]. For low-Earth orbit (LEO) spacecraft, the SSC obtains observation data primarily from dedicated radar sensors of the Russian ballistic missile warning system [Ref 26]. However, these radars are incapable of tracking GEO space objects [Ref 26]. Instead, the SSC uses optical sensors for monitoring GEO satellites [Ref 26]. Locations and affiliations of these optical sensors are given in the following list, taken from Khutorovsky [Ref 26].

- Uzhgorod, Ukraine; 49° N, 22° E; Uzhgorod State University

- Simeiz, Ukraine; 44° N, 34° E; Institute of Astronomy of Russian Academy of Sciences
- Zvenigorod, Russia; 56° N, 37° E; Institute of Astronomy of Russian Academy of Sciences
- Zelenchuk, Russia; 41° N, 44° E; Scientific Center “Cosmoten”
- Ashkhabad, Turkmenistan; 38° N, 58° E; Astronomical Center “Asman”
- Kourovka, Russia; 57° N, 60° E; Urals State University
- Dushanbe, Tadjikistan; 38° N, 69° E; Institute of Astrophysics of Tadjikistan Academy of Sciences
- Alma-Ata, Kazakhstan; 43° N, 77° E; Astrophysics Institute of Kazakhstan Academy of Sciences
- Mondy, Russia; 52° N, 101° E; Institute of Sun and Earth Physics of the Siberian Branch of Russian Academy of Sciences

These sensors are capable of covering approximately half of the GEO belt, from approximately 30° W longitude to 160° E longitude [Ref 26]. Unfortunately, not all of these optical sensors are directly controlled by the SSC [Ref 26]. Additionally, space surveillance is not the primary mission for most of the sensors, leading to significant gaps in the observation data [Ref 26]. Both of these issues present challenges to the SSC in maintaining the catalog of GEO spacecraft [Ref 26]. Additional details about the Russian SSC GEO catalog maintenance can be found in Khutorovsky’s article, “Monitoring of GEO Satellites in Russian Space Surveillance Center,” in the proceedings of the Third US/Russian Space Surveillance Workshop [Ref 26].

1.2.5 European Space Surveillance

Donath, et al. studied the of requirements and recommendations for European space surveillance activities [Ref 27]. The study makes the statement, “Europe needs an independent space surveillance system in order to manage its space assets and to control international space treaties application.” [Ref 27]. The requirements for the system as set out in the study are to be able to track 10 cm LEO space objects and 1 m GEO space objects, similar to the U.S. space surveillance requirements [Ref 27]. The study’s recommendations for the sensors that make up the system are also similar to the existing U.S. space surveillance system: using phased-array radars to track LEO space objects, and using optical systems, including possible space-based systems, to track GEO space objects [Ref 27].

1.3 Previous Work on Improved Radiative Force Modeling

1.3.1 Ron Proulx’ One-panel Model

Dr. Ron Proulx of Draper Laboratory implemented a one-panel model for solar radiation pressure and atmospheric drag in support of the PowerSail spacecraft project [Ref 28]. This model assumed a specified angular pointing offset between the panel normal vector and the spacecraft-to-sun vector [Ref 28]. Additionally, the model specified a coefficient of incoming radiation absorbed and a coefficient of reflected radiation reflected diffusely, which were in turn used to calculate specular and diffuse reflectivity coefficients for the single flat plate [Ref 28]. This parameterization is based upon the formulation used by Hughes [Ref 29], and is covered in greater detail in Chapter 3.5 of this thesis. Proulx implemented the one-panel model for both solar radiation

pressure and atmospheric drag in the standalone version of the Draper Semi-analytical Satellite Theory orbit propagation software [Ref 28].

1.3.2 Ken Chan's Two-plate Model and Work on Complex Spacecraft Structures

Dr. Ken Chan has done extensive work on modeling both solar radiation pressure and drag. In the early 1980s, he showed that the solar radiation pressure effects on the TDRSS spacecraft could be approximated with a two-plate model [Ref 30]. One of the plates was oriented such that it was hinged to an axis normal to the orbit plane and always rotated so that its plate normal made a minimum angle with the spacecraft-to-sun vector (sun-tracking) [Ref 30]. The other plate was always oriented toward the earth (nadir-pointing) [Ref 30]. The parameters specified in this model included the area and a single reflectivity coefficient for each plate [Ref 30]. Chan performed differential correction tests that attempted to minimize the position difference between the two-plate model and the high-fidelity 69-plate TDRSS model that was in use at the time [Ref 30]. His results indicate that solving for three of the parameters (specifically the area of the sun-tracking plate, and the area and reflectivity of the nadir-pointing plate) achieved an accuracy of one meter in maximum position error [Ref 30].

Additionally, Chan has done work on solar radiation and aerodynamic force on complex spacecraft structures [Ref 31]. His work in this area includes developing methods that include self-shadowing effects, secondary reflection, and non-Lambertian reflection and re-radiation [Ref 31].

1.3.3 Kay Pechenick's TDRS Solar Radiation Pressure Model

Kay Pechenick did work in the mid-1980s on modeling solar radiation pressure acting on spacecraft, as well as on modeling thermal radiation emitted by spacecraft [Ref 32]. Pechenick gives expressions for the acceleration acting on satellites of various shapes, including flat plates, spheres, and cylinders [Ref 32]. The parameters in these models included diffuse and specular reflectivity coefficients for the spacecraft [Ref 32]. Pechenick also presents techniques for finding expressions for the mean acceleration averaged over all orientations with respect to the sun for the various satellite shapes, as well as variances and covariances for the acceleration components [Ref 32]. Pechenick includes an in-depth discussion of calculating the solar radiation pressure acceleration acting on a paraboloid-shaped spacecraft, including the possibility of secondary re-reflection within the paraboloid [Ref 32]. Additionally, the effect of thermal radiation emitted by the spacecraft due to thermal imbalance is discussed, including coupled conduction and radiation models for the evolution of the spacecraft temperature over time [Ref 32].

Pechenick went on to develop a model for solar radiation pressure acting on the TDRSS spacecraft, ignoring thermal emission acceleration [Ref 33]. The model represented the spacecraft as two flat plates and a pseudo-sphere, and used the expressions documented earlier by Pechenick for solar radiation pressure acting on structures of various shapes [Ref 33]. One flat plate was used to represent the solar panels [Ref 33]. The other flat plate was used to represent the Earth-pointing solar sail and antennae [Ref 33]. The pseudo-sphere was used to represent the assembly of the hexagonal spacecraft bus, the various cylindrical sensors, and the parabolic single-access

antennae [Ref 33]. Pechenick's TDRSS model included three parameters that could be estimated as part of the state in the orbit determination process [Ref 33]:

- The mass of the spacecraft, which was unknown due to the changing fuel supply.
- A single specular reflectivity coefficient for the flat plates. The assumption was made that the two flat plates in the model had identical reflectivity coefficients. Furthermore, the assumption was made that the absorptivity of the flat plates was zero, so the specular and diffuse reflectivity coefficients summed to one, thus requiring only one reflectivity parameter to be estimated for the flat plates.
- A single reflectivity coefficient for the pseudo-sphere.

Pechenick showed that the TDRSS spacecraft model was an improvement over the existing solar radiation pressure model in GTDS [Ref 33]. The existing model treated the spacecraft as a spherical body, while Pechenick's model was able to account for solar radiation pressure acceleration in directions other than along the spacecraft-to-sun vector [Ref 33]. Pechenick's model also accounted for the changing orientation of the spacecraft with respect to the sun, including the effects of the orientation of the solar panels and the Earth-pointing structures [Ref 33].

1.3.4 Scott Luthcke et al.'s TOPEX/POSEIDON and TDRSS Macro-models

Scott Luthcke, Dave Rowlands, and their colleagues at Goddard Space Flight Center are responsible for the development of macro-models for radiative forces on NASA's TOPEX/Poseidon [Refs 34, 35] and TDRSS spacecraft [Ref 36]. Their work was done in the early 1990s in an attempt to reduce the computational complexity

associated with the micro-models for radiative forces, while achieving an improvement in orbit determination accuracy over the common spherical model or “cannonball.” The micro-models were based on high-precision finite element analyses of the spacecraft. Unfortunately, the high computational cost associated with the micro-models outweighed their high accuracy in operational orbit determination applications.

The macro-model for TOPEX/Poseidon modeled the spacecraft using a “box-wing” satellite form [Ref 34]. This form was an assembly of flat plates arranged in the shape of a box and a connected solar array [Ref 34]. The forces acting on each of the eight surfaces were computed independently, and the resulting vector accelerations were then summed to calculate the total effect on the spacecraft center-of-mass [Ref 34]. This macro-model approach was later applied to the TDRSS spacecraft by Luthcke and Marshall [Ref 36], and is also the approach applied in this thesis for improved radiative force modeling. Even though the true form of a box and connected solar array cannot be applied to all spacecraft, the name “box-wing” came to be interchangeable with the term “macro-model” in referring to the approach of representing the spacecraft as a collection of flat plates.

The work of Luthcke and Marshall included comparisons between the macro-model and micro-model for the TOPEX/Poseidon (T/P) spacecraft [Ref 34]. The radiative forces they took into account were solar radiation pressure, Earth albedo, Earth infrared radiation, and spacecraft radiation due to thermal imbalance [Ref 34]. In their testing, they first compared simulated acceleration profiles using both the micro-model and macro-model in a variety of orbit orientations [Ref 34]. They also simulated orbits using the micro-model and subsequently fit the macro-model to these reference orbits

with the GEODYN orbit determination system [Ref 34]. In the process, they were able to adjust the reflectivity coefficients of the various plates in the macro-model [Ref 34]. Their results demonstrated a radial RMS orbit error for a 10-day arc of less than 7 cm, with the state, a single drag coefficient, and a single solar radiation pressure coefficient as the solve-for parameters [Ref 34].

Subsequent work by Luthcke and Marshall included studies on how to estimate the area and reflectivity coefficient parameters for individual plates within the macro-model [Ref 35]. They call this process “tuning” the macro-model [Ref 35].

As mentioned earlier, Luthcke and Marshall applied the macro-model approach to the Tracking and Data Relay Satellite System (TDRSS) spacecraft [Ref 36]. The macro-model represented the spacecraft as an assembly of 24 flat plates, and is described in greater detail in Chapter 5.1 of this thesis [Ref 36]. The macro-model, implemented in the GEODYN orbit determination software, was used to process both precision ground ranging data obtained with the Bilateral Transponder System (BRTS), a ground network of transponders distributed around the equator, as well as TDRSS-T/P tracking data, including range and range-rate measurements [Ref 36]. Luthcke and Marshall found that the macro-model demonstrated a definite improvement over the spherical spacecraft model for radiative forces [Ref 36]. As mentioned before, the macro-model approach used in this thesis is based in large part upon their work.

1.3.5 Ed Harvie et al.’s GOES Solar Radiation Torque Model

Ed Harvie, John Tsui, and others in NOAA’s GOES flight operations team developed a solar radiation torque model for the GOES I-M spacecraft [Ref 37]. Their aim was to model GOES during its on-orbit storage and safe modes, when the attitude

dynamics were driven primarily by solar radiation pressure [Ref 37]. Their model was based on a more sophisticated model developed by Space Systems/Loral in the analysis for the design of the trim tab on the GOES spacecraft, which is used to minimize the solar radiation pressure torque imbalance on the spacecraft caused by the solar array and the solar sail [Ref 38].

The lower-fidelity model developed by the GOES flight operations team included 15 plates [Ref 39]. Specifically, these were [Ref 39]:

- 6 main body plates
- Solar array front and back plates
- Solar array yoke front and back plates
- Trim tab front and back plates
- Solar sail top and bottom plates
- Solar sail cylinder

They were able to sufficiently model the long-term attitude dynamics of the GOES spacecraft, while improving the computational efficiency compared to the higher-fidelity model [Ref 37]. The model was also used in determining the trim tab offsets to minimize the thruster firings and number of magnetic torquer coils used to dump momentum for the GOES attitude control system [Ref 37].

1.4 Outline of Thesis

This thesis is intended as a standalone document. As such, Chapter 2 gives an overview of mathematical details regarding basic orbit propagation techniques, including two-body motion and orbital elements. Reference frames are covered, including inertial frames as well as spacecraft coordinate frames that are important for specifying the

orientation of the plates in the macro-model. An introduction is given to special, general, and semi-analytical perturbation techniques. The space-based visible observation model is detailed, and observation corrections are discussed, including light-time corrections, ionosphere refraction corrections, and bias estimation.

Chapter 3 includes mathematical details about solar radiation pressure models, including the traditional spherical (“cannonball”) model, the macro-model (“box-wing”), and the DSST one-panel (alternate parameterization) model. A set of “default” reflectivity coefficients is derived that can be used to replicate the spherical model using a single plate macro-model or the DSST one-panel model. These reflectivity values are used for testing presented in Chapter 7. The Earth albedo and Earth infrared radiation pressure model used in this study is also introduced.

Chapter 4 details partial derivatives of the various solar radiation pressure models, for both the Cowell and DSST propagators. Partial derivatives are developed for the macro-model parameterization as well as for the alternate parameterization used by the DSST one-panel model. These partials are important for differential correction applications using the improved models.

Chapter 5 presents the macro-models used in this study. The 24-plate TDRSS spacecraft macro-model developed by Luthcke and Marshall is presented in detail. The development and details of the macro-model for the GOES I-M spacecraft are also included.

Chapter 6 introduces the software tools used in this study. The status of UNIX R&D GTDS at MIT/Lincoln Laboratory is discussed, along with an overview of other problems studied using the system. The integration of the improved radiative force

models into GTDS is then described. This section begins by describing integration of a better spherical model and the one-panel model from the DSST Standalone. Integration of the box-wing model for solar radiation pressure, as well as the Earth radiation pressure (albedo and IR) model, from the GEODYN software is also described. Modifications to GTDS to enable Differential Correction capability with the new radiative force models are also included.

Chapter 7 presents results of simulated data testing using the new radiative force models. It begins with regression testing to ensure that the new models can replicate the prior capability of GTDS. Next, in order to gain an understanding of the behavior of the box-wing model compared to the cannonball model, solar radiation acceleration profiles for each are compared. Propagation runs were then completed that compare both the short-periodic effects as well as the mean element evolution of the macro-model and spherical models. Results are then presented that test the “default” reflectivity values determined in Chapter 2, comparing the improved radiative force models to the spherical model. The simulated data testing is concluded with Precise Conversion of Elements (PCE) testing, which tests the Differential Correction capability of both the Cowell and DSST theories.

Chapter 8 includes results of real data processing. The first group of test cases uses the TDRSS spacecraft macro-model. These include differential correction test cases that combine HANDS optical data with SSN data for the TDRS-05 spacecraft. There are also initial real data filter test cases applying the Extended Semi-analytical Kalman Filter (ESKF) to the TDRSS data, for both the HANDS optical data alone as well as the combined data set. The second group of test cases uses the GOES spacecraft macro-

model. These include differential correction test cases that combine owner/operator ranging data from NOAA with SSN data for the GOES-10 spacecraft. The ESKF is also applied in initial real data filter test cases to the GOES data, for both the NOAA ranging data alone as well as the combined data set.

Chapter 9 presents the conclusions of this study.

Chapter 10 includes future work topics that can be investigated to extend this research.

Appendix A includes a complete set of the plots from the simulated data testing described in Chapter 7, for a multitude of test cases. The large number of plots made it impossible to include all of them in the main body of the text.

Appendix B includes details about all of the GTDS subroutines modified, all of the new GTDS subroutines created, and all subroutines incorporated from external code as part of this project. It also includes details about the Concurrent Versions System (CVS) [Ref 40] used to control the GTDS software development environment at MIT/Lincoln Laboratory.

Appendix C presents descriptions of the new GTDS keywords developed throughout this study.

Appendix D presents sample GTDS input data files using the new models. Appendices B, C, and D are intended to assist future researchers who use GTDS.

Appendix E describes a one-panel model for atmospheric drag and lift based on Proulx' model that was implemented into GTDS as a side study to this thesis work during March – May 2003. This effort was part of the analysis of the re-entry of the Day 2 fragment that separated from the Space Shuttle Columbia in January 2003 [Ref 41].

[This page intentionally left blank.]

Chapter 2 **Mathematical Background in Orbit Propagation and Observations Models**

2.1 **Keplerian (Two-body) Motion**

Newton's law of gravitation states that two particles attract each other with a force proportional to the product of their masses and inversely proportional to the square of the distance between them, acting along the line joining them [Ref 42, pp 95].

For a system of n particles, whose masses are m_1, m_2, \dots, m_n , let the following be the position and velocity vectors for each of the particles [Ref 42, pp 95]:

$$\mathbf{r}_i = \begin{bmatrix} x_i \\ y_i \\ z_i \end{bmatrix} \qquad \mathbf{v}_i = \begin{bmatrix} dx_i/dt \\ dy_i/dt \\ dz_i/dt \end{bmatrix} \qquad (2.1)$$

Also, let [Ref 42, pp 95]:

$$\mathbf{r}_{ij} = \mathbf{r}_j - \mathbf{r}_i \qquad (2.2a)$$

and [Ref 42, pp 95]:

$$r_{ij} = |\mathbf{r}_{ij}| = |\mathbf{r}_j - \mathbf{r}_i| = \sqrt{(\mathbf{r}_j - \mathbf{r}_i) \cdot (\mathbf{r}_j - \mathbf{r}_i)} \qquad (2.2b)$$

so that the magnitude of the force of attraction between the i^{th} and j^{th} particles is [Ref 42, pp 95]:

$$f_{ij} = \frac{Gm_i m_j}{r_{ij}^2} \qquad (2.3)$$

where G is a proportionality factor called the *universal gravitation constant* (approximately $6.672 \times 10^{-11} \text{ Nm}^2/\text{kg}^2$) [Ref 42, pp 95].

The vector force acting on each particle is given by the following equation [Ref 42, pp 96]:

$$\mathbf{f}_i = G \sum_{j=1}^n \frac{m_i m_j}{r_{ij}^3} (\mathbf{r}_j - \mathbf{r}_i) \quad (2.4)$$

Assuming constant mass, Newton's second law of motion is [Ref 42, pp 96]:

$$\mathbf{f}_i = m_i \frac{d^2 \mathbf{r}_i}{dt^2} \equiv m_i \frac{d\mathbf{v}_i}{dt} \quad (2.5)$$

Setting Eq (2.4) equal to Eq (2.5), we obtain the equations of motion of n mutually attracting particles, in the form of n second-order vector differential equations [Ref 42, pp 96]:

$$m_i \frac{d^2 \mathbf{r}_i}{dt^2} = G \sum_{j=1}^n \frac{m_i m_j}{r_{ij}^3} (\mathbf{r}_j - \mathbf{r}_i) \quad (2.6)$$

The case of two mutually attracting particles can thus be described by the following pair of second-order vector differential equations [Ref 42, pp 108]:

$$m_1 \frac{d^2 \mathbf{r}_1}{dt^2} = \frac{G m_1 m_2}{r_{12}^3} (\mathbf{r}_2 - \mathbf{r}_1) \quad (2.7a)$$

$$m_2 \frac{d^2 \mathbf{r}_2}{dt^2} = \frac{G m_2 m_1}{r_{21}^3} (\mathbf{r}_1 - \mathbf{r}_2) \quad (2.7b)$$

By subtracting Eq (2.7b) from Eq (2.7a), we are left with the basic two-body equation of motion. This equation describes the motion of one body with respect to another, taking into account only the gravitational force between the two bodies:

$$\frac{d^2 \mathbf{r}}{dt^2} + \frac{\mu}{r^3} \mathbf{r} = \mathbf{0} \quad (2.8)$$

where $\mu = G(m_1 + m_2)$ is called the *gravitational parameter*.

In the case of an artificial satellite orbiting the Earth, the mass of the satellite is infinitesimal compared to the mass of the Earth. The assumption is made that $m_{\text{sat}} \rightarrow 0$ and that the gravitational parameter $\mu \rightarrow G(m_{\text{Earth}})$, which is a constant (approximately $398600.4415 \text{ km}^3/\text{s}^2$) [Ref 10, pp 7].

The two-body equation is developed with several assumptions. First, as previously mentioned, we assume that the mass of the second body is negligible compared to the mass of the primary body. Second, we assume that we are dealing with an inertial coordinate system. Third, we assume that the two bodies are spherical with uniform density, which allows us to treat them as point masses (particles). Fourth, we assume that the only force acting on the two bodies is due to the gravitational attraction between them and acts along the line joining the centers of the two bodies.

Real-world problems do not behave according to the assumptions made for the two-body problem. The actual motion of spacecraft will vary due to the gravitational attraction of the Sun and Moon (and other bodies), as well as other forces not considered in the two-body equation, including solar radiation pressure, drag, and the nonspherical central body. These additional forces are collectively called perturbations, or deviations from the normal, idealized motion [Ref 10].

2.2 Orbital Elements

Six quantities and time are required to completely specify the state of a satellite in space [Ref 42]. The six quantities can take the form of either a state vector, which usually includes the spacecraft position and velocity vectors, or an element set, which represents the orbit using scalar quantities and angle measurements called orbital elements [Ref 10].

2.2.1 Integrals of the Two-body Problem

The basic two-body equation of motion is a second-order nonlinear differential equation; however, it can be solved for an analytical solution [Ref 42, pp 114]. By performing some vector operations with Eq (2.8), we can obtain equations that are perfect differentials and can thus be integrated [Ref 42, pp 114]. The constants of integration that result are called *integrals* of the two-body problem, and are also orbital elements [Ref 42, pp 114]. These constants give insight into the properties of the solution of the two-body problem.

2.2.1.1 Specific Angular Momentum Vector

An expression for the angular momentum that is independent of the satellite's mass and constant for the orbit can be obtained by first taking the cross product of the position vector with Eq (2.8) [Ref 42, pp 115]:

$$\mathbf{r} \times \ddot{\mathbf{r}} = -\frac{\mu}{r^3} \mathbf{r} \times \mathbf{r} \quad \rightarrow \quad \frac{d}{dt}(\mathbf{r} \times \dot{\mathbf{r}}) = \mathbf{0} \quad (2.9)$$

Integrating Eq (2.9), and substituting the velocity (\mathbf{v}) for the time derivative of the position ($\dot{\mathbf{r}}$), yields [Ref 42, pp 115]:

$$\mathbf{h} = \mathbf{r} \times \mathbf{v} \quad (2.10)$$

where \mathbf{h} is the vector constant of integration that is interpreted as the specific angular momentum. This shows that the angular momentum is constant. The specific angular momentum vector is normal to the orbital plane. The \mathbf{i}_h vector is the unit vector pointing in the direction of the angular momentum vector, and is shown in Figure 2-1.

2.2.1.2 Specific Mechanical Energy

The constant energy of the satellite, which is also independent of mass, can be obtained by taking the dot product of the velocity vector with Eq (2.8) [Ref 10, pp 108]:

$$\mathbf{v} \cdot \ddot{\mathbf{r}} = -\frac{\mu}{r^3} \mathbf{v} \cdot \mathbf{r} \quad (2.11)$$

The following identity comes from the fact that the scalar quantity \dot{r} is the magnitude of the radial component of the velocity vector [Ref 10, pp 107]:

$$\mathbf{r} \cdot \mathbf{v} = rv \cos \theta = r\dot{r} \quad (2.12)$$

A similar operation for the velocity and acceleration vectors and substitution into Eq (2.11) yields [Ref 10, pp 108]:

$$v\dot{v} = -\frac{\mu}{r^3} r\dot{r} \quad (2.13)$$

The two sides of Eq (2.13) can be recognized as the following time derivatives [Ref 10, pp 108]:

$$\frac{d}{dt} \left(\frac{v^2}{2} \right) = v\dot{v} \quad \frac{d}{dt} \left(\frac{\mu}{r} \right) = -\frac{\mu}{r^2} \dot{r} \quad (2.14)$$

Substituting Eqs (2.14) into Eq (2.13) yields [Ref 10, pp 108]:

$$\frac{d}{dt} \left(\frac{v^2}{2} \right) = \frac{d}{dt} \left(\frac{\mu}{r} \right) \quad (2.15)$$

Integrating Eq (2.15) gives [Ref 10, pp 109]:

$$\xi = \frac{v^2}{2} - \frac{\mu}{r} \quad (2.16)$$

where ξ is a constant called the specific mechanical energy. It can be seen to be the sum of the kinetic and potential energy.

2.2.1.3 Eccentricity Vector

Taking the cross product of Eq (2.8) with the angular momentum vector gives [Ref 42, pp 115]:

$$\ddot{\mathbf{r}} \times \mathbf{h} = -\frac{\mu}{r^3} \mathbf{r} \times \mathbf{h} \quad (2.17)$$

Because \mathbf{h} is constant, the left-hand side of Eq (2.17) is simply:

$$\ddot{\mathbf{r}} \times \mathbf{h} = \frac{d}{dt}(\dot{\mathbf{r}} \times \mathbf{h}) = \frac{d}{dt}(\mathbf{v} \times \mathbf{h}) \quad (2.18)$$

The right-hand side of Eq (2.17) is [Ref 10, pp 110]:

$$-\frac{\mu}{r^3} \mathbf{r} \times \mathbf{h} = -\frac{\mu}{r^3} \mathbf{r} \times (\mathbf{r} \times \mathbf{v}) = -\frac{\mu}{r^3} [(\mathbf{r} \cdot \mathbf{v})\mathbf{r} - (\mathbf{r} \cdot \mathbf{r})\mathbf{v}] = -\frac{\mu}{r^3} [(\mathbf{r} \cdot \mathbf{v})\mathbf{r} - r^2 \mathbf{v}] \quad (2.19)$$

Substituting Eq (2.12) into Eq (2.19) gives [Ref 10, pp 110]:

$$-\frac{\mu}{r^3} \mathbf{r} \times \mathbf{h} = -\frac{\mu}{r^3} (r\dot{r}\mathbf{r} - r^2 \mathbf{v}) = -\frac{\mu}{r^2} \dot{r}\mathbf{r} + \frac{\mu}{r} \mathbf{v} \quad (2.20)$$

which can be recognized as the following time derivative [Ref 10, pp 110]:

$$\mu \frac{d}{dt} \left(\frac{\mathbf{r}}{r} \right) = -\frac{\mu}{r^2} \dot{r}\mathbf{r} + \frac{\mu}{r} \mathbf{v} \quad (2.21)$$

Substituting Eqs (2.18) and (2.21) into Eq (2.17) yields [Ref 42, pp 115]:

$$\frac{d}{dt}(\mathbf{v} \times \mathbf{h}) = \mu \frac{d}{dt} \left(\frac{\mathbf{r}}{r} \right) \quad (2.22)$$

Integrating Eq (2.22) yields [Ref 42, pp 115]:

$$\mu \mathbf{e} = \mathbf{v} \times \mathbf{h} - \frac{\mu}{r} \mathbf{r} \quad (2.23)$$

where the vector constant of integration $\mu \mathbf{e}$ is called the Laplace vector [Ref 42, pp 115]. The \mathbf{e} vector is called the eccentricity vector because its magnitude e is the eccentricity of the orbit [Ref 42, pp 115]. The eccentricity vector points toward periapsis,

which is the point of closest approach of the satellite to the attracting body [Ref 10, pp 132]. The \mathbf{i}_e vector is the unit vector pointing in the direction of the eccentricity vector, and is shown in Figure 2-1.

2.2.1.4 Parameter and Vis-viva Integral

Two constants of motion can be obtained by calculating the magnitude of the eccentricity vector. This is done by taking the dot product of the \mathbf{e} vector from Eq (2.23) with itself [Ref 42, pp 116]:

$$e^2 = \mathbf{e} \cdot \mathbf{e} = \frac{1}{\mu^2} (\mathbf{v} \times \mathbf{h}) \cdot (\mathbf{v} \times \mathbf{h}) - \frac{2}{\mu r} \mathbf{r} \cdot (\mathbf{v} \times \mathbf{h}) + 1 \quad (2.24)$$

This simplifies to [Ref 42, pp 116]:

$$1 - e^2 = \frac{h^2}{\mu} \left(\frac{2}{r} - \frac{v^2}{\mu} \right) \quad (2.25)$$

The first term on the right hand side is a constant called the *parameter* or *semilatus rectum*, p , and has the dimension of length [Ref 42, pp 116]:

$$p = \frac{h^2}{\mu} \quad (2.26)$$

The second term on the right-hand side is the inverse of a constant called the *semimajor axis*, a , which also has the dimension of length [Ref 42, pp 116]:

$$a = \left(\frac{2}{r} - \frac{v^2}{\mu} \right)^{-1} \quad (2.27)$$

Eq (2.27) can be rearranged to give [Ref 42, pp 116]:

$$-\frac{\mu}{2a} = \frac{v^2}{2} - \frac{\mu}{r} \quad (2.28)$$

Substituting Eq (2.28) into Eq (2.16) gives a relation between the specific mechanical energy and the semimajor axis [Ref 10, pp 109]:

$$\xi = -\frac{\mu}{2a} \quad (2.29)$$

Eq (2.27) can be rearranged again, into the form called the *energy integral* or *vis-viva integral*. [Ref 42, pp 116]:

$$v^2 = \mu \left(\frac{2}{r} - \frac{1}{a} \right) \quad (2.30)$$

Substitution of Eqs (2.26) and (2.27) into Eq (2.25) gives the relationship between the parameter, semimajor axis, and eccentricity [Ref 42, pp 117]:

$$p = a(1 - e^2) \quad (2.31)$$

2.2.1.5 Equation of Orbit and Kepler's First Law

The shape of a Keplerian orbit can be found by taking the dot product of Eq (2.23) with the \mathbf{r} vector [Ref 42, pp 117]:

$$\mathbf{e} \cdot \mathbf{r} = \frac{1}{\mu} \mathbf{v} \times \mathbf{h} \cdot \mathbf{r} - \frac{1}{r} \mathbf{r} \cdot \mathbf{r} = \frac{h^2}{\mu} - r \quad \rightarrow \quad p = r + \mathbf{e} \cdot \mathbf{r} \quad (2.32)$$

Defining the *true anomaly*, ν , as the angle between the \mathbf{e} and \mathbf{r} vectors, Eq (2.32) can be rewritten as [Ref 42, pp 117]:

$$r = \frac{p}{1 + e \cos \nu} \quad (2.33)$$

which is the *equation of orbit* in polar coordinates [Ref 42, pp 117].

It can be seen from Eq (2.33) that a Keplerian orbit is symmetric about the eccentricity vector, is bounded for $e < 1$, and unbounded for $e \geq 1$ [Ref 42, pp 117].

Converting Eq (2.33) to rectangular coordinates, with the x,y-plane as the orbital plane

and the x-axis directed along the eccentricity vector, reveals that the shape of a Keplerian orbit must be a conic section, i.e. an ellipse, a parabola, or a hyperbola. The eccentricity defines which conic section describes the orbit, with $e = 0$ a circle, $0 < e < 1$ an ellipse, $e = 1$ a parabola, and $e > 1$ a hyperbola. The property of two-body orbits being described by conic sections is actually Kepler's first law, which states, "The orbit of each planet is an ellipse with the Sun at one focus." [Ref 10, pp 100].

2.2.1.6 Period and Mean Motion (Kepler's Second and Third Laws)

Kepler's second law states, "The line joining the planet to the Sun sweeps out equal areas in equal times." [Ref 10, pp 100]. We can apply this law to obtain the *period* of an elliptical orbit, which is the time required for the radius vector to sweep over the entire closed area [Ref 42, pp 119]. The period, P , can be expressed as the area of the ellipse (πab) divided by the areal velocity ($h/2$) [Ref 42, pp 119]:

$$P = \frac{2\pi ab}{h} \quad (2.34)$$

where h is the specific angular momentum, a is the semimajor axis, and b is the *semiminor axis* of the ellipse, given by [Ref 10, pp 113]:

$$b = \sqrt{a^2(1 - e^2)} = \sqrt{ap} \quad (2.35)$$

Substituting Eqs (2.26) and (2.35) into Eq (2.34) gives the period as a function of the semimajor axis [Ref 42, pp 119]:

$$P = 2\pi \sqrt{\frac{a^3}{\mu}} \quad (2.36)$$

Eq (2.36) is actually an expression of Kepler's third law, which states, "The square of the period of a planet is proportional to the cube of its mean distance to the

Sun.” [Ref 10, pp 100]. An alternate expression for Kepler’s third law can be obtained by defining the *mean motion*, n , with units of radians per unit time [Ref 10, pp 113]:

$$n = \frac{2\pi}{P} = \sqrt{\frac{\mu}{a^3}} \quad (2.37)$$

Eq (2.37) can be rearranged to give an expression showing that the product of the square of the mean motion with the cube of the semimajor axis is a constant [Ref 10, pp 114]:

$$n^2 a^3 = \mu \quad (2.38)$$

2.2.2 Keplerian Elements

The most common element sets used to describe elliptical orbits (including circular orbits) are Keplerian elements, also called classical orbital elements (COEs), or two-body elements [Ref 10, pp 129].

The *semimajor axis*, a , specifies the size of the orbit. (Alternately, the *parameter*, p , or *mean motion*, n , can be used to specify the size.) The *eccentricity*, e , specifies the shape of the ellipse, and is the magnitude of the eccentricity vector, which points toward periapsis. The tilt of the orbit plane is specified by the *inclination*, i , which is defined as the angle between the angular momentum vector, \mathbf{h} , and the positive z-axis, \mathbf{i}_z :

$$\cos(i) = \frac{\mathbf{i}_z \cdot \mathbf{h}}{|\mathbf{i}_z| |\mathbf{h}|} \quad (2.39)$$

The *longitude of the ascending node*, Ω , is the angle from the positive x-axis, \mathbf{i}_x , to the ascending node vector, \mathbf{n} . (This orbital element is also called the *right ascension of the ascending node*, or RAAN.) A quadrant check must be done because Ω can vary from 0 to 2π [Ref 10, pp 133]:

$$\cos(\Omega) = \frac{\mathbf{i}_x \cdot \mathbf{n}}{|\mathbf{i}_x| |\mathbf{n}|} \quad (2.40)$$

$$\text{if } (n_j < 0) \text{ then } \Omega = 2\pi - \Omega$$

The ascending node is the point on the equatorial plane where the orbit crosses from south to north. The *argument of perigee*, ω , is measured from the ascending node to the point of closest approach, or periapsis. The eccentricity vector, \mathbf{e} , points toward periapsis. A quadrant check must be done because ω can vary from 0 to 2π [Ref 10, pp 134]:

$$\cos(\omega) = \frac{\mathbf{n} \cdot \mathbf{e}}{|\mathbf{n}| |\mathbf{e}|} \quad (2.41)$$

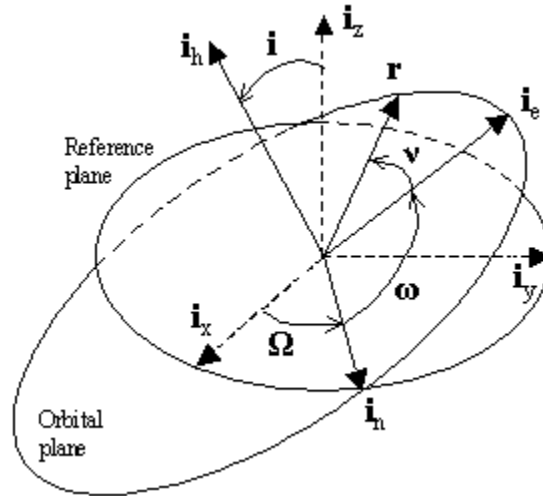
$$\text{if } (e_k < 0) \text{ then } \omega = 2\pi - \omega$$

The *true anomaly*, ν , specifies the position of the satellite within its orbit, and is the angle between periapsis and the current satellite position vector, \mathbf{r} . A quadrant check must be done because ν can vary from 0 to 2π [Ref 10, pp 134]:

$$\cos(\nu) = \frac{\mathbf{e} \cdot \mathbf{r}}{|\mathbf{e}| |\mathbf{r}|} \quad (2.42)$$

$$\text{if } (\mathbf{r} \cdot \mathbf{v} < 0) \text{ then } \nu = 2\pi - \nu$$

The Keplerian orbital elements are shown in Figure 2-1:



Source – Battin [Ref 42]

Figure 2-1 – Keplerian Orbital Elements

Keplerian elements suffer from two main singularities. The first occurs with circular orbits, which have eccentricity near zero, and leave the line of apsides undefined. The second occurs with equatorial orbits, which have inclination near zero, and leave the ascending node undefined.

In the special case of an elliptical equatorial orbit, the ascending node is undefined. In this case, the *true longitude of periapsis*, ϖ_{true} , is defined as the angle between the vernal equinox measured positive eastward to the eccentricity vector (periapsis):

$$\varpi_{true} = \frac{\mathbf{i}_x \cdot \mathbf{e}}{|\mathbf{i}_x| |\mathbf{e}|} \quad (2.43a)$$

For all orbits, the *longitude of periapsis*, ϖ , is defined by the following sum:

$$\varpi = \Omega + \omega \quad (2.43b)$$

It should be noted that this element is not necessarily a true longitude in the normal sense, because Ω and ω are measured in two different planes if the orbit is inclined [Ref 42, pp 124].

In the case of a circular inclined orbit, there is no periapsis, so argument of perigee and true anomaly cannot be defined. In this case, the *argument of latitude*, u , is the angle eastward from the ascending node to the spacecraft position vector. A relation in terms of the classical orbital elements for u is:

$$u = \omega + \nu \quad (2.44)$$

This relation is always true because ω and ν are in the same plane [Ref 10, pp 137].

For the special case of a circular equatorial orbit, neither the ascending node nor periapsis are defined. The *true longitude*, L , is the angle positive eastward from the positive x-axis to the spacecraft position vector

$$\cos(L) = \frac{\mathbf{i}_x \cdot \mathbf{r}}{|\mathbf{i}_x| |\mathbf{r}|} \quad (2.45a)$$

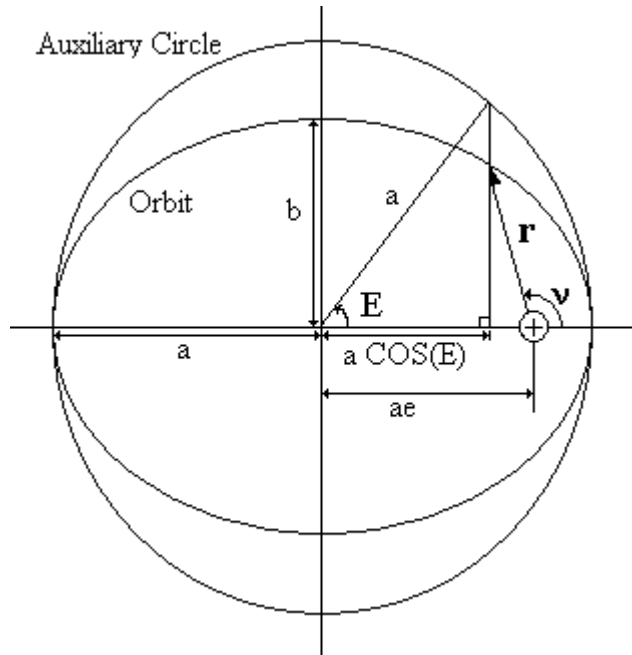
The true longitude can be approximated as [Ref 10, pp 137]:

$$L \approx \Omega + \omega + \nu \quad (2.45b)$$

because the angles are in different planes when the orbit is inclined.

2.2.2.1 True, Eccentric, and Mean Anomalies

The true anomaly is not a constant in two-body motion; it varies with time and is sometimes called the fast variable. Other orbital elements can be used instead of the true anomaly to describe the satellite's position within its orbit. The first of these is the *eccentric anomaly*, E . This angle is defined on the auxiliary circle of radius a , that can be drawn around an elliptical orbit, as shown in Figure 2-2.



Source – Battin, pp 158

Figure 2-2 – Orbital Anomalies for Elliptic Motion

From Figure 2-2, if the x,y-plane is defined as the orbital plane, the origin is the center of the Earth, and the x-axis points toward periapsis, the r vector can be expressed as follows [Ref 43, pp 22]:

$$\mathbf{r} = \begin{bmatrix} r_x \\ r_y \end{bmatrix} = \begin{bmatrix} r \cos \nu \\ r \sin \nu \end{bmatrix} = \begin{bmatrix} a(\cos E - e) \\ a\sqrt{1-e^2} \sin E \end{bmatrix} \quad (2.46)$$

The magnitude of the r vector in terms of the eccentric anomaly is then [Ref 42, pp 158]:

$$r = a(1 - e \cos E) \quad (2.47)$$

Eqs (2.33), (2.46) and (2.47) can be solved for several relationships between the true and eccentric anomalies [Ref 42, pp 159]:

$$\cos \nu = \frac{\cos E - e}{1 - e \cos E} \quad \cos E = \frac{e + \cos \nu}{1 + e \cos \nu} \quad (2.48a)$$

$$\sin \nu = \frac{\sqrt{1-e^2} \sin E}{1-e \cos E} \quad \sin E = \frac{\sqrt{1-e^2} \sin \nu}{1+e \cos \nu} \quad (2.48b)$$

$$\tan \frac{\nu}{2} = \sqrt{\frac{1+e}{1-e}} \tan \frac{E}{2} \quad \tan \frac{E}{2} = \sqrt{\frac{1-e}{1+e}} \tan \frac{\nu}{2} \quad (2.48c)$$

Eqs (2.48c) are useful because $(\nu/2)$ and $(E/2)$ are always in the same quadrant, so no quadrant check is required when using these relationships [Ref 42, pp 159].

Kepler's equation expresses the position in the orbit as a function of time, in terms of the eccentric anomaly [Ref 42, pp 160]:

$$E - e \sin E = n(t - \tau) \quad (2.49)$$

where n is the mean motion from Eq (2.37) and τ is the time of periapsis passage [Ref 42, pp 160].

The right-hand side of Eq (2.49) is also called the *mean anomaly*, M [Ref 10, pp 212]:

$$M = n(t - \tau) \quad (2.50)$$

The mean anomaly has no geometric interpretation, but instead is related to time and corresponds to the angular position of a body moving with constant angular velocity on the auxiliary circle of Figure 2-2 [Ref 42, pp 160].

We can then rewrite Kepler's Equation so that it relates the mean and eccentric anomalies:

$$M = E - e \sin E \quad (2.51)$$

It should be noted that calculating the eccentric or true anomalies given the mean anomaly using Kepler's equation is a transcendental operation [Ref 10, pp 230]. One must use an iterative method in order to solve for E to a sufficient accuracy given M and

e. The inverse problem of calculating the mean anomaly given the eccentric or true anomalies is a straightforward calculation that does not require iteration.

Similar anomalies to the eccentric anomaly are defined for parabolic and hyperbolic orbits, namely, the *parabolic anomaly* and *hyperbolic anomaly*, respectively.

2.2.2.2 Keplerian Elements from Position and Velocity

To obtain the Keplerian elements from the satellite position and velocity vectors, we first calculate the angular momentum vector as the cross product of the satellite position and velocity vectors using Eq (2.10).

$$\mathbf{h} = \mathbf{r} \times \mathbf{v}$$

The \mathbf{i}_h vector is the unit vector pointing in the direction of the angular momentum vector, and is shown in Figure 2-1.

Next, we calculate the ascending node vector as the cross product of the z unit vector and the angular momentum vector. The \mathbf{n} vector points toward the ascending node. The \mathbf{i}_n vector is the unit vector pointing in the direction of the ascending node vector, and is shown in Figure 2-1.

$$\mathbf{n} = \mathbf{i}_z \times \mathbf{h} \tag{2.52}$$

We calculate the eccentricity vector using Eq (2.23).

$$\mu \mathbf{e} = \mathbf{v} \times \mathbf{h} - \frac{\mu}{r} \mathbf{r}$$

To actually calculate the Keplerian elements, we begin by obtaining the semimajor axis using the vis-viva integral (Eq (2.27)). The eccentricity e is simply the magnitude of the \mathbf{e} vector. We calculate the Euler angles, i , Ω , and ω , using Eqs (2.39), (2.40), and (2.41), respectively. Finally, we calculate the true anomaly using Eq (2.42).

2.2.2.3 Position and Velocity from the Keplerian Elements

To transform from the Keplerian elements to Cartesian position and velocity vectors, it is convenient to first express the position and velocity vectors in the perifocal coordinate system (PQW), and then rotate the vectors to the reference coordinate system. In the PQW coordinate system, the P axis points toward perigee, and the Q axis is 90 deg from the P axis in the direction of the satellite motion [Ref 10, pp 41]. The W axis is normal to the orbital plane [Ref 10, pp 41].

The position vector in the PQW coordinate system is a function of the semimajor axis (or parameter), eccentricity, and true anomaly. The magnitude of the r vector is expressed in the equation of orbit (Eq (2.33)), and the P and Q components of the r vector are dependent on the true anomaly [Ref 10, pp 149]:

$$\mathbf{r}_{PQW} = \begin{bmatrix} r \cos \nu \\ r \sin \nu \\ 0 \end{bmatrix} = \begin{bmatrix} \frac{p \cos \nu}{1 + e \cos \nu} \\ \frac{p \sin \nu}{1 + e \cos \nu} \\ 0 \end{bmatrix} = \begin{bmatrix} \frac{a(1 - e^2) \cos \nu}{1 + e \cos \nu} \\ \frac{a(1 - e^2) \sin \nu}{1 + e \cos \nu} \\ 0 \end{bmatrix} \quad (2.53)$$

The velocity vector in the PQW system is obtained by differentiating the position vector [Ref 10, pp 149]:

$$\mathbf{v}_{PQW} = \begin{bmatrix} \dot{r} \cos \nu - r \dot{\nu} \sin \nu \\ \dot{r} \sin \nu + r \dot{\nu} \cos \nu \\ 0 \end{bmatrix} = \begin{bmatrix} -\sqrt{\frac{\mu}{p}} \sin \nu \\ \sqrt{\frac{\mu}{p}} (e + \cos \nu) \\ 0 \end{bmatrix} = \begin{bmatrix} -\sqrt{\frac{\mu}{a(1 - e^2)}} \sin \nu \\ \sqrt{\frac{\mu}{a(1 - e^2)}} (e + \cos \nu) \\ 0 \end{bmatrix} \quad (2.54)$$

The rotation of the position and velocity vectors from the PQW coordinate system to the reference coordinate system is simplified through the use of rotation matrices. The number after “ROT” designates the principal axis of the rotation, and the angle in parenthesis is the angle through which we are rotating [Ref 10, pp 48]. The three rotation matrices for a right-handed coordinate system are as follows [Ref 10, pp 49]:

$$ROT1(\alpha) = \begin{bmatrix} 1 & 0 & 0 \\ 0 & \cos \alpha & \sin \alpha \\ 0 & -\sin \alpha & \cos \alpha \end{bmatrix} \quad (2.55a)$$

$$ROT2(\alpha) = \begin{bmatrix} \cos \alpha & 0 & -\sin \alpha \\ 0 & 1 & 0 \\ \sin \alpha & 0 & \cos \alpha \end{bmatrix} \quad (2.55b)$$

$$ROT3(\alpha) = \begin{bmatrix} \cos \alpha & \sin \alpha & 0 \\ -\sin \alpha & \cos \alpha & 0 \\ 0 & 0 & 1 \end{bmatrix} \quad (2.55c)$$

The rotation from the PQW frame to the reference frame is a series of three rotations. The first is a rotation about the W axis through the angle $-\omega$, the second is a rotation about the new P axis (aligned with the \mathbf{n} vector) through the angle $-i$, and the third is a rotation about the new W axis (aligned with the z-axis) through the angle $-\Omega$, as follows [Ref 10, pp 151]:

$$\mathbf{r}_{IJK} = ROT3(-\Omega)ROT1(-i)ROT3(-\omega)\mathbf{r}_{PQW} \quad (2.56a)$$

$$\mathbf{v}_{IJK} = ROT3(-\Omega)ROT1(-i)ROT3(-\omega)\mathbf{v}_{PQW} \quad (2.56b)$$

2.2.3 Delaunay Variables

Canonical variables have special relationships that make them convenient for use in astrodynamics. Specifically, if the equations of motion for two-body motion are

expressed as a 6x6 matrix multiplied by a 6x1 state vector, the 6x6 matrix turns out to contain only diagonal elements when using canonical variables [Ref 10, pp 143]. The Lagrange or Poisson brackets thus take on values of ± 1 [Ref 10]. One set of canonical variables is the satellite position and velocity vectors [Ref 10, pp 569; Ref 42]. This thesis will discuss two other sets of canonical variables. The first set is the Delaunay variables. The second set is the Poincaré variables, introduced in Chapter 2.2.4.

The Delaunay variables are the canonical counterpart to the Keplerian orbital elements. The Delaunay variables are used in the development of the Brouwer theory, which is the basis for the GP4 and PPT2 theories. They suffer from the same singularities as the Keplerian elements for low eccentricity and low inclination [Ref 10, pp 143]. They also suffer from a singularity near the critical inclination ($\sim 63.4^\circ$) that appears as a small divisor in the Hamiltonian VOP canonical transformations [Ref 10, pp 594].

The Delaunay variables are defined in terms of the Keplerian elements as follows [Ref 44, pp 169]:

$$L = \sqrt{\mu a} \quad (2.57a)$$

$$G = L\sqrt{1 - e^2} \quad (2.57b)$$

$$H = G \cos i \quad (2.57c)$$

$$l = M \quad (2.57d)$$

$$g = \omega \quad (2.57e)$$

$$h = \Omega \quad (2.57f)$$

2.2.3.1 Delaunay Variables from Position and Velocity

To transform from the Cartesian position and velocity vectors to the Delaunay variables, begin by calculating the specific angular momentum vector using Eq (2.10), the ascending node vector using Eq (2.52), and the eccentricity vector using Eq (2.23):

$$\mathbf{h} = \mathbf{r} \times \mathbf{v}$$

$$\mathbf{n} = \mathbf{i}_z \times \mathbf{h}$$

$$\mu \mathbf{e} = \mathbf{v} \times \mathbf{h} - \frac{\mu}{r} \mathbf{r}$$

The Delaunay variable G is simply the magnitude of the specific angular momentum vector:

$$G = |\mathbf{h}| = \sqrt{h_x^2 + h_y^2 + h_z^2} \quad (2.58)$$

The variable H is thus the z component of the specific angular momentum:

$$H = h_z \quad (2.59)$$

We calculate the semimajor axis from the vis-viva integral of Eq (2.27):

$$a = \left(\frac{2}{r} - \frac{v^2}{\mu} \right)^{-1}$$

The variable L is related to the total mechanical energy:

$$L = \sqrt{\mu a} \quad (2.60)$$

The Delaunay variables h and g are equivalent to the Keplerian elements Ω and ω , respectively, and are calculated using Eqs (2.40) and (2.41):

$$\cos(h) = \frac{\mathbf{i}_x \cdot \mathbf{n}}{|\mathbf{i}_x| |\mathbf{n}|}$$

$$\cos(g) = \frac{\mathbf{n} \cdot \mathbf{e}}{|\mathbf{n}| |\mathbf{e}|}$$

The variable l is equivalent to the mean anomaly, which we obtain by first calculating the true anomaly using Eq (2.42) and the eccentric anomaly using Eqs (2.48). We then calculate the mean anomaly using Kepler's equation (Eq (2.51)).

2.2.3.2 Position and Velocity from the Delaunay Variables

To transform from the Delaunay variables to Cartesian position and velocity, we take the same approach as we did with the Keplerian elements. We first express the position and velocity vectors in the PQW coordinate frame, and then rotate to the reference frame. We first obtain an expression for the parameter in terms of G :

$$p = \frac{G^2}{\mu} \quad (2.61)$$

We then express the eccentricity in terms of G and L :

$$e^2 = \sqrt{1 - \frac{G^2}{L^2}} \quad (2.62)$$

The inclination can be expressed in terms of H and G :

$$\cos i = \frac{H}{G} \quad (2.63)$$

We next calculate the true anomaly, v , from the Delaunay variable l , which is equivalent to the mean anomaly. An iterative method must be used to solve Kepler's equation (Eq (2.51)) for the eccentric anomaly. Eqs (2.48) can then be used to calculate v from E .

We can now calculate \mathbf{r}_{PQW} and \mathbf{v}_{PQW} using Eqs (2.53) and (2.54), respectively.

The rotation from the PQW coordinate system to the reference coordinate system is done using a form of Eqs (2.56) that uses Delaunay variables in place of Keplerian elements:

$$\mathbf{r}_{JK} = ROT3(-h)ROT1(-i)ROT3(-g)\mathbf{r}_{PQW} \quad (2.64a)$$

$$\mathbf{v}_{JK} = ROT3(-h)ROT1(-i)ROT3(-g)\mathbf{v}_{PQW} \quad (2.64b)$$

2.2.4 Equinoctial Elements

The equinoctial elements avoid the singularities encountered when using Keplerian elements. The equinoctial elements were originally developed by Lagrange in 1774 [Ref 42, pp 492]. Eqs (2.65a) – (2.65f) give the equinoctial elements in terms of the Keplerian elements [Ref 45].

$$a = a \quad (2.65a)$$

$$h = e \sin(\omega + I\Omega) \quad (2.65b)$$

$$k = e \cos(\omega + I\Omega) \quad (2.65c)$$

$$p = \tan^I(i/2)\sin\Omega \quad (2.65d)$$

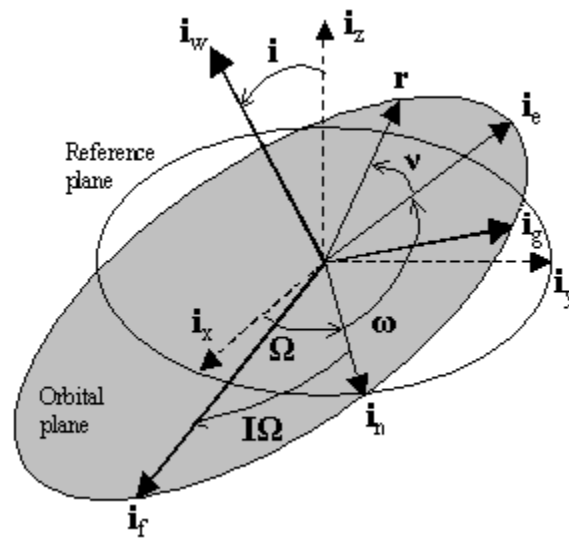
$$q = \tan^I(i/2)\cos\Omega \quad (2.65e)$$

$$\lambda = M + \omega + I\Omega \quad (2.65f)$$

True retrograde equatorial orbits ($i = 180$) cause problems because p and q are undefined. This problem is solved by introducing a retrograde factor, I , which is $+1$ for direct orbits and -1 for retrograde orbits.

The equinoctial coordinate frame is shown in Figure 2-3, and can be obtained from the reference frame by a rotation through the angle Ω about the \mathbf{i}_z axis, followed by a rotation through the angle i about the new x axis (which points in the same direction as

the \mathbf{i}_h vector), followed by a rotation through the angle $-\Omega$ about the new z axis (which points in the same direction as the \mathbf{i}_h vector). The resulting equinoctial coordinate frame axes are specified as \mathbf{i}_f , \mathbf{i}_g , and \mathbf{i}_w . The equinoctial coordinate frame is thus a coordinate frame with the satellite orbital plane as the fundamental plane, the principal direction, \mathbf{i}_f , oriented toward the point in the orbit offset by the angle $-\Omega$ from the ascending node, and the third axis, \mathbf{i}_w , oriented in the same direction as the angular momentum vector.



Source – McClain [Ref 45]

Figure 2-3 – Equinoctial Coordinate Frame

The elements h and k represent the projection of the eccentricity vector onto the \mathbf{i}_g and \mathbf{i}_f directions, respectively. The elements p and q represent the projection of the vector oriented in the direction of the ascending node with magnitude $\tan(i/2)$, onto the \mathbf{i}_g and \mathbf{i}_f directions, respectively. The element λ is the mean longitude, which is a variation of the true longitude, L , defined in Eq (2.45).

It is noted that the equinoctial element set is sometimes expressed in a slightly different fashion. In the PPT2 and USM theories, the elements p and q are given with “ $\sin(i/2)$ ” replacing the “ $\tan(i/2)$ ” terms in Eqs (2.65d) and (2.65e). Other sources

express p and q using “ $\sin(i)$ ” or even just “ i ” in place of the “ $\tan(i/2)$ ” terms. These differences change the elements p and q to represent the projection of the vector oriented in the direction of the ascending node with a different magnitude (equal to whatever term replaces “ $\tan(i/2)$ ”), onto the \mathbf{i}_g and \mathbf{i}_f directions, respectively.

The reverse transformations from equinoctial to Keplerian elements are [Ref 45]:

$$a = a \quad (2.66a)$$

$$e = \sqrt{h^2 + k^2} \quad (2.66b)$$

$$i = \cos^{-1} \left[\frac{(1 - p^2 - q^2)I}{1 + p^2 + q^2} \right] \quad (2.66c)$$

$$\omega = \tan^{-1} \left(\frac{h}{k} \right) - I \tan^{-1} \left(\frac{p}{q} \right) \quad (2.66d)$$

$$\Omega = \tan^{-1} \left(\frac{p}{q} \right) \quad (2.66e)$$

$$M = \lambda - \omega - I\Omega \quad (2.66f)$$

It should be noted that Eqs (2.65) and (2.66), giving the transformations between the Keplerian and equinoctial elements, apply in osculating element space. This is an important distinction when considering real-world orbits, whose trajectories do not truly behave according to the two-body equation of motion, Eq (2.8). In the perturbed case, the orbital elements are no longer constants of the motion, and are instead time-varying parameters.

Osculating elements refer to those elements that are defined at any particular instant in time by the corresponding position and velocity vectors [Ref 10, pp 546]. The word “osculate” comes from a Latin word meaning “to kiss”; thus the osculating orbit “kisses” the true orbit at that particular instant [Ref 10, pp 546]. The *osculating ellipse*

refers to the two-body orbit that the satellite would follow if the perturbing forces were removed at that time [Ref 10, pp 546]. Thus, each point on the perturbed trajectory has a corresponding set of osculating elements [Ref 10, pp 546]. Osculating elements track the long-periodic, short-periodic, and secular variations in the perturbed orbit, and are useful for high-precision trajectory analysis [Ref 10, pp 546].

Mean elements, in contrast, are averaged over some appropriate time interval [Ref 10, pp 546]. They can also be averaged over an appropriate angular displacement such as true anomaly, eccentric anomaly, mean anomaly, or longitude [Ref 10, pp 546]. As a result, mean elements are smoothly-varying compared to osculating elements, and do not chase the short-periodic variations that the osculating elements experience [Ref 10, pp 546]. Mean elements are useful for orbit propagations with a long time span because they give an idea of the satellite's long-term behavior [Ref 10, pp 546]. Additionally, mean elements are useful in recursive estimation and filtering applications because they are slowly-varying and behave more linearly than osculating elements [Ref 46].

2.2.4.1 Equinoctial Elements from Position and Velocity

To obtain the equinoctial elements from the satellite position and velocity vectors, we first calculate the angular momentum vector as the cross product of the satellite position and velocity vectors using Eq (2.10).

$$\mathbf{h} = \mathbf{r} \times \mathbf{v}$$

The \mathbf{i}_w vector is the unit vector pointing in the direction of the angular momentum vector, and is shown in Figure 2-3:

$$\mathbf{i}_w = \mathbf{i}_h = \frac{\mathbf{h}}{|\mathbf{h}|} = \frac{\mathbf{h}}{\sqrt{h_x^2 + h_y^2 + h_z^2}} \quad (2.67)$$

We calculate the eccentricity vector using Eq (2.23).

$$\mu \mathbf{e} = \mathbf{v} \times \mathbf{h} - \frac{\mu}{r} \mathbf{r}$$

We obtain the semimajor axis using the vis-viva integral (Eq (2.27)).

$$a = \left(\frac{2}{r} - \frac{v^2}{\mu} \right)^{-1}$$

The elements p and q can be obtained from components of the \mathbf{i}_w vector [Ref 45]:

$$p = \frac{\mathbf{i}_{wx}}{1 + \mathbf{Ii}_{wz}} \quad (2.68)$$

$$q = \frac{-\mathbf{i}_{wy}}{1 + \mathbf{Ii}_{wz}} \quad (2.69)$$

These elements are then used to calculate the \mathbf{i}_f and \mathbf{i}_g vectors [Ref 45]:

$$\mathbf{i}_f = \frac{1}{1 + p^2 + q^2} \begin{bmatrix} 1 - p^2 - q^2 \\ 2pq \\ -2pI \end{bmatrix} \quad (2.70)$$

$$\mathbf{i}_g = \frac{1}{1 + p^2 + q^2} \begin{bmatrix} 2pqI \\ (1 - p^2 - q^2)I \\ 2q \end{bmatrix} \quad (2.71)$$

The elements h and k are calculated as the dot product of the eccentricity vector with the \mathbf{i}_g and \mathbf{i}_f vectors, respectively [Ref 45]:

$$h = \mathbf{e} \cdot \mathbf{i}_g \quad (2.72)$$

$$k = \mathbf{e} \cdot \mathbf{i}_f \quad (2.73)$$

The final equinoctial element to be calculated is the mean longitude, λ . We first calculate the position of the satellite in x,y coordinates, with the x,y-plane as the orbital plane and the x-axis oriented along the \mathbf{i}_f vector. The x and y components are a function

of the magnitude of the position vector and the true longitude, L , and can thus be calculated by taking the dot product of the position vector with the \mathbf{i}_f and \mathbf{i}_g vectors, respectively [Ref 45]:

$$\mathbf{r} = \begin{bmatrix} r_x \\ r_y \end{bmatrix} = \begin{bmatrix} r \cos L \\ r \sin L \end{bmatrix} = \begin{bmatrix} \mathbf{r} \cdot \mathbf{i}_f \\ \mathbf{r} \cdot \mathbf{i}_g \end{bmatrix} \quad (2.74)$$

We then calculate the sine and cosine of the eccentric longitude, F [Ref 45]:

$$\cos F = k + \frac{(1 - k^2 \beta)r_x - (hk\beta)r_y}{a\sqrt{1 - h^2 - k^2}} \quad (2.75a)$$

$$\sin F = h + \frac{(1 - h^2 \beta)r_y - (hk\beta)r_x}{a\sqrt{1 - h^2 - k^2}} \quad (2.75b)$$

where [Ref 45]:

$$\beta = \frac{1}{1 + \sqrt{1 - h^2 - k^2}}$$

The mean longitude, λ , can then be calculated by using Eqs (2.75) in an alternate form of Kepler's equation [Ref 45]:

$$\lambda = F - k \sin F + h \cos F \quad (2.76)$$

2.2.4.2 Position and Velocity from the Equinoctial Elements

To transform from the equinoctial elements to Cartesian position and velocity, we first express the position and velocity vectors in the equinoctial coordinate frame, and then rotate to the reference frame. We first calculate the true longitude, L (defined in Eq (2.45)), from the mean longitude. To do this, we use an iterative method to solve the alternate form of Kepler's equation given in Eq (2.76) for the eccentric longitude. We then calculate the true longitude from the eccentric longitude.

The position vector in the equinoctial coordinate system is a function of the semimajor axis, h , k , and true longitude. The magnitude of the \mathbf{r} vector is simply the equation of orbit (Eq (2.33)), expressed in terms of the equinoctial elements [Ref 45]:

$$\mathbf{r}_{FGW} = \begin{bmatrix} r \cos L \\ r \sin L \\ 0 \end{bmatrix} \quad (2.77)$$

where [Ref 45]:

$$r = \frac{a(1-h^2-k^2)}{1+k \cos L + h \sin L}$$

The velocity vector in the equinoctial system is obtained by differentiating the position vector [Ref 45]:

$$\mathbf{v}_{FGW} = \begin{bmatrix} \dot{r} \cos L - r\dot{L} \sin L \\ \dot{r} \sin L + r\dot{L} \cos L \\ 0 \end{bmatrix} = \begin{bmatrix} \frac{-na(h + \sin L)}{\sqrt{1-h^2-k^2}} \\ \frac{na(k + \cos L)}{\sqrt{1-h^2-k^2}} \\ 0 \end{bmatrix} \quad (2.78)$$

The rotation from the equinoctial frame to the reference frame can be expressed as a matrix constructed from the \mathbf{i}_f , \mathbf{i}_g , and \mathbf{i}_w unit vectors in the reference frame. We can obtain expressions for these vectors from Eqs (2.67), (2.70), and (2.71). The resulting rotation matrix is equivalent to performing a series of three rotations - the first is about the \mathbf{i}_w axis through the angle $I\Omega$, the second is about the new \mathbf{i}_f axis (aligned with the \mathbf{n} vector) through the angle $-i$, and the third is about the new \mathbf{i}_w axis (aligned with the z -axis) through the angle $-\Omega$ [Ref 45]:

$$\mathbf{r}_{LJK} = ROT3(-\Omega)ROT1(-i)ROT3(I\Omega)\mathbf{r}_{FGW} = \begin{bmatrix} \mathbf{i}_f \\ \mathbf{i}_g \\ \mathbf{i}_w \end{bmatrix} \mathbf{r}_{FGW} \quad (2.79a)$$

$$\mathbf{v}_{JK} = ROT3(-\Omega)ROT1(-i)ROT3(I\Omega)\mathbf{v}_{FGW} = \begin{bmatrix} \mathbf{i}_f & \mathbf{i}_g & \mathbf{i}_w \end{bmatrix} \mathbf{v}_{FGW} \quad (2.79b)$$

2.2.5 Poincaré Variables

The Poincaré variables are the canonical counterpart of the equinoctial elements. Like the equinoctial elements, they are a nonsingular element set [Ref 10, pp 143].

Smart gives the Poincaré variables as follows, in terms of the Keplerian elements [Ref 44, pp 173-174]:

$$\Lambda = \sqrt{\mu a} \quad (2.80a)$$

$$\xi = e \sin(\omega + \Omega) \sqrt{2\Lambda / (1 + \sqrt{1 - e^2})} \quad (2.80b)$$

$$\eta = e \cos(\omega + \Omega) \sqrt{2\Lambda / (1 + \sqrt{1 - e^2})} \quad (2.80c)$$

$$u = \sin i \sin \Omega \sqrt{2\Lambda \sqrt{1 - e^2} / (1 + \cos i)} \quad (2.80d)$$

$$v = \sin i \cos \Omega \sqrt{2\Lambda \sqrt{1 - e^2} / (1 + \cos i)} \quad (2.80e)$$

$$\lambda = \lambda \quad (2.80f)$$

It can be seen that the expressions for ξ and η include terms that are similar to the eccentric equinoctial elements h and k (which are given in Equations (2.65b) and (2.65c), respectively). It can also be seen that the expressions for u and v include terms that are nearly equal to the equinoctial elements p and q (which are given in Equations (2.65d) and (2.65e), respectively), with the exception of $\sin(i)$ terms instead of $\tan(i/2)$ terms. The expressions for u and v can be rewritten in terms of p and q by using the following identity, which is derived using trigonometric double-angle and half-angle identities:

$$\begin{aligned}
\sin i &= 2 \sin(i/2) \cos(i/2) \\
&= 2 \tan(i/2) \cos^2(i/2) \\
&= 2 \tan(i/2) \left(\frac{1 + \cos i}{2} \right) \\
&= (1 + \cos i) \tan(i/2)
\end{aligned} \tag{2.81}$$

By making the above substitution for the $\sin(i)$ terms, bringing the $(1 + \cos(i))$ terms under the radicals, and simplifying, the equations for u and v become:

$$u = \tan(i/2) \sin \Omega \sqrt{2\Lambda \sqrt{1-e^2} (1 + \cos i)} \tag{2.82a}$$

$$v = \tan(i/2) \cos \Omega \sqrt{2\Lambda \sqrt{1-e^2} (1 + \cos i)} \tag{2.82b}$$

which are seen to include terms that are similar to the equinoctial elements p and q .

The Poincaré variables are thus defined in terms of the Keplerian and equinoctial elements as follows:

$$\Lambda = \sqrt{\mu a} \tag{2.83a}$$

$$\xi = h \sqrt{2\Lambda / (1 + \sqrt{1-e^2})} \tag{2.83b}$$

$$\eta = k \sqrt{2\Lambda / (1 + \sqrt{1-e^2})} \tag{2.83c}$$

$$u = p \sqrt{2\Lambda \sqrt{1-e^2} (1 + \cos i)} \tag{2.83d}$$

$$v = q \sqrt{2\Lambda \sqrt{1-e^2} (1 + \cos i)} \tag{2.83e}$$

$$\lambda = \lambda \tag{2.83f}$$

2.2.5.1 Poincaré Variables from Position and Velocity

To transform from the Cartesian position and velocity vectors to the Poincaré variables, we use a similar method as the calculation of the equinoctial elements, because both sets of orbital elements reference the equinoctial coordinate system. In fact, to

calculate the Poincaré variables we must first calculate the equinoctial elements using the same method given in Chapter 2.2.4.1. Obtaining the Poincaré variables from the equinoctial elements then requires only a few calculations. First, Λ is related to the total mechanical energy:

$$\Lambda = \sqrt{\mu a} \quad (2.84)$$

Next, the calculations for ξ and η can be simplified by recognizing that the eccentricity can be expressed as a function of h and k :

$$e^2 = h^2 + k^2 \quad (2.85)$$

so that we can calculate ξ and η from:

$$\xi = h \sqrt{2\Lambda / (1 + \sqrt{1 - h^2 - k^2})} \quad (2.86)$$

$$\eta = k \sqrt{2\Lambda / (1 + \sqrt{1 - h^2 - k^2})} \quad (2.87)$$

The calculations for u and v can be simplified by recognizing that part of the term under the radical is equal to the magnitude of the specific angular momentum vector:

$$\Lambda \sqrt{1 - e^2} = |\mathbf{h}| = \sqrt{h_x^2 + h_y^2 + h_z^2} \quad (2.88)$$

Also, recognize that $\cos(i)$ can be expressed using the following trigonometric relationship:

$$\cos i = \frac{h_z}{|\mathbf{h}|} \quad (2.89)$$

so that we can calculate u and v as:

$$u = p \sqrt{2|\mathbf{h}| \left(1 + \frac{h_z}{|\mathbf{h}|} \right)} = p \sqrt{2(|\mathbf{h}| + h_z)} \quad (2.90)$$

$$v = q \sqrt{2|\mathbf{h}| \left(1 + \frac{h_z}{|\mathbf{h}|}\right)} = q \sqrt{2(|\mathbf{h}| + h_z)} \quad (2.91)$$

We already have the mean longitude, λ , from the method in Chapter 2.2.4.1.

2.2.5.2 Position and Velocity from the Poincaré Variables

To convert from the Poincaré variables to Cartesian position and velocity vectors, we first express the position and velocity vectors in the equinoctial coordinate frame, and then rotate to the reference frame. This is similar to the method used to convert the equinoctial elements to position and velocity.

We first require expressions for the equinoctial elements in terms of the Poincaré variables. The following relationships are derived from Eqs (2.80) and (2.83):

$$a = \frac{\Lambda^2}{\mu} \quad (2.92a)$$

$$h = \xi \sqrt{\frac{1}{\Lambda} - \frac{\xi^2 + \eta^2}{4\Lambda^2}} \quad (2.92b)$$

$$k = \eta \sqrt{\frac{1}{\Lambda} - \frac{\xi^2 + \eta^2}{4\Lambda^2}} \quad (2.92c)$$

$$p = \frac{u}{\sqrt{1 + 2\Lambda - \xi^2 - \eta^2 - u^2 - v^2}} \quad (2.92d)$$

$$q = \frac{v}{\sqrt{1 + 2\Lambda - \xi^2 - \eta^2 - u^2 - v^2}} \quad (2.92e)$$

We also calculate the true longitude, L (defined in Eq (2.45)), from the mean longitude. To do this, we use an iterative method to solve the alternate form of Kepler's equation given in Eq (2.76) for the eccentric longitude. We then calculate the true longitude from the eccentric longitude.

We next calculate the position and velocity vectors in the equinoctial coordinate frame using Eqs (2.77) and (2.78), respectively.

Next, we rotate the position and velocity vectors to the reference frame. We require i and Ω to do this. These angles are calculated using the following relationships, derived from Eqs (2.80):

$$i = \cos^{-1} \left(\frac{1 - u^2 - v^2}{2\Lambda - \xi^2 - \eta^2} \right) \quad (2.93)$$

$$\Omega = \tan^{-1} \left(\frac{u}{v} \right) \quad (2.94)$$

The rotation from the equinoctial coordinate frame to the reference frame is then performed using Eqs (2.79).

2.3 Reference Frames

When defining the orbit of a satellite, an important first step is to specify the reference frame, which means defining a coordinate system [Ref 10, pp 31]. To define a coordinate system, four specifications must be made [Ref 47].

The first specification is the origin, which defines the center and starting point of the coordinate system. Examples of origins include [Ref 48]:

- the center of the Sun (heliocentric)
- the center of the Earth (geocentric)
- the position of an observer (topocentric)
- the center-of-mass of a spacecraft or system (barycentric)

The second specification is the fundamental plane, which contains two axes of the coordinate system. Examples of fundamental planes include [Ref 48]:

- the ecliptic – the Earth-Sun orbital plane
- the equator – the plane normal to the Earth’s axis of rotation
- the horizon – the plane tangent to the oblate Earth ellipsoid at a specified point on the surface
- the orbital plane

The third specification is the principal direction. Examples of principal directions include [Ref 48]:

- the vernal equinox – designated by Υ , and roughly defined by the intersection of the ecliptic and the Earth’s equator, but precisely defined as the point where the Sun’s declination angle is 0 deg as it changes from negative to positive values (these two definitions are slightly different because the ecliptic is the mean path of the Sun, not the actual path)
- the Greenwich meridian – the Earth’s meridian plane that passes through Greenwich, England
- the local meridian – Earth’s meridian plane that passes through the observer’s position
- the ascending node – intersection of the orbital plane and the reference plane

The fourth specification is the third axis, which is found using the right-hand rule.

Examples of third axes include [Ref 48]:

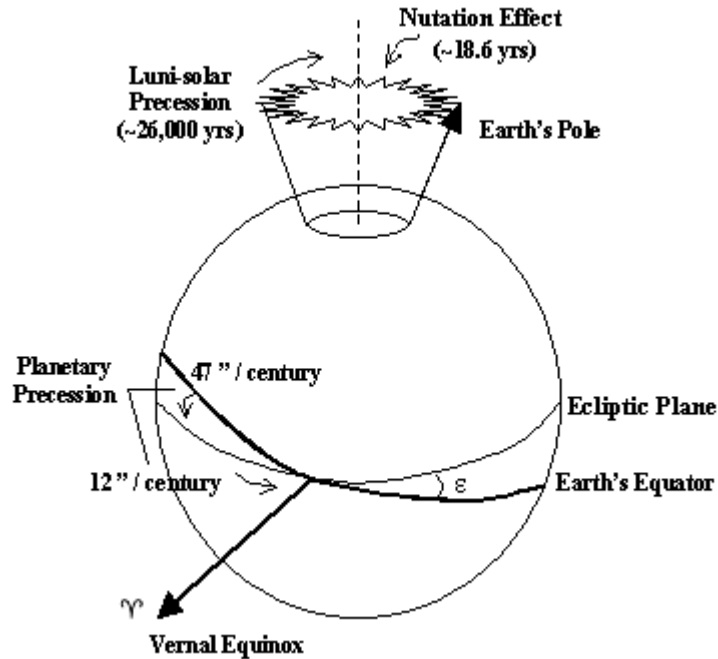
- the ecliptic pole
- the North pole
- the local zenith
- the angular momentum vector

An inertial reference frame refers to one that is not accelerating; this is important because an inertial system is one in which Newton's laws of motion are valid [Ref 10].

2.3.1 Geocentric Equatorial Coordinate System (IJK)

As the name suggests, the origin of this system is the center of the Earth, and the fundamental plane is the Earth's equator. The I axis points toward the vernal equinox, the J axis is 90 degrees to the east in the equatorial plane, and the K axis points toward the North Pole. This coordinate system is non-rotating and assumed to be fixed in space, and is often referred to as the Earth-Centered Inertial (ECI) coordinate system [Ref 10].

Earth-Centered Inertial is actually a bit of a misnomer, due to the fact that the equinox and equatorial plane vary slightly over time. The Earth's equator is not fixed in inertial space. The gravitational force of the sun and moon on the Earth's equatorial bulge drive the equator's motion [Ref 48]. This motion consists of both precession and nutation. Luni-solar precession is the westward motion of the equator's mean pole about the ecliptic pole, and has a period of approximately 26,000 years [Ref 48]. Nutation is the shorter-period motion of the equator's true pole about the mean pole, which is caused by the moon and has a period of approximately 18.6 years [Ref 48]. Likewise, the ecliptic plane varies due to perturbations by the planets on the Earth's orbital plane [Ref 10]. The slow rotation of the ecliptic, called planetary precession, causes an eastward movement of the equinox (approximately 12 arcseconds per century) and a decrease in the obliquity of the ecliptic, ϵ , which is the angle between the Earth's equator and the ecliptic (approximately 47 arcseconds per century) [Ref 48]. Figure 2-4 gives a diagram of the precession and nutation effects [Ref 10].



Sources – Vallado [Ref 10], Carter [Ref 49]

Figure 2-4 – Precession and Nutation Effects

Thus, the ECI frame is time-dependent. The ECI system at a particular time is referred to as either a true-of-date or mean-of-date inertial system. If we account for both precession and nutation effects, we have a true-of-date system that references the true equator and true equinox (TETE) of date [Refs 10, 48]. If we ignore the nutation effect, we are left with a mean-of-date system that references the mean equator and mean equinox (MEME) of date [Refs 10, 48].

In order to achieve a sufficiently inertial coordinate system for precision orbit determination, the equinox and equator can be specified at a particular epoch. The two most commonly used inertial frames are J2000 and B1950. The J2000 system references the mean equator and mean equinox at the J2000 epoch [Ref 48]. Similarly, the B1950 system references the mean equator and mean equinox at the B1950 epoch, which corresponds to January 0.923, 1950, the beginning of the Besselian solar year [Ref 48].

Calculations are done that transform true-of-date and mean-of-date systems to J2000 or B1950 systems, and vice-versa.

2.3.2 Earth-Centered Earth-Fixed Coordinate System (ECEF)

The geocentric coordinate system may be allowed to rotate with the Earth, and is referred to as the Earth-Centered Earth-Fixed (ECEF) coordinate system. The origin is the center of the Earth, and the fundamental plane is the equatorial plane at a specified epoch. The principal axis is always aligned with a particular meridian, usually the Greenwich meridian. This system is important in processing observations of spacecraft, and calculations are done to convert observations from this system to either J2000 or B1950.

2.3.3 Coordinate Transformations

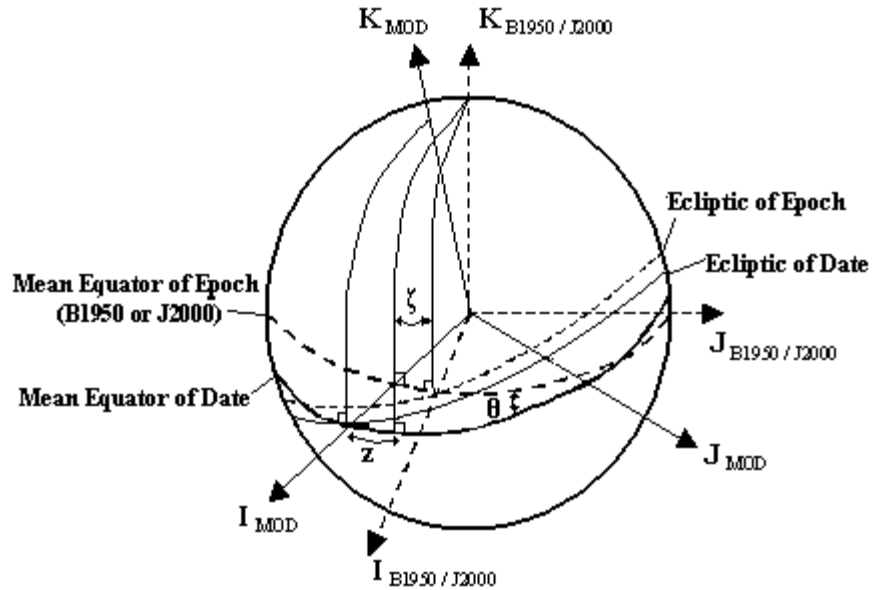
2.3.3.1 Precession

The combined effects of luni-solar precession and planetary precession are known as general precession. The effects of general precession are expressed using the rotation angles ζ , z , and θ , as shown in Figure 2-5. The angle ζ represents a rotation along the mean equator of the fundamental epoch (B1950 or J2000), the angle θ represents a translation to the mean equator of date, and the angle z represents a final rotation to the mean equinox of date [Ref 10, pp 78]. The precession matrix, \mathbf{P} , is thus defined by:

$$\mathbf{P} = \text{ROT3}(-z)\text{ROT2}(-\theta)\text{ROT3}(-\zeta) \quad (2.95a)$$

so that the transformation from B1950 or J2000 to mean-of-date is:

$$\mathbf{r}_{MOD} = [\mathbf{P}] \mathbf{r}_{B1950/J2000} = \text{ROT3}(-z)\text{ROT2}(-\theta)\text{ROT3}(-\zeta)\mathbf{r}_{B1950/J2000} \quad (2.95b)$$



Sources – Vallado [Ref 10], Carter [Ref 49]

Figure 2-5 – Precession Angles

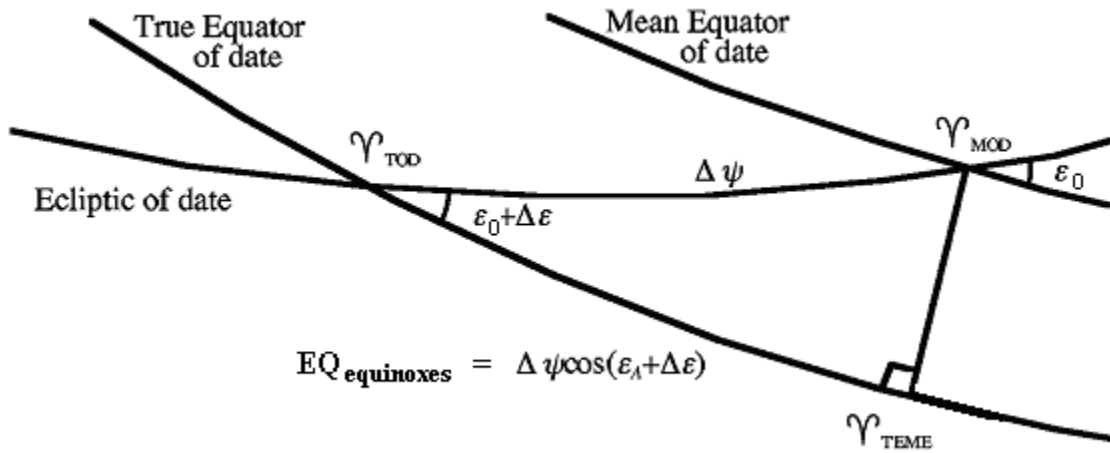
2.3.3.2 Nutation

Nutation accounts for the periodic motion of the equator and equinox contributed primarily by the moon [Ref 10, pp 79]. The calculation of nutation includes several trigonometric terms that represent a short-periodic effect (relative to precession) [Ref 10, pp 79]. These terms are evaluated to obtain the nutation in longitude, $\Delta\Psi$, and the nutation in obliquity $\Delta\varepsilon$. These two values, along with the mean obliquity of the ecliptic at the fundamental epoch (B1950 or J2000), ε_0 , allow us to transform from mean-of-date to true-of-date using the nutation matrix, \mathbf{N} :

$$\mathbf{N} = \text{ROT1}(-\varepsilon_0 - \Delta\varepsilon) \text{ROT3}(-\Delta\Psi) \text{ROT1}(\varepsilon_0) \quad (2.96a)$$

$$\mathbf{r}_{\text{TOT}} = [\mathbf{N}] \mathbf{r}_{\text{MOD}} = \text{ROT1}(-\varepsilon_0 - \Delta\varepsilon) \text{ROT2}(-\Delta\Psi) \text{ROT3}(\varepsilon_0) \mathbf{r}_{\text{MOD}} \quad (2.96b)$$

The nutation angles are shown in Figure 2-6.

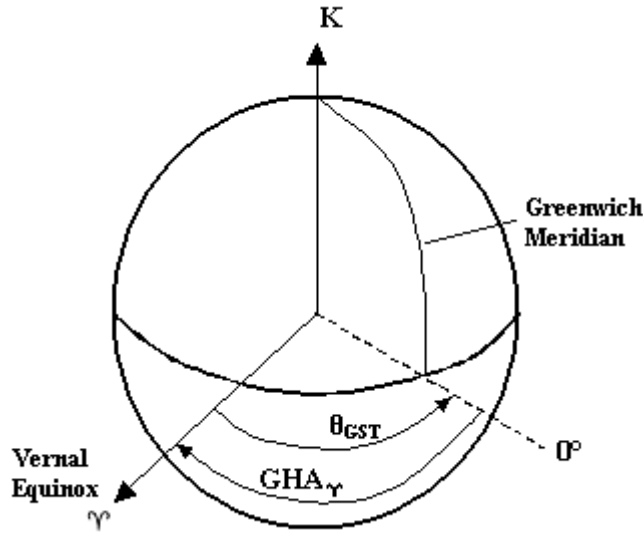


Source: John Seago [Ref 50]

Figure 2-6 – Nutation Angles, the Equation of the Equinoxes, and Relationship Between True (TOD), Mean (MOD), and Uniform (TEME) Equinoxes of Date

2.3.3.3 Sidereal Time

The sidereal time transformation transforms the non-rotating true-of-date coordinate frame to the Earth-fixed coordinate frame. This transformation involves a rotation through the Greenwich apparent sidereal time, θ_{GST} , which is the hour angle of the true equinox from the Greenwich meridian, measured in an easterly direction about the true equator [Ref 48]. The Greenwich Hour Angle, or GHA, is equal in magnitude to the Greenwich sidereal time, but has the opposite sign because it is measured in a westerly direction in the equatorial plane [Ref 10, pp 59]. The θ_{GST} and GHA are shown in Figure 2-7 [Ref 48, pp 3-24].



Source – Vallado, GTDS Math Spec [Ref 10, Ref 48]

Figure 2-7 – Greenwich Sidereal Time (θ_{GST}) and Greenwich Hour Angle (GHA)

It is important to note the difference between the Greenwich apparent sidereal time and the Greenwich mean sidereal time, θ_{GMST} , which is the hour angle of the mean equinox from the Greenwich meridian, measured in an easterly direction about the mean equator [Ref 10, pp 81]. The difference between the two is the Equation of the Equinoxes, which is obtained by projecting the difference between the true and mean equinoxes onto the true equator, as shown in Figure 2-6 [Ref 50]. The Equation of the Equinoxes, $EQ_{equinox}$, and the relationship between Greenwich apparent and mean sidereal time are given in Eqs (2.97) [Ref 10, pp 82]:

$$EQ_{equinox} = \Delta\Psi \cos(\varepsilon_0 + \Delta\varepsilon) \quad (2.97a)$$

$$\theta_{GMT} = \theta_{GMST} + EQ_{equinox} \quad (2.97b)$$

The sidereal time transformation from true-of-date to Earth-centered Earth-fixed is given by:

$$\mathbf{r}_{ECEF \text{ w/o PM}} = [\mathbf{R}] \mathbf{r}_{TOD} = ROT3(\theta_{GST}) \mathbf{r}_{TOD} \quad (2.98)$$

2.3.3.4 Polar Motion

The final transformation accounts for the changing location of the North Pole, which occurs because the Earth’s principal moment of inertia is not coincident with the Earth’s spin axis [Ref 48, pp 3-26]. The motion of the spin axis on the Earth’s surface is unpredictable due to random shifts in the Earth’s crust, although it is “semiregular” and roughly follows a circular spiral [Ref 10, pp 82; Ref 48, pp 3-27]. The polar motion transformation is used to transform the Earth-fixed coordinate system from the Celestial Ephemeris Pole (CEP), which is the “instantaneous” pole and is normal to the true equator of date, to the Conventional International Origin (CIO), which is the “adopted” pole or mean pole of 1903.0, based on observations between 1900 and 1905 [Ref 10, pp 82]. The CIO is important because the third axis of the International Terrestrial Reference Frame (ITRF) extends from the center of the Earth through the CIO, and the ITRF is the reference frame in which station location coordinates are usually expressed [Ref 50]. The polar motion correction is thus needed to correctly perform coordinate transformations from Earth-fixed coordinate systems to inertial coordinate systems, and vice-versa.

The polar motion correction, if applied rigorously, would involve two rotations through the displacements of the CEP from the CIO in the \mathbf{i}_x and \mathbf{i}_y directions. However, the maximum amplitude of the polar motion is about 9 m in either direction, so the polar region can be considered a plane and small-angle identities can be used to simplify the polar motion transformation matrix, \mathbf{W} [Ref 10, pp 82]:

$$\mathbf{W} = ROT2(-x_p)ROT1(-y_p) \approx \begin{bmatrix} 1 & 0 & x_p \\ 0 & 1 & -y_p \\ -x_p & y_p & 1 \end{bmatrix} \quad (2.99a)$$

$$\mathbf{r}_{ECEF \text{ w PM}} = [\mathbf{W}] \mathbf{r}_{ECEF \text{ w/o PM}} \quad (2.99b)$$

2.3.3.5 Coordinate Transformation Summary

Combining all of the coordinate transformations gives the complete transformation from an inertial coordinate system at the fundamental epoch (B1950 or J2000) to an Earth-fixed coordinate system [Ref 50]:

$$\mathbf{r}_{ECEF \text{ w PM}} = [\mathbf{W}] [\mathbf{R}] [\mathbf{N}] [\mathbf{P}] \mathbf{r}_{B1950/J2000} \quad (2.100)$$

Use of the chain rule for differentiation, and making the assumption that the sidereal time transformation is the only transformation that is not slowly-varying, yields the transformation for the velocity vector [Ref 10, pp 85]:

$$\mathbf{v}_{ECEF \text{ w PM}} = [\mathbf{W}] [\dot{\mathbf{R}}] [\mathbf{N}] [\mathbf{P}] \mathbf{r}_{B1950/J2000} + [\mathbf{W}] [\mathbf{R}] [\mathbf{N}] [\mathbf{P}] \mathbf{v}_{B1950/J2000} \quad (2.101)$$

2.3.4 NORAD True Equator/Mean Equinox (TEME) Coordinate System

The NORAD two-line element sets (TLEs) are specified with respect to the true equator and mean equinox (TEME) of date coordinate system [Ref 50]. The name, “true equator and mean equinox (TEME) of date,” is actually a misnomer because it refers to a coordinate system whose fundamental plane is the true equator of date, but whose principal axis is the “uniform equinox” of date. Such a system arises when the Greenwich mean sidereal time (the angle from the Greenwich meridian to the mean equinox) is substituted for the Greenwich apparent sidereal time (the angle from the Greenwich meridian to the true equinox) in transformations of coordinate systems from Earth-fixed to inertial systems. The TEME coordinate system can be obtained by breaking up the sidereal time rotation matrix, \mathbf{R} , into two component matrices (see Chapter 2.3.3.3) [Ref 50]:

$$\mathbf{R} = ROT3(\theta_{GST}) = [\mathfrak{R}] [\mathbf{Q}] \quad (2.102a)$$

where [Ref 50]:

$$[\mathfrak{R}] = ROT3(\theta_{GMST}) \quad (2.102b)$$

and [Ref 50]:

$$[\mathbf{Q}] = ROT3(EQ_{equinox}) \quad (2.102c)$$

The transformation from an inertial coordinate system at the fundamental epoch to the TEME coordinate system is then given by:

$$\mathbf{r}_{TEME} = [\mathbf{Q}] [\mathbf{N}] [\mathbf{P}] \mathbf{r}_{B1950/J2000} \quad (2.103)$$

The uniform equinox is not really an equinox in the same sense as the true and mean equinoxes, because it is not defined by the intersection of the equator and the ecliptic planes [Ref 50]. Instead, the uniform equinox of date is defined by the true equinox of date minus the Equation of the Equinoxes, which is obtained by projecting the difference between the true and mean equinoxes onto the true equator [Ref 50]. Figure 2-6 shows the geometric relationship between the true, mean, and uniform equinoxes of date [Ref 50].

2.3.5 Topocentric Coordinate Systems

A topocentric coordinate system is one whose origin is the position of the observer on the surface of the Earth [Ref 48].

The Topocentric Horizon (SEZ) coordinate system rotates with the observation site. The fundamental plane is the local horizon, and the principal direction is the S axis, which points south from the site [Ref 10, pp 39]. The E axis points east from the site, and the Z axis, or zenith, points radially outward from the site, and is normal to the local horizon plane [Ref 10, pp 39]. The SEZ system is useful for modeling radar observations

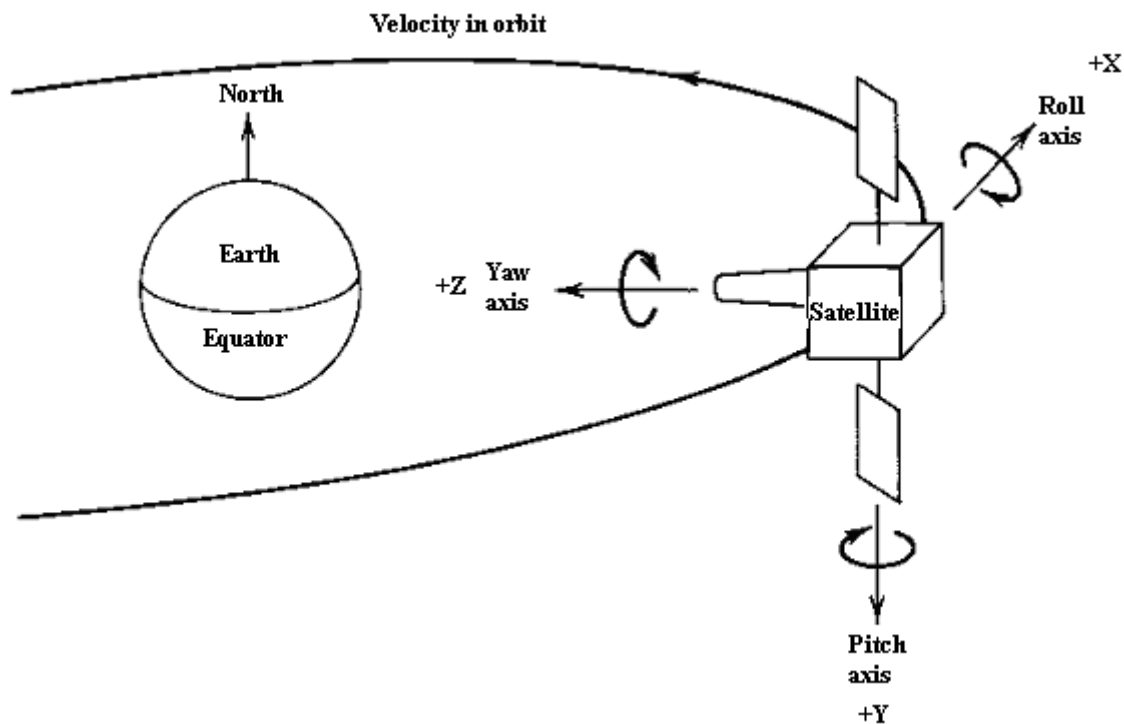
of spacecraft. Azimuth, β , is the angle from north measured clockwise to the location beneath the object of interest, and may take values between 0 and 360 deg [Ref 10, pp 39]. Elevation, e_l , is the angle from the local horizon measured positive up to the object of interest, and may take values between -90 and 90 deg [Ref 10, pp 39].

The Topocentric Equatorial ($I_t J_t K_t$) coordinate system is essentially the geocentric equatorial coordinate system with the origin translated from the center of the Earth to the position of the observer [Ref 10, pp 39]. The fundamental plane is thus the plane parallel to the Earth's equator that intersects the location of the observation site [Ref 10, pp 41]. The orientation of the axes is the same as the IJK coordinate system, with the I_t axis being the principal axis that points in the direction of the vernal equinox [Ref 10, pp 40]. This frame is typically used for modeling optical observations of spacecraft, including GEODSS observations [Ref 10, pp 40]. The topocentric right ascension, α_t , is the angle from the principal axis measured positive to the east to the location beneath the object of interest, and may take values between 0 and 360 deg [Ref 10, pp 35]. The topocentric declination, δ_t , is the angle from the fundamental plane measured positive up to the object of interest, and may take values between -90 and 90 deg [Ref 10, pp 40].

2.3.6 Spacecraft Body-Fixed Coordinate System (SBF)

The origin of the Spacecraft Body Fixed (SBF) system is the center-of-mass of the spacecraft, and the fundamental plane is normal to the spacecraft position vector. The principal axis is the +X axis, which points in the along-track direction and is perpendicular to the spacecraft position vector. This means that the +X axis is not perfectly aligned with the velocity vector, except in the case of a circular orbit or in the case of an elliptical orbit at apogee or perigee [Ref 10, pp 42]. The +Y axis points in the

cross-track direction, and is perpendicular to the principal axis as well as to the spacecraft position vector. The third axis is the +Z axis, which is nadir-pointing in the direction opposite the spacecraft position vector. The SBF +X, +Y, and +Z axes are also called the longitudinal, lateral and vertical axes, or roll, pitch, and yaw axes, respectively [Ref 48]. The SBF frame is the satellite coordinate system that is generally applied to 3-axis stabilized geostationalary spacecraft [Ref 51]. This is convenient because instruments on such spacecraft are typically oriented to be nadir-pointing along the SBF +Z axis, while the solar panels are typically oriented north-south and rotate about the SBF +Y axis.



Source: Gordon and Morgan [Ref 51]

Figure 2-8 – Spacecraft Body-Fixed (SBF) Coordinate System

In this study, the orientations of the various plates in the spacecraft macro-model are specified with respect to the Spacecraft Body-Fixed frame. The SBF coordinate system for a typical 3-axis stabilized geostationalary spacecraft is shown in Figure 2-8 [Ref 51].

Another spacecraft-dependent coordinate frame used in specifying the orientations of the plates in the spacecraft macro-model is the Solar Array (SA) frame. Specifically, the orientations of the solar panels and any other sun-tracking plates are specified with respect to the SA frame. The principal axis is the SA +X axis, and is oriented such that it is normal to the SBF +Y axis and makes the minimum possible angle with the spacecraft-to-sun vector. The SA +X axis can thus be considered to be sun-tracking, rotating about the SBF +Y axis. The SA +Y axis is normal to both the SA +X axis and the SBF +Y axis. The SA +Z axis is aligned along the SBF +Y axis, completing the orthogonal right-handed triad. An illustration of the SA frame, relative to the SBF frame, is shown in Figure 2-9.

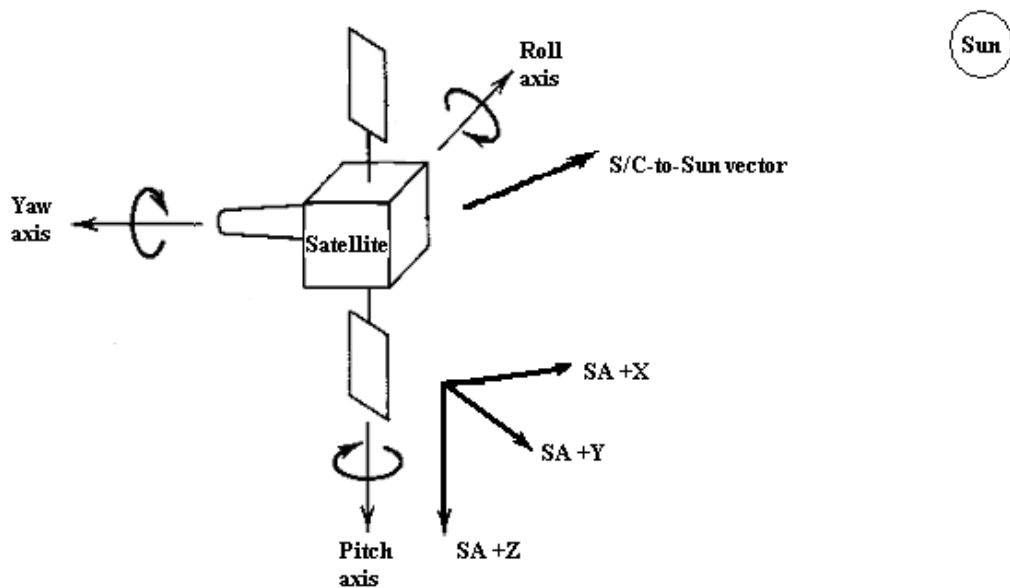


Figure 2-9 – Solar Array (SA) Coordinate Frame

2.4 Special Perturbations, General Perturbations, and Semi-analytical Methods

2.4.1 Special Perturbations (Cowell Method)

In special perturbation methods, all of the modeled perturbing accelerations are included in the equations of motion. The differential equations are solved by numerical integration techniques. The term “special” perturbations comes from the fact that, because numerical integration is involved, the solution is only valid for the initial conditions and force model parameters used as inputs to the problem [Ref 10, pp 468].

The best-known orbit propagation technique that falls into the special perturbations category is the Cowell method [Ref 48, pp 5-1]. This method was developed by Philip Herbert Cowell at the end of the nineteenth century by applying integration formulas first given by Carl Friedrich Gauss, and is a step-by-step numerical integration method of the planetary equations of motion in rectangular coordinates [Ref 42, pp 447]. Today, any technique that numerically integrates the equations of motion in rectangular coordinates is referred to as Cowell’s method [Ref 42, pp 447]. In Cowell’s formulation, the perturbing accelerations are included in the equations of motion as follows [Ref 10, pp 474]:

$$\ddot{\mathbf{r}} = -\frac{\mu}{r^3}\mathbf{r} + \mathbf{Q}(\mathbf{r}, \dot{\mathbf{r}}, t) \quad (2.104)$$

where \mathbf{Q} is the vector sum of the perturbing accelerations on the satellite, which can be a function of position, velocity, and time. As mentioned earlier, perturbing accelerations can include nonspherical central body, third-body effects, atmospheric drag, solar radiation pressure, thrust, and tides [Ref 10, pp 474].

The three second-order differential equations are sometimes expressed as six first-order differential equations so that a wider array of integration methods can be applied. This first-order system is a variation of Cowell's formulation, where \mathbf{x} is the satellite state vector [Ref 10, pp 474]:

$$\mathbf{x} = \begin{bmatrix} r_I \\ r_J \\ r_K \\ v_I \\ v_J \\ v_K \end{bmatrix} \quad \dot{\mathbf{x}} = \begin{bmatrix} v_I \\ v_J \\ v_K \\ -\frac{\mu r_I}{r^3} + a_{pI} \\ -\frac{\mu r_J}{r^3} + a_{pJ} \\ -\frac{\mu r_K}{r^3} + a_{pK} \end{bmatrix} \quad (2.105)$$

2.4.1.1 Numerical Integration Techniques

Numerical integration techniques can be classified into several categories. The two main categories are *single-step* and *multi-step*, and refer to the number of steps used when integrating to the next point [Ref 52]. Single-step techniques combine the state at the epoch time with the rates from several other times to calculate the update [Ref 10, pp 475]. Multi-step techniques, also called predictor-corrector algorithms, calculate an initial estimate based on previous estimates of the rate of change (predictor), and then use the estimated value to further refine the result (corrector) [Ref 10, pp 475]. Multi-step techniques are generally faster than single-step techniques, although they suffer some drawbacks, including the need for a start-up routine because they require back values (i.e. they are not self-starting) [Ref 52]. Multi-step techniques can be further classified as either summed or non-summed, depending on whether the integration is performed from epoch or step-by-step [Ref 52].

Numerical integration techniques can have either fixed or variable step sizes. Variable step sizes can reduce the number of step sizes used at apogee, where velocity is at a minimum, thus making them more efficient for highly elliptical orbits [Ref 52]. Time regularization is one example of stepsize control that is used in GTDS [Ref 48].

Numerical integration techniques can also be classified according to the type of formulation. Single-integration techniques calculate the velocity given the acceleration, and then the position given the velocity [Ref 52]. Double-integration techniques calculate the position directly from the acceleration [Ref 52].

Finally, the order of a numerical integration technique refers to the number of intermediate evaluations of the equations of motion required to move forward one time step [Ref 10]. Higher order techniques tend to be more accurate, but less stable [Ref 48].

GTDS primarily uses the Störmer-Cowell and Adams techniques for numerical integration [Ref 48]. Both methods are multi-step, non-summed integration techniques [Ref 52]. They differ in that the Störmer-Cowell technique is a double-integration technique, while the Adams technique is a single-integration technique [Ref 52]. As such, when these integration techniques are used with the Cowell method in GTDS, the Störmer-Cowell technique is used to solve the three second-order differential equations for the position, and the Adams technique is used to solve the three first-order differential equations for the velocity [Ref 48]. A single-step fourth-order Runge-Kutta (RK4) is also used for sequential estimation and as a starter for multi-step techniques [Ref 48].

2.4.2 Variation of Parameters (VOP)

The method of Variation of Parameters (VOP), also called the variation of orbital elements or the variation of constants, was originally developed by Euler and later

improved by Lagrange [Ref 42, pp 471]. VOP differs from Cowell's method in that, while Cowell's method integrates the rectangular coordinates of the satellite, VOP integrates the orbital elements or some other set of parameters that specify the satellite's position [Ref 53]. VOP is based on the idea that the general form of the solution for the unperturbed (two-body) system is suitable for the perturbed system [Refs 10, 45]. The assumptions are made that the perturbations are small, and the constants of motion for the unperturbed system are generalized to be time-dependent parameters in the perturbed system [Refs 10, 45].

The development follows the derivation presented by Wayne McClain in A Semianalytic Artificial Satellite Theory [Ref 45]. It begins with the equations of motion for the unperturbed and perturbed systems, given by Eq (2.8) and Eq (2.104), respectively. The general solution for the satellite position for the unperturbed system is assumed to have the following form [Ref 45]:

$$\mathbf{r} = \mathbf{f}(c_1, c_2, \dots, c_6, t) \quad (2.106a)$$

For the perturbed system, the general solution is assumed to have the following form [Ref 45]:

$$\mathbf{r} = \mathbf{f}(a_1, a_2, \dots, a_6, t) \quad (2.106b)$$

The difference between (2.106a) and (2.106b) is that the constants c_k of the unperturbed system are replaced by the time-dependent parameters $a_k(t)$ [Ref 45].

The velocity is obtained as the time derivative of the position. For the unperturbed case, the velocity is simply [Ref 45]:

$$\dot{\mathbf{r}} = \frac{d}{dt} \mathbf{r}(c_1, c_2, \dots, c_6, t) = \frac{\partial \mathbf{r}}{\partial t} \quad (2.107a)$$

For the perturbed system, we must use the chain rule to obtain the velocity because of the time-dependent parameters a_k [Ref 45]:

$$\dot{\mathbf{r}} = \frac{d}{dt}\mathbf{r}(a_1, a_2, \dots, a_6, t) = \frac{\partial \mathbf{r}}{\partial t} + \sum_{j=1}^6 \frac{\partial \mathbf{r}}{\partial a_j} \dot{a}_j \quad (2.107b)$$

In order that the general form of the velocity for the perturbed system (Eq (2.107b)) maintain the same form as the unperturbed system (Eq (2.107a)), we must impose the following constraint [Ref 45]:

$$\sum_{j=1}^6 \frac{\partial \mathbf{r}}{\partial a_j} \dot{a}_j \equiv \mathbf{0} \quad (2.108)$$

which is called the *condition of osculation*, because it defines the condition for the osculating orbit [Ref 10, pp 551].

Applying Eq (2.108) to the velocity for the perturbed system, given in Eq (2.107b), gives the same form as the unperturbed system, given in Eq (2.107a). Taking the time derivative of the velocity, we must again use the chain rule to obtain the acceleration for the perturbed system [Ref 45]:

$$\ddot{\mathbf{r}} = \frac{\partial^2 \mathbf{r}}{\partial t^2} + \sum_{k=1}^6 \frac{\partial \dot{\mathbf{r}}}{\partial a_k} \dot{a}_k \quad (2.109)$$

By substituting Eq (2.109) into the equations of motion for the perturbed system, given in Eq (2.20), we obtain [Ref 45]:

$$\frac{\partial^2 \mathbf{r}}{\partial t^2} + \sum_{k=1}^6 \frac{\partial \dot{\mathbf{r}}}{\partial a_k} \dot{a}_k + \frac{\mu}{r^3} \mathbf{r} = \mathbf{Q}(\mathbf{r}, \dot{\mathbf{r}}, t) \quad (2.110)$$

Next, by applying the two-body equations of motion given in Eq (2.8), The two-body terms in Eq (2.110) go to zero, and the equations of motion for the perturbed system are reduced to [Ref 45]:

$$\sum_{k=1}^6 \frac{\partial \dot{\mathbf{r}}}{\partial a_k} \dot{a}_k = \mathbf{Q}(\mathbf{r}, \dot{\mathbf{r}}, t) \quad (2.111)$$

This shows that the equations of motion for the unperturbed and perturbed systems differ only by the terms that explicitly contain the time-dependent parameters [Ref 45].

The previous form of the equations of motion for the perturbed system is inconvenient to actually use because the left hand side is a linear combination of the element rates [Ref 45]. Instead, we seek the VOP equations of motion as a system of first-order differential equations that describe the rates of change of the time-varying parameters, in the following form [Ref 45]:

$$\frac{da_i}{dt} = G_i \quad (2.112)$$

where the G_i are functions that depend on the Cartesian state or on the parameters a_k .

2.4.2.1 Gaussian VOP

Gauss' form of the VOP equations express the orbital element rates explicitly in terms of the perturbing forces, rather than in terms of a potential function as in Lagrangian VOP. As such, Gaussian VOP works for both nonconservative and conservative forces [Ref 10, pp 559].

To obtain the Gaussian VOP form, take the dot product of the vector $\frac{\partial a_j}{\partial \dot{\mathbf{r}}}$ with Eq (2.111) and the dot product of the vector $\frac{\partial a_j}{\partial \mathbf{r}}$ with Eq (2.108), and then sum the results to obtain [Ref 45]:

$$\sum_{k=1}^6 \left(\frac{\partial a_j}{\partial \dot{\mathbf{r}}} \cdot \frac{\partial \dot{\mathbf{r}}}{\partial a_k} + \frac{\partial a_j}{\partial \mathbf{r}} \cdot \frac{\partial \mathbf{r}}{\partial a_k} \right) \dot{a}_k = \frac{\partial a_j}{\partial \dot{\mathbf{r}}} \cdot \mathbf{Q} \quad j = 1, 2, \dots, 6 \quad (2.113)$$

The elements are mutually independent and are functions of position and velocity only, hence the quantity in the parenthesis reduces to the Kronecker delta function, $\delta_{j,k} = 1$ for $j = k$ and $\delta_{j,k} = 0$ for $j \neq k$ [Ref 45]:

$$\frac{\partial a_j}{\partial \dot{\mathbf{r}}} \cdot \frac{\partial \dot{\mathbf{r}}}{\partial a_k} + \frac{\partial a_j}{\partial \mathbf{r}} \cdot \frac{\partial \mathbf{r}}{\partial a_k} = \delta_{j,k} \quad j, k = 1, 2, \dots, 6 \quad (2.114)$$

Eqs (2.113) then take the form [Ref 45]:

$$\sum_{k=1}^6 \delta_{j,k} \dot{a}_k = \frac{\partial a_j}{\partial \dot{\mathbf{r}}} \cdot \mathbf{Q} \quad j = 1, 2, \dots, 6 \quad (2.115a)$$

which simplify to [Ref 45]:

$$\dot{a}_j = \frac{\partial a_j}{\partial \dot{\mathbf{r}}} \cdot \mathbf{Q} \quad j = 1, 2, \dots, 6 \quad (2.115b)$$

The Gaussian VOP equations have two advantages over the Lagrangian VOP equations. As mentioned earlier, they are appropriate for both conservative and nonconservative perturbations [Ref 45]. Also, the Gaussian VOP equations allow for closed-form expressions for the equations of motion due to the G function being formulated explicitly in terms of the perturbing acceleration [Ref 45]. Unfortunately, the Gaussian form also suffers from some weaknesses. First, the conversions from the elements to position and velocity must be applied every time the element rates are evaluated [Ref 45]. Second, periodic phenomena are not readily isolated from the acceleration model, because most perturbing accelerations are formulated in terms of position or position and velocity, rather than as a Fourier series expansion [Ref 45]. This

necessitates a numerical procedure for isolating specific frequencies in the motion [Ref 45].

2.4.2.2 Lagrangian VOP (Lagrange Planetary Equations)

This form of the VOP equations of motion was developed by Lagrange to describe the disturbances on the planets' motion about the Sun due to the gravitational attraction of the planets [Ref 10, pp 552]. As a result, this form of VOP assumes that the disturbing acceleration is due to a conservative force, and that the disturbing acceleration can be modeled as the gradient of a potential function [Ref 45]:

$$\mathbf{Q}(\mathbf{r}) = \frac{\partial R(\mathbf{r})}{\partial \mathbf{r}} \quad (2.116)$$

The potential function is referred to as the *disturbing function*, and is represented by R [Ref 45].

To obtain the Lagrangian VOP form, take the dot product of the vector $\frac{\partial \mathbf{r}}{\partial a_j}$ with Eq (2.111) and the dot product of the vector $\frac{\partial \dot{\mathbf{r}}}{\partial a_j}$ with Eq (2.108), and then difference the results to obtain [Ref 45]:

$$\sum_{k=1}^6 \left(\frac{\partial \mathbf{r}}{\partial a_j} \cdot \frac{\partial \dot{\mathbf{r}}}{\partial a_k} - \frac{\partial \dot{\mathbf{r}}}{\partial a_j} \cdot \frac{\partial \mathbf{r}}{\partial a_k} \right) \dot{a}_k = \frac{\partial R}{\partial \mathbf{r}} \cdot \frac{\partial \mathbf{r}}{\partial a_j} \quad j = 1, 2, \dots, 6 \quad (2.117)$$

We next introduce the quantity $[a_j, a_k]$, known as a *Lagrange bracket*, for simplification [Ref 45]:

$$[a_j, a_k] = \frac{\partial \mathbf{r}}{\partial a_j} \cdot \frac{\partial \dot{\mathbf{r}}}{\partial a_k} - \frac{\partial \dot{\mathbf{r}}}{\partial a_j} \cdot \frac{\partial \mathbf{r}}{\partial a_k} \quad (2.118)$$

Eqs (2.117) then simplify to [Ref 45]:

$$\sum_{k=1}^6 [a_j, a_k] \dot{a}_k = \frac{\partial R}{\partial a_j} \quad j = 1, 2, \dots, 6 \quad (2.119)$$

The indices j and k each vary between 1 and 6, which implies that there are a total of 36 Lagrange brackets [Ref 45]. However, only 15 distinct Lagrange brackets exist, due to the following two relations, which are clear from inspection of the Lagrange bracket definition [Ref 45]:

$$[a_j, a_j] = 0 \quad (2.120a)$$

$$[a_j, a_k] = -[a_k, a_j] \quad (2.120b)$$

The matrix \mathbf{L} is defined as the matrix of Lagrange brackets [Ref 45]:

$$\mathbf{L} = \begin{bmatrix} [a_1, a_1] & \cdots & [a_1, a_6] \\ \vdots & \ddots & \vdots \\ [a_6, a_1] & \cdots & [a_6, a_6] \end{bmatrix} \quad (2.121)$$

The Lagrangian VOP equations of motion (Eqs (2.119)) can then be expressed in matrix notation as follows [Ref 45]:

$$\mathbf{L}\dot{\mathbf{a}} = \frac{\partial R}{\partial \mathbf{a}} \quad (2.122)$$

The Lagrange brackets depend only on the relationship between the orbital elements and the position and velocity vectors for the unperturbed (two-body) problem [Ref 45]. As a result, the Lagrange brackets are time-independent [Ref 45]. This property allows for the calculation of the Lagrange brackets at any time, at potentially advantageous points in the orbit [Ref 45].

An alternate derivation of the Lagrange Planetary Equations can be obtained using the following relation, defined by Broucke [Ref 45]:

$$\frac{\partial a_k}{\partial \dot{\mathbf{r}}} = -\sum_{j=1}^6 (a_k, a_j) \frac{\partial \mathbf{r}}{\partial a_j} \quad (2.123)$$

where the quantity (a_k, a_j) is the *Poisson bracket*, defined as follows [Ref 45]:

$$(a_k, a_j) = \frac{\partial a_k}{\partial \mathbf{r}} \cdot \frac{\partial a_j}{\partial \dot{\mathbf{r}}} - \frac{\partial a_k}{\partial \dot{\mathbf{r}}} \cdot \frac{\partial a_j}{\partial \mathbf{r}} \quad (2.124)$$

The Poisson brackets share the properties of the Lagrange brackets given in Eqs (2.120a) and (2.120b) [Ref 45]. Additionally, it can be seen that the relationship between the matrix of Lagrange brackets, \mathbf{L} , and the matrix of Poisson brackets, \mathbf{P} , is [Ref 45]:

$$\mathbf{L}^{-1} = \mathbf{P}^T = -\mathbf{P}$$

Substituting Eq (2.116) into Eq (2.115b) gives Gauss' form of the VOP equations in terms of the disturbing function [Ref 45]:

$$\dot{a}_k = \frac{\partial a_k}{\partial \dot{\mathbf{r}}} \cdot \frac{\partial R}{\partial \mathbf{r}} \quad k = 1, 2, \dots, 6 \quad (2.125)$$

Substituting Eq (2.123) into Eqs (2.125) then yields [Ref 45]:

$$\dot{a}_k = -\sum_{j=1}^6 (a_k, a_j) \frac{\partial \mathbf{r}}{\partial a_j} \cdot \frac{\partial R}{\partial \mathbf{r}} \quad k = 1, 2, \dots, 6 \quad (2.126)$$

which simplifies to [Ref 45]:

$$\dot{a}_k = -\sum_{j=1}^6 (a_k, a_j) \frac{\partial R}{\partial a_j} \quad k = 1, 2, \dots, 6 \quad (2.127)$$

Expressing Eq (2.127) in matrix notation yields the Poisson Bracket representation of the Lagrange Planetary Equations [Ref 45]:

$$\dot{\mathbf{a}} = -\mathbf{P} \frac{\partial R}{\partial \mathbf{a}} \quad (2.128)$$

A modified version of Eq (2.128) is used in the development of DSST in Chapter 2.4.6, to avoid differencing two large secular terms in the VOP equations [Ref 45]. This

modification defines the fast variable, ℓ , which is a rapidly rotating phase angle, as a linear combination of time with an element as follows [Ref 45]:

$$\ell = nt + a_6 \quad (2.129)$$

The Lagrange Planetary Equations can then be expressed as follows [Ref 45]:

$$\frac{da_i}{dt} = -\sum_{j=1}^6 (a_i, a_j) \frac{\partial R}{\partial a_j} \quad i = 1, 2, \dots, 5 \quad (2.130a)$$

$$\frac{d\ell}{dt} = n - \sum_{j=1}^6 (\ell, a_j) \frac{\partial R}{\partial a_j} \quad (2.130b)$$

2.4.2.3 Hamiltonian VOP

The canonical form, also known as the Hamiltonian form, was developed by William Rowen Hamilton [Ref 10, pp 569]. Hamilton showed that, if the parameters used to represent the motion were canonical variables, the equations of motion for a conservative force became simple [Ref 10, pp 569]. The Hamiltonian formulation is different from the Lagrange planetary equations because the element rates depend not only on the disturbing function, but also on the total specific mechanical energy of the perturbed system [Ref 10, pp 569]. The total specific mechanical energy is the sum of the potential and kinetic energy, and is also called the Hamiltonian, H [Ref 10, pp 569]:

$$\begin{aligned} H &= KE - U \\ &= \frac{1}{2}v^2 - U_{Two-body} - R \\ &= \frac{1}{2}v^2 - \frac{\mu}{r} - R \end{aligned} \quad (2.131)$$

where the potential, U, is the sum of the two-body potential, $U_{Two-body}$, and the disturbing function, R [Ref 10, pp 569].

Making use of the vis-viva integral for two-body motion, given in Eq (2.30), the Hamiltonian of Eq (2.131) becomes [Ref 54]:

$$H = -\frac{\mu}{2a} - R \quad (2.132)$$

Written in terms of the Delaunay variables, the Hamiltonian becomes [Ref 10, pp 569]:

$$H = -\frac{\mu^2}{2L^2} - R(L, G, H, l, g, h) \quad (2.133)$$

The canonical equations of motion, or the rate of change of the Delaunay variables, then take the form [Ref 54]:

$$\begin{aligned} \frac{\partial L}{\partial t} &= -\frac{\partial H}{\partial l} & \frac{\partial l}{\partial t} &= \frac{\partial H}{\partial L} \\ \frac{\partial G}{\partial t} &= -\frac{\partial H}{\partial g} & \frac{\partial g}{\partial t} &= \frac{\partial H}{\partial G} \\ \frac{\partial H}{\partial t} &= -\frac{\partial H}{\partial h} & \frac{\partial h}{\partial t} &= \frac{\partial H}{\partial H} \end{aligned} \quad (2.134)$$

In the development of the Brouwer theory, the canonical equations are written in terms of another Hamiltonian, F, to avoid confusion between the original Hamiltonian, H, and the Delaunay variable, H, and to avoid the negative sign in the disturbing function [Ref 55]:

$$\begin{aligned} \frac{\partial L}{\partial t} &= \frac{\partial F}{\partial l} & \frac{\partial l}{\partial t} &= -\frac{\partial F}{\partial L} \\ \frac{\partial G}{\partial t} &= \frac{\partial F}{\partial g} & \frac{\partial g}{\partial t} &= -\frac{\partial F}{\partial G} \\ \frac{\partial H}{\partial t} &= \frac{\partial F}{\partial h} & \frac{\partial h}{\partial t} &= -\frac{\partial F}{\partial H} \end{aligned} \quad (2.135)$$

where [Ref 54]:

$$F = -H = \frac{\mu^2}{2L^2} + R(L, G, H, l, g, h) \quad (2.136)$$

Brouwer then transforms his Hamiltonian, F , using canonical transformations. Any transformation that maps a set of canonical variables to another set of variables, as long as the form of the equations of motion remain the same, is called a canonical transformation [Ref 10, pp 570]. Brouwer uses two canonical transformations in his method. The first canonical transformation arrives at a set of single-primed elements, which are mean elements that represent both the long-period and secular effects of the perturbations on the satellite motion (these elements are analogous to the mean elements of the DSST) [Ref 45, pp 33]. The second canonical transformation arrives at a set of double-primed elements, which are mean elements that represent only the secular effects of the perturbations [Ref 45, pp 33]. The doubly-transformed Hamiltonian, F^{**} , is a function of only three of the variables. The equations of motion are thus easily solved. The transformations are then inverted to yield the single-primed elements in terms of the double-primed elements, and again to yield the original elements in terms of the single-primed elements [Ref 10, pp 571].

2.4.3 General Perturbations from VOP

In general perturbation methods, the equations of motion are replaced with an analytical approximation [Ref 10, pp 543]. The perturbing accelerations are expressed using series expansions that are truncated in practice to produce simpler expressions. This speeds up computation but decreases accuracy compared to special perturbations techniques. The term “general” perturbations comes from the fact that, unlike numerical

integration methods, the approximate analytical results are valid over some limited time interval for any initial conditions [Ref 10, pp 543].

The Variation of Parameters method described earlier is well-suited to be used as the basis for general perturbations methods. In the Lagrangian VOP form, the disturbing function, R , is often expressed using a series expansion. For example, the geopotential function can be expressed as a series of Legendre polynomials [Ref 42, pp 404].

Examples of general perturbations methods include:

- Kozai's method, which was developed in 1959, uses the Lagrangian VOP equations and solves them using an ad hoc averaging technique [Ref 10, pp 624]. This method takes into account perturbations due to the nonsphericity of the Earth ($J_2 - J_5$ only) [Ref 10, pp 624].
- Brouwer's method, which was also developed in 1959, uses the Hamiltonian VOP formulation, the Delaunay canonical variables, and canonical transformations [Ref 55]. This method is discussed briefly in the earlier chapter on Hamiltonian VOP (Chapter 2.4.2.3).
- Brouwer's method has been refined considerably since 1960. Significant contributions include those of Lyddane in 1963, which addressed the zero eccentricity and inclination singularities that were inherent to Brouwer's theory because of the use of Delaunay variables [Ref 56]. The Brouwer-Lyddane theory is the basis of the Air Force's GP4 and the Navy's PPT2 theories.

- André Deprit also made significant contributions to the refinement of the Brouwer theory [Ref 56]. He addressed the singularity in the Hamiltonian that appeared around the critical inclination (~ 63.4 deg) [Ref 56].

In developing general perturbations techniques, it is important to distinguish between the effects that perturbations can have on the orbital elements. *Secular* effects vary over time, either linearly or proportionally to some power of time [Ref 10, pp 545]. Errors in secular terms thus produce unbounded error growth, and are the primary cause of the degradation of analytical solutions over long time intervals [Ref 10, pp 545]. *Periodic* effects are cyclic over some time interval, and are further classified depending on the time they take to repeat. *Short-periodic* effects typically repeat on the order of the satellite's orbital period or less, while *long-periodic* effects repeat on a longer time scale that can be on the order of weeks up to a year. Defining short-periodic effects is further described in the context of the Generalized Method of Averaging in Chapter 2.4.5.

It is also important to classify orbital elements by their rate of change in the perturbed problem. *Slow variables* are those elements that vary only slightly over one orbital revolution. Variations in these elements are caused entirely by perturbations. Thus, in the two-body case, these elements would be constant. *Fast variables* change dramatically over one orbital revolution, and are usually a rapidly rotating phase angle, such as mean, true, and eccentric anomalies.

Finally, the distinction between osculating and mean elements is important in developing general perturbations theories. The difference between the two types of elements is explained in Chapter 2.2.4. To summarize, osculating elements are valid at a particular instant of time and correspond to the satellite's position and velocity vectors at

that time, while mean elements are averaged over some time interval or angular measurement.

2.4.4 Semi-analytical Techniques

There is a trade-off between computational speed and accuracy depending on whether special or general perturbations methods are used. Numerical techniques have high accuracy, but can be computationally expensive [Ref 10, pp 543]. Analytical techniques, on the other hand, are computationally efficient at the expense of accuracy [Ref 10, pp 543]. Semi-analytical techniques attempt to combine the features of both special and general perturbations methods to give the best speed and accuracy [Ref 10, pp 543].

The basic approach in semi-analytical methods is to separate the short-periodic perturbations from the long-periodic and secular effects, so that the mean element rates can be numerically integrated [Ref 10, pp 629]. The short-periodic effects constrain the integration step size, so removing them allows the numerical integration of the equations of motion for the mean elements to use a large step size, typically on the order of a day [Ref 10, pp 629]. The short-periodic contributions are 2π periodic in the fast variable, and they are modeled analytically using a Fourier series [Ref 10, pp 629]. The mean elements are recovered by numerically integrating the averaged equations of motion to the integrator's step size times and interpolating to any desired output time [Ref 57]. The short-periodic variations are obtained by evaluating the slowly-varying short-periodic coefficients and interpolating to the desired output time [Ref 57]. The short-periodic variations are then added to the mean elements to obtain the osculating elements that solve the original equations of motion [Ref 57].

The semi-analytical theory used in this study is the Draper Semi-analytical Satellite Theory (DSST), which was developed by Paul Cefola, Leo Early, Wayne McClain, Ron Proulx, Mark Slutsky, and their colleagues at Draper Laboratory in the mid-1970s and early 1980s [Refs 45, 57]. Advantages of DSST over other methods include its extensive treatment of perturbing forces, use of non-singular mean elements, flexibility in its application, good documentation, and widespread use [Ref 10, pp 629]. The philosophy of DSST is to model conservative perturbing forces using Lagrangian VOP, model non-conservative perturbing forces using Gaussian VOP, and use the Generalized Method of Averaging to separate the short-periodic effects from the long-periodic and secular contributions to the motion, obtaining the averaged VOP equations of motion and short-periodic models [Ref 45]. The theory is discussed in detail in the following chapters, which follow the development of the theory presented in McClain's A Semianalytic Artificial Satellite Theory [Ref 45].

2.4.5 Generalized Method of Averaging

When Lagrange originally made use of the Lagrange Planetary Equations to investigate the long-period and secular motion of the planets, the disturbing function was expanded in a literal Fourier series [Ref 45]. The terms contributing to the long-period and secular motion of the satellite at first order were isolated by inspection, and this technique produced excellent results with small perturbations [Ref 45]. However, higher order solutions are necessary when the perturbations grow larger or the solution must be valid over greater time intervals [Ref 45].

The Generalized Method of Averaging (GMA) is applied to the VOP equations of motion to eliminate the short-periodic terms and isolate the long-periodic and secular

effects of the perturbations on the satellite motion [Ref 45]. The solution of the resulting averaged equations of motion is a set of mean elements, similar to Brouwer's single-primed elements, which represent the long-period and secular effects [Ref 45]. The DSST mean elements take into account more perturbations than the Brouwer single-primed elements. Background on authors contributing to the development of the GMA can be found in McClain's A Semianalytic Satellite Theory [Ref 45].

The GMA theory can be applied to both the Lagrangian and Gaussian forms of the VOP equations of motion [Ref 45]. The following general expression for the VOP element rates is the starting point for the derivation presented by McClain [Ref 45]:

$$\frac{da_i}{dt} = \varepsilon F_i(\mathbf{a}, \ell) \quad i = 1, 2, \dots, 5 \quad (2.137a)$$

$$\frac{d\ell}{dt} = n(a_1) + \varepsilon F_6(\mathbf{a}, \ell) \quad (2.137b)$$

where the a_i are the slowly-varying elements and ℓ is the fast variable [Ref 45].

The first step in applying the GMA theory to the VOP equations is to define which terms are short-periodic [Ref 45]. The perturbation with the shortest period effectively constrains the step size when integrating the equations of motion [Ref 45]. For computational efficiency, we wish to maximize the integration step size (by removing the short-period terms), while still retaining the fundamental characteristics of the motion over time [Ref 45].

In applying the GMA to the problem of artificial satellites, in general, terms with periods of the same or lesser order of magnitude as the satellite period are considered short-periodic terms. This includes all terms dependent on the satellite fast variable, ℓ ,

and on multiples of ℓ [Ref 45]. Such terms are short-periodic compared to the terms containing the slowly-varying angular elements [Ref 45].

The nonspherical gravitational field of the Earth, usually represented with a spherical harmonic expansion, contributes short-periodic effects to the satellite motion [Ref 45]. *Zonal harmonics* are purely latitude-dependent [Ref 10, pp 494]. The dominant zonal harmonic term is J_2 , which is much larger than any other zonal short-periodic contributions [Ref 45].

Tesseral harmonics model the nonsphericity of the Earth's gravitational field using a checkerboard array [Ref 10, pp 496]. Tesseral harmonics that contribute short-periodic effects to the motion due to their dependence on the Greenwich Hour Angle (θ) are referred to as θ -dependent short-period terms, or *tesseral m-dailies*, and contribute short-periodic effects with periods between about one day and fractions of a day [Ref 45]. Tesseral harmonics also contribute terms that are *linear combinations* of the satellite fast variable and θ [Ref 45]. Furthermore, the coupling between J_2 and tesseral m-dailies contributes additional short-periodic terms to the equations of motion.

Another possible source of short-periodic terms is the *third-body* effect, also called the *lunar-solar* effect, which contributes terms with a fundamental period of approximately 28 days for the Moon and approximately one year for the Sun [Ref 45]. These effects can be included in the equations of motion using various approaches. If a single-averaging theory is used (averaging only over the satellite's fast variable), third-bodies contribute long-period effects relative to the satellite's period for the majority of artificial Earth satellites [Ref 45]. If a double-averaging theory is used (averaging over both the satellite's and third-body's fast variables), third-bodies contribute short-periodic

terms that are dependent on the third-body's fast variable and are referred to as *m-monthly* or *m-yearly* terms. These are analogous to the tesseral m-dailies mentioned earlier.

Third-bodies contribute short-periodic terms that are functions of the satellite's fast variable and are usually expressed in terms of the eccentric longitude. If double-averaging is used, third-bodies also contribute terms that are linear combinations of the satellite's and third-body's fast variables.

2.4.6 The Draper Semi-analytical Satellite Theory (DSST)

As stated earlier, the mean elements used in the DSST contain the secular and long-periodic variations. The *near-identity transformation* expresses the osculating elements in terms of mean elements, and is assumed to take the following form [Ref 45]:

$$a_i = \bar{a}_i + \sum_{j=1}^N \varepsilon^j \eta_{i,j}(\bar{\mathbf{a}}, \bar{\ell}) + \mathcal{O}(\varepsilon^{N+1}) \quad i = 1, 2, \dots, 5 \quad (2.138a)$$

$$\ell = \bar{\ell} + \sum_{j=1}^N \varepsilon^j \eta_{6,j}(\bar{\mathbf{a}}, \bar{\ell}) + \mathcal{O}(\varepsilon^{N+1}) \quad (2.138b)$$

where $\eta_{i,j}$ represents the short-periodic variation of order j in element \bar{a}_i , the \bar{a}_i are the slowly-varying mean elements, $\bar{\ell}$ is the *mean* mean longitude, and the quantity ε is assumed to be a small parameter in the perturbation model [Ref 45].

The equations of motion for the mean elements are assumed to take the form [Ref 45]:

$$\frac{d\bar{a}_i}{dt} = \sum_{j=1}^N \varepsilon^j A_{i,j}(\bar{\mathbf{a}}) + \mathcal{O}(\varepsilon^{N+1}) \quad i = 1, 2, \dots, 5 \quad (2.139a)$$

$$\frac{d\bar{\ell}}{dt} = n(\bar{a}_1) + \sum_{j=1}^N \varepsilon^j A_{6,j}(\bar{\mathbf{a}}) + \mathcal{O}(\varepsilon^{N+1}) \quad (2.139b)$$

where $n(\bar{a}_1)$ is the *mean* mean motion [Ref 10, pp 630]. These equations show that the rate of change of the mean elements depends only on the slowly-varying mean elements [Ref 45].

We wish to construct expressions for the $\eta_{i,j}$, which are the as-yet unknown short-periodic variations, and the $A_{i,j}$, which are the as-yet unknown functions of the slowly-varying mean elements.

To obtain the mean element equations of motion, we first differentiate Eqs (2.138), obtaining expressions for the osculating element rates [Ref 45]:

$$\frac{da_i}{dt} = \frac{d\bar{a}_i}{dt} + \sum_{j=1}^N \varepsilon^j \sum_{k=1}^6 \frac{\partial \eta_{i,j}}{\partial \bar{a}_k} \frac{d\bar{a}_k}{dt} + \mathcal{O}(\varepsilon^{N+1}) \quad i = 1,2,\dots,5 \quad (2.140a)$$

$$\frac{d\ell}{dt} = \frac{d\bar{\ell}}{dt} + \sum_{j=1}^N \varepsilon^j \sum_{k=1}^6 \frac{\partial \eta_{6,j}}{\partial \bar{a}_k} \frac{d\bar{a}_k}{dt} + \mathcal{O}(\varepsilon^{N+1}) \quad (2.140b)$$

where \bar{a}_6 designates the *mean* mean longitude under the summation [Ref 45].

Next, substitute Eqs (2.139) into Eqs (2.140), which introduces the $A_{i,j}$ into the osculating element equations of motion [Ref 45]:

$$\frac{da_i}{dt} = \sum_{j=1}^N \varepsilon^j \left[A_{i,j}(\bar{\mathbf{a}}) + n(\bar{a}_1) \frac{\partial \eta_{i,j}}{\partial \bar{\ell}} + \sum_{m=1}^{N-j} \varepsilon^m \sum_{k=1}^6 A_{k,m} \frac{\partial \eta_{i,j}}{\partial \bar{a}_k} \right] + \mathcal{O}(\varepsilon^{N+1}) \quad i = 1,2,\dots,5 \quad (2.141a)$$

$$\frac{d\ell}{dt} = n(\bar{a}_1) + \sum_{j=1}^N \varepsilon^j \left[A_{6,j}(\bar{\mathbf{a}}) + n(\bar{a}_1) \frac{\partial \eta_{6,j}}{\partial \bar{\ell}} + \sum_{m=1}^{N-j} \varepsilon^m \sum_{k=1}^6 A_{k,m} \frac{\partial \eta_{6,j}}{\partial \bar{a}_k} \right] + \mathcal{O}(\varepsilon^{N+1}) \quad (2.141b)$$

Rearranging Eqs (2.141) so that there is only a single summation over ε results in [Ref 45]:

$$\frac{da_i}{dt} = \sum_{j=1}^N \varepsilon^j \left[A_{i,j}(\bar{\mathbf{a}}) + n(\bar{a}_1) \frac{\partial \eta_{i,j}}{\partial \bar{\ell}} + \sum_{k=1}^6 \sum_{p=1}^{j-1} A_{k,p} \frac{\partial \eta_{i,j-p}}{\partial \bar{a}_k} \right] + \mathcal{O}(\varepsilon^{N+1}) \quad i = 1,2,\dots,5 \quad (2.142a)$$

$$\frac{d\ell}{dt} = n(\bar{a}_1) + \sum_{j=1}^N \varepsilon^j \left[A_{6,j}(\bar{\mathbf{a}}) + n(\bar{a}_1) \frac{\partial \eta_{6,j}}{\partial \bar{\ell}} + \sum_{k=1}^6 \sum_{p=1}^{j-1} A_{k,p} \frac{\partial \eta_{6,j-p}}{\partial \bar{a}_k} \right] + \mathcal{O}(\varepsilon^{N+1}) \quad (2.142b)$$

We now expand the perturbing functions in the right-hand side of the VOP equations (Eqs (2.137)) about the mean elements using a Taylor series:

$$F_i(\mathbf{a}, \ell) = \sum_{n=0}^{\infty} \frac{1}{n!} \left(\sum_{k=1}^6 \Delta a_k \frac{\partial}{\partial a_k} \right)^n F_i(\mathbf{a}, \ell) \Bigg|_{\substack{\mathbf{a}=\bar{\mathbf{a}} \\ \ell=\bar{\ell}}} \quad (2.143)$$

where $\Delta a_k = a_k - \bar{a}_k$ and are defined by Eqs (2.138).

We define $\frac{\partial}{\partial \bar{a}_k}$ to mean $\frac{\partial}{\partial a_k} \Big|_{a=\bar{a}_k}$, and rearrange Eqs (2.143) as a power series in

ε to obtain [Ref 45]:

$$F_i(\mathbf{a}, \ell) = \sum_{j=0}^N \varepsilon^j f_{i,j}(\bar{\mathbf{a}}, \bar{\ell}) + \mathcal{O}(\varepsilon^{N+1}) \quad (2.144)$$

where [Ref 45]:

$$f_{i,0}(\bar{\mathbf{a}}, \bar{\ell}) = F_i(\mathbf{a}, \ell) \quad (2.145a)$$

$$f_{i,1}(\bar{\mathbf{a}}, \bar{\ell}) = \sum_{k=1}^6 \eta_{k,1} \frac{\partial F_i}{\partial \bar{a}_k} \quad (2.145b)$$

$$f_{i,2}(\bar{\mathbf{a}}, \bar{\ell}) = \sum_{k=1}^6 \left(\eta_{k,2} \frac{\partial F_i}{\partial \bar{a}_k} + \frac{1}{2} \sum_{l=1}^6 \eta_{k,1} \eta_{l,1} \frac{\partial^2 F_i}{\partial \bar{a}_k \partial \bar{a}_l} \right) \quad (2.145c)$$

etc.

We also expand the mean motion about the *mean* mean motion [Ref 45]:

$$n(a_1) = \sum_{k=0}^{\infty} \frac{(\Delta a_k)^k}{k!} \frac{\partial^k n}{\partial \bar{a}_1^k} \quad (2.146)$$

We then rearrange Eq (2.146) as a power series in ε to obtain [Ref 45]:

$$n(a_1) = \sum_{k=0}^{\infty} \varepsilon^k N_k(\bar{\mathbf{a}}, \bar{\ell}) \quad (2.147)$$

where [Ref 45]:

$$N_0(\bar{\mathbf{a}}, \bar{\ell}) = n(\bar{a}_1) = \bar{n} \quad (2.148a)$$

$$N_1(\bar{\mathbf{a}}, \bar{\ell}) = -\frac{3}{2} \frac{\bar{n}}{\bar{a}_1} \eta_{1,1} \quad (2.148b)$$

$$N_2(\bar{\mathbf{a}}, \bar{\ell}) = \frac{15}{4} \frac{\bar{n}}{\bar{a}_1^2} \eta_{1,1}^2 - \frac{3}{2} \frac{\bar{n}}{\bar{a}_1} \eta_{1,2} \quad (2.148c)$$

etc.

We now substitute Eqs (2.142) into the left-hand side of Eqs (2.137), and Eqs (2.144) and (2.147) into the right-hand side of Eqs (2.137) [Ref 45]. Because both sides are power series in ε , terms containing like powers of ε must be equal [Ref 10, pp 631]. Equating such terms, we obtain the expressions for the j^{th} -order contribution to the osculating element rates [Ref 45]:

$$A_{i,j}(\bar{\mathbf{a}}) + \bar{n} \frac{\partial \eta_{i,j}}{\partial \bar{\ell}} + \sum_{k=1}^6 \sum_{p=1}^{j-1} A_{k,p} \frac{\partial \eta_{i,j-p}}{\partial \bar{a}_k} = f_{i,j-1}(\bar{\mathbf{a}}, \bar{\ell}) \quad i = 1, 2, \dots, 5 \quad (2.149a)$$

$$A_{6,j}(\bar{\mathbf{a}}) + \bar{n} \frac{\partial \eta_{6,j}}{\partial \bar{\ell}} + \sum_{k=1}^6 \sum_{p=1}^{j-1} A_{k,p} \frac{\partial \eta_{6,j-p}}{\partial \bar{a}_k} = f_{6,j-1}(\bar{\mathbf{a}}, \bar{\ell}) + N_j(\bar{\mathbf{a}}, \bar{\ell}) \quad (2.149b)$$

These expressions relate the $A_{i,j}$ (which are unknown functions of the slowly-varying mean elements), and the partial derivatives of the $\eta_{i,j}$ (which are unknown short-periodic variations), to the known terms of the power series expansion of the osculating perturbing function, $f_{i,j}$ [Ref 10, pp 632]. To get rid of the dependence on the mean fast variable, $\bar{\ell}$, we take advantage of the constraint that the $\eta_{i,j}$ are 2π periodic in $\bar{\ell}$ [Ref 45]. We can then integrate both sides of Eqs (2.149) from 0 to 2π over the mean fast variable,

$\bar{\ell}$, which eliminates the partial derivatives $\frac{\partial \eta_{i,j}}{\partial \ell}$ [Ref 45]. This integration is known as

the *averaging operation* and is defined mathematically as [Ref 45]:

$$\langle H(\bar{\mathbf{a}}, \bar{\ell}) \rangle_{\bar{\ell}} = \frac{1}{2\pi} \int_0^{2\pi} H(\bar{\mathbf{a}}, \bar{\ell}) d\bar{\ell} \quad (2.150)$$

Because the $\eta_{i,j}$ are 2π periodic in $\bar{\ell}$, partial derivatives of the $\eta_{i,j}$ are also 2π periodic in $\bar{\ell}$, so [Ref 45]:

$$\left\langle \bar{n} \frac{\partial \eta_{i,j}}{\partial \ell} \right\rangle_{\bar{\ell}} = 0 \quad (2.151)$$

Applying the averaging operation to Eqs (2.149) thus yields [Ref 45]:

$$A_{i,j}(\bar{\mathbf{a}}) = \langle f_{i,j-1}(\bar{\mathbf{a}}, \bar{\ell}) \rangle_{\bar{\ell}} + \sum_{p=1}^{j-1} \sum_{k=1}^6 A_{k,p} \left\langle \frac{\partial \eta_{i,j-p}}{\partial \bar{a}_k} \right\rangle_{\bar{\ell}} \quad i = 1, 2, \dots, 5 \quad (2.152a)$$

$$A_{6,j}(\bar{\mathbf{a}}) = \langle f_{6,j-1}(\bar{\mathbf{a}}, \bar{\ell}) + N_j(\bar{\mathbf{a}}, \bar{\ell}) \rangle_{\bar{\ell}} + \sum_{p=1}^{j-1} \sum_{k=1}^6 A_{k,p} \left\langle \frac{\partial \eta_{6,j-p}}{\partial \bar{a}_k} \right\rangle_{\bar{\ell}} \quad (2.152b)$$

Eqs (2.152) may be simplified by applying the following constraint, which imposes that the $\eta_{i,j}$ functions not contain any long-period or secular terms [Ref 45]:

$$\left\langle \frac{\partial \eta_{i,j-p}}{\partial \bar{a}_k} \right\rangle_{\bar{\ell}} \equiv 0 \quad \begin{array}{l} i = 1, 2, \dots, 6 \\ k = 1, 2, \dots, 6 \end{array} \quad (2.153)$$

By applying the averaging operation to Eqs (2.140), and then applying Eqs (2.153), the constraint is seen to be equivalent to [Ref 45]:

$$\left\langle \frac{da_i}{dt} \right\rangle_{\bar{\ell}} = \frac{d\bar{a}_i}{dt} \quad i = 1, 2, \dots, 5 \quad (2.154a)$$

$$\left\langle \frac{d\ell}{dt} \right\rangle_{\bar{\ell}} = \frac{d\bar{\ell}}{dt} \quad (2.154b)$$

Applying Eqs (2.151) and (2.153) shows that the mean elements represent the long-period and secular contributions to the osculating elements plus a constant, i.e. [Ref 45]:

$$\langle \eta_{i,j}(\bar{\mathbf{a}}, \bar{\ell}) \rangle_{\bar{\ell}} = C_{i,j} \quad (2.155)$$

A logical constraint to impose is that the $\eta_{i,j}$ functions not contain any constant terms, which means that the [Ref 45]:

$$C_{i,j} \equiv 0 \quad (2.156)$$

so that, by applying the averaging operation to Eqs (2.138) [Ref 45]:

$$\langle a_i \rangle_{\bar{\ell}} = \bar{a}_i \quad i = 1, 2, \dots, 5 \quad (2.157a)$$

$$\langle \ell \rangle_{\bar{\ell}} = \bar{\ell} \quad (2.157b)$$

The result of the constraints of Eqs (2.153) and (2.156) is that the $\eta_{i,j}$ functions contain only pure and mixed short-period terms [Ref 45]. Eqs (2.152) now reduce to [Ref 45]:

$$A_{i,j}(\bar{\mathbf{a}}) = \langle f_{i,j-1}(\bar{\mathbf{a}}, \bar{\ell}) \rangle_{\bar{\ell}} \quad i = 1, 2, \dots, 5 \quad (2.158a)$$

$$A_{6,j}(\bar{\mathbf{a}}) = \langle f_{6,j-1}(\bar{\mathbf{a}}, \bar{\ell}) + N_j(\bar{\mathbf{a}}, \bar{\ell}) \rangle_{\bar{\ell}} \quad (2.158b)$$

We can now express the averaged equations of motion in terms of the power series expansion of the disturbing function and, in the case of the *mean* mean motion, also in terms of the power series expansion of the osculating mean motion [Ref 45]. Substitution into Eqs (2.139) yields the averaged equations of motion [Ref 45]:

$$\frac{d\bar{a}_i}{dt} = \sum_{j=1}^N \varepsilon^j \langle f_{i,j-1}(\bar{\mathbf{a}}, \bar{\ell}) \rangle_{\bar{\ell}} + O(\varepsilon^{N+1}) \quad i = 1, 2, \dots, 5 \quad (2.159a)$$

$$\frac{d\bar{\ell}}{dt} = n(\bar{a}_1) + \sum_{j=1}^N \varepsilon^j \left\langle f_{6,j-1}(\bar{\mathbf{a}}, \bar{\ell}) + N_j(\bar{\mathbf{a}}, \bar{\ell}) \right\rangle_{\bar{\ell}} + \mathcal{O}(\varepsilon^{N+1}) \quad (2.159b)$$

It should be noted that the $f_{i,j}$ and N_j for $j \geq 1$ still contain terms of the short-periodic functions $\eta_{i,j}$, as can be seen in Eqs (2.145) and (2.148) [Ref 45]. The averaging operation does not remove all dependence on the short-period terms, since products of the osculating force function, F_i , with the $\eta_{i,j}$ functions appear, as do products of two or more $\eta_{i,j}$ functions [Ref 45]. These products can produce long-period terms that are independent of $\bar{\ell}$ [Ref 45].

To determine the short-period functions $\eta_{i,j}$, we first obtain a partial differential equation by subtracting Eqs (2.152) from Eqs (2.149) [Ref 45]:

$$\bar{n} \frac{\partial \eta_{i,j}}{\partial \bar{\ell}} + \sum_{p=1}^{j-1} \sum_{k=1}^6 A_{k,p} \left(\frac{\partial \eta_{i,j-p}}{\partial \bar{a}_k} - \left\langle \frac{\partial \eta_{i,j-p}}{\partial \bar{a}_k} \right\rangle_{\bar{\ell}} \right) = f_{i,j-1} - \langle f_{i,j-1} \rangle_{\bar{\ell}} \quad i = 1, 2, \dots, 5 \quad (2.160a)$$

$$\bar{n} \frac{\partial \eta_{6,j}}{\partial \bar{\ell}} + \sum_{p=1}^{j-1} \sum_{k=1}^6 A_{k,p} \left(\frac{\partial \eta_{6,j-p}}{\partial \bar{a}_k} - \left\langle \frac{\partial \eta_{6,j-p}}{\partial \bar{a}_k} \right\rangle_{\bar{\ell}} \right) = f_{6,j-1} + N_j - \langle f_{6,j-1} + N_j \rangle_{\bar{\ell}} \quad (2.160b)$$

Defining the superscript s to be the short-periodic part of a function, so that [Ref 45]:

$$f_{i,j-1}^s = f_{i,j-1} - \langle f_{i,j-1} \rangle_{\bar{\ell}} \quad (2.161)$$

Eqs (2.160) can be rewritten as follows [Ref 45]:

$$\bar{n} \frac{\partial \eta_{i,j}}{\partial \bar{\ell}} = f_{i,j-1}^s - \sum_{p=1}^{j-1} \sum_{k=1}^6 A_{k,p} \frac{\partial \eta_{i,j-p}^s}{\partial \bar{a}_k} \quad i = 1, 2, \dots, 5 \quad (2.162a)$$

$$\bar{n} \frac{\partial \eta_{6,j}}{\partial \bar{\ell}} = f_{6,j-1}^s + N_j^s - \sum_{p=1}^{j-1} \sum_{k=1}^6 A_{k,p} \frac{\partial \eta_{6,j-p}^s}{\partial \bar{a}_k} \quad (2.162b)$$

As stated earlier, $\eta_{i,j}$ represents the short-periodic variation of order j in element \bar{a}_i [Ref 45]. Inspection of Eqs (2.162) shows that the $\eta_{i,j}$ depend only on quantities of lower order [Ref 45]. The lone exception is in the case of the mean fast variable $\bar{\ell}$, because $\eta_{6,j}$ is dependent on $\eta_{1,j}$ through the term N_j , which means that the function $\eta_{1,j}$ must be determined before the function $\eta_{6,j}$ [Ref 45].

Multiplying Eqs (2.162) by $1/n$ bar, and integrating with respect to $\bar{\ell}$ yields the short-periodic functions to within an arbitrary function of the slowly-varying mean elements [Ref 45]:

$$\eta_{i,j}(\bar{\mathbf{a}}, \bar{\ell}) = \alpha_{i,j}(\bar{\mathbf{a}}, \bar{\ell}) + C_{i,j}(\bar{\mathbf{a}}) \quad (2.163)$$

where $C_{i,j}$ is an arbitrary function of integration, and $\alpha_{i,j}$ is defined as follows [Ref 45]:

$$\alpha_{i,j} = \frac{1}{\bar{n}} \int \left[f_{i,j-1}^S - \sum_{k=1}^6 \sum_{p=1}^{j-1} A_{k,p} \frac{\partial \eta_{i,j-p}^S}{\partial \bar{a}_k} \right] d\bar{\ell} \quad i = 1, 2, \dots, 5 \quad (2.164a)$$

$$\alpha_{i,j} = \frac{1}{\bar{n}} \int \left[\{f_{6,j-1}^S + N_j^S\} - \sum_{k=1}^6 \sum_{p=1}^{j-1} A_{k,p} \frac{\partial \eta_{6,j-p}^S}{\partial \bar{a}_k} \right] d\bar{\ell} \quad (2.164b)$$

Averaging Eq (2.163) yields [Ref 45]:

$$\langle \eta_{i,j} \rangle_{\bar{\ell}} = C_{i,j}(\bar{\mathbf{a}}) \quad (2.165)$$

which shows that the constraints imposed in Eqs (2.153) and (2.155) are valid [Ref 45]. As we did before, we assume that the $C_{i,j}$ are equal to zero, reproducing the constraint of Eq (2.156) [Ref 45]. This constraint requires that the $\eta_{i,j}$ be purely short-periodic and mixed short-periodic, that is, $\eta_{i,j} = \eta_{i,j}^S$ [Ref 45].

Thus, a set of functions $\eta_{i,j}$ that contain only short-periodic terms can be obtained, and the near-identity transformation of Eqs (2.138) can be expressed as follows [Ref 45]:

$$a_i = \bar{a}_i + \frac{1}{\bar{n}} \sum_{j=1}^N \varepsilon^j \int \left[f_{i,j-1}^S - \sum_{k=1}^6 \sum_{p=1}^{j-1} A_{k,p} \frac{\partial \eta_{i,j-p}^S}{\partial \bar{a}_k} \right] d\bar{\ell} + \mathcal{O}(\varepsilon^{N+1}) \quad i = 1, 2, \dots, 5 \quad (2.166a)$$

$$\ell = \bar{\ell} + \frac{1}{\bar{n}} \sum_{j=1}^N \varepsilon^j \int \left[\{f_{6,j-1}^S + N_j^S\} - \sum_{k=1}^6 \sum_{p=1}^{j-1} A_{k,p} \frac{\partial \eta_{6,j-p}^S}{\partial \bar{a}_k} \right] d\bar{\ell} + \mathcal{O}(\varepsilon^{N+1}) \quad (2.166b)$$

The first order short-periodic effects can be formulated as closed-form expressions, if the appropriate fast variable is used. For example, zonal short-periodics are formulated in terms of the true longitude, tesseral m-dailies are formulated in terms of the Greenwich Hour Angle, and third-body short-periodics are formulated in terms of the eccentric longitude. The coefficients of the periodic terms in these expressions are slowly-varying because they are functions of the mean elements. These closed-form short-periodic motion formulae, together with an efficient interpolation scheme, are used to solve Eqs (2.166) for the second order mean element rates, as required.

2.5 Observations Models

2.5.1 Space-Based Visible Observations Model

Space-based visible observations of satellites are available via the Space Surveillance Network. Including space-based visible observations has been shown to add observability for geosynchronous orbit determination [Ref 21]. In the course of this study, the capability to process these observations was incorporated into GTDS by Dr. Paul Cefola and Mr. Zach Folcik at the MIT/Lincoln Laboratory.

With optical observations, the angular coordinates right ascension and declination are obtained. These are designated α and δ , respectively. The right ascension and declination are related with the position vector of the target satellite whose orbit is to be determined, $\mathbf{r}(x, y, z)$, and the position vector of the observer, $\mathbf{R}(X, Y, Z)$. We assume

that the observer is the SBV telescope, so that (X, Y, Z) represent the position coordinates of the SBV.

The two lines of information supplied with each SBV observation include the observation time, the space-based right ascension and declination, and the position of the SBV. Coordinate systems were an issue in integrating the SBV observations model into GTDS. The space-based right ascension and declination are given in the J2000.0 coordinate system, while the SBV position coordinates are given in the ECEF coordinate system.

In order to calculate the SBV observation residuals (observed minus computed), we must obtain the computed space-based right ascension and declination in the J2000.0 coordinate system (so that they are compatible with the observed α and δ). To do this, we must transform the position coordinates of the SBV from ECEF to J2000.0 prior to calculating the computed right ascension and declination at each observation time. It is also important to note that the transformation is from the true ECEF coordinate system, so we must include the polar motion transformation described in Chapter 2.3.3.4. We must also transform the computed target satellite position and velocity from the integration coordinate system (B1950 in GTDS) to J2000.0 if we are not integrating in J2000.0.

The right ascension and declination are related to the target satellite position and the observer (SBV) position via the following formulae [Ref 58]:

$$\begin{aligned}
 \rho_x &= \rho \cos \delta \cos \alpha = x - X \\
 \rho_y &= \rho \cos \delta \sin \alpha = y - Y \\
 \rho_z &= \rho \sin \delta = z - Z \\
 \rho &= \sqrt{\rho_x^2 + \rho_y^2 + \rho_z^2}
 \end{aligned}
 \tag{2.167}$$

Where the vector rho is the relative position of the target satellite with respect to the SBV. Assuming that both the satellite positions x, y, and z and the SBV positions X, Y, and Z are known, and are expressed in the correct coordinate system, at the observation time, then we can compute ρ using Eqs (2.167). Dividing Eqs (2.167) by ρ gives:

$$\begin{aligned}\cos \delta \cos \alpha &= (x - X) / \rho \\ \cos \delta \sin \alpha &= (y - Y) / \rho \\ \sin \delta &= (z - Z) / \rho\end{aligned}\tag{2.168}$$

Eqs (2.168) can be solved for the computed space-based right ascension and declination. Right ascension and declination can be expressed in terms of the inverse trigonometric functions as follows:

$$\alpha = ATAN2\left[\left(\frac{y - Y}{\rho}\right), \left(\frac{x - X}{\rho}\right)\right]\tag{2.169}$$

$$\delta = ASIN\left(\frac{z - Z}{\rho}\right)\tag{2.170}$$

2.5.1.1 Partial Derivatives of the SBV Data Type in GTDS.

In GTDS, the calculation of the observation partials with respect to the solve-for parameters is partitioned as follows (see Chapter 4.1.3 for the derivation):

$$\left[\frac{\partial \text{observations}}{\partial \mathbf{x}_0}\right] = \left[\frac{\partial \text{observations}}{\partial \mathbf{r}} \quad \vdots \quad \frac{\partial \text{observations}}{\partial \dot{\mathbf{r}}}\right] \begin{bmatrix} \frac{\partial \mathbf{r}}{\partial \mathbf{x}_0} \\ \frac{\partial \dot{\mathbf{r}}}{\partial \mathbf{x}_0} \end{bmatrix}\tag{2.171}$$

The matrix $\begin{bmatrix} \frac{\partial \mathbf{r}}{\partial \mathbf{x}_0} \\ \frac{\partial \dot{\mathbf{r}}}{\partial \mathbf{x}_0} \end{bmatrix}$ is obtained from the variational equations, either Cowell or

semi-analytical (see Chapter 4.2).

The observation partials matrix, $\begin{bmatrix} \frac{\partial \text{observations}}{\partial \mathbf{r}} & \vdots & \frac{\partial \text{observations}}{\partial \dot{\mathbf{r}}} \end{bmatrix}$, is specific to the SBV optical observations. Coordinate systems again become an issue, because the SBV observations are given in J2000.0, but the integration coordinate system in GTDS is B1950. As a result, we must calculate the observations partials matrix using the chain rule as follows:

$$\begin{bmatrix} \frac{\partial \text{observations}}{\partial \mathbf{r}} & \vdots & \frac{\partial \text{observations}}{\partial \dot{\mathbf{r}}} \end{bmatrix} = \begin{bmatrix} \frac{\partial \text{observations}}{\partial \mathbf{r}_{J2000}} & \vdots & \frac{\partial \text{observations}}{\partial \dot{\mathbf{r}}_{J2000}} \end{bmatrix} \begin{bmatrix} \frac{\partial \mathbf{r}_{J2000}}{\partial \mathbf{r}_{B1950}} & \frac{\partial \mathbf{r}_{J2000}}{\partial \dot{\mathbf{r}}_{B1950}} \\ \frac{\partial \dot{\mathbf{r}}_{J2000}}{\partial \mathbf{r}_{B1950}} & \frac{\partial \dot{\mathbf{r}}_{J2000}}{\partial \dot{\mathbf{r}}_{B1950}} \end{bmatrix} \quad (2.172)$$

To calculate the first matrix on the right-hand side of Eq (2.172), we require the partial derivatives of the space-based right ascension and declination with respect to the target satellite position components (x, y, z). The partials with respect to the target satellite's velocity are zero because the velocity does not appear explicitly in the expressions for right ascension and declination.

There are two ways to obtain the required analytical partial derivatives. The first approach is to differentiate Eqs (2.169) and (2.170) using results from the differential calculus for the inverse trigonometric functions [Ref 59]:

$$\frac{d(\tan^{-1} u)}{dx} = \frac{du/dx}{1+u^2} \quad (2.173)$$

$$\frac{d(\sin^{-1} u)}{dx} = \frac{du/dx}{\sqrt{1-u^2}} \quad (2.174)$$

An alternate approach is to consider the implicit definition of RA and DEC given in Eqs (2.167). The first two of Eqs (2.167) can be differentiated with respect to x. Then we can solve the resulting pair of equations for $\frac{\partial \alpha}{\partial x}$ and $\frac{\partial \delta}{\partial x}$. In a similar fashion, by differentiating the first two of Eqs (2.167) with respect to y, we obtain $\frac{\partial \alpha}{\partial y}$ and $\frac{\partial \delta}{\partial y}$. The partial derivative of the right ascension with respect to z is zero. The partial derivative of the declination is obtained by differentiating the third of Eqs (2.167) with respect to z.

With either approach, the same results are obtained [Ref 58]:

$$\frac{\partial \alpha}{\partial x} = \frac{-\sin \alpha}{\rho \cos \delta} \quad (2.175a)$$

$$\frac{\partial \alpha}{\partial y} = \frac{\cos \alpha}{\rho \cos \delta} \quad (2.175b)$$

$$\frac{\partial \alpha}{\partial z} = 0 \quad (2.175c)$$

$$\frac{\partial \delta}{\partial x} = \frac{-\cos \alpha \sin \delta}{\rho} \quad (2.175d)$$

$$\frac{\partial \delta}{\partial y} = \frac{-\sin \alpha \sin \delta}{\rho} \quad (2.175e)$$

$$\frac{\partial \delta}{\partial z} = \frac{\cos \delta}{\rho} \quad (2.175f)$$

2.5.2 Observations Corrections

2.5.2.1 Light-time Correction

Aberration is the angular displacement of an apparent position due to the relative motion of an object and the observer [Ref 10, pp 90]. *Light-time correction* accounts for the fact that the path between the space object and the observer is no longer a straight line between the points in the observed direction [Ref 10, pp 90]. This is because light travels at a finite speed, so the travel time of light must be accounted when the direction of an object is measured [Ref 10, pp 90].

In GTDS, the light-time correction is applied to the time tag associated with the observation measurement. The time t_V corresponds to the time when the signal (either a radio signal or light) leaves the satellite [Ref 48, pp 7-95]. The time t_R corresponds to the actual measurement time-tag when the signal is received at the ground station [Ref 48, pp 7-96]. The light-time correction in GTDS involves approximating t_V by correcting the measurement time tag as follows [Ref 48, pp 7-96]:

$$t_V = t_R - \frac{\rho}{c} \quad (2.176)$$

ρ is the relative range from the spacecraft to the tracking station and c is the speed of light [Ref 48, pp 7-96]. In GTDS, ρ is approximated by calculating the relative range vector at the measurement time t_R using the spacecraft position vector at t_R [Ref 48, pp 7-96].

2.5.2.2 SBV Light-time Correction

For the space-based visible observations model, the light-time correction is handled differently than it is with ground-based sensors. Instead of correcting the

observation time, the position of the target satellite at the observation time is corrected. This change is made because the position of the SBV is time-dependent and quickly-varying.

To apply the SBV light-time correction, we first divide the computed relative position by the speed of light, giving us the light-time:

$$L.T. = \frac{\rho}{c} \quad (2.177)$$

We next multiply the light time by the velocity vector of the target satellite, giving us the correction that must be applied to the position vector of the target satellite:

$$\Delta \mathbf{r} = \begin{bmatrix} \Delta x \\ \Delta y \\ \Delta z \end{bmatrix} = L.T. \begin{bmatrix} \dot{x} \\ \dot{y} \\ \dot{z} \end{bmatrix} \quad (2.178)$$

It is noted that this correction assumes that the satellite trajectory is linear over the light-time interval. It is for this reason that the position of the target satellite, rather than the position of the SBV, is adjusted in the correction. With the target satellite in GEO orbit, and the SBV in LEO orbit, the target satellite's trajectory behaves more linearly over the light-time interval.

The light-time correction calculated in Eq (2.178) must then be applied to the relative position (ρ), right ascension (α), and declination (δ) when obtaining the computed observations at each time step. This means that the correction in each component direction must be applied to the target satellite position components (x, y, z) in Eqs (2.168), (2.169), and (2.170) in Chapter 2.5.1.1 when calculating the observation residuals.

2.5.2.3 Ionospheric Refraction Correction

Ionospheric refraction is caused by deflection in electromagnetic waves as they pass through the electron plasma of the ionosphere, which extends from approximately 80 km to beyond 1000 km altitude [Ref 10, pp 91]. The deflection causes distortion in observations that can be corrected using various models [Ref 10, pp 91]. In GTDS, ionospheric refraction corrections are computed from an electron density profile, which is dependent on the latitude and longitude where the electromagnetic wave from the observer to the spacecraft penetrates the ionosphere [Ref 48, pp 7-88]. This so-called subionospheric point is calculated as a function of the station latitude and longitude, and the azimuth and elevation angles from the station to the satellite [Ref 48, pp 7-88]. The total vertical electron content is calculated based on the height of the ionosphere above the subionospheric point and the position of the satellite within the ionosphere [Ref 48, pp 7-88]. A range correction can then be calculated from the total vertical electron content and the elevation angle that the electromagnetic wave passes through the ionosphere [Ref 48, pp 7-90]. Finally, a range-rate correction can be found from two successive range corrections [Ref 48, pp 7-92].

Tropospheric refraction is caused by the local temperature, humidity, and pressure conditions over the observation site [Ref 10, pp 91]. The troposphere is the region of the Earth's atmosphere extending from the surface up to approximately 30 km altitude [Ref 48, pp 7-61]. In GTDS, tropospheric refraction corrections are computed in a similar manner as ionospheric refraction corrections [Ref 48]. The refractivity and scale height of the troposphere are used to calculate corrections to the elevation angle, range, and range-rate [Ref 48, pp 7-84].

2.5.2.4 Measurement Bias Estimation

Observations are subject to errors that cause them to vary from their true value. These errors can be caused by a number of things, including sensor maintenance, sensor miscalibration equipment failure, or operator error [Ref 10, pp 664]. Bias is a constant offset from the true value, noise is random variation about the mean value, and drift is slow variation of the mean value over time [Ref 10, pp 664]. Measurement bias can be solved-for as part of the solution state and simply added or subtracted to correct the observations in differential correction applications. The measurement bias will often appear as a large mean residual for a particular sensor. In GTDS, the measurement bias estimate is added to or subtracted from all observations from that sensor in the next iteration of the DC. This process is repeated until the measurement bias gets small enough that it reaches a specified tolerance. GEO orbit determination experience at MIT/Lincoln Laboratory has shown that it is often necessary to estimate the measurement biases for owner/operator-provided ranging data when these data are combined with SSN observation data [Ref 21].

Chapter 3 Solar Radiation Pressure Force Modeling

3.1 Introduction

A photon of light carries an amount of momentum equal to its energy divided by the velocity of light [Ref 60, pp 48]. This momentum can be exchanged upon interaction with a solid surface, such as a spacecraft [Ref 60, pp 48]. The result is that the solid surface experiences radiation pressure, or force per unit area, that is equal to the vector difference between the incident and reflected momentum flux [Ref 11, pp 570]. Solar radiation thus behaves like a flux of particles continuously emitted by the sun [Ref 60, pp 48]. Other sources of electromagnetic radiation pressure are Earth albedo, which is solar radiation reflected by the Earth's atmosphere, Earth infrared radiation, and the spacecraft's own thermal emission. Of these sources, solar radiation is the dominant source of radiation pressure.

3.2 Spherical Spacecraft Model

The spherical model for solar radiation pressure, or 'cannonball' model, assumes that the spacecraft is an invariant sphere with constant thermo-optical properties. This model specifies a cross-sectional area exposed to the sun, and a coefficient of reflectivity, C_R .

As defined by Vallado, the coefficient of reflectivity indicates how the spacecraft reflects incoming radiation, and can take on values between 0.0 and 2.0 [Ref 10]. A value of 0.0 indicates that the spacecraft is translucent to incoming radiation, meaning that none of the radiative force is transferred to the spacecraft [Ref 10]. A value of 1.0

indicates that the spacecraft behaves as a black body, so that all incoming radiation is absorbed and re-radiated, and all of the radiative force is transferred to the spacecraft [Ref 10]. A value of 2.0 indicates that the spacecraft behaves as a flat mirror perpendicular to the incoming radiation, so that all the incoming radiation is reflected, and twice the radiative force is transferred to the spacecraft [Ref 10].

The equation for force due to solar radiation pressure acting on a uniformly reflecting sphere is [Refs 10, 48]:

$$\mathbf{F} = -\frac{\Phi A}{c} C_R \hat{\mathbf{s}} \quad (3.1)$$

where:

- \mathbf{F} = force due to solar radiation pressure on the sphere, N
- Φ = solar flux, W/m^2
- A = projected surface area of the spacecraft, m^2
- c = speed of light, m/s
- C_R = spacecraft reflectivity coefficient
- $\hat{\mathbf{s}}$ = spacecraft - to - sun unit vector

3.3 Macro-model Approach

Radiative forces may be modeled by assuming that the incident radiation on a surface is either absorbed, reflected specularly, or reflected diffusely. This assumes that none of the radiation is transmitted through the spacecraft. Figures 3-1 – 3-3 show the possible absorption and reflection that may occur [Refs 11, 29, 30].

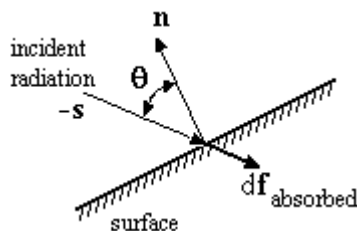


Figure 3-1 – Absorption

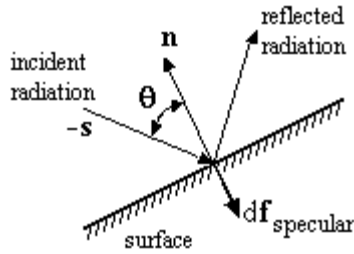


Figure 3-2 – Specular Reflection

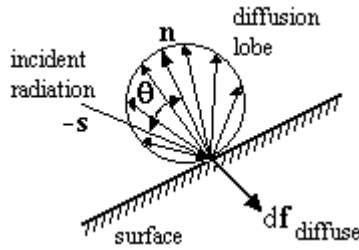


Figure 3-3 – Diffuse Reflection

For each surface area element dA of the spacecraft, the coefficients α , ρ , and δ represent the fraction of the incident radiation that is absorbed, reflected, or diffused, respectively. In this work, they will be referred to as absorptivity, specular reflectivity, and diffuse reflectivity coefficients. For each surface area element of the spacecraft, these coefficients are related through Equation (3.2):

$$\alpha + \rho + \delta = 1 \quad (3.2)$$

This development makes the following assumptions [Ref 60]:

- (1) The spacecraft transmissivity is zero; that is, absorbed radiation is not re-emitted at the same wavelength. The absorbed energy is usually re-emitted as infrared radiation of a longer wavelength.
- (2) The diffusion is Lambertian. This means that the intensity of diffused radiation in a given direction is proportional to the cosine of the angle ϕ between that direction and the unit normal vector \mathbf{n} that is perpendicular to dA . This gives rise to a spherical diffusion lobe, as shown in Figure 3-3.

- (3) The specular reflection is perfectly specular. (See Chapter 3.3.2.)
- (4) The surface area element dA behaves like a linear combination of a black body, a perfect mirror, and a Lambertian diffuser. This means that α , ρ , and δ completely specify the optical properties of the area element. Furthermore, the coefficients do not vary depending on the angle θ between the surface normal vector \mathbf{n} and the spacecraft-to-sun vector \mathbf{s} .

3.3.1 Absorption

The differential force due to the portion of the incident radiation that is absorbed by a surface area element of the spacecraft is directed along the $-\hat{\mathbf{s}}$ vector (opposite the spacecraft-to-sun vector). The differential force has a magnitude proportional to the cross-sectional area element, given by $dA \cdot \cos(\theta)$. Thus, the differential force is given by the following equation [Refs 11, 29, 60]:

$$d\mathbf{f}_{\text{absorbed}} = -\frac{\Phi dA \cos \theta}{c} \alpha \hat{\mathbf{s}} \quad (3.3)$$

where:

$d\mathbf{f}$ = differential force due to solar radiation pressure on the area element, N

Φ = solar flux, W/m^2

dA = elementary area of the spacecraft, m^2

θ = angle between surface normal and spacecraft - to - sun vector

c = speed of light, m/s

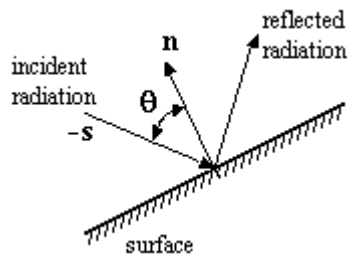
α = absorptivity coefficient of surface area element

$\hat{\mathbf{s}}$ = spacecraft - to - sun unit vector

If $\cos(\theta)$ is negative, then the area element is not illuminated by the sun and will not experience any solar radiation force.

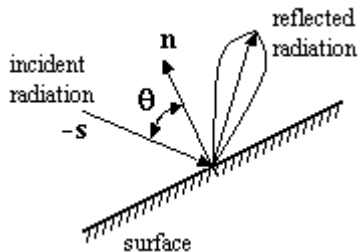
3.3.2 Specular Reflection

In this study, one assumption is that the reflection is perfectly specular, which means that all of the specularly reflected incident radiation is reflected in the direction offset by the angle θ on the opposite side of the surface normal vector. Figures 3-4 and 3-5 illustrate the difference between perfect and near-perfect specular reflection, which results in a small diffusion lobe [Ref 30].



Source: Dr. Ken Chan, The Aerospace Corporation [Ref 30]

Figure 3-4 – Perfect Specular Reflection



Source: Dr. Ken Chan, The Aerospace Corporation [Ref 30]

Figure 3-5 – Near-perfect Specular Reflection

The differential force due to the portion of the incident radiation that is reflected specularly by a surface area element of the spacecraft is directed along the $-\mathbf{n}$ vector (opposite the surface normal vector). The differential force has a magnitude proportional to both the cross-sectional area ($dA \cdot \cos(\theta)$) and the \mathbf{n} component of the momentum

transferred to the area element ($2\cos(\theta)$). The differential force is thus given by the following equation [Refs 29, 60]:

$$d\mathbf{f}_{\text{specular}} = -\frac{\Phi dA \cos \theta}{c} 2 \cos \theta \rho \hat{\mathbf{n}} \quad (3.4)$$

where:

$d\mathbf{f}$ = differential force due to solar radiation pressure on the area element, N

Φ = solar flux, W/m^2

dA = elementary area of the spacecraft, m^2

θ = angle between surface normal and spacecraft - to - sun vector

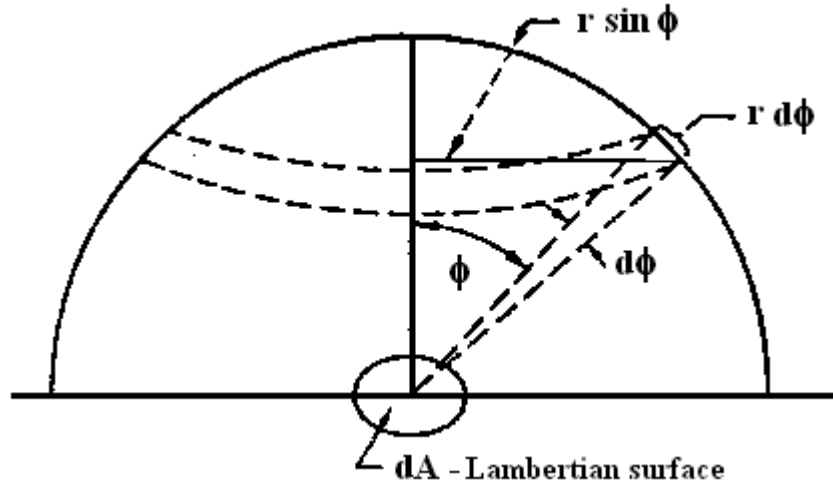
c = speed of light, m/s

ρ = specular reflectivity coefficient of surface area element

$\hat{\mathbf{n}}$ = surface area element unit normal vector

3.3.3 Diffuse Reflection

The differential force due to the portion of the incident radiation that is reflected diffusely is directed along both the $-\mathbf{s}$ and $-\mathbf{n}$ vectors. This is due to the fact this radiation is assumed to be first absorbed, transferring its linear momentum to the surface area element along the $-\mathbf{s}$ direction, and then re-emitted according to Lambert's law. The force due to the re-emitted radiation acts along the $-\mathbf{n}$ direction due to symmetry of the spherical diffusion lobe (Figure 3-3), and can be found by integrating the diffused radiation intensity over a hemisphere external to dA , shown in Figure 3-6 [Ref 30].



Source: Dr. Ken Chan, The Aerospace Corporation [Ref 30]

Figure 3-6 – Geometry of Hemispherical Interception of Radiant Flux from a Lambertian Surface

Since the intensity at each angle ϕ from \mathbf{n} is proportional to $\cos \phi$, the following integral is proportional to the total amount of diffused radiation intensity over the hemisphere [Ref 60]:

$$\int_0^{\pi} 2\pi \sin \phi \cos \phi d\phi = \pi \quad (3.5)$$

If we add another $\cos \phi$ term, the result is the integral which is proportional to the \mathbf{n} component of diffused radiation intensity over the hemisphere [Ref 60]:

$$\int_0^{\pi} 2\pi \sin \phi \cos^2 \phi d\phi = \frac{2}{3} \pi \quad (3.6)$$

Dividing Equation (3.6) by Equation (3.5) gives the result that the force along the $-\mathbf{n}$ direction is proportional to $2/3$ of the total diffused radiation [Ref 60].

The differential force on a surface area element due to diffuse reflection is thus given by the following equation [Refs 29, 60]:

$$d\mathbf{f}_{diffuse} = -\frac{\Phi dA \cos \theta}{c} \delta \left(\hat{\mathbf{s}} + \frac{2}{3} \hat{\mathbf{n}} \right) \quad (3.7)$$

where:

- $d\mathbf{f}$ = differential force due to solar radiation pressure on the area element, N
- Φ = solar flux, W/m²
- dA = elementary area of the spacecraft, m²
- θ = angle between surface normal and spacecraft - to - sun vector
- c = speed of light, m/s
- δ = diffuse reflectivity coefficient of surface area element
- $\hat{\mathbf{s}}$ = spacecraft - to - sun unit vector
- $\hat{\mathbf{n}}$ = surface area element unit normal vector

3.3.4 Total Differential Force on a Surface Area Element

The total differential force due to solar radiation pressure on a surface area element is found by summing Equations (3.3), (3.4), and (3.7):

$$d\mathbf{F} = d\mathbf{f}_{\text{absorbed}} + d\mathbf{f}_{\text{specular}} + d\mathbf{f}_{\text{diffuse}} \quad (3.8)$$

which gives:

$$d\mathbf{F} = -\frac{\Phi dA \cos \theta}{c} \left[\alpha \hat{\mathbf{s}} + \delta \hat{\mathbf{s}} + 2 \cos \theta \rho \hat{\mathbf{n}} + \frac{2}{3} \delta \hat{\mathbf{n}} \right] \quad (3.9)$$

Simplifying, and applying Equation (3.2), gives the end result for the differential radiative force on a surface area element:

$$d\mathbf{F} = -\frac{\Phi dA \cos \theta}{c} \left[(1 - \rho) \hat{\mathbf{s}} + 2 \left(\frac{\delta}{3} + \rho \cos \theta \right) \hat{\mathbf{n}} \right] \quad (3.10)$$

3.4 Macro-model Force Acting on a Flat Plate

In the macro-model approach to solar radiation pressure, the spacecraft is modeled as an assembly of flat plates. The orientation, area, and specular and diffuse reflectivities of each plate within the model are specified. This model assumes Lambertian reflection, which allows us to characterize the reflection in terms of specular and diffuse reflectivities.

The equation for the force due to solar pressure acting on each flat plate is obtained by integrating Equation (3.10) over the surface area, A , of the flat plate [Refs 36, 60, 61]:

$$\mathbf{F} = -\frac{\Phi A \cos \theta}{c} \left[(1 - \rho) \hat{\mathbf{s}} + 2 \left(\frac{\delta}{3} + \rho \cos \theta \right) \hat{\mathbf{n}} \right] \quad (3.11)$$

where:

- \mathbf{F} = force due to solar radiation pressure on the flat plate, N
- A = surface area of the flat plate, m^2
- θ = angle between surface normal and spacecraft - to - sun vector
- ρ = specular reflectivity coefficient
- δ = diffuse reflectivity coefficient
- $\hat{\mathbf{s}}$ = spacecraft - to - sun unit vector
- $\hat{\mathbf{n}}$ = surface normal vector

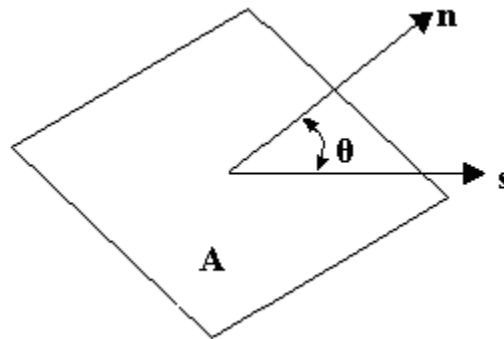


Figure 3-7 – Solar Radiation Pressure Acting on a Flat Plate

3.5 One-panel Spacecraft Model (Alternate Parameterization)

There is an alternate parameterization for the force due to solar pressure acting on a flat plate, expressed in terms of the percentage of radiation absorbed, σ_a , and the percent of reflected radiation diffusely reflected, σ . The specular and diffuse reflectivity coefficients, σ_{rd} and σ_{rs} , respectively, are expressed in this representation as functions of σ_a and σ . This representation is presented by Hughes and used by the one-panel model in the DSST Standalone orbit propagator system [Refs 28, 29].

The expressions for the specular and diffuse reflectivity coefficients in terms of the two other parameters are [Refs 28, 29]:

$$\sigma_{rs} = (1 - \sigma)(1 - \sigma_a) \quad (3.12a)$$

and:

$$\sigma_{rd} = \sigma(1 - \sigma_a) \quad (3.12b)$$

It should be noted that:

$$\sigma_{rs} + \sigma_{rd} = (1 - \sigma)(1 - \sigma_a) + \sigma(1 - \sigma_a) = [(1 - \sigma) + \sigma](1 - \sigma_a) = (1 - \sigma_a)$$

which reduces to:

$$\sigma_a + \sigma_{rs} + \sigma_{rd} = 1 \quad (3.13)$$

Equation (3.13) describes the relationship between the absorptivity and reflectivity coefficients of the alternate parameterization for solar radiation pressure, and also sets physical limitations for the values of these coefficients. It is seen to be analogous to Equation (3.2) for the macro-model coefficients.

The alternate equation for the force due to solar radiation pressure acting on a single flat plate is as follows [Refs 28, 29]:

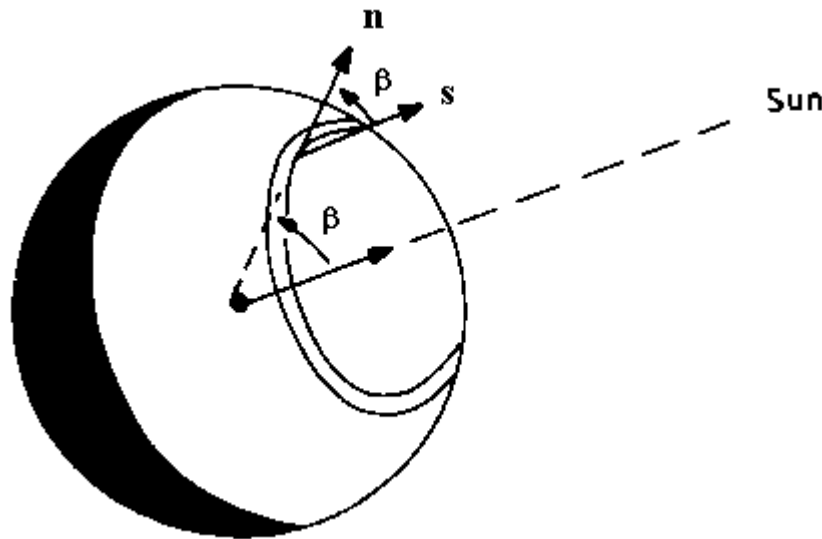
$$\mathbf{F} = -\frac{\Phi A \cos \theta}{c} \left[(\sigma_a + \sigma_{rd}) \hat{\mathbf{s}} + 2 \left(\frac{\sigma_{rd}}{3} + \sigma_{rs} \cos \theta \right) \hat{\mathbf{n}} \right] \quad (3.14)$$

where:

- \mathbf{F} = force due to solar radiation pressure on the flat plate, N
- A = surface area of the flat plate, m²
- θ = angle between surface normal and spacecraft - to - sun vector
- σ_a = percent of incident radiation absorbed
- σ = percent of reflected radiation diffusely reflected
- σ_{rs} = measure of specularly reflected radiation
- σ_{rd} = measure of diffusely reflected radiation
- $\hat{\mathbf{s}}$ = spacecraft - to - sun unit vector
- $\hat{\mathbf{n}}$ = surface normal vector

3.6 Macro-model Force Acting on a Sphere

In addition to modeling a spacecraft as an assembly of flat plates, it is sometimes useful to characterize some spacecraft structures as other simple geometric shapes in the macro-model approach. This report will also consider the force acting on a sphere and right circular cylinder.



Source: Milani, et al., pp 74 [Ref 60]

Figure 3-8 – Spherical Spacecraft Hemisphere Illuminated by the Sun

To obtain the force acting on a sphere of radius R from the macro-model approach, we make similar assumptions as were made with the basic spherical spacecraft model; that is, the sphere is invariant with constant optical properties. Equation (3.10) is integrated over the illuminated hemisphere, as shown in Figure 3-8 [Ref 60, pp 74].

Due to symmetry, the component of force acting normal to the $-\mathbf{s}$ direction integrates to zero over the hemisphere. Thus, integrating Eq (3.10) results in a force acting only in the $-\mathbf{s}$ direction:

$$\mathbf{F} = -\frac{\Phi}{c} \left[\begin{array}{l} (1-\rho) \int_0^{\frac{\pi}{2}} \int_0^{2\pi} \cos \beta R^2 \sin \beta d\theta d\beta \\ + \frac{2}{3} \delta \int_0^{\frac{\pi}{2}} \int_0^{2\pi} \cos^2 \beta R^2 \sin \beta d\theta d\beta \\ + 2\rho \int_0^{\frac{\pi}{2}} \int_0^{2\pi} \cos^3 \beta R^2 \sin \beta d\theta d\beta \end{array} \right] \hat{\mathbf{s}} \quad (3.15)$$

$$\mathbf{F} = -\frac{\Phi}{c} \left[\begin{array}{l} (1-\rho) \int_0^{\frac{\pi}{2}} \cos \beta 2\pi R^2 \sin \beta d\beta \\ + \frac{2}{3} \delta \int_0^{\frac{\pi}{2}} \cos^2 \beta 2\pi R^2 \sin \beta d\beta \\ + 2\rho \int_0^{\frac{\pi}{2}} \cos^3 \beta 2\pi R^2 \sin \beta d\beta \end{array} \right] \hat{\mathbf{s}} \quad (3.16)$$

$$\mathbf{F} = -\frac{\Phi}{c} \left[(1-\rho)\pi R^2 + \frac{2}{3} \delta \frac{2}{3} \pi R^2 + 2\rho \frac{1}{2} \pi R^2 \right] \hat{\mathbf{s}} \quad (3.17)$$

Simplifying gives the following equation for the force due to solar radiation pressure acting on a sphere of radius R [Refs 11, 60]:

$$\mathbf{F} = -\frac{\Phi}{c} \pi R^2 \left(1 + \frac{4}{9} \delta \right) \hat{\mathbf{s}} \quad (3.18)$$

where:

- \mathbf{F} = force due to solar radiation pressure on the sphere, N
- Φ = solar flux, W/m²
- c = speed of light, m/s
- R = radius of the sphere, m
- δ = spacecraft diffuse reflectivity coefficient
- $\hat{\mathbf{s}}$ = spacecraft - to - sun unit vector

Equation (3.18) is seen to be quite similar to Equation (3.1). The projected area of a sphere of radius R is πR^2 ; so the A term in Equation (3.1) is in fact equivalent to the πR^2 term in Equation (3.18). The other difference is that C_R in Equation (3.1) is replaced by the $(1 + 4/9 \delta)$ term in Equation (3.18), which results from different parameters being used to express the reflectivity of the sphere.

3.7 Macro-model Force Acting on a Cylinder

To obtain the force acting on a right circular cylinder of radius R and height h from the macro-model approach, we assume that all parts of the cylinder have invariant optical properties.

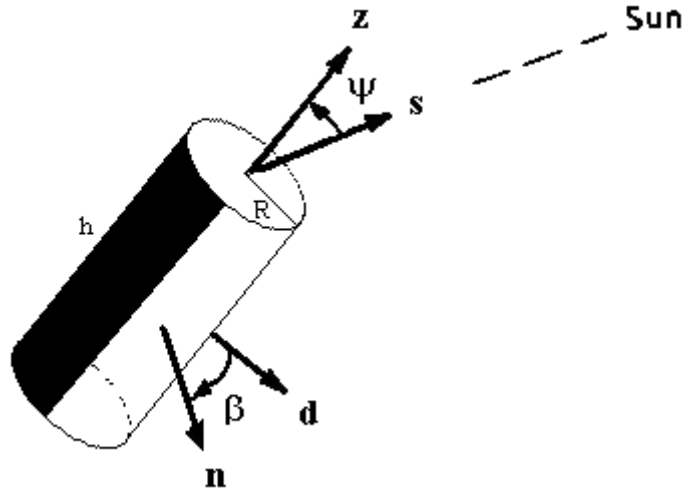


Figure 3-9 – Right Circular Cylinder Illuminated by the Sun

We wish to express the force in components acting along the spacecraft-to-sun vector, \hat{s} , and along the cylinder's main axis, \hat{z} . To obtain the force, we integrate over the illuminated area of the cylinder, which includes the illuminated circular end piece and the illuminated curved portion. The geometry of the problem is shown in Figure 3-9.

We begin by integrating Eq (3.10) over the illuminated circular end piece, which obtains the expression for force acting on a circular flat plate:

$$\mathbf{F}_{\text{illuminate d end}} = -\frac{\Phi \pi R^2 \cos \psi}{c} \left[(1 - \rho) \hat{s} + 2 \left(\frac{\delta}{3} + \rho \cos \psi \right) \hat{z} \right] \quad (3.19)$$

The integration of Eq (3.10) over the illuminated curved portion of the cylinder is more complex. The sun-to-spacecraft vector is offset from each surface area element dA

of the curved portion by the angle $(\pi/2 - \psi)$ about the pitch axis of the cylinder, plus the angle β about the longitudinal (roll) axis of the cylinder. The $\hat{\mathbf{s}}$ component of the force acting on the curved portion is given by then integrating the $\hat{\mathbf{s}}$ component of Eq (3.10):

$$\mathbf{F}_{\text{curved } \hat{\mathbf{s}}} = -\frac{\Phi \cos\left(\frac{\pi}{2} - \psi\right)}{c} (1 - \rho) 2 \int_0^{\frac{\pi}{2}} \int_0^h \cos \beta R dz d\beta \hat{\mathbf{s}} \quad (3.20)$$

Performing the integration, and applying the co-function trigonometric identity $\cos(\pi/2 - \psi) = \sin(\psi)$, yields:

$$\mathbf{F}_{\text{curved } \hat{\mathbf{s}}} = -\frac{\Phi \sin \psi}{c} (1 - \rho) 2Rh \hat{\mathbf{s}} \quad (3.21)$$

The $\hat{\mathbf{n}}$ component of the force acting on the curved portion has components acting in both the $\hat{\mathbf{s}}$ direction as well as the $\hat{\mathbf{z}}$ direction. In order to break the force down into these components, it is convenient to first express the force acting in the $\hat{\mathbf{d}}$ direction, as shown in Figure 3-9.

By symmetry of the illuminated curved portion of the cylinder, the component of the force normal to the $\hat{\mathbf{d}}$ direction integrates to zero over the illuminated region. Thus, integrating the $\hat{\mathbf{n}}$ component of Eq (3.10) results in a force only in the $-\hat{\mathbf{d}}$ direction:

$$\mathbf{F}_{\text{curved } \hat{\mathbf{n}}} = -\frac{\Phi \cos\left(\frac{\pi}{2} - \psi\right)}{c} \left[\begin{aligned} &\frac{2}{3} \delta 2 \int_0^{\frac{\pi}{2}} \int_0^h \cos^2 \beta R dz d\beta \\ &+ 2\rho \cos\left(\frac{\pi}{2} - \psi\right) 2 \int_0^{\frac{\pi}{2}} \int_0^h \cos^3 \beta R dz d\beta \end{aligned} \right] \hat{\mathbf{d}} \quad (3.22)$$

$$\mathbf{F}_{\text{curved } \hat{\mathbf{n}}} = -\frac{\Phi \sin \psi}{c} \left[\begin{aligned} &\frac{2}{3} \delta 2 \int_0^{\frac{\pi}{2}} \cos^2 \beta R h d\beta \\ &+ 2\rho \sin \psi 2 \int_0^{\frac{\pi}{2}} \cos^3 \beta R h d\beta \end{aligned} \right] \hat{\mathbf{d}} \quad (3.23)$$

$$\mathbf{F}_{\text{curved } \hat{\mathbf{n}}} = -\frac{\Phi \sin \psi}{c} \left[\frac{2}{3} \delta 2Rh \frac{\pi}{4} + 2\rho \sin \psi 2Rh \left(1 - \frac{1}{3}\right) \right] \hat{\mathbf{d}} \quad (3.24)$$

$$\mathbf{F}_{\text{curved } \hat{\mathbf{n}}} = -\frac{\Phi \sin \psi}{c} 2Rh \left[\frac{\pi}{6} \delta + \frac{4}{3} \rho \sin \psi \right] \hat{\mathbf{d}} \quad (3.25)$$

The $\hat{\mathbf{n}}$ component of the force acting on the illuminated curved portion can be expressed in terms of components in the $\hat{\mathbf{s}}$ and $\hat{\mathbf{z}}$ directions by using the following relationships, which are obtained from Figure 3-9:

$$\sin \psi = \frac{\mathbf{F}_D}{\mathbf{F}_S} \quad \text{and} \quad \tan \psi = \frac{\mathbf{F}_D}{\mathbf{F}_Z}$$

The $\hat{\mathbf{n}}$ component of the force on the illuminated curved portion can then be expressed as follows:

$$\mathbf{F}_{\text{curved } \hat{\mathbf{n}}} = -\frac{\Phi}{c} 2Rh \left[\left(\frac{\pi}{6} \delta + \frac{4}{3} \rho \sin \psi \right) \hat{\mathbf{s}} - \left(\frac{\pi}{6} \delta + \frac{4}{3} \rho \sin \psi \right) \cos \psi \hat{\mathbf{z}} \right] \quad (3.26)$$

Summing Eqs (3.21) and (3.26) gives the total force acting on the illuminated curved portion of the cylinder:

$$\mathbf{F}_{\text{curved portion}} = -\frac{\Phi}{c} 2Rh \left\{ \begin{array}{l} \left[(1 - \rho) \sin \psi + \frac{\pi}{6} \delta + \frac{4}{3} \rho \sin \psi \right] \hat{\mathbf{s}} \\ - \left(\frac{\pi}{6} \delta + \frac{4}{3} \rho \sin \psi \right) \cos \psi \hat{\mathbf{z}} \end{array} \right\} \quad (3.27)$$

$$\mathbf{F}_{\text{curved portion}} = -\frac{\Phi}{c} 2Rh \left\{ \left[\left(1 + \frac{1}{3} \rho \right) \sin \psi + \frac{\pi}{6} \delta \right] \hat{\mathbf{s}} - \left(\frac{4}{3} \rho \sin \psi + \frac{\pi}{6} \delta \right) \cos \psi \hat{\mathbf{z}} \right\} \quad (3.28)$$

The final step in developing the expression for the total force due to solar radiation pressure acting on a right circular cylinder is to sum the force acting on the illuminated end (Eq (3.19)) with the force acting on the illuminated curved portion (Eq (3.28)).

Simplifying the resulting equation gives the total force due to solar radiation pressure acting on a right circular cylinder of radius R , height h , and symmetry axis $\hat{\mathbf{z}}$ [Ref 11, pp 573]:

$$\mathbf{F} = -\frac{\Phi}{c} \left(\left\{ \left[\left(1 + \frac{1}{3} \rho \right) \sin \psi + \frac{\pi}{6} \delta \right] 2Rh + (1 - \rho) \cos \psi \pi R^2 \right\} \hat{\mathbf{s}} + \left[\left(-\frac{4}{3} \rho \sin \psi - \frac{\pi}{6} \delta \right) \cos \psi 2Rh + 2 \left(\rho \cos \psi + \frac{1}{3} \delta \right) \cos \psi \pi R^2 \right] \hat{\mathbf{z}} \right) \quad (3.29)$$

where:

- \mathbf{F} = force due to solar radiation pressure on the cylinder, N
- Φ = solar flux, W/m²
- c = speed of light, m/s
- R = radius of the cylinder, m
- h = height of the cylinder, m
- ψ = sun angle from symmetry axis
- ρ = specular reflectivity coefficient
- δ = diffuse reflectivity coefficient
- $\hat{\mathbf{s}}$ = spacecraft - to - sun unit vector
- $\hat{\mathbf{z}}$ = symmetry axis of the cylinder

The force acting on a right circular cylinder is of particular interest in this study, because the GOES I-M spacecraft has a solar sail that can be represented as a cylinder in the macro-model.

3.8 Earth Albedo and Earth Infrared Radiation Pressure Model

The Earth albedo and Earth infrared radiation pressure model implemented in this study is the one defined by Knocke, et al. [Ref 62]. This model divides the portion of the Earth's surface that is visible to the satellite into discrete segments [Ref 62]. Each segment is approximated as a plane surface tangent to the center of the segment [Ref 62]. The acceleration on the spacecraft due to shortwave (Earth albedo) and longwave (Earth IR) radiation from each segment on the Earth grid is calculated using Lambert's law of

diffusion [Ref 62]. The vector acceleration from all segments is summed to obtain the total Earth radiation effect on the spacecraft [Ref 62].

The model assumes that the Earth segments act as diffusers of the shortwave radiation, and diffuse emitters of the longwave radiation. The assumption of diffusion of the shortwave radiance is intuitively justified by the fact that the only sources of true specular reflection would be calm bodies of water such as lakes [Ref 62]. Furthermore, Knocke cites Wyatt, who states that the specularly reflected shortwave flux would equal only 10% of the diffused shortwave flux if the Earth-atmosphere system were modeled as a combination of specular and diffuse components [Refs 62, 63]. The assumption of diffuse emission of the longwave radiation is justified because the Earth behaves essentially as a black body, resulting in nearly isotropic thermal re-radiation [Ref 62].

The flux out of an Earth surface segment with area dA , intercepted by spacecraft surface area element dA_s is [Ref 62]:

$$d\Phi = L \frac{dA_s}{r^2} dA \cos \alpha \quad (3.30)$$

where L is the radiance of the segment, dA is the area of the segment, r is the distance from the segment to the spacecraft, and α is the angle between the segment normal and the vector from the segment to the satellite.

This can be rewritten as the sum of shortwave and longwave flux [Ref 62]:

$$d\Phi = d\Phi_{SW} + d\Phi_{LW} = (L_{SW} + L_{LW}) \frac{dA_s}{r^2} dA \cos \alpha \quad (3.31)$$

We now seek to find expressions for the shortwave and longwave radiance in Eq (3.31). The albedo of a segment is defined as [Ref 62]:

$$a = \frac{\Phi_{OUT}}{\Phi_{IN}} \quad (3.32)$$

where Φ_{OUT} is the total shortwave flux out of dA intercepted by a hemisphere above dA , as shown in Figure 3-6, and Φ_{IN} is the total solar flux incident on dA .

The total shortwave flux out of dA is obtained by integrating over the hemisphere, and can be expressed [Ref 62]:

$$\Phi_{OUT} = \pi L_{SW} dA \quad (3.33)$$

The total solar flux incident on dA can be expressed [Ref 62]:

$$\Phi_{IN} = E_S \cos \theta_S dA \quad (3.34)$$

where θ_S is the angle between the sun incidence vector and the surface normal of dA and E_S is the local solar irradiance as defined by [Ref 62]:

$$E_S = \frac{\Phi_{SR}}{4\pi r_{Earth}^2} \quad (3.35)$$

where Φ_{SR} is the solar flux defined in Eq (1.2).

Substituting Eqs (3.33) and (3.34) into Eq (3.32) gives [Ref 62]:

$$a = \frac{\pi L_{SW}}{E_S \cos \theta_S} \quad (3.36a)$$

which can be rearranged to obtain an expression for the shortwave radiance of a segment in terms of the albedo [Ref 62]:

$$L_{SW} = \frac{a E_S \cos \theta_S}{\pi} \quad (3.36b)$$

The emissivity of a segment is defined as [Ref 62]:

$$e = \frac{M_{LW}}{M_B} \quad (3.37)$$

where M_{LW} is the longwave exitance of dA , and M_B is the exitance of dA under the assumption that the Earth is a perfect black body [Ref 62].

Exitance is defined as the flux over area, and so [Ref 62]:

$$M_B = \frac{\text{Earth – intercepted solar flux}}{\text{surface area of the Earth}} = \frac{E_S \pi R_E^2}{4 \pi R_E^2} = \frac{E_S}{4} \quad (3.38)$$

and:

$$M_{LW} = \frac{\text{Longwave flux out of } dA}{\text{surface area of source spot}} = \frac{\Phi_{OUT}}{dA} = \frac{\pi L_{LW} dA}{dA} = \pi L_{LW} \quad (3.39)$$

Substituting Eqs (3.37) and (3.38) into Eq (3.36) gives [Ref 62]:

$$e = \frac{4 \pi L_{LW}}{E_S} \quad (3.40a)$$

which can be rearranged to obtain an expression for the longwave radiance of a segment in terms of the emissivity [Ref 62]:

$$L_{LW} = \frac{e E_S}{4 \pi} \quad (3.40b)$$

Substituting Eqs (3.36) and (3.40) into Eq (3.31) gives the flux out of an Earth surface segment with area dA , intercepted by spacecraft surface area element dA_s , in terms of the albedo and emissivity of the segment [Ref 62]:

$$d\Phi = \left(a E_S \cos \theta_s + \frac{e E_S}{4} \right) \frac{dA_s}{\pi r^2} dA \cos \alpha \quad (3.41)$$

As stated earlier, the grid of Earth segments is set up such that each segment has the same attenuated, projected area as viewed from the satellite. This definition saves several math steps in the calculation of the flux from each segment. The attenuated projected area of the segment, A' , is defined as follows [Ref 62]:

$$A' = \frac{dA \cos \alpha}{\pi r^2} \quad (3.42)$$

In developing the expression for the force acting on the macro-model due to Earth radiation pressure, a rigorous evaluation would integrate Eq (3.41) over the entire surface area of the Earth visible to the spacecraft. However, as mentioned earlier, we make the approximation that the force can be expressed as a summation over 19 individual segments on an Earth grid. Using Eqs (3.41) and (3.42), we can write an expression for the flux out of Earth grid segment i that intercepts spacecraft surface area element dA_s :

$$d\Phi_i = \left(aE_s \cos \theta_s + \frac{eE_s}{4} \right) A' dA_s \quad (3.43)$$

The force acting on a differential spacecraft surface area element is then:

$$d\mathbf{F} = - \sum_i^{19} \frac{d\Phi_i \cos \theta_i}{c} \left[(1 - \rho) \hat{\mathbf{s}}_i + 2 \left(\frac{\delta}{3} + \rho \cos \theta_i \right) \hat{\mathbf{n}} \right] \quad (3.44)$$

Equation (3.44) is then integrated over the surface area, A , of a flat plate to give the force acting on a flat plate due to Earth radiation pressure [Ref 36, 62]:

$$\mathbf{F} = - \sum_i^{19} \frac{\Phi_i A \cos \theta_i}{c} \left[(1 - \rho) \hat{\mathbf{s}}_i + 2 \left(\frac{\delta}{3} + \rho \cos \theta_i \right) \hat{\mathbf{n}} \right] \quad (3.45)$$

where:

\mathbf{F} = force due to Earth albedo/infrared pressure on the flat plate, N

Φ_i = Earth grid source radiation flux, $\text{W/m}^2 = \left(aE_s \cos \theta_s + \frac{eE_s}{4} \right) A'$

θ_i = angle between surface normal and spacecraft - to - Earth grid source vector

$\hat{\mathbf{s}}_i$ = spacecraft - to - Earth grid source unit vector

The Earth radiation effect model uses a purely latitude-dependent model for the albedo and emissivity values of the Earth segments, which are required to calculate the Φ_i in Eq (3.45). A spherical harmonic representation similar to that used for modeling the

geopotential could be used for the albedo and emissivity models, and would provide the most general analytical representation of the Earth radiation. However, satellite data indicate that the albedo and emissivity of the Earth show strong variations in latitude and weaker variations in longitude [Refs 62, 64]. Additionally, the Earth's rotation likely averages out any long-period effects caused by longitudinal variations in Earth radiation [Ref 62]. As a result, a purely zonal representation of the distribution of the Earth radiation is used.

The albedo and emissivity values are modeled using zeroeth, first, and second degree zonal harmonics as follows [Ref 62]:

$$a = a_0 + a_1 P_1(\sin \phi) + a_2 P_2(\sin \phi) \quad (3.46a)$$

$$e = e_0 + e_1 P_1(\sin \phi) + e_2 P_2(\sin \phi) \quad (3.46b)$$

where [Ref 62]:

$$a_1 = c_0 + c_1 \cos[\omega(JD - t_0)] + c_2 \sin[\omega(JD - t_0)] \quad (3.46c)$$

$$e_1 = k_0 + k_1 \cos[\omega(JD - t_0)] + k_2 \sin[\omega(JD - t_0)] \quad (3.46d)$$

t_0 = Epoch of the periodic terms

$$\omega = 2\pi/365.25 \text{ days}^{-1}$$

As can be seen, the time-dependent terms in the model are limited to seasonal effects [Ref 62]. The values used for the various coefficients in the Earth radiation pressure model for this study are the same ones used by Knocke and implemented in the GEODYN albedo model [Ref 62]:

$$\begin{aligned} a_0 &= 0.34 & a_1 &: (c_0 = 0.0, c_1 = 0.10, c_2 = 0.0) & a_2 &= 0.29 \\ e_0 &= 0.68 & e_1 &: (k_0 = 0.0, k_1 = -0.07, k_2 = 0.0) & e_2 &= -0.18 \\ t_0 &= 22 \text{ December 1981} \end{aligned}$$

3.9 “Default” Reflectivity Value Analysis

In order to facilitate test cases that compare the macro-model to the spherical model, “default” values of the reflectivity coefficients are determined in this chapter. “Default” values refer to those reflectivity values that cause a macro-model consisting of a single flat plate to replicate the spherical satellite model for solar radiation pressure.

The equation for force due to solar radiation pressure acting on a flat plate is given in Eq (3.11). In cases when the single flat plate model is configured to replicate the spherical model, the surface normal of the plate is pointed directly at the sun. Thus, $\theta = 0$ and $\mathbf{s} = \mathbf{n}$, and the equation for force on the flat plate reduces to:

$$\mathbf{F} = -\frac{\Phi A}{c} \left[(1 - \rho) \hat{\mathbf{s}} + 2 \left(\frac{\delta}{3} + \rho \right) \hat{\mathbf{s}} \right] \quad (3.31)$$

or:

$$\mathbf{F} = -\frac{\Phi A}{c} \left(1 + \rho + \frac{2}{3} \delta \right) \hat{\mathbf{s}} \quad (3.32)$$

The equation for force due to solar radiation pressure acting on a uniformly-reflecting sphere is given in Eq (3.1).

Combining Eqs (3.1) and (3.32), it can be seen that, for the nominal or “default” case in which the single flat plate macro-model replicates the spherical model:

$$C_R = 1 + \rho + \frac{2}{3} \delta \quad (3.33)$$

In GTDS, $C_R = 1.2$ is programmed as the default value for the spherical model. Thus,

$$1.2 = 1 + \rho + \frac{2}{3} \delta \quad (3.34)$$

which reduces to:

$$0.2 = \rho + \frac{2}{3}\delta \quad (3.35)$$

Any combination of ρ and δ that satisfy the above equation, as well the physical limits of Eq (3.2), will replicate the spherical model with a $C_R = 1.2$. In Fundamentals of Astrodynamics and Applications (First Edition), Dave Vallado states, “We’ll consider only specular reflection because analyzing diffuse reflection requires us to have complex three-dimensional models of the satellite.” [Ref 10, pp 519]. He then goes on to develop the equation for the SRP acceleration on the spherical satellite model. This indicates that one set of “default” reflectivity values can be found by setting the diffuse reflectivity value to zero. This would mean that:

$$\delta = 0.0 \text{ and } \rho = 0.2$$

This corresponds to:

$$\sigma_a = 0.8 \text{ and } \sigma = 0.0$$

for the alternative representation (DSST standalone one-panel model) to give:

$$\delta = \sigma_{rd} = \sigma(1 - \sigma_a) = 0(1 - 0.8) = 0.0$$

and:

$$\rho = \sigma_{rs} = (1 - \sigma)(1 - \sigma_a) = (1 - 0)(1 - 0.8) = 0.2$$

These “default” reflectivity coefficient values will replicate the spherical satellite model using the DSST one-panel model or the macro-model set up as a single-panel test case. Test cases with these values are described in Chapter 7.5.

[This page intentionally left blank.]

Chapter 4 Solar Radiation Pressure Variational Equations

4.1 Introduction to Statistical Orbit Determination

Prior to developing the required partial derivatives related to the improved solar radiation pressure models, it is important to understand why we need the partial derivatives. As such, the first section of Chapter 4 will introduce statistical orbit determination methods, including linear least squares and nonlinear least squares differential correction, as a motivation for developing the variational equations. The subsequent sections of Chapter 4 will then develop the variational equations for both the Cowell theory and Semi-analytical Satellite Theory (DSST), and will also develop the required partial derivatives for the new solar radiation pressure models.

When attempting to determine the orbit of a satellite based on observations, we begin with a mathematical model of the satellite's motion that allows us to propagate the state of the satellite to the time of each observation. We typically have more observations than unknowns in this model. This results in an overdetermined system, where our model of the orbit cannot be made to satisfy exactly all of the constraints imposed by the observations. We instead seek to adjust the parameters in the model to satisfy the constraints as nearly as possible. The adjustable parameters in the model of the orbit are collectively referred to as the solve-for vector, and typically include the state of the satellite at the epoch time as well as perturbation model parameters, including solar radiation pressure model parameters.

4.1.1 Gauss' Method of Least Squares

The Method of Least Squares was developed by Carl Friedrich Gauss in 1795 [Ref 42, pp 646]. The method is used to approximate the solution to a set of linear algebraic equations that have more equations than unknowns [Ref 42, pp 646]. The set of overdetermined linear algebraic equations are of the form [Ref 42, pp 646]:

$$\sum_{j=1}^n m_{ij} x_j = c_i \quad i = 1, \dots, N > n \quad (4.1a)$$

In vector-matrix form, the previous equation is [Ref 42, pp 647]:

$$\mathbf{M}\mathbf{x} = \mathbf{c} \quad (4.1b)$$

The objective is to determine the x_j so that Eqs (4.1) are “as nearly satisfied as possible” [Ref 42, pp 646]. To do this, we define the residual, e , as the difference between the computed and observed values at a given point [Ref 42, pp 646]:

$$e_i = \sum_{j=1}^n m_{ij} x_j - c_i \quad (4.2a)$$

In vector-matrix form, the previous equation is [Ref 42, pp 647]:

$$\mathbf{e} = \mathbf{M}\mathbf{x} - \mathbf{c} \quad (4.2b)$$

We also choose a set of weighing factors, w , which depend on the accuracy of each observation. The cost function, J , is then the weighted sum of the squares of the residuals [Ref 42, pp 647]:

$$J = w_1 e_1^2 + w_2 e_2^2 + \dots + w_N e_N^2 \quad (4.3a)$$

Defining the weighting matrix, \mathbf{W} , as follows [Ref 42, pp 647]:

$$\mathbf{W} = \begin{bmatrix} w_1 & 0 & \dots & 0 \\ 0 & w_2 & \dots & 0 \\ \vdots & \vdots & \ddots & \vdots \\ 0 & 0 & \dots & w_N \end{bmatrix}$$

we can write the cost function in vector-matrix form [Ref 42, pp 647]:

$$\begin{aligned}
 J &= \mathbf{e}^T \mathbf{W} \mathbf{e} \\
 &= (\mathbf{x}^T \mathbf{M}^T - \mathbf{c}^T) \mathbf{W} (\mathbf{M} \mathbf{x} - \mathbf{c}) \\
 &= \mathbf{x}^T \mathbf{M}^T \mathbf{W} \mathbf{M} \mathbf{x} - \mathbf{c}^T \mathbf{W} \mathbf{M} \mathbf{x} - \mathbf{x}^T \mathbf{M}^T \mathbf{W} \mathbf{c} + \mathbf{c}^T \mathbf{W} \mathbf{c}
 \end{aligned} \tag{4.3b}$$

To minimize the cost function, we set the partial derivative of J with respect to \mathbf{x} equal to zero [Ref 42, pp 647]:

$$\frac{\partial J}{\partial \mathbf{x}} = 2 \mathbf{x}^T \mathbf{M}^T \mathbf{W} \mathbf{M} - 2 \mathbf{c}^T \mathbf{W} \mathbf{M} = \mathbf{0}^T \tag{4.4}$$

which yields [Ref 42, pp 647]:

$$\mathbf{M}^T \mathbf{W} \mathbf{M} \mathbf{x} = \mathbf{M}^T \mathbf{W} \mathbf{c} \tag{4.5}$$

Solving for \mathbf{x} yields the best estimate of the state [Ref 42, pp 647]:

$$\hat{\mathbf{x}} = (\mathbf{M}^T \mathbf{W} \mathbf{M})^{-1} \mathbf{M}^T \mathbf{W} \mathbf{c} \tag{4.6}$$

The covariance matrix, \mathbf{P} , contains estimates for the closeness of the solution state to the actual observations, expressed as variances and covariances [Ref 10, pp 673]:

$$\mathbf{P} = (\mathbf{M}^T \mathbf{W} \mathbf{M})^{-1} = E \left\{ [\hat{\mathbf{x}} - \mathbf{x}][\hat{\mathbf{x}} - \mathbf{x}]^T \right\} \tag{4.7}$$

where $\hat{\mathbf{x}}$ is the best estimate of the state, \mathbf{x} is the actual state, and the operator $E\{ \}$ denotes the expected value of the quantity in the brackets.

4.1.2 Nonlinear Least Squares

Gauss' Method of Least Squares is suited to linear systems; however, real-world orbit determination problems are nonlinear. To address this issue, the problem is linearized and the resulting solution is iterated to obtain the best estimate for the state. The form of the nonlinear equations is assumed to be [Ref 48]:

$$\mathbf{y} = \mathbf{f}(\mathbf{x}) + \mathbf{n} \tag{4.8}$$

where \mathbf{y} is the m -dimensioned vector of observations, \mathbf{f} is the nonlinear vector function of a set of solve-for parameters (the p -dimensioned \mathbf{x} vector), and \mathbf{n} is random modeling or system noise [Ref 48]. The objective is to estimate \mathbf{x} given \mathbf{y} , the functional form of \mathbf{f} , and the statistical properties of \mathbf{n} [Ref 48].

The cost function, J , in the nonlinear case is as follows [Ref 48]:

$$J = [\mathbf{y} - \mathbf{f}(\mathbf{x})]^T \mathbf{W}[\mathbf{y} - \mathbf{f}(\mathbf{x})] \quad (4.9)$$

To minimize the cost function, we take the partial derivative of J with respect to \mathbf{x} and set it equal to zero:

$$\frac{\partial J}{\partial \mathbf{x}} = -2[\mathbf{y} - \mathbf{f}(\mathbf{x})]^T \mathbf{W} \left(\frac{\partial \mathbf{f}}{\partial \mathbf{x}} \right) = \mathbf{0}^T \quad (4.10)$$

To solve this nonlinear minimization, we linearize Eq (4.10) by expanding $\mathbf{f}(\mathbf{x})$ in a Taylor series about the a priori state estimate \mathbf{x}_0 and truncating higher-order terms [Ref 48]:

$$\mathbf{f}(\mathbf{x}) = \mathbf{f}(\mathbf{x}_0) + \mathbf{F} \delta \mathbf{x} \quad (4.11)$$

where [Ref 48]:

$$\delta \mathbf{x} = \mathbf{x} - \mathbf{x}_0 \quad (4.12)$$

and \mathbf{F} is the $(m \times p)$ -dimensioned matrix of partial derivatives of $\mathbf{f}(\mathbf{x})$ with respect to \mathbf{x} , evaluated at $\mathbf{x} = \mathbf{x}_0$ [Ref 48]:

$$\mathbf{F} = \left(\frac{\partial \mathbf{f}}{\partial \mathbf{x}} \right)_{\mathbf{x}=\mathbf{x}_0} \quad (4.13)$$

Substituting Eq (4.11) into Eq (4.8) gives the linearized observation vector:

$$\delta \mathbf{y} = \mathbf{F} \delta \mathbf{x} + \mathbf{n} \quad (4.14)$$

where $\delta \mathbf{y}$ is the vector of observation residuals [Ref 48]:

$$\delta\mathbf{y} = \mathbf{y} - \mathbf{f}(\mathbf{x}_0) \quad (4.15)$$

Substituting Eqs (4.11) and (4.14) into Eq (4.10) yields the linearized partial derivative of the cost function [Ref 48]:

$$\frac{\partial J}{\partial \mathbf{x}} = -2[\delta\mathbf{y} - \mathbf{F}\delta\mathbf{x}]^T \mathbf{W}\mathbf{F} = \mathbf{0}^T \quad (4.16)$$

Solving Eq (4.16) for $\delta\mathbf{x}$ yields the solution for the best estimate of the correction to the state vector [Ref 48]:

$$\delta\hat{\mathbf{x}} = (\mathbf{F}^T \mathbf{W}\mathbf{F})^{-1} \mathbf{F}^T \mathbf{W}\delta\mathbf{y} \quad (4.17)$$

Due to the linearization in this development, $\delta\mathbf{x}$ must be small, which means that the a priori estimate \mathbf{x}_0 must be close to the true solution of the problem [Ref 48]. The process of iteratively improving the estimate of \mathbf{x} is known as Differential Correction. The process continues until the correction to the state vector ($\delta\mathbf{x}$) approaches zero within a given tolerance, or the root mean square error of the observation residuals stops changing within a certain tolerance.

4.1.3 Calculating the Partial Derivative Matrix

The partial derivative matrix, \mathbf{F} , was defined in the previous section. By using the subscript “0” to denote the epoch time, the notation can be simplified as [Ref 10, pp 686]:

$$\mathbf{F} = \left(\frac{\partial \mathbf{f}}{\partial \mathbf{x}} \right)_{\mathbf{x}=\mathbf{x}_0} = \left[\frac{\partial \text{observations}}{\partial \mathbf{x}_0} \right]_{m \times p} \quad (4.18)$$

This partial derivative can be rewritten using the chain rule for differentiation [Ref 10, pp 686]:

$$\mathbf{F} = \left[\frac{\partial \text{observations}}{\partial \mathbf{x}_0} \right] = \left\{ \left[\begin{array}{c|c} \frac{\partial \text{observations}}{\partial \mathbf{r}} & \frac{\partial \text{observations}}{\partial \dot{\mathbf{r}}} \end{array} \right]_{m \times 6} \left[\begin{array}{c} \frac{\partial \mathbf{r}}{\partial \mathbf{x}_0} \\ \frac{\partial \dot{\mathbf{r}}}{\partial \mathbf{x}_0} \end{array} \right]_{6 \times p} \right\} = \mathbf{H}\Phi \quad (4.19)$$

where the matrix \mathbf{H} is the matrix of observation partial derivatives with respect to the state, called the *observation partials matrix* or *sensitivity matrix*. The matrix Φ is called the *state transition matrix*, or the matrix of *variational equations*.

4.2 Cowell Theory and Associated Variational Equations

For the Cowell theory, the matrix of variational equations includes the partial derivatives of the position and velocity at the observation time (\mathbf{r} and $\dot{\mathbf{r}}$, respectively), with respect to the vector of solve-for parameters, \mathbf{p} , which includes the epoch state as well as perturbation model parameters. Mathematically, the matrix of variational equations from Eq (4.19) can be expressed as follows:

$$\left[\begin{array}{c} \frac{\partial \mathbf{r}}{\partial \mathbf{x}_0} \\ \frac{\partial \dot{\mathbf{r}}}{\partial \mathbf{x}_0} \end{array} \right]_{6 \times p} = \left[\begin{array}{c} \frac{\partial \mathbf{r}}{\partial \mathbf{p}} \\ \frac{\partial \dot{\mathbf{r}}}{\partial \mathbf{p}} \end{array} \right]_{6 \times p} \quad (4.20)$$

The \mathbf{p} vector includes the epoch position and velocity (or epoch mean elements) as well as perturbation model parameters, including the solar radiation pressure model parameters. For either differential correction or Kalman filtering applications, we require the partial derivatives of the spacecraft motion with respect to both the spacecraft position and velocity and the model parameters. For the spherical solar radiation pressure model, the adjustable model parameter is C_R . For the macro-model, the adjustable model parameters are the specular and diffuse reflectivity coefficients for each plate, area of each plate, as well as an overall C_R that scales the entire model and whose nominal value

is 1.0. For the one-panel model using alternate parameterization, the adjustable model parameters are the panel reflectivity coefficients.

In the numerical Cowell orbit generator, the equations of motion may be expressed in the form [Ref 48]:

$$\ddot{\mathbf{r}} = \mathbf{f}(\mathbf{r}, \dot{\mathbf{r}}, t, \mathbf{p}) \quad (4.21)$$

where:

- $\ddot{\mathbf{r}}$ = the spacecraft acceleration vector
- \mathbf{r} = the spacecraft position vector
- $\dot{\mathbf{r}}$ = the spacecraft velocity vector
- t = time
- \mathbf{p} = the vector of solve- for parameters

and the vector function \mathbf{f} includes two-body and perturbation terms; \mathbf{f} is assumed to be continuous and to possess continuous first order partial derivatives with respect to the states and the parameters [Ref 48].

To obtain the parameter variational equations, Eq (4.21) is differentiated with respect to the \mathbf{p} vector [Ref 48]:

$$\frac{\partial \ddot{\mathbf{r}}}{\partial \mathbf{p}} = \frac{\partial \ddot{\mathbf{r}}}{\partial \mathbf{r}} \frac{\partial \mathbf{r}}{\partial \mathbf{p}} + \frac{\partial \ddot{\mathbf{r}}}{\partial \dot{\mathbf{r}}} \frac{\partial \dot{\mathbf{r}}}{\partial \mathbf{p}} + \left(\frac{\partial \ddot{\mathbf{r}}}{\partial \mathbf{p}} \right)_{\text{explicit}} \quad (4.22)$$

If we assume that the \mathbf{r} vector has sufficient continuous partial derivatives, we can interchange the order of the time derivatives and partials with respect to the \mathbf{p} vector as follows [Ref 48]:

$$\frac{d^2}{dt^2} \left(\frac{\partial \mathbf{r}}{\partial \mathbf{p}} \right) = \frac{\partial \ddot{\mathbf{r}}}{\partial \mathbf{r}} \frac{\partial \mathbf{r}}{\partial \mathbf{p}} + \frac{\partial \ddot{\mathbf{r}}}{\partial \dot{\mathbf{r}}} \frac{d}{dt} \left(\frac{\partial \mathbf{r}}{\partial \mathbf{p}} \right) + \left(\frac{\partial \ddot{\mathbf{r}}}{\partial \mathbf{p}} \right)_{\text{explicit}} \quad (4.23)$$

These variational equations can be expressed as a system of linear differential equations [Ref 48]:

$$\ddot{\mathbf{Y}} = \mathbf{A}(t)\mathbf{Y} + \mathbf{B}(t)\dot{\mathbf{Y}} + \mathbf{C}(t) \quad (4.24)$$

where:

$$\mathbf{Y}(t) = \left[\frac{\partial \mathbf{r}(t)}{\partial \mathbf{p}} \right], \mathbf{A}(t) = \left[\frac{\partial \ddot{\mathbf{r}}(t)}{\partial \mathbf{r}} \right], \mathbf{B}(t) = \left[\frac{\partial \ddot{\mathbf{r}}(t)}{\partial \dot{\mathbf{r}}} \right], \mathbf{C}(t) = \left[\frac{\partial \ddot{\mathbf{r}}(t)}{\partial \mathbf{p}_{\text{explicit}}} \right]$$

There is a contribution from solar radiation pressure in the \mathbf{A} matrix, which contains the partial derivatives of the acceleration with respect to the spacecraft position. However, it is common practice to use a low degree and order geopotential or even a J_2 approximation for the \mathbf{A} matrix. There is no contribution from solar radiation pressure to the \mathbf{B} matrix, since the solar pressure acceleration is not a function of the spacecraft velocity. The columns of the \mathbf{C} matrix represent the partial derivatives of the acceleration with respect to the model parameters, including the solar radiation pressure model parameters.

For the spherical solar radiation pressure model, the \mathbf{C} matrix column requires the partial derivative of the acceleration with respect to C_R :

$$\frac{\partial \ddot{\mathbf{r}}_{SR}}{\partial C_R} = -\frac{\Phi A}{cm} \hat{\mathbf{s}} \quad (4.25)$$

where the definitions for the right-hand side of Eq (4.25) are the same as for Eq (3.1) with the addition that m is the spacecraft mass.

The variational equations in Eq (4.24) are solved to obtain \mathbf{Y} and $\dot{\mathbf{Y}}$, which contain the required partial derivatives for differential correction or Kalman filtering applications [Ref 48].

4.3 Semi-analytical Satellite Theory and Averaged Partial Generator

For the Semi-analytical Satellite Theory (DSST), because the equations of motion are expressed in terms of mean element rates, the matrix of variational equations from Eq (4.19) is further broken down using the chain rule:

$$\begin{bmatrix} \frac{\partial \mathbf{r}}{\partial \mathbf{x}_0} \\ \frac{\partial \dot{\mathbf{r}}}{\partial \mathbf{x}_0} \end{bmatrix}_{6 \times p} = \left\{ \begin{bmatrix} \frac{\partial \mathbf{r}}{\partial \mathbf{a}} \\ \frac{\partial \dot{\mathbf{r}}}{\partial \mathbf{a}} \end{bmatrix}_{6 \times 6} \begin{bmatrix} \frac{\partial \mathbf{a}}{\partial \mathbf{p}} \end{bmatrix}_{6 \times p} \right\} \quad (4.26)$$

As in the Cowell formulation, the \mathbf{p} vector includes the epoch state as well as perturbation model parameters, including the solar radiation pressure model parameters. The \mathbf{a} vector includes the osculating equinoctial elements at the observation time.

The first matrix on the right-hand side of Eq (4.26) contains the partial derivatives of the unperturbed (two-body) motion, and can be obtained directly from the two-body relationships between position and velocity and the osculating equinoctial orbital elements given in Chapter 2.2.4. The second matrix, denoted \mathbf{G} , contains the partial derivatives of the perturbed motion, and can be further broken down as follows [Ref 65]:

$$\mathbf{G} = \begin{bmatrix} \frac{\partial \mathbf{a}}{\partial \mathbf{p}} \end{bmatrix}_{6 \times p} = \begin{bmatrix} \frac{\partial \mathbf{a}}{\partial \bar{\mathbf{a}}_0} \vdots \frac{\partial \mathbf{a}}{\partial \mathbf{c}} \end{bmatrix}_{6 \times p} \quad (4.27)$$

where $\bar{\mathbf{a}}_0$ is the vector of mean elements at the epoch time and \mathbf{c} is the vector of perturbation model parameters.

Using the chain rule gives [Ref 65]:

$$\mathbf{G} = \left\{ \begin{bmatrix} \frac{\partial \mathbf{a}}{\partial \bar{\mathbf{a}}} \end{bmatrix} \begin{bmatrix} \frac{\partial \bar{\mathbf{a}}}{\partial \bar{\mathbf{a}}_0} \end{bmatrix} \begin{bmatrix} \frac{\partial \mathbf{a}}{\partial \bar{\mathbf{a}}} \end{bmatrix} \begin{bmatrix} \frac{\partial \bar{\mathbf{a}}}{\partial \mathbf{c}} \end{bmatrix} + \frac{\partial \mathbf{a}}{\partial \mathbf{c}_{\text{explicit}}} \right\}_{6 \times p} \quad (4.28)$$

This can be rewritten as follows [Ref 65]:

$$\mathbf{G} = \left\{ \begin{bmatrix} \frac{\partial \mathbf{a}}{\partial \bar{\mathbf{a}}} \end{bmatrix} \begin{bmatrix} \frac{\partial \bar{\mathbf{a}}}{\partial \bar{\mathbf{a}}_0} \vdots \frac{\partial \bar{\mathbf{a}}}{\partial \mathbf{c}} \end{bmatrix} + \begin{bmatrix} \mathbf{0} & \frac{\partial \mathbf{a}}{\partial \mathbf{c}_{\text{explicit}}} \end{bmatrix} \right\} \quad (4.29)$$

From the near-identity transformation given in Eqs (2.138) [Ref 65]:

$$\begin{bmatrix} \frac{\partial \mathbf{a}}{\partial \bar{\mathbf{a}}} \end{bmatrix} = \begin{bmatrix} \mathbf{I} + \frac{\partial \boldsymbol{\varepsilon} \boldsymbol{\eta}_1(\bar{\mathbf{a}})}{\partial \bar{\mathbf{a}}} \end{bmatrix} \quad (4.30)$$

and

$$\begin{bmatrix} \frac{\partial \mathbf{a}}{\partial \mathbf{c}} \end{bmatrix}_{\text{explicit}} = \begin{bmatrix} \frac{\partial \boldsymbol{\varepsilon} \boldsymbol{\eta}_1(\bar{\mathbf{a}})}{\partial \mathbf{c}} \end{bmatrix} \quad (4.31)$$

Substituting Eqs (4.30) and (4.31) into Eq (4.29) yields [Ref 65]:

$$\mathbf{G} = \left\{ \begin{bmatrix} \mathbf{I} + \mathbf{B}_1 \end{bmatrix}_{6 \times 6} \begin{bmatrix} \mathbf{B}_2 \vdots \mathbf{B}_3 \end{bmatrix}_{6 \times p} + \begin{bmatrix} \mathbf{0} \vdots \mathbf{B}_4 \end{bmatrix}_{6 \times p} \right\} \quad (4.32)$$

where:

$$\mathbf{B}_1 = \begin{bmatrix} \frac{\partial \boldsymbol{\varepsilon} \boldsymbol{\eta}_1(\bar{\mathbf{a}})}{\partial \bar{\mathbf{a}}} \end{bmatrix}, \mathbf{B}_2 = \begin{bmatrix} \frac{\partial \bar{\mathbf{a}}}{\partial \bar{\mathbf{a}}_0} \end{bmatrix}, \mathbf{B}_3 = \begin{bmatrix} \frac{\partial \bar{\mathbf{a}}}{\partial \mathbf{c}} \end{bmatrix}, \mathbf{B}_4 = \begin{bmatrix} \frac{\partial \boldsymbol{\varepsilon} \boldsymbol{\eta}_1(\bar{\mathbf{a}})}{\partial \mathbf{c}} \end{bmatrix}$$

The matrices \mathbf{B}_1 and \mathbf{B}_4 represent the short periodic portion of the semi-analytical partial derivatives and are called the Short Periodic Partial Generator (SPPG) [Ref 65]. The matrices \mathbf{B}_2 and \mathbf{B}_3 contain the partial derivatives of the mean elements with respect to the solve-for parameters and are called the Averaged Partial Generator (APG) [Ref 65].

In the Semi-analytical Satellite Theory (DSST), the averaged equations of motion can be expressed in the form [Ref 65]:

$$\dot{\bar{\mathbf{a}}} = \mathbf{g}(\bar{\mathbf{a}}, t, \mathbf{p}) \quad (4.33)$$

where:

$\dot{\bar{\mathbf{a}}}$ = the mean element rate vector
 $\bar{\mathbf{a}}$ = the mean element vector
 t = time
 \mathbf{p} = the vector of solve- for parameters

To obtain the Averaged Partial Generator (APG) equations, we take the partial derivative of Eq (4.33) with respect to the solve-for vector, \mathbf{p} , which includes both the epoch mean element vector (the $\bar{\mathbf{a}}_0$ vector), as well as the vector of perturbation model parameters (the \mathbf{c} vector) [Ref 65]:

$$\frac{\partial \dot{\bar{\mathbf{a}}}}{\partial \bar{\mathbf{a}}_0} = \frac{\partial \dot{\bar{\mathbf{a}}}}{\partial \bar{\mathbf{a}}} \frac{\partial \bar{\mathbf{a}}}{\partial \bar{\mathbf{a}}_0} \quad (4.34a)$$

$$\frac{\partial \dot{\bar{\mathbf{a}}}}{\partial \mathbf{c}} = \frac{\partial \dot{\bar{\mathbf{a}}}}{\partial \bar{\mathbf{a}}} \frac{\partial \bar{\mathbf{a}}}{\partial \mathbf{c}} + \left(\frac{\partial \dot{\bar{\mathbf{a}}}}{\partial \mathbf{c}} \right)_{\text{explicit}} \quad (4.34b)$$

Assuming that the mean element rates have sufficient continuous partial derivatives, we can interchange the order of the derivatives on the left-hand side of these equations as follows [Ref 65]:

$$\frac{d}{dt} \frac{\partial \bar{\mathbf{a}}}{\partial \bar{\mathbf{a}}_0} = \frac{\partial \dot{\bar{\mathbf{a}}}}{\partial \bar{\mathbf{a}}} \frac{\partial \bar{\mathbf{a}}}{\partial \bar{\mathbf{a}}_0} \quad (4.35a)$$

$$\frac{d}{dt} \frac{\partial \bar{\mathbf{a}}}{\partial \mathbf{c}} = \frac{\partial \dot{\bar{\mathbf{a}}}}{\partial \bar{\mathbf{a}}} \frac{\partial \bar{\mathbf{a}}}{\partial \mathbf{c}} + \left(\frac{\partial \dot{\bar{\mathbf{a}}}}{\partial \mathbf{c}} \right)_{\text{explicit}} \quad (4.35b)$$

At the epoch time, the quantity $\frac{\partial \bar{\mathbf{a}}(t_0)}{\partial \bar{\mathbf{a}}_0}$ is equal to the identity matrix and $\frac{\partial \bar{\mathbf{a}}(t_0)}{\partial \mathbf{c}}$ is equal to the zero matrix. Therefore, the APG equations can be expressed as

the following linear differential equations [Ref 65]:

$$\begin{aligned} \dot{\mathbf{B}}_2 &= \mathbf{A}\mathbf{B}_2 & \text{with} & & \mathbf{B}_2(t_0) &= \mathbf{I} \\ \dot{\mathbf{B}}_3 &= \mathbf{A}\mathbf{B}_3 + \mathbf{D} & & & \mathbf{B}_3(t_0) &= \mathbf{0} \end{aligned} \quad (4.36)$$

where:

$$\mathbf{B}_2 = \begin{bmatrix} \frac{\partial \bar{\mathbf{a}}}{\partial \bar{\mathbf{a}}_0} \end{bmatrix}, \mathbf{A} = \begin{bmatrix} \frac{\partial \dot{\bar{\mathbf{a}}}}{\partial \bar{\mathbf{a}}} \end{bmatrix}, \mathbf{B}_3 = \begin{bmatrix} \frac{\partial \bar{\mathbf{a}}}{\partial \mathbf{c}} \end{bmatrix}, \mathbf{D} = \begin{bmatrix} \frac{\partial \dot{\bar{\mathbf{a}}}}{\partial \mathbf{c}} \end{bmatrix}$$

A useful approximation is to base the \mathbf{A} matrix in Eqs (4.36) on the J_2 secular terms. In GTDS, this is done in subroutine J2PART.

The columns of the \mathbf{D} matrix represent the partial derivatives of the mean element rates with respect to the model parameters, including the solar radiation pressure model parameters. In GTDS, these partial derivatives are calculated in the subroutine VARDIF.

For the spherical solar radiation pressure model, the \mathbf{D} matrix column requires the partial derivative of the mean element rates with respect to C_R , obtained via the following algorithm:

$$\frac{\partial \dot{\bar{\mathbf{a}}}}{\partial C_R} = \frac{(\dot{\bar{\mathbf{a}}})_{\text{solar radiation pressure}}}{C_R} \quad (4.37)$$

The APG equations in Eq (4.36) are solved to obtain \mathbf{B}_2 and \mathbf{B}_3 , which contain the required partial derivatives for differential correction or Kalman filtering applications.

4.4 Macro-model (Box-wing) Partial Derivatives

4.4.1 Cowell Variational Equations

For the box-wing macro-model, we generalize the Cowell equations of motion as follows:

$$\ddot{\mathbf{r}} = \mathbf{f}(\mathbf{r}, \dot{\mathbf{r}}, t, \delta, \rho) \quad (4.38)$$

Differentiating Eq (4.38) with respect to δ , we get:

$$\frac{\partial}{\partial \delta} \ddot{\mathbf{r}} = \frac{\partial \ddot{\mathbf{r}}}{\partial \mathbf{r}} \frac{\partial \mathbf{r}}{\partial \delta} + \frac{\partial \ddot{\mathbf{r}}}{\partial \dot{\mathbf{r}}} \frac{\partial \dot{\mathbf{r}}}{\partial \delta} + \frac{\partial \ddot{\mathbf{r}}}{\partial \delta} \quad (4.39)$$

Using the definitions for \mathbf{A} and \mathbf{B} from Eq (4.24), we get:

$$\frac{\partial}{\partial \delta} \ddot{\mathbf{r}} = \mathbf{A} \frac{\partial \mathbf{r}}{\partial \delta} + \mathbf{B} \frac{\partial \dot{\mathbf{r}}}{\partial \delta} + \frac{\partial \ddot{\mathbf{r}}}{\partial \delta} \quad (4.40)$$

The explicit partial derivative of the acceleration on a flat plate with respect to the diffuse reflectivity coefficient is:

$$\frac{\partial \ddot{\mathbf{r}}}{\partial \delta} = -\frac{2\Phi A \cos \theta}{3cm} \hat{\mathbf{n}} \quad (4.41)$$

Differentiating Eq (4.38) with respect to ρ , we get:

$$\frac{\partial}{\partial \rho} \ddot{\mathbf{r}} = \mathbf{A} \frac{\partial \mathbf{r}}{\partial \rho} + \mathbf{B} \frac{\partial \dot{\mathbf{r}}}{\partial \rho} + \frac{\partial \ddot{\mathbf{r}}}{\partial \rho} \quad (4.42)$$

The explicit partial derivative of the acceleration on a flat plate with respect to the specular reflectivity coefficient is:

$$\frac{\partial \ddot{\mathbf{r}}}{\partial \rho} = -\frac{\Phi A \cos \theta}{cm} [(2 \cos \theta) \hat{\mathbf{n}} - \hat{\mathbf{s}}] \quad (4.43)$$

The variational equations (Eqs (4.40) and (4.42)) are solved simultaneously in the combined system of equations along with the equations of motion.

For the macro-model for solar radiation pressure acting on a flat plate, there are two columns (per plate) of the \mathbf{C} matrix, which was defined in Eq (4.24). The first is the partial derivative of the acceleration on a flat plate with respect to diffuse reflectivity (Eq (4.41)), and the second is the partial derivative of the acceleration on a flat plate with respect to specular reflectivity (Eq (4.43)).

Additionally, if we wish to solve for a single C_R that scales the entire macro-model, then we introduce C_R as a solve-for parameter, which means that there is another column in the \mathbf{C} matrix. This column contains the partial derivative of the acceleration with respect to the single C_R . Since the C_R multiplies the vector sum of the solar

radiation pressure acceleration acting on all plates in the model, this partial derivative is a trivial calculation and is as follows, for the case where the macro-model is an assembly of flat plates:

$$\frac{\partial \ddot{\mathbf{r}}}{\partial C_R} = -\frac{\Phi}{cm} \sum_{i=1}^n A_i \cos \theta_i \left[(1 - \rho_i) \hat{\mathbf{s}} + 2 \left(\frac{\delta_i}{3} + \rho_i \cos \theta_i \right) \hat{\mathbf{n}}_i \right] \quad (4.44)$$

where n is the number of *illuminated* flat plates in the model.

4.4.2 Averaged Equations of Motion Variational Equations

We generalize the averaged equations of motion as:

$$\dot{\bar{\mathbf{a}}} = \mathbf{g}(\bar{\mathbf{a}}, t, \delta, \rho) \quad (4.45)$$

Differentiating Eq (4.45) with respect to δ and ρ , and using the partial derivatives obtained in Chapter 4.3, results in:

$$\frac{d}{dt} \left(\frac{\partial \bar{\mathbf{a}}}{\partial \delta} \right) = \mathbf{A} \frac{\partial \bar{\mathbf{a}}}{\partial \delta} + \frac{\partial \mathbf{g}}{\partial \delta} \quad (4.46)$$

and

$$\frac{d}{dt} \left(\frac{\partial \bar{\mathbf{a}}}{\partial \rho} \right) = \mathbf{A} \frac{\partial \bar{\mathbf{a}}}{\partial \rho} + \frac{\partial \mathbf{g}}{\partial \rho} \quad (4.47)$$

where the \mathbf{A} matrix is defined in Eq (4.36).

In terms of software, the partial derivatives $\frac{\partial \mathbf{g}}{\partial \delta}$ and $\frac{\partial \mathbf{g}}{\partial \rho}$ are evaluated within

GTDS in subroutine VARDIF. The following algorithms are used:

$$\frac{\partial \dot{\bar{\mathbf{a}}}}{\partial \delta} = \frac{(\dot{\bar{\mathbf{a}}})_{diffuse_reflectivity_term}}{\delta} \quad (4.48a)$$

$$\frac{\partial \dot{\bar{\mathbf{a}}}}{\partial \rho} = \frac{(\dot{\bar{\mathbf{a}}})_{specular_reflectivity_term}}{\rho} \quad (4.48b)$$

The variational equations (Eqs (4.46) and (4.47)) are solved simultaneously in the combined system of equations along with the averaged equations of motion.

For the macro-model for solar radiation pressure, we calculate two columns (per plate) for the \mathbf{D} matrix, which was defined in Eq (4.36). The first is the partial derivative of the mean element rates with respect to diffuse reflectivity (Eq (4.48a)), and the second is the partial derivative of the mean element rates with respect to specular reflectivity (Eq (4.48b)).

As before, if we wish to solve for a single C_R that scales the entire macro-model, then we introduce C_R as a solve-for parameter, which means that there is another column in the \mathbf{D} matrix. This column contains the partial derivative of the acceleration with respect to the single C_R . To obtain this partial derivative, the following algorithm is used:

$$\frac{\partial \dot{\mathbf{a}}}{\partial C_R} = \frac{(\dot{\mathbf{a}})_{\text{solar radiation pressure}}}{C_R} \quad (4.49)$$

4.5 One-panel Model (Alternate Parameterization) Partial Derivatives

While the physical parameters that explicitly appear in Eq (3.14) are σ_a , σ_{rs} , and σ_{rd} , the solve-for parameters for differential correction and filter applications are σ_a and σ , the percent of incident radiation absorbed and the percent of reflected radiation diffusely reflected, respectively. This choice of solve-for parameters corresponds to the input parameters for the one-panel model detailed in Hughes' book [Ref 29], and used in the DSST Standalone for the PowerSail project [Ref 28].

Because σ does not appear explicitly in Eq (3.14), and because σ_{rs} , and σ_{rd} are functions of both σ and σ_a , the variational differential equations for the partial

derivatives of the motion using the alternate representation of solar radiation pressure require additional discussion.

To repeat the definition for σ_{rs} in terms of σ and σ_a , given in Eq (3.12a):

$$\sigma_{rs}(\sigma, \sigma_a) = (1 - \sigma)(1 - \sigma_a)$$

From Eq (3.12a), we obtain the following partial derivatives:

$$\frac{\partial}{\partial \sigma_a} \sigma_{rs}(\sigma, \sigma_a) = \sigma - 1 \quad (4.50a)$$

$$\frac{\partial}{\partial \sigma} \sigma_{rs}(\sigma, \sigma_a) = \sigma_a - 1 \quad (4.50b)$$

Also, the definition for σ_{rd} in terms of σ and σ_a is given in Eq (3.12b):

$$\sigma_{rd}(\sigma, \sigma_a) = \sigma(1 - \sigma_a)$$

From Eq (3.12a), we obtain the following partial derivatives:

$$\frac{\partial}{\partial \sigma_a} \sigma_{rd}(\sigma, \sigma_a) = -\sigma \quad (4.51a)$$

$$\frac{\partial}{\partial \sigma} \sigma_{rd}(\sigma, \sigma_a) = 1 - \sigma_a \quad (4.51b)$$

4.5.1 Cowell Variational Equations (Alternate Parameterization)

We generalize the Cowell equations of motion as follows:

$$\ddot{\mathbf{r}} = \mathbf{f}(\mathbf{r}, \dot{\mathbf{r}}, t, \sigma_a, \sigma_{rs}, \sigma_{rd}) \quad (4.52)$$

Differentiating Eq (4.52) with respect to σ_a , we get

$$\frac{\partial}{\partial \sigma_a} \ddot{\mathbf{r}} = \frac{\partial \ddot{\mathbf{r}}}{\partial \dot{\mathbf{r}}} \frac{\partial \dot{\mathbf{r}}}{\partial \sigma_a} + \frac{\partial \ddot{\mathbf{r}}}{\partial \dot{\mathbf{r}}} \frac{\partial \dot{\mathbf{r}}}{\partial \sigma_a} + \frac{\partial \ddot{\mathbf{r}}}{\partial \sigma_a} + \frac{\partial \ddot{\mathbf{r}}}{\partial \sigma_{rs}} \frac{\partial \sigma_{rs}}{\partial \sigma_a} + \frac{\partial \ddot{\mathbf{r}}}{\partial \sigma_{rd}} \frac{\partial \sigma_{rd}}{\partial \sigma_a} \quad (4.53)$$

Substituting Eqs (4.50a) and (4.51a) into Eq. (4.53) gives

$$\frac{\partial}{\partial \sigma_a} \ddot{\mathbf{r}} = \frac{\partial \ddot{\mathbf{r}}}{\partial \mathbf{r}} \frac{\partial \mathbf{r}}{\partial \sigma_a} + \frac{\partial \ddot{\mathbf{r}}}{\partial \dot{\mathbf{r}}} \frac{\partial \dot{\mathbf{r}}}{\partial \sigma_a} + \frac{\partial \ddot{\mathbf{r}}}{\partial \sigma_a} + \frac{\partial \ddot{\mathbf{r}}}{\partial \sigma_{rs}} (\sigma - 1) - \frac{\partial \ddot{\mathbf{r}}}{\partial \sigma_{rd}} \sigma \quad (4.54)$$

Using the definitions for \mathbf{A} and \mathbf{B} from Eq (4.24), we get

$$\frac{d^2}{dt^2} \left(\frac{\partial \mathbf{r}}{\partial \sigma_a} \right) = \mathbf{A} \frac{\partial \mathbf{r}}{\partial \sigma_a} + \mathbf{B} \frac{d}{dt} \left(\frac{\partial \mathbf{r}}{\partial \sigma_a} \right) + \frac{\partial \ddot{\mathbf{r}}}{\partial \sigma_a} + \frac{\partial \ddot{\mathbf{r}}}{\partial \sigma_{rs}} (\sigma - 1) - \frac{\partial \ddot{\mathbf{r}}}{\partial \sigma_{rd}} \sigma \quad (4.55)$$

where the ‘explicit’ terms in Eq (4.55) are given by

$$\frac{\partial \ddot{\mathbf{r}}}{\partial \sigma_a} = -\frac{\Phi A \cos \theta}{cm} \hat{\mathbf{s}} \quad (4.56a)$$

$$\frac{\partial \ddot{\mathbf{r}}}{\partial \sigma_{rs}} = -\frac{\Phi A \cos \theta}{cm} (2 \cos \theta \hat{\mathbf{n}}) \quad (4.56b)$$

$$\frac{\partial \ddot{\mathbf{r}}}{\partial \sigma_{rd}} = -\frac{\Phi A \cos \theta}{cm} \left(\hat{\mathbf{s}} + \frac{2}{3} \hat{\mathbf{n}} \right) \quad (4.56c)$$

Using the same approach, we also obtain

$$\frac{d^2}{dt^2} \left(\frac{\partial \mathbf{r}}{\partial \sigma} \right) = \mathbf{A} \frac{\partial \mathbf{r}}{\partial \sigma} + \mathbf{B} \frac{d}{dt} \left(\frac{\partial \mathbf{r}}{\partial \sigma} \right) + \frac{\partial \ddot{\mathbf{r}}}{\partial \sigma_{rs}} (\sigma_a - 1) + \frac{\partial \ddot{\mathbf{r}}}{\partial \sigma_{rd}} (1 - \sigma_a) \quad (4.57)$$

where we use Eqs (4.50b) and (4.51b) to evaluate the RHS, and the ‘explicit’ partial derivative terms are given by Eqs (4.56b) and (4.56c).

Eqs (4.55) and (4.57) are the primary variational differential equations for the parameter partials for the Cowell orbit propagator for this alternate parameterization of the solar radiation pressure perturbation on a flat plate. Similar to the previous Cowell case, these are solved simultaneously with the equations of motion.

4.5.2 Averaged Equations of Motion Variational Equations (Alt Parameterization)

With the alternate parameterization for solar radiation pressure acting on a one-panel model, we generalize the averaged equations of motion as:

$$\dot{\bar{\mathbf{a}}} = \mathbf{g}(\bar{\mathbf{a}}, t, \sigma_a, \sigma_{rs}, \sigma_{rd}) \quad (4.58)$$

Differentiating Eq (4.58) with respect to σ_a and σ , and using the partial derivatives obtained in Eqs (4.50) and (4.51) and in Chapter 4.3, results in:

$$\frac{d}{dt} \left(\frac{\partial \bar{\mathbf{a}}}{\partial \sigma_a} \right) = \mathbf{A} \frac{\partial \bar{\mathbf{a}}}{\partial \sigma_a} + \frac{\partial \mathbf{g}}{\partial \sigma_a} + (\sigma - 1) \frac{\partial \mathbf{g}}{\partial \sigma_{rs}} - \sigma \frac{\partial \mathbf{g}}{\partial \sigma_{rd}} \quad (4.59)$$

and

$$\frac{d}{dt} \left(\frac{\partial \bar{\mathbf{a}}}{\partial \sigma} \right) = \mathbf{A} \frac{\partial \bar{\mathbf{a}}}{\partial \sigma} + (\sigma_a - 1) \frac{\partial \mathbf{g}}{\partial \sigma_{rs}} + (1 - \sigma_a) \frac{\partial \mathbf{g}}{\partial \sigma_{rd}} \quad (4.60)$$

where the \mathbf{A} matrix is defined by Eq (4.36).

In terms of software, the partial derivatives $\frac{\partial \mathbf{g}}{\partial \sigma_a}$, $\frac{\partial \mathbf{g}}{\partial \sigma_{rs}}$, and $\frac{\partial \mathbf{g}}{\partial \sigma_{rd}}$ are evaluated within GTDS in subroutine VARDIF. The following algorithms are used:

$$\frac{\partial \mathbf{g}}{\partial \sigma_a} = \frac{(\dot{\bar{\mathbf{a}}})_{\text{sigma_a_terms}}}{\sigma_a} \quad (4.61a)$$

$$\frac{\partial \mathbf{g}}{\partial \sigma_{rs}} = \frac{(\dot{\bar{\mathbf{a}}})_{\text{sigma_rs_terms}}}{\sigma_{rs}} \quad (4.61b)$$

$$\frac{\partial \mathbf{g}}{\partial \sigma_{rd}} = \frac{(\dot{\bar{\mathbf{a}}})_{\text{sigma_rd_terms}}}{\sigma_{rd}} \quad (4.61c)$$

4.6 Partial Derivatives With Respect to Position

As mentioned earlier, it is common practice to use a low degree and order geopotential or even a J_2 approximation for the \mathbf{A} matrix, which contains the partial derivatives of the acceleration with respect to the spacecraft position in Eq (4.24).

However, if this assumption is not made, then there is a contribution from solar radiation pressure in the \mathbf{A} matrix.

4.6.1 Spherical Model Position Partial Derivatives

From Eq (3.1), the acceleration due to solar radiation pressure acting on a uniformly-respecting sphere is:

$$\ddot{\mathbf{R}}_{SRP} = -\frac{\Phi A}{cm} C_R \hat{\mathbf{s}} \quad (4.62)$$

We must take into account that the solar flux is scaled from the value at 1 AU to the value at the actual spacecraft location [Ref 48, pp 4-60-4-63]:

$$\ddot{\mathbf{R}}_{SRP} = -\frac{\Phi_{1AU} A}{cm} \frac{R_{SUN}^2}{\|\mathbf{R}_{SUN} - \mathbf{R}\|^2} C_R \hat{\mathbf{s}} \quad (4.63)$$

To get the partial derivative with respect to the spacecraft position vector:

$$\begin{aligned} \frac{\partial \ddot{\mathbf{R}}_{SRP}}{\partial \mathbf{R}} &= \frac{\partial}{\partial \mathbf{R}} \left(-\frac{\Phi A}{cm} \frac{R_{SUN}^2}{\|\mathbf{R}_{SUN} - \mathbf{R}\|^2} C_R \hat{\mathbf{s}} \right) \\ &= -\frac{\Phi A}{cm} R_{SUN}^2 C_R \frac{\partial}{\partial \mathbf{R}} \left(\frac{\hat{\mathbf{s}}}{\|\mathbf{R}_{SUN} - \mathbf{R}\|^2} \right) \\ &= -\frac{\Phi A}{cm} R_{SUN}^2 C_R \left[\frac{1}{\|\mathbf{R}_{SUN} - \mathbf{R}\|^2} \frac{\partial}{\partial \mathbf{R}} (\hat{\mathbf{s}}) + \hat{\mathbf{s}} \frac{\partial}{\partial \mathbf{R}} \left(\frac{1}{\|\mathbf{R}_{SUN} - \mathbf{R}\|^2} \right) \right] \end{aligned} \quad (4.64)$$

We need the partial derivative of the spacecraft-to-sun unit vector with respect to the spacecraft position vector:

$$\begin{aligned} \frac{\partial}{\partial \mathbf{R}} (\hat{\mathbf{s}}) &= \frac{\partial}{\partial \mathbf{R}} \left(\frac{(\mathbf{R}_{SUN} - \mathbf{R})}{\|\mathbf{R}_{SUN} - \mathbf{R}\|} \right) \\ &= \frac{1}{\|\mathbf{R}_{SUN} - \mathbf{R}\|} \frac{\partial}{\partial \mathbf{R}} (\mathbf{R}_{SUN} - \mathbf{R}) + (\mathbf{R}_{SUN} - \mathbf{R}) \frac{\partial}{\partial \mathbf{R}} \left(\frac{1}{\|\mathbf{R}_{SUN} - \mathbf{R}\|} \right) \\ &= -\frac{\mathbf{I}}{\|\mathbf{R}_{SUN} - \mathbf{R}\|} - \frac{(\mathbf{R}_{SUN} - \mathbf{R})}{\|\mathbf{R}_{SUN} - \mathbf{R}\|^2} \frac{\partial}{\partial \mathbf{R}} (\|\mathbf{R}_{SUN} - \mathbf{R}\|) \end{aligned} \quad (4.65)$$

We also need the partial of the spacecraft-to-sun vector magnitude with respect to the spacecraft position vector:

$$\begin{aligned}
\frac{\partial}{\partial \mathbf{R}} (\|\mathbf{R}_{SUN} - \mathbf{R}\|) &= \frac{\partial}{\partial \mathbf{R}} \left(\sqrt{(x_{SUN} - x)^2 + (y_{SUN} - y)^2 + (z_{SUN} - z)^2} \right) \\
&= \left[\frac{\partial}{\partial x} \left(\sqrt{(x_{SUN} - x)^2 + (y_{SUN} - y)^2 + (z_{SUN} - z)^2} \right) \quad \frac{\partial}{\partial y} \left(\sqrt{(x_{SUN} - x)^2 + (y_{SUN} - y)^2 + (z_{SUN} - z)^2} \right) \quad \frac{\partial}{\partial z} \left(\sqrt{(x_{SUN} - x)^2 + (y_{SUN} - y)^2 + (z_{SUN} - z)^2} \right) \right] \\
&= \left[\frac{1}{2\|\mathbf{R}_{SUN} - \mathbf{R}\|} \frac{\partial}{\partial x} (x_{SUN} - x)^2 \quad \frac{1}{2\|\mathbf{R}_{SUN} - \mathbf{R}\|} \frac{\partial}{\partial y} (y_{SUN} - y)^2 \quad \frac{1}{2\|\mathbf{R}_{SUN} - \mathbf{R}\|} \frac{\partial}{\partial z} (z_{SUN} - z)^2 \right] \\
&= \left[\frac{-2(x_{SUN} - x)}{2\|\mathbf{R}_{SUN} - \mathbf{R}\|} \quad \frac{-2(y_{SUN} - y)}{2\|\mathbf{R}_{SUN} - \mathbf{R}\|} \quad \frac{-2(z_{SUN} - z)}{2\|\mathbf{R}_{SUN} - \mathbf{R}\|} \right] \\
&= -\frac{(\mathbf{R}_{SUN} - \mathbf{R})^T}{\|\mathbf{R}_{SUN} - \mathbf{R}\|} \\
&= -\hat{\mathbf{s}}^T
\end{aligned} \tag{4.66}$$

Plugging Eq (4.66) into Eq (4.65) gives:

$$\begin{aligned}
\frac{\partial}{\partial \mathbf{R}} (\hat{\mathbf{s}}) &= -\frac{\mathbf{I}}{\|\mathbf{R}_{SUN} - \mathbf{R}\|} + \frac{(\mathbf{R}_{SUN} - \mathbf{R})(\mathbf{R}_{SUN} - \mathbf{R})^T}{\|\mathbf{R}_{SUN} - \mathbf{R}\|^3} \\
&= -\frac{\mathbf{I}}{\|\mathbf{R}_{SUN} - \mathbf{R}\|} + \frac{\hat{\mathbf{s}}\hat{\mathbf{s}}^T}{\|\mathbf{R}_{SUN} - \mathbf{R}\|} \\
&= -\frac{1}{\|\mathbf{R}_{SUN} - \mathbf{R}\|} (\mathbf{I} - \hat{\mathbf{s}}\hat{\mathbf{s}}^T)
\end{aligned} \tag{4.67}$$

Plugging Eq (4.67) into Eq (4.64) gives:

$$\begin{aligned}
\frac{\partial \ddot{\mathbf{R}}_{SRP}}{\partial \mathbf{R}} &= -\frac{\Phi A}{cm} R_{SUN}^2 C_R \left[\frac{1}{\|\mathbf{R}_{SUN} - \mathbf{R}\|^2} \frac{\partial}{\partial \mathbf{R}} (\hat{\mathbf{s}}) + \hat{\mathbf{s}} \frac{\partial}{\partial \mathbf{R}} \left(\frac{1}{\|\mathbf{R}_{SUN} - \mathbf{R}\|^2} \right) \right] \\
&= -\frac{\Phi A}{cm} R_{SUN}^2 C_R \left[-\frac{1}{\|\mathbf{R}_{SUN} - \mathbf{R}\|^3} (\mathbf{I} - \hat{\mathbf{s}}\hat{\mathbf{s}}^T) - \frac{2\hat{\mathbf{s}}}{\|\mathbf{R}_{SUN} - \mathbf{R}\|^3} \frac{\partial}{\partial \mathbf{R}} (\|\mathbf{R}_{SUN} - \mathbf{R}\|) \right] \\
&= -\frac{\Phi A}{cm} R_{SUN}^2 C_R \left[-\frac{1}{\|\mathbf{R}_{SUN} - \mathbf{R}\|^3} (\mathbf{I} - \hat{\mathbf{s}}\hat{\mathbf{s}}^T) + \frac{2\hat{\mathbf{s}}\hat{\mathbf{s}}^T}{\|\mathbf{R}_{SUN} - \mathbf{R}\|^3} \right] \\
&= \frac{\Phi A}{cm} C_R \frac{R_{SUN}^2}{\|\mathbf{R}_{SUN} - \mathbf{R}\|^3} (\mathbf{I} - 3\hat{\mathbf{s}}\hat{\mathbf{s}}^T)
\end{aligned} \tag{4.68}$$

Thus, for the spherical SRP model:

$$\frac{\partial \ddot{\mathbf{R}}_{SRP}}{\partial \mathbf{R}} = \frac{\Phi A}{cm} C_R \frac{R_{SUN}^2}{\|\mathbf{R}_{SUN} - \mathbf{R}\|^3} (\mathbf{I} - 3\hat{\mathbf{s}}\hat{\mathbf{s}}^T) \quad (4.69)$$

4.6.2 Macro-model Position Partial Derivatives

From Eq (3.11), the equation for acceleration due to solar radiation pressure acting on a single flat plate is:

$$\ddot{\mathbf{R}}_{SRP} = -\frac{\Phi A \cos \theta}{cm} \left[(1 - \rho)\hat{\mathbf{s}} + 2\left(\frac{\delta}{3} + \rho \cos \theta\right)\hat{\mathbf{n}} \right] \quad (4.70)$$

Again, the solar flux is scaled from the value at 1 AU:

$$\ddot{\mathbf{R}}_{SRP} = -\frac{\Phi_{1AU} A \cos \theta}{cm} \frac{R_{SUN}^2}{\|\mathbf{R}_{SUN} - \mathbf{R}\|^2} \left[(1 - \rho)\hat{\mathbf{s}} + 2\left(\frac{\delta}{3} + \rho \cos \theta\right)\hat{\mathbf{n}} \right] \quad (4.71)$$

We will require the partial derivative of $\cos(\theta)$ with respect to the spacecraft position vector:

$$\begin{aligned} \frac{\partial}{\partial \mathbf{R}} (\cos \theta) &= \frac{\partial}{\partial \mathbf{R}} (\hat{\mathbf{n}} \cdot \hat{\mathbf{s}}) = \hat{\mathbf{n}}^T \frac{\partial}{\partial \mathbf{R}} (\hat{\mathbf{s}}) + \hat{\mathbf{s}}^T \frac{\partial}{\partial \mathbf{R}} (\hat{\mathbf{n}}) \\ &= -\frac{\hat{\mathbf{n}}^T}{\|\mathbf{R}_{SUN} - \mathbf{R}\|} (\mathbf{I} - \hat{\mathbf{s}}\hat{\mathbf{s}}^T) + \hat{\mathbf{s}}^T \frac{\partial}{\partial \mathbf{R}} (\hat{\mathbf{n}}) \\ &= -\frac{1}{\|\mathbf{R}_{SUN} - \mathbf{R}\|} (\hat{\mathbf{n}}^T - \hat{\mathbf{n}}^T \hat{\mathbf{s}}\hat{\mathbf{s}}^T) + \hat{\mathbf{s}}^T \frac{\partial}{\partial \mathbf{R}} (\hat{\mathbf{n}}) \\ &= -\frac{1}{\|\mathbf{R}_{SUN} - \mathbf{R}\|} (\hat{\mathbf{n}}^T - \cos \theta \hat{\mathbf{s}}^T) + \hat{\mathbf{s}}^T \frac{\partial}{\partial \mathbf{R}} (\hat{\mathbf{n}}) \end{aligned} \quad (4.72)$$

Also, we will require the following partial derivative (using Eqs (4.66) and (4.72)):

$$\begin{aligned}
\frac{\partial}{\partial \mathbf{R}} \left(\frac{\cos \theta}{\|\mathbf{R}_{SUN} - \mathbf{R}\|^2} \right) &= \frac{1}{\|\mathbf{R}_{SUN} - \mathbf{R}\|^2} \frac{\partial}{\partial \mathbf{R}} (\cos \theta) + \cos \theta \frac{\partial}{\partial \mathbf{R}} \left(\frac{1}{\|\mathbf{R}_{SUN} - \mathbf{R}\|^2} \right) \\
&= -\frac{1}{\|\mathbf{R}_{SUN} - \mathbf{R}\|^3} (\hat{\mathbf{n}}^T - \cos \theta \hat{\mathcal{S}}^T) + \frac{1}{\|\mathbf{R}_{SUN} - \mathbf{R}\|^2} \hat{\mathbf{s}}^T \frac{\partial}{\partial \mathbf{R}} (\hat{\mathbf{n}}) - \frac{2 \cos \theta}{\|\mathbf{R}_{SUN} - \mathbf{R}\|^3} \frac{\partial}{\partial \mathbf{R}} (\|\mathbf{R}_{SUN} - \mathbf{R}\|) \\
&= -\frac{1}{\|\mathbf{R}_{SUN} - \mathbf{R}\|^3} (\hat{\mathbf{n}}^T - \cos \theta \hat{\mathcal{S}}^T) + \frac{1}{\|\mathbf{R}_{SUN} - \mathbf{R}\|^2} \hat{\mathbf{s}}^T \frac{\partial}{\partial \mathbf{R}} (\hat{\mathbf{n}}) + \frac{2 \cos \theta \hat{\mathcal{S}}^T}{\|\mathbf{R}_{SUN} - \mathbf{R}\|^3} \\
&= -\frac{1}{\|\mathbf{R}_{SUN} - \mathbf{R}\|^3} (\hat{\mathbf{n}}^T - 3 \cos \theta \hat{\mathcal{S}}^T) + \frac{1}{\|\mathbf{R}_{SUN} - \mathbf{R}\|^2} \hat{\mathbf{s}}^T \frac{\partial}{\partial \mathbf{R}} (\hat{\mathbf{n}})
\end{aligned} \tag{4.73}$$

Additionally, we will require (using Eqs (4.72) and (4.73)):

$$\begin{aligned}
\frac{\partial}{\partial \mathbf{R}} \left(\frac{\cos^2 \theta}{\|\mathbf{R}_{SUN} - \mathbf{R}\|^2} \right) &= \frac{\cos \theta}{\|\mathbf{R}_{SUN} - \mathbf{R}\|^2} \frac{\partial}{\partial \mathbf{R}} (\cos \theta) + \cos \theta \frac{\partial}{\partial \mathbf{R}} \left(\frac{\cos \theta}{\|\mathbf{R}_{SUN} - \mathbf{R}\|^2} \right) \\
&= -\frac{\cos \theta}{\|\mathbf{R}_{SUN} - \mathbf{R}\|^3} (\hat{\mathbf{n}}^T - \cos \theta \hat{\mathcal{S}}^T) + \frac{\cos \theta}{\|\mathbf{R}_{SUN} - \mathbf{R}\|^2} \hat{\mathbf{s}}^T \frac{\partial}{\partial \mathbf{R}} (\hat{\mathbf{n}}) \\
&\quad - \frac{\cos \theta}{\|\mathbf{R}_{SUN} - \mathbf{R}\|^3} (\hat{\mathbf{n}}^T - 3 \cos \theta \hat{\mathcal{S}}^T) + \frac{\cos \theta}{\|\mathbf{R}_{SUN} - \mathbf{R}\|^2} \hat{\mathbf{s}}^T \frac{\partial}{\partial \mathbf{R}} (\hat{\mathbf{n}}) \\
&= -\frac{\cos \theta}{\|\mathbf{R}_{SUN} - \mathbf{R}\|^3} (2\hat{\mathbf{n}}^T - 4 \cos \theta \hat{\mathcal{S}}^T) + \frac{2 \cos \theta}{\|\mathbf{R}_{SUN} - \mathbf{R}\|^2} \hat{\mathbf{s}}^T \frac{\partial}{\partial \mathbf{R}} (\hat{\mathbf{n}}) \\
&= \frac{2 \cos \theta}{\|\mathbf{R}_{SUN} - \mathbf{R}\|^2} \left(\hat{\mathbf{s}}^T \frac{\partial}{\partial \mathbf{R}} (\hat{\mathbf{n}}) - \frac{1}{\|\mathbf{R}_{SUN} - \mathbf{R}\|} (\hat{\mathbf{n}}^T - 2 \cos \theta \hat{\mathcal{S}}^T) \right)
\end{aligned} \tag{4.74}$$

We now obtain the partial derivative of the acceleration on a flat plate with respect to the spacecraft position vector (using Eqs (4.68), (4.72), (4.73), and (4.74)):

$$\begin{aligned}
\frac{\partial \ddot{\mathbf{R}}_{SRP}}{\partial \mathbf{R}} \frac{\partial}{\partial \mathbf{R}} \left(-\frac{\Phi A \cos \theta}{cm} \frac{R_{SUN}^2}{\|\mathbf{R}_{SUN} - \mathbf{R}\|^2} \left[(1 - \rho) \hat{\mathbf{s}} + 2 \left(\frac{\delta}{3} + \rho \cos \theta \right) \hat{\mathbf{n}} \right] \right) \\
&= -\frac{\Phi A}{cm} R_{SUN}^2 \frac{\partial}{\partial \mathbf{R}} \left(\frac{1}{\|\mathbf{R}_{SUN} - \mathbf{R}\|^2} \cos \theta \left[(1 - \rho) \hat{\mathbf{s}} + 2 \left(\frac{\delta}{3} + \rho \cos \theta \right) \hat{\mathbf{n}} \right] \right) \\
&= -\frac{\Phi A}{cm} R_{SUN}^2 \frac{\partial}{\partial \mathbf{R}} \left((1 - \rho) \frac{\cos \theta}{\|\mathbf{R}_{SUN} - \mathbf{R}\|^2} \hat{\mathbf{s}} + 2 \left(\frac{\delta}{3} \frac{\cos \theta}{\|\mathbf{R}_{SUN} - \mathbf{R}\|^2} + \rho \frac{\cos^2 \theta}{\|\mathbf{R}_{SUN} - \mathbf{R}\|^2} \right) \hat{\mathbf{n}} \right)
\end{aligned} \tag{4.75}$$

$$\begin{aligned}
\frac{\partial \ddot{\mathbf{R}}_{SRP}}{\partial \mathbf{R}} &= -\frac{\Phi A}{cm} R_{SUN}^2 \left(\begin{aligned} &(1-\rho) \frac{\partial}{\partial \mathbf{R}} \left(\frac{\cos \theta}{\|\mathbf{R}_{SUN} - \mathbf{R}\|^2} \hat{\mathbf{s}} \right) \\ &+ \frac{2\delta}{3} \frac{\partial}{\partial \mathbf{R}} \left(\frac{\cos \theta}{\|\mathbf{R}_{SUN} - \mathbf{R}\|^2} \hat{\mathbf{n}} \right) + 2\rho \frac{\partial}{\partial \mathbf{R}} \left(\frac{\cos^2 \theta}{\|\mathbf{R}_{SUN} - \mathbf{R}\|^2} \hat{\mathbf{n}} \right) \end{aligned} \right) \\
&= -\frac{\Phi A}{cm} R_{SUN}^2 \left(\begin{aligned} &(1-\rho) \left(\cos \theta \frac{\partial}{\partial \mathbf{R}} \left(\frac{\hat{\mathbf{s}}}{\|\mathbf{R}_{SUN} - \mathbf{R}\|^2} \right) + \frac{\hat{\mathbf{s}}}{\|\mathbf{R}_{SUN} - \mathbf{R}\|^2} \frac{\partial}{\partial \mathbf{R}} (\cos \theta) \right) \\ &+ \frac{2\delta}{3} \hat{\mathbf{n}} \frac{\partial}{\partial \mathbf{R}} \left(\frac{\cos \theta}{\|\mathbf{R}_{SUN} - \mathbf{R}\|^2} \right) + \frac{2\delta}{3} \frac{\cos \theta}{\|\mathbf{R}_{SUN} - \mathbf{R}\|^2} \frac{\partial}{\partial \mathbf{R}} (\hat{\mathbf{n}}) \\ &+ 2\rho \hat{\mathbf{n}} \frac{\partial}{\partial \mathbf{R}} \left(\frac{\cos^2 \theta}{\|\mathbf{R}_{SUN} - \mathbf{R}\|^2} \right) + 2\rho \frac{\cos^2 \theta}{\|\mathbf{R}_{SUN} - \mathbf{R}\|^2} \frac{\partial}{\partial \mathbf{R}} (\hat{\mathbf{n}}) \end{aligned} \right) \\
&= -\frac{\Phi A}{cm} R_{SUN}^2 \left(\begin{aligned} &(1-\rho) \left(\begin{aligned} &\cos \theta \left(-\frac{1}{\|\mathbf{R}_{SUN} - \mathbf{R}\|^3} (\mathbf{I} - 3\hat{\mathbf{s}}\hat{\mathbf{s}}^T) \right) \\ &+ \frac{\hat{\mathbf{s}}}{\|\mathbf{R}_{SUN} - \mathbf{R}\|^2} \left(-\frac{1}{\|\mathbf{R}_{SUN} - \mathbf{R}\|} (\hat{\mathbf{n}}^T - \cos \theta \hat{\mathcal{C}}^T) + \hat{\mathbf{s}}^T \frac{\partial}{\partial \mathbf{R}} (\hat{\mathbf{n}}) \right) \end{aligned} \right) \\ &+ \frac{2\delta}{3} \left(\begin{aligned} &\hat{\mathbf{n}} \left(-\frac{1}{\|\mathbf{R}_{SUN} - \mathbf{R}\|^3} (\hat{\mathbf{n}}^T - 3\cos \theta \hat{\mathcal{C}}^T) + \frac{1}{\|\mathbf{R}_{SUN} - \mathbf{R}\|^2} \hat{\mathbf{s}}^T \frac{\partial}{\partial \mathbf{R}} (\hat{\mathbf{n}}) \right) \\ &+ \frac{\cos \theta}{\|\mathbf{R}_{SUN} - \mathbf{R}\|^2} \frac{\partial}{\partial \mathbf{R}} (\hat{\mathbf{n}}) \end{aligned} \right) \\ &+ 2\rho \left(\begin{aligned} &\frac{\hat{\mathbf{n}} 2\cos \theta}{\|\mathbf{R}_{SUN} - \mathbf{R}\|^2} \left(\hat{\mathbf{s}}^T \frac{\partial}{\partial \mathbf{R}} (\hat{\mathbf{n}}) - \frac{1}{\|\mathbf{R}_{SUN} - \mathbf{R}\|} (\hat{\mathbf{n}}^T - 2\cos \theta \hat{\mathcal{C}}^T) \right) \\ &+ \frac{\cos^2 \theta}{\|\mathbf{R}_{SUN} - \mathbf{R}\|^2} \frac{\partial}{\partial \mathbf{R}} (\hat{\mathbf{n}}) \end{aligned} \right) \end{aligned} \right) \\
\frac{\partial \ddot{\mathbf{R}}_{SRP}}{\partial \mathbf{R}} &= \frac{\Phi A}{cm} \frac{R_{SUN}^2}{\|\mathbf{R}_{SUN} - \mathbf{R}\|^2} \left(\begin{aligned} &\frac{1}{\|\mathbf{R}_{SUN} - \mathbf{R}\|} \left((1-\rho) (\cos \theta (\mathbf{I} - 3\hat{\mathbf{s}}\hat{\mathbf{s}}^T) + (\hat{\mathbf{s}}\hat{\mathbf{n}}^T - \cos \theta \hat{\mathcal{C}}\hat{\mathbf{s}}^T)) \right. \\ &\left. + \frac{2\delta}{3} (\hat{\mathbf{n}}\hat{\mathbf{n}}^T - 3\cos \theta \hat{\mathcal{C}}\hat{\mathbf{n}}^T) + 4\rho \cos \theta (\hat{\mathbf{n}}\hat{\mathbf{n}}^T - 2\cos \theta \hat{\mathcal{C}}\hat{\mathbf{n}}^T) \right) \\ &- \left(\begin{aligned} &\hat{\mathbf{s}}\hat{\mathbf{s}}^T \frac{\partial}{\partial \mathbf{R}} (\hat{\mathbf{n}}) + \frac{2\delta}{3} \left(\hat{\mathbf{n}}\hat{\mathbf{s}}^T \frac{\partial}{\partial \mathbf{R}} (\hat{\mathbf{n}}) + \cos \theta \frac{\partial}{\partial \mathbf{R}} (\hat{\mathbf{n}}) \right) \\ &+ 2\rho \cos \theta \left(2\hat{\mathbf{n}}\hat{\mathbf{s}}^T \frac{\partial}{\partial \mathbf{R}} (\hat{\mathbf{n}}) + \cos \theta \frac{\partial}{\partial \mathbf{R}} (\hat{\mathbf{n}}) \right) \end{aligned} \right) \end{aligned} \right)
\end{aligned}$$

(4.76)

Thus, for each flat plate in the solar radiation pressure macro-model:

$$\frac{\partial \ddot{\mathbf{R}}_{SRP}}{\partial \mathbf{R}} = \frac{\Phi A}{cm} \frac{R_{SUN}^2}{\|\mathbf{R}_{SUN} - \mathbf{R}\|^2} \left(\begin{array}{l} \frac{1}{\|\mathbf{R}_{SUN} - \mathbf{R}\|} \left(\begin{array}{l} (1 - \rho)(\cos \theta + \hat{\mathbf{s}} \hat{\mathbf{n}}^T - 4 \cos \theta \hat{\mathbf{s}} \hat{\mathbf{s}}^T) \\ + \left(\frac{2\delta}{3} + 4\rho \cos \theta \right) \hat{\mathbf{n}} \hat{\mathbf{n}}^T \\ - (2\delta \cos \theta + 8\rho \cos^2 \theta) \hat{\mathbf{n}} \hat{\mathbf{s}}^T \end{array} \right) \\ - \left(\begin{array}{l} \hat{\mathbf{s}} \hat{\mathbf{s}}^T \frac{\partial}{\partial \mathbf{R}}(\hat{\mathbf{n}}) + \left(\frac{2\delta}{3} + 4\rho \cos \theta \right) \hat{\mathbf{n}} \hat{\mathbf{s}}^T \frac{\partial}{\partial \mathbf{R}}(\hat{\mathbf{n}}) \\ + \left(\frac{2\delta}{3} \cos \theta + 2\rho \cos^2 \theta \right) \frac{\partial}{\partial \mathbf{R}}(\hat{\mathbf{n}}) \end{array} \right) \end{array} \right) \quad (4.77)$$

For the complete macro-model, the partial derivative of the acceleration due to solar radiation pressure acting on the model with respect to position would be the vector sum of Eq (4.77) for each plate.

For the one-panel (alternate parameterization) model, the partial with respect to position is identical, except for the notation for the reflectivity coefficients:

$$\frac{\partial \ddot{\mathbf{R}}_{SRP}}{\partial \mathbf{R}} = \frac{\Phi A}{cm} \frac{R_{SUN}^2}{\|\mathbf{R}_{SUN} - \mathbf{R}\|^2} \left(\begin{array}{l} \frac{1}{\|\mathbf{R}_{SUN} - \mathbf{R}\|} \left(\begin{array}{l} (1 - \sigma_{rs})(\cos \theta + \hat{\mathbf{s}} \hat{\mathbf{n}}^T - 4 \cos \theta \hat{\mathbf{s}} \hat{\mathbf{s}}^T) \\ + \left(\frac{2\sigma_{rd}}{3} + 4\sigma_{rs} \cos \theta \right) \hat{\mathbf{n}} \hat{\mathbf{n}}^T \\ - (2\sigma_{rd} \cos \theta + 8\sigma_{rs} \cos^2 \theta) \hat{\mathbf{n}} \hat{\mathbf{s}}^T \end{array} \right) \\ - \left(\begin{array}{l} \hat{\mathbf{s}} \hat{\mathbf{s}}^T \frac{\partial}{\partial \mathbf{R}}(\hat{\mathbf{n}}) + \left(\frac{2\sigma_{rd}}{3} + 4\sigma_{rs} \cos \theta \right) \hat{\mathbf{n}} \hat{\mathbf{s}}^T \frac{\partial}{\partial \mathbf{R}}(\hat{\mathbf{n}}) \\ + \left(\frac{2\sigma_{rd}}{3} \cos \theta + 2\sigma_{rs} \cos^2 \theta \right) \frac{\partial}{\partial \mathbf{R}}(\hat{\mathbf{n}}) \end{array} \right) \end{array} \right) \quad (4.78)$$

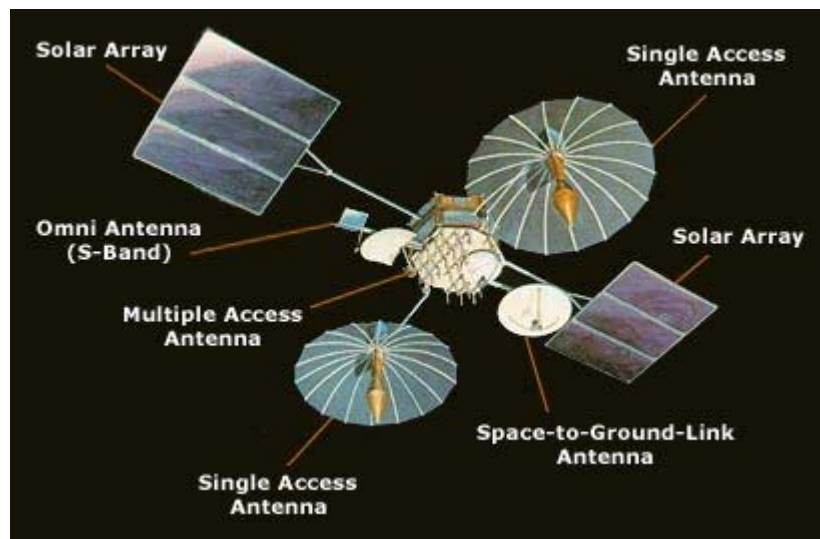
It is noted that the partial derivative of the panel unit normal vector with respect to position involves the rotation from the spacecraft body-fixed (SBF) coordinate frame to the inertial coordinate frame:

$$\frac{\partial}{\partial \mathbf{R}}(\hat{\mathbf{n}}) = \frac{\partial}{\partial \mathbf{R}}([ROT_{SBF \rightarrow INERTIAL} \hat{\mathbf{n}}_{SBF}]) \quad (4.79)$$

Chapter 5 Macro-model Specifications

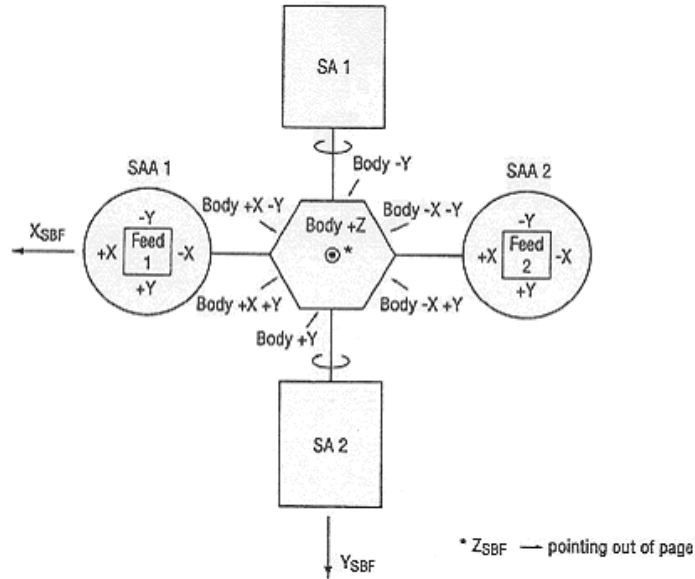
5.1 TDRSS Macro-model

The Tracking and Data Relay Satellite System (TDRSS) is a NASA program that includes several geosynchronous spacecraft whose mission is to provide command, telemetry, and tracking support for a large number of user spacecraft [Ref 36]. Six of the spacecraft were built by TRW, and one replenishment satellite was built by Boeing [Ref 66]. The system includes the seven Tracking and Delay Relay Satellites, two ground terminals at the White Sands Complex (New Mexico), a ground terminal extension on the island of Guam, and customer and data handling facilities [Ref 66]. This constellation of satellites provides global communication and data relay services for the Space Shuttle, International Space Station, Hubble Space Telescope, and several low earth orbiting satellites, balloons and research aircraft [Ref 66].



Source: Luthcke et al. [Ref 36]

Figure 5-1 – TDRS-05 Spacecraft Graphic



Source: Luthcke, et al. [Ref 36]

Figure 5-2 – Spacecraft Body-Fixed (SBF) Coordinate Frame for the TDRS-05 S/C

The macro-model implemented in this study for the TDRSS satellites was the one developed at Goddard Space Flight Center by Luthcke, et al., introduced in Chapter 1.3.4 of this thesis [Ref 36]. It consists of 24 flat plates [Ref 36]. The orientation of these plates is specified with respect to the spacecraft body-fixed (SBF) coordinate frame (See Chapter 2.3.6). Figure 5-1 shows an artist’s rendering of the TDRS-05 spacecraft, and Figure 5-2 shows the macro-model representation of the spacecraft with respect to the SBF frame [Ref 36]. Four of the plates represent the front and backsides of the sun-tracking solar panels and are moveable with respect to the SBF frame; the other twenty plates have a fixed orientation with respect to the SBF frame [Ref 36]. For each plate in the model, the orientation, area, absorptivity, specular reflectivity, and diffuse reflectivity are specified [Ref 36].

Table 5-1 – TDRS-05 Macro-model Plate Specifications

Source: Luthcke, et al. [Ref 36]

Plate	Plate Number	Area (m²)	Absorptivity	Diffuse Reflectivity	Specular Reflectivity
SAA 1 and 2 +Z/-Z	1-4	18.86	0.25	0.60	0.15
Body +Z	5	11.34	0.63	0.29	0.08
Body -Z	6	10.76	0.74	0.21	0.05
Body +Y	7	1.45	0.47	0.19	0.34
Body +X+Y	8	1.41	0.56	0.20	0.24
Body +X-Y	9	1.45	0.59	0.20	0.21
Body -Y	10	1.45	0.57	0.20	0.23
Body -X-Y	11	1.45	0.37	0.18	0.45
Body -X+Y	12	1.45	0.58	0.20	0.22
SAA Feed (all sides)	13-20	1.11	0.80	0.16	0.04
SA Cell Side	21, 23	14.76	0.81	0.15	0.04
SA Back	22, 24	14.76	0.86	0.11	0.03

The plate specifications for the TDRSS spacecraft are listed in Table 5-1. Four of the fixed-orientation plates (Plates 1 – 4) are used to represent two nadir-pointing single-access antennae. In addition to the absorptivity and reflectivity coefficients, these antennae have a transmissivity that varies depending on the solar incidence angle. Eight of the fixed-orientation plates (Plates 5 – 12) are used to represent the six sides, the top, and the bottom of the spacecraft’s main body structure. The remaining eight fixed-orientation plates (Plates 13 – 20) are used to represent the sides of the two single-access antennae feeds. The four moveable plates in the TDRSS model are used to represent the cell sides and back sides of the two solar panels. These plates are allowed to rotate about the SBF +Y axis, and are oriented so that the cell side surface normal vectors make the minimum possible angle with the spacecraft-to-sun vector. In other words, the solar panels are sun-tracking.

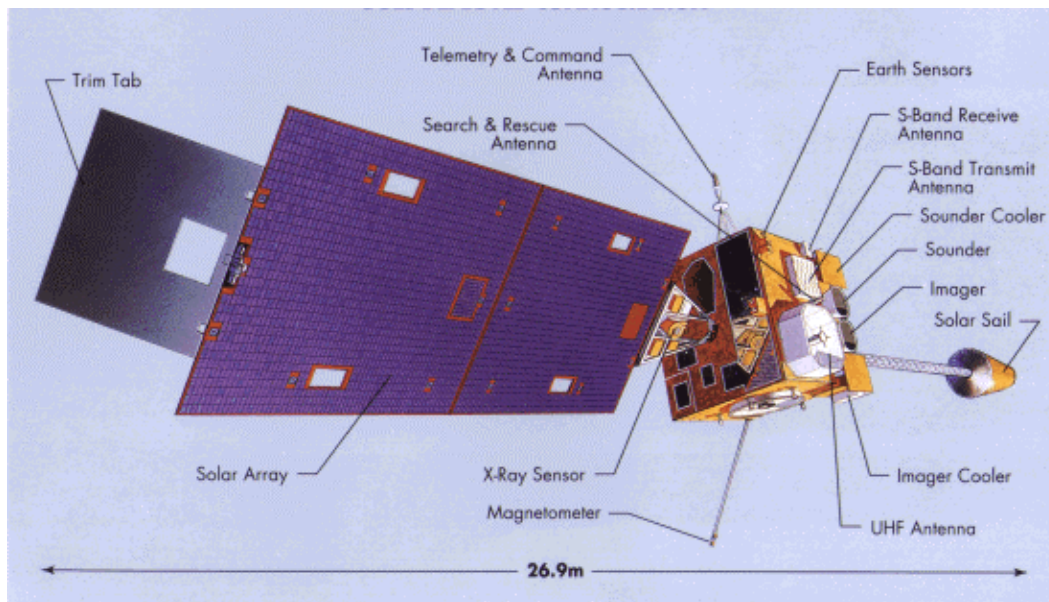
5.2 GOES Macro-model

The Geostationary Operational and Environmental Satellites (GOES) are operated by the National Oceanic and Atmospheric Administration (NOAA). These spacecraft monitor the Earth for atmospheric “triggers” for severe weather conditions including tornadoes, flash floods, hail storms, and hurricanes [Ref 67]. They also are used to estimate rainfall and snowfall accumulations, which help meteorologists issue flash flood warnings, winter storm warning, and spring snow melt advisories [Ref NOASSIS Gateway]. The spacecraft also detect ice fields and map the movements of sea and lake ice [Ref 67].

NASA launched the first two GOES spacecraft for NOAA in 1975 and 1977 [Ref 67]. NOAA currently operates two GOES spacecraft. GOES-12, or GOES-East, is located at 75° W longitude, while GOES-10, or GOES-West, is positioned at 135° W longitude [Ref 67]. The full-time coverage extends from approximately 20° W longitude to 265° E longitude [Ref 67]. GOES-9 is partially operational, and is being provided to the Japanese Meteorological Agency to replace a failing geostationary satellite [Ref 67]. GOES-11 is being stored in orbit as a replacement for either GOES-12 or GOES-10 in the event of failure [Ref 67].

The two primary instruments used by the GOES spacecraft are the Imager and Sounder [Ref 68]. The multispectral Imager uses one visible and four infrared channels to provide visual and infrared images of the Earth’s surface, oceans, cloud cover, and severe storm developments [Ref 68]. The Sounder provides data in nineteen spectral bands (one visible and eighteen infrared), that are used to determine the vertical atmospheric temperature and moisture profiles, surface and cloud top temperatures, and

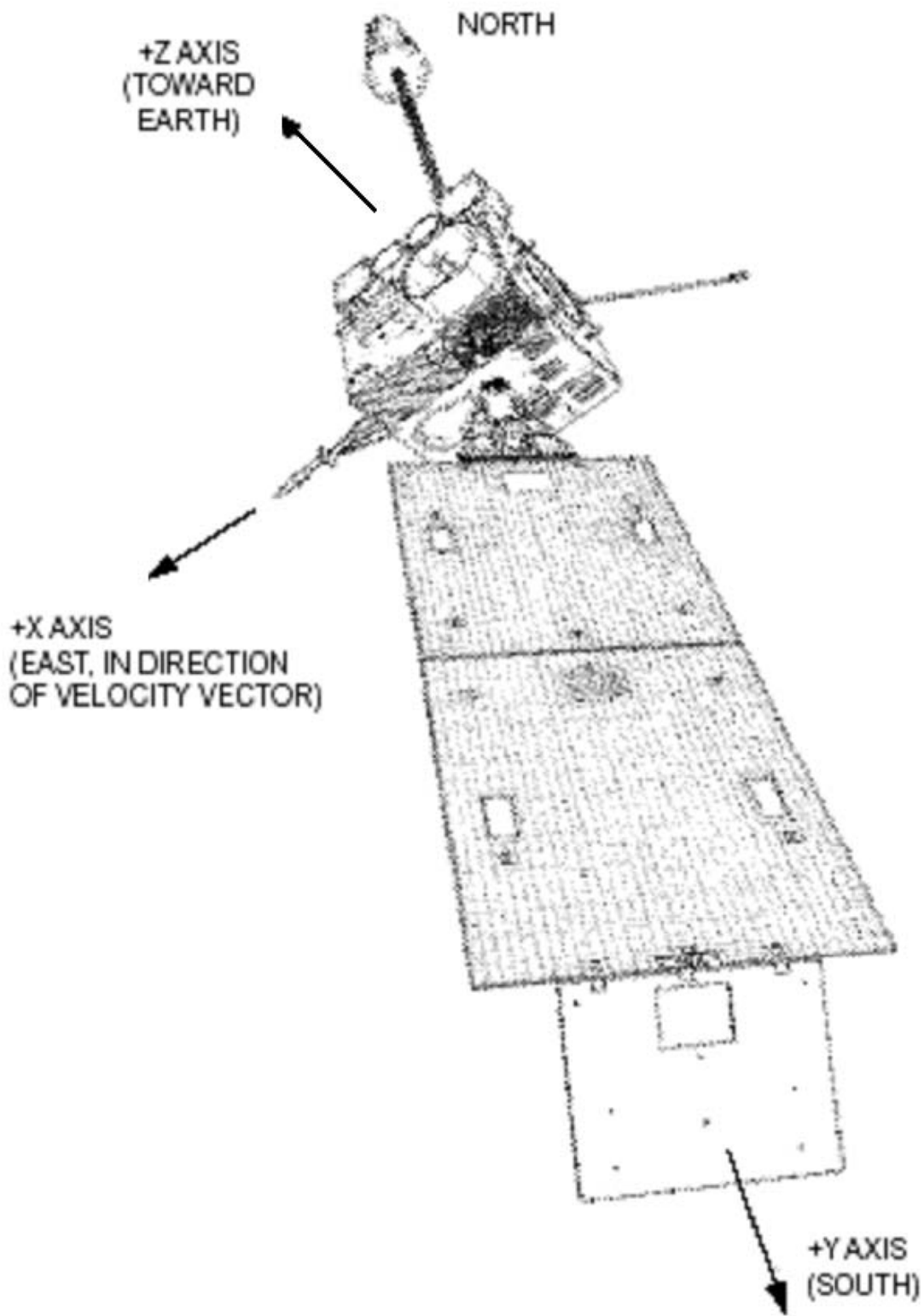
atmospheric ozone distribution [Ref 68]. The Imager and Sounder are positioned on the nadir-pointing face of the spacecraft. The three-axis stabilized design of the GOES spacecraft enables the sensors to remain fixed on the Earth and collect data more frequently [Ref 68].



Source: GOES I-M Data Book [Ref 68]

Figure 5-3 – GOES I-M Spacecraft Graphic

Figure 5-3 depicts an artist's rendering of the GOES I-M spacecraft, with several of the major spacecraft components labeled [Ref 68]. Figure 5-4 shows the SBF coordinate frame for the spacecraft [Ref 68].



Source: GOES I-M Data Book

Figure 5-4 – Spacecraft Body-Fixed (SBF) Coordinate Frame for the GOES I-M S/C

The macro-model for the GOES spacecraft was initially constructed by consulting the GOES I-M Data Book [Ref 68]. This allowed for determination of which plates should be included in the model, and their orientation within the SBF coordinate frame (see Chapter 2.3.6). Specific data on each of the plates was provided by Mike Wong, Space Systems/Loral, and included absorptivity values, specular and diffuse reflectivity values, and dimensions for the plates within the model [Ref 69]. Some of this information, including the reflectivity values and dimensions of the plates, is Space Systems/Loral proprietary. As such, a complete listing of the plate specifications cannot be given in this thesis. (For more information, please contact the author or Space Systems/Loral.)

The initial GOES macro-model constructed for this study included 20 plates. Six of the flat plates modeled the main body of the spacecraft. Four plates were used to model the two solar panels, one plate for each solar array cell side and one for each solar array back side. Two flat plates represented the solar array yoke front and back, and two flat plates represented the trim tab front and back. Two flat plates were used to model the solar sail top and bottom. An assembly of four flat plates was used to model the main structure of the solar sail. Out of the 20 plates in the model, eight were non-moveable with respect to the SBF frame. These plates were the ones to model the main body and the solar sail top and bottom. All other plates were able to rotate about the SBF -Y axis, and had their orientations specified with respect to the SA frame, with the SA +X axis sun-tracking. Table 5-2 lists the non-proprietary plate specifications for the 20-plate macro-model of the GOES I-M spacecraft.

Table 5-2 – 20-plate GOES Macro-model Plate Specifications

Source: Wong, Space Systems/Loral [Ref 69]

STATIONARY PLATES

Plate #	Description	Plate Normal (SBF Frame)		
		x	y	z
1	East Body Panel (+X)	1	0	0
2	West Body Panel (-X)	-1	0	0
3	South Body Panel (+Y)	0	1	0
4	North Body Panel (-Y)	0	-1	0
5	Earth Body Panel (+Z)	0	0	1
6	Anti-Earth Body Panel (-Z)	0	0	-1
7	Solar Sail Top	0	-1	0
8	Solar Sail Bottom	0	1	0

MOVEABLE PLATES

Plate #	Description	Plate Normal (Moving SA Frame)		
		x	y	z
9	SA Panel 1 Cell Side	1	0	0
10	SA Panel 1 Back Side	-1	0	0
11	SA Panel 2 Cell Side	1	0	0
12	SA Panel 2 Back Side	-1	0	0
13	SA Yoke Cell Side	1	0	0
14	SA Yoke Back Side	-1	0	0
15	Trim Tab Cell Side	1	0	0
16	Trim Tab Back Side	-1	0	0
17	Solar Sail Side (+X)	1	0	0
18	Solar Sail Side (-X)	-1	0	0
19	Solar Sail Side (+Y)	0	1	0
20	Solar Sail Side (-Y)	0	-1	0

Later, the GOES macro-model was refined by referencing the macro-model used by the GOES Flight Operations Team for modeling solar radiation torque [Refs 37, 39]. This macro-model consists of 15 plates. Six of the flat plates modeled the main body of the spacecraft. The solar panels were modeled using two flat plates only, one for the cell side and one for the back side. Two flat plates represented the solar array yoke front and back, and two flat plates represented the trim tab front and back. Two flat plates were used to model the solar sail top and bottom. Finally, a right circular cylinder was used to model the main structure of the solar sail.

Table 5-3 lists the non-proprietary plate specifications for the plates in the 15-plate GOES macro-model, including the plate number, plate description, and plate unit normal vector. The non-moveable plates in the model, which include the main body plates, are specified with respect to the spacecraft body-fixed (SBF) coordinate system. As with the TDRSS macro-model, the SBF coordinate system is oriented such that the +X axis is velocity-pointing, the +Y axis is normal to the orbit plane, and the +Z axis is nadir-pointing. The moveable plates, including the solar array, yoke, trim tab, and solar

sail, are specified with respect to the solar array (SA) frame. This frame rotates about the $-Y$ SBF axis so that the $+X$ SA axis always makes the minimum possible angle with the spacecraft-to-sun vector. In other words, the SA frame $+X$ axis is sun-tracking. Additionally, the refined GOES macro-model takes into account the rotation of the trim tab about the end of the solar array. The two plates that model the trim tab thus rotate in two degrees of freedom relative to the SBF coordinate frame.

Table 5-3 – 15-plate GOES Macro-model Plate Specifications

Source: Harvie, et al. [Refs 37, 39]

STATIONARY PLATES

Plate #	Description	Plate Normal (SBF Frame)		
		x	y	z
1	East Body Panel (+X)	1	0	0
2	West Body Panel (-X)	-1	0	0
3	South Body Panel (+Y)	0	1	0
4	North Body Panel (-Y)	0	-1	0
5	Earth Body Panel (+Z)	0	0	1
6	Anti-Earth Body Panel (-Z)	0	0	-1

MOVEABLE PLATES

Plate #	Description	Plate Normal (Moving SA Frame)		
		x	y	z
7	SA Panel Cell Side	1	0	0
8	SA Panel Back Side	-1	0	0
9	Trim Tab Cell Side	1	0	0
10	Trim Tab Back Side	-1	0	0
11	SA Yoke Cell Side	1	0	0
12	SA Yoke Back Side	-1	0	0
13	Solar Sail Bottom	0	0	-1
14	Solar Sail Cylinder	-	-	-
15	Solar Sail Top	0	0	1

[This page intentionally left blank.]

Chapter 6 Tools and Software

6.1 UNIX GTDS

For this study, it was decided to use the UNIX version of the Goddard Trajectory Determination System (GTDS) at the MIT/Lincoln Laboratory. Background information about GTDS can be found in the GTDS Mathematical Specification [Ref 48]. GTDS has a proven record of supporting similar investigations, including force model and estimation algorithm enhancements. Recently, George Granholm and Sarah Bergstrom completed atmospheric density estimation studies as part of their MIT SM theses using UNIX GTDS as the development and test platform [Refs 70, 71]. Additional background information on UNIX GTDS can be found in their theses:

- George Granholm's 2000 MIT SM thesis on atmospheric density model correction, which included porting GTDS to the UNIX environment [Ref 70]
- Sarah Bergstrom's 2002 MIT SM thesis that extended Granholm's atmospheric density correction work to use real-time observation data [Ref 71]

Also, versions of R&D GTDS on other computing platforms were used as the primary orbit tool in several other theses, including:

- Dan Fonte's 1993 MIT SM thesis on implementing a 50 x 50 geopotential model in GTDS [Ref 72]
- Scott Carter's 1996 MIT SM thesis on the integration of the J2000 coordinate system, the 50 x 50 geopotential model, and solid earth tides into GTDS [Ref 49]

- Jack Fischer's 1998 MIT SM thesis on the evolution and decay of Molniya orbits [Ref 53]
- Chris Sabol's 1998 University of Colorado Ph.D. thesis on using angular measurements for geosynchronous orbit determination [Ref 18]

Additionally, UNIX GTDS is available at the MIT/Lincoln Laboratory, making it an ideal choice for the orbit determination software to be used in this study.

6.1.1 Status of UNIX GTDS at Lincoln

The UNIX version of the GTDS software has been undergoing additional development at the MIT/Lincoln Laboratory. There are several projects in which it is being used. These applications and research areas include, but are not limited to:

- De-orbit mission analysis
- Geosynchronous satellite maneuver detection using the GTDS Extended Semi-analytical Kalman Filter (ESKF)
- Atmospheric density correction [Refs 70, 71, 72]
- Comparison of the Draper Semi-analytical Satellite Theory (DSST) and the Universal Semi-analytical Method (USM) [Ref 73]
- Inclusion of Space-Based Visible (SBV) observations

Work is also being done to port GTDS to the Linux platform. This includes comparing regression test results originally developed by Richard Metzinger at Draper Laboratory [Ref 74] against those produced on both the SGI UNIX and Linux platforms at MIT LL. SGI UNIX is a platform on which GTDS and its many components have already been verified. Also at Lincoln Laboratory there have been changes made to the GTDS source code to allow input and output in the J2000 reference frame and in a Quasi-

Inertial frame. Any software changes that have been made to the version of GTDS at Lincoln Laboratory have been managed in a Concurrent Versions System (CVS) [Ref 40] controlled environment. With several developers contributing to the source code, such a version control system is essential.

6.2 Implementation of External Subroutines

6.2.1 Introduction

In this study, subroutines from external systems were incorporated into UNIX GTDS at MIT/Lincoln Laboratory in order to implement the improved radiative force models. Specifically, subroutines for an improved spherical solar radiation pressure model, as well as the DSST one-panel model, were incorporated from the Draper Semi-analytical Satellite Theory (DSST) Standalone orbit propagation software [Ref 75]. Details can be found in Chapter 6.3. Subroutines for the box-wing macro-model and the Earth albedo/Earth IR radiation pressure model were incorporated from the GEODYN orbit determination software [Ref 36]. Details can be found in Chapter 6.4.

6.2.2 ‘Middle-ware’ Approach

A ‘middle-ware’ approach was used in the software design to include the improved radiative force model external subroutines into GTDS. This means including subroutines directly into GTDS from the external orbit determination programs to gain the desired functionality, while minimizing the changes to both the existing GTDS code as well as the incorporated external subroutines. To do this, structures are created to handle the variables used by the external subroutines. ‘Driver’ subroutines are also created, which transfer necessary variables from existing common blocks in GTDS to the

newly-created structures; these ‘drivers’ also call and run the external subroutines. This ‘middle-ware’ layer of structures and drivers is located in the software between the existing GTDS subroutine, SOLRAD, which handles solar radiation pressure acceleration, and the newly incorporated external subroutines. This ‘middle-ware’ approach is similar to the approach used by Darrell Herriges for the inclusion of the NORAD GP theories [Ref 76], and by Dan Fonte for the inclusion of the Naval Space Command satellite theory PPT2 into GTDS [Ref 77].

6.2.3 New GTDS Input Keywords

Data files consisting of input keywords are used to control UNIX GTDS. These keywords define the programs, initial conditions, coordinate systems, observations, databases, models, solve-for parameters, etc., that are to be used in a run of GTDS. Each keyword consists of seven input values, shown in Figure 6-1 [Ref 53]:

- Keyword name – Columns 1-8: Alphanumeric variable of up to eight characters that represents some program option or data quantity.
- Three integer fields – Columns 9-11, 12-14, and 15-17: Integer input options.
- Three real fields – Columns 18-38, 39-59, and 60-80: Real number input options.

Keyword Name	Integer Fields			Real Fields		
ELEMENT1	1	2	1	42167.16	0.000275	0.23

Source: Jack Fischer’s MIT SM Thesis [Ref 53]

Figure 6-1 – UNIX GTDS Input Keyword Structure

Several new input keywords were introduced into UNIX GTDS throughout this study. A complete set of keyword descriptions for all of the new keywords can be found in Appendix C of this thesis. This chapter will list the new keywords, and give a few details about their function and usage. Table 6-1 gives a summary:

Table 6-1 – Summary and Classification of New GTDS Input Keywords

General Solar Radiation Pressure Keyword:	
SOLRADMD	
One-panel Model (Alternate Parameterization) Keywords:	
Force Model Keywords	Differential Correction Keywords
SRPPANOF SRPPANRE	SRPPANSL SRPAPGSP
Box-wing Model (Macro-model) Keywords:	
Force Model Keywords	Differential Correction Keywords
SRPBWNUM SRPBWNRM SRPBWREF	SRPBWSLV SRPAPGBW
General Earth Radiation Pressure Keyword:	
ALBEDOMD	

Brief details about the usage of the new keywords follow:

- SOLRADMD – keyword to select which solar radiation pressure model should be used. The default is to use the spherical model. Other options include a cylindrical model and a cylindrical model with solar panels, which were options that previously existed in GTDS, the new DSST one-panel model, and the box-wing model. The particular spacecraft configuration to be used with the box-wing model can also be set using the SOLRADMD card. Options include a single-plate model, a two-plate model, the TDRSS spacecraft model, and the GOES spacecraft model.
- SRPPANOF – keyword to set the pointing offsets for the one-panel (alternate parameterization) solar radiation pressure model. Two rotation angle offsets from the sun-pointing direction, $d\theta$ and $d\phi$, are specified.
- SRPPANRE – keyword to set the reflectivity coefficients for the one-panel model. Values for the percent of radiation absorbed (σ) and the percent of reflected radiation diffusely reflected (σ_a) are specified.
- SRPPANSL – keyword to set the solve-for parameters for the one-panel solar radiation pressure model. Options include solving for σ , σ_a , and/or panel area.
- SRPAPGSP – keyword to include the parameters for the one-panel solar radiation pressure model in the element rate partial derivatives.
- SRPBWNUM – keyword to set the number of plates, as well as the number of moveable plates, for the box-wing (macro-model) solar radiation pressure model.

- SRPBWNRM – keyword to set the direction of the unit normal vector for each plate in the box-wing model. The normal vectors are specified in the spacecraft body-fixed (SBF) coordinate system.
- SRPBWREF – keyword to set the reflectivity coefficient values for each plate in the box-wing model. Values for the diffuse reflectivity coefficient (δ) and specular reflectivity coefficient (ρ) are specified.
- SRPBWSLV – keyword to set the solve-for parameters for the box-wing solar radiation pressure model. Options include solving for δ , ρ , and/or panel area for each plate. Additionally, a single C_R that scales the entire box-wing model can be specified as a solve-for parameter.
- SRPAPGBW – keyword to include the parameters for the box-wing solar radiation pressure model in the element rate partial derivatives.
- ALBEDOMD – keyword to set the options for the Earth albedo and Earth infrared radiation pressure model. Options include turning the model on or off, as well as the number of Earth segment rings surrounding the central cap to be used in the model.

Two existing GTDS subroutines were modified to handle the input processing of the new keywords. These subroutines are as follows:

- SETORB – Modified to handle the initial processing of the new keywords. The total number of keywords was increased, and the keyword names were entered in this subroutine.
- SETOG1 – Modified to handle the detailed processing of the new input keywords.

Two new block data subroutines were created in GTDS to support this study:

- SOLPREBD – Creates the SOLPRE common block, which handles variables used by the improved solar radiation pressure models
- ALBPRED – Creates the ALBPRED common block, which handles variables used by the new Earth radiation pressure model

6.3 DSST Standalone Subroutine Incorporation

Prior to incorporating the full box-wing model into GTDS, it was decided to begin by incorporating two simpler solar pressure models from the DSST standalone orbit propagator. The first is a more modern version of the uniformly reflecting spherical satellite (‘cannonball’) model. In particular, this version uses structures and records and has improved software maintainability characteristics [Ref 75]. The second is the one-panel solar pressure model, whose area, mass, orientation, specular reflectivity, and diffuse reflectivity can be specified [Ref 28]. The reason these two simpler models were incorporated was to develop a methodology for the software development before attempting to incorporate the full box-wing model capability into GTDS. The simpler models also allowed test cases to be run that demonstrated the continued functionality of GTDS, as well as accuracy comparisons between the various solar pressure models.

6.3.1 DSST Standalone Spherical Solar Radiation Pressure Model

The spherical solar radiation pressure model incorporated from the DSST Standalone has the same functionality as the solar radiation pressure model that previously existed in the GTDS subroutine SOLRAD. The model as coded in the DSST Standalone is an improvement over the version in GTDS for several reasons:

- (1) The code from the DSST Standalone is more maintainable. Specifically, it is better-documented, easier to read, and avoids the numerous GO TO statements included in the previous version of SOLRAD.
- (2) The DSST Standalone subroutines use structures and records to handle variables that are passed between subroutines, rather than the common block architecture previously used by GTDS. The use of structures and records ensures common variable names between subroutines and avoids improper referencing of common block locations.
- (3) The DSST Standalone subroutines use IMPLICIT NONE statements, rather than IMPLICIT REAL*8 statements used previously in GTDS. This usage requires that all variables be explicitly declared prior to use in subroutines and avoids errors due to variable name misspellings.

The spherical solar radiation pressure model incorporated from the DSST Standalone includes two subroutines:

- SUNFLX – Calculates the solar radiation flux at the spacecraft’s position.
- SOLSFR – Calculates the acceleration on a uniformly-reflecting spherical spacecraft due to solar radiation pressure.

To implement the improved version of the spherical spacecraft model, the issue of how to pass common variables between subroutines had to be addressed. In the DSST Standalone, the solar radiation pressure subroutines referenced the structure FRC to store common variables. In GTDS, however, an existing common block is called FRC. To avoid confusion and issues with identical names, the structure from the DSST Standalone was renamed FRC_PNL for incorporation into GTDS. The name was chosen because

this structure was then used to handle variables for all of the subroutines incorporated from the DSST Standalone, including the spherical and one-panel model subroutines.

A ‘middle-ware’ driver subroutine, SOLSFR_DRV, was created to pass variables from the GTDS common block architecture to the structure FRC_PNL. SOLSFR_DRV is called by SOLRAD within GTDS, and in turn calls the subroutines from the DSST Standalone listed above. The previously-existing spherical solar radiation pressure model in SOLRAD was commented-out. Chapter 7 of this thesis describes regression testing completed to demonstrate that the new model was incorporated correctly into GTDS.

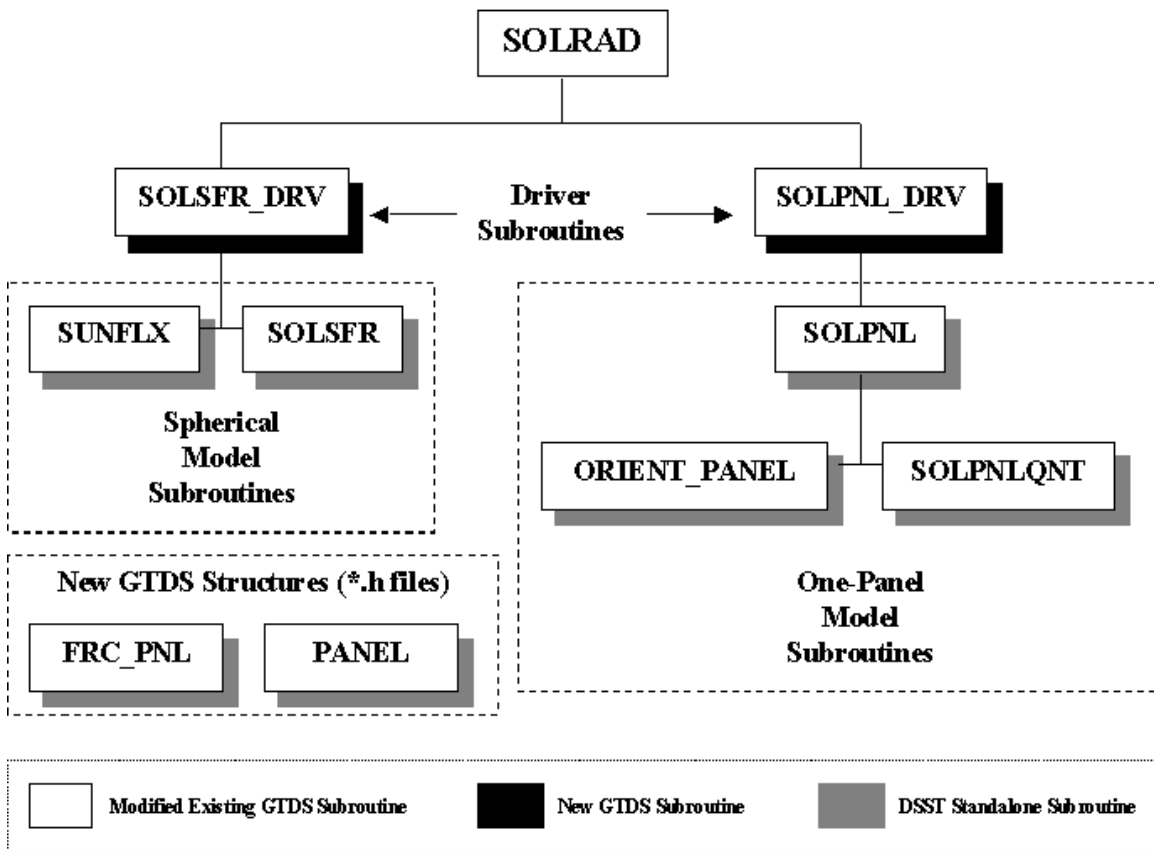


Figure 6-2 – Software Design Tree for Incorporation of DSST Standalone Solar

Radiation Pressure Model Subroutines into GTDS

The software design tree for the new spherical satellite model incorporated from the DSST Standalone into GTDS is shown in Figure 6-2.

6.3.2 One-panel Solar Radiation Pressure Model

The one-panel model for solar radiation pressure incorporated from the DSST Standalone uses the alternate representation for solar radiation pressure acting on a single flat plate (see Chapter 3.5). As a result, this model has the area, mass, orientation, σ , and σ_a values for the flat plate as the input parameters. The one-panel solar radiation pressure model incorporated from the DSST Standalone includes three subroutines:

- ORIENT_PANEL – Calculates the orientation of the flat panel with a given angular offset from the spacecraft-to-sun vector.
- SOLPNLQNT – Calculates the cross-sectional area of the flat panel projected toward the sun.
- SOLPNL – Calculates the solar radiation pressure acceleration on the one-panel model. Calls ORIENT_PANEL and SOLPNLQNT.

Similarly to the spherical model subroutines, the DSST Standalone one-panel model subroutines referenced the structure FRC to store common variables. As mentioned earlier, to avoid confusion with the GTDS common block FRC, the structure from the DSST Standalone was renamed FRC_PNL for incorporation into GTDS, and all references to the structure FRC were renamed to FRC_PNL within the incorporated subroutines. The one-panel model subroutines also use the structure PANEL to store variables related to the orientation of the panel with respect to the spacecraft-to-sun vector.

The ‘middle-ware’ driver subroutine created for the DSST one-panel model was named SOLPNL_DRV. SOLPNL_DRV is called by SOLRAD within GTDS, and in turn calls the subroutines from the DSST Standalone listed above.

The software design tree for the one-panel spacecraft model incorporated from the DSST Standalone into GTDS is shown in Figure 6-2.

6.4 GEODYN Subroutine Incorporation

The actual incorporation of the full box-wing model capability from GSFC's GEODYN orbit determination software into GTDS was broken up into several phases. The first phase was incorporation of the capability to compute the acceleration due to solar pressure using the macro-model. The second phase was incorporation of the capability to compute the partial derivatives of acceleration with respect to the various model parameters, including plate area, specular reflectivity, and diffuse reflectivity, as well as a single C_R that scales the entire macro-model. This allowed for differential correction runs that included macro-model parameters as solve-for parameters. The third phase was incorporation of the Earth albedo and Earth infrared radiation pressure model, including both the force model and partial derivatives.

6.4.1 GEODYN Box-wing Solar Radiation Pressure Model

Prior to incorporation into GTDS, the entire GEODYN orbit determination system code was stored in a CVS-controlled repository on the UNIX system at MIT/Lincoln Laboratory. The GEODYN macro-model subroutines primarily make use of an extensive common block architecture to pass variables between subroutines. Unfortunately, the names of the GEODYN common blocks and the organization of the GEODYN architecture have very little in common with the GTDS common block architecture. Additionally, the GEODYN code passes several variables into and out of subroutines via their calling sequences, which is another difference from GTDS, whose

subroutines pass only a few variables at most via the calling sequences. Although the two orbit determination systems were both developed at NASA Goddard Space Flight Center (GSFC), GTDS and GEODYN have evolved separately, and these issues show that subroutines from one system are not compatible with the other. The incompatibility of the subroutines made incorporation of the functionality from GEODYN a complex task.

In implementing the functionality of the macro-model from GEODYN, it was desired not only to minimize the changes to the external code, but also to modernize the resulting code as much as possible. This involved converting `IMPLICIT REAL*8` statements to `IMPLICIT NONE`, explicitly declaring all variables, and making use of structures and records instead of common blocks. This process made the resulting code similar to the more modern DSST Standalone code.

The box-wing model for solar radiation pressure incorporated from the GEODYN software included the following subroutines:

- TDRSAT – Rotates the plate unit normal vectors from the spacecraft body-fixed (SBF) coordinate frame to the inertial frame for the TDRSS macro-model.
- TDRSTN – Calculates the transmissivity of the single-access antennae within the TDRSS macro-model based on the solar incidence angle.
- BWSOLR – Calculates the solar radiation pressure acceleration on the box-wing model. Calls TDRSTN to include the transmissivity of the single-access antennae in the calculations.

The subroutines listed above are sufficient to provide the force model for solar radiation pressure, using the TDRS macro-model. In order to run the GOES macro-model, a new GTDS subroutine had to be created as follows:

- GOESAT – Rotates the plate unit normal vectors from the spacecraft body-fixed (SBF) coordinate frame to the inertial frame for the GOES macro-model. This subroutine was based on the subroutine TDRSAT, and modified for the GOES spacecraft.

It is envisioned that future applications of the box-wing model to other spacecraft will require a similar subroutine to be written, due to differences in the SBF coordinate frame and differences in the number and orientation of moving plates in the macro-model.

The structure FRC_BW was created to handle the variables used in the GEODYN box-wing model subroutines. All references to variables that previously were handled via common blocks were renamed to “FRC_BW.<variable name>” within the incorporated subroutines.

The ‘middle-ware’ driver subroutine created for the GEODYN box-wing model was named BWSOLR_DRV. BWSOLR_DRV is called by SOLRAD within GTDS, and transfers necessary variables between GTDS common blocks and the structure FRC_BW. BWSOLR_DRV also calls the subroutines from GEODYN listed above.

Figure 6-3 shows the software design tree for the solar radiation pressure macro-model incorporated from GEODYN into GTDS:

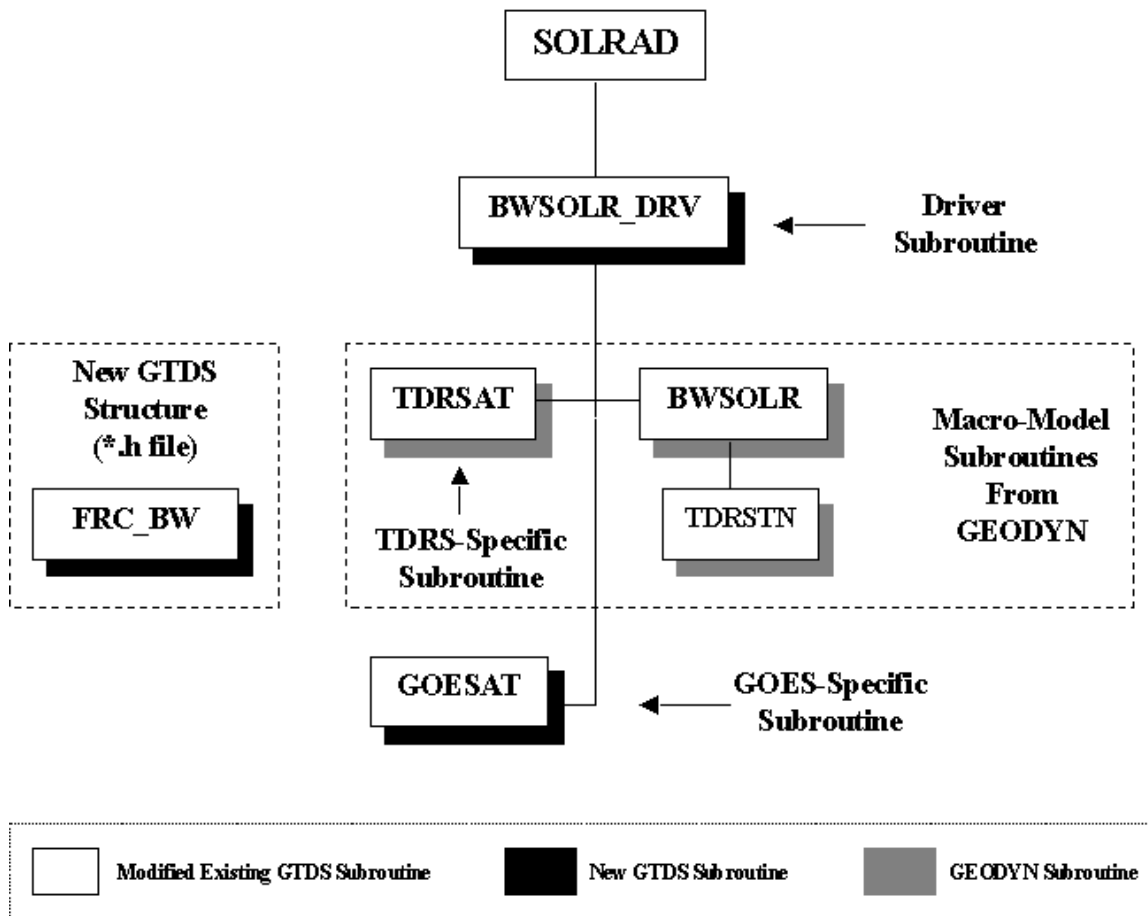


Figure 6-3 – Software Design Tree for Incorporation of GEODYN Solar Radiation Pressure Model Subroutines into GTDS

6.4.2 GEODYN Earth Albedo and Earth Infrared Radiation Pressure Model

The same issues that were encountered in incorporating the solar radiation pressure macro-model from GEODYN into GTDS arose during incorporation of the model for Earth radiation pressure effects. This meant that it was again necessary to resolve the issues of incompatible methods of handling variable I/O between GEODYN and GTDS (different common block architectures and different calling sequence styles). These issues, coupled with the desire to modernize the resultant code, meant again

converting IMPLICIT REAL*8 statements to IMPLICIT NONE, explicitly declaring all variables, and making use of structures and records instead of common blocks.

An additional issue stemmed from the fact that UNIX GTDS did not previously include an Earth radiation pressure model for albedo or Earth infrared. The issue was in deciding where to incorporate the Earth radiation pressure model. One option was to incorporate it as a new force model on the same level as the existing perturbing force models such as solar radiation pressure and drag. The second option was to incorporate the model subordinate to the existing solar radiation pressure model, and sum the force due to Earth albedo and Earth IR with the force due to solar radiation pressure.

An evaluation was completed of the anticipated modifications to the existing GTDS software that each option would require. It was concluded that the second option, which would place the Earth radiation pressure model as subordinate to the solar radiation pressure model, would require the least amount of modification, and thus would be the least intrusive on the existing functionality of GTDS.

Integrating the Earth albedo and Earth IR model in this way did involve resolution of a particular issue regarding when the solar radiation pressure force model was called. Specifically, in the case of the spacecraft being in eclipse (shadowed) at an integration time step, GTDS did not call SOLRAD, because it was assumed that there was no force due to solar radiation pressure acting on the spacecraft. This is a valid assumption, considering that GTDS uses a cylindrical shadow model, which effectively acts as a discrete “on/off” switch for the force due to solar radiation pressure. In GTDS, if the spacecraft is in shadow, the variable FSUNLT is set to a value of 0. Otherwise, if the spacecraft is in sunlight, FSUNLT has a value of 1.

However, it is possible that the spacecraft could experience force due to Earth albedo or Earth IR, even if it does not experience direct solar radiation pressure. As a result, since the Earth radiation pressure model is called beneath the solar radiation pressure model, an IF...THEN statement had to be put into the subroutines that call SOLRAD, specifically ACCEL and GQFUN. If the Earth radiation pressure model was turned on, this statement called SOLRAD even if the spacecraft was shadowed. Additionally, there are some points in GTDS that multiply the solar radiation pressure acceleration by FSUNLT. It is assumed that these are checks to make sure that there is no solar radiation pressure perturbation when the spacecraft is in shadow. These checks had to be addressed in implementing the new model, to ensure that they did not negate the Earth radiation pressure perturbation as well.

It is anticipated that similar issues regarding the variable FSUNLT will have to be addressed if and when an improved conical shadow model is implemented in GTDS. In the case of a penumbra region, the spacecraft will experience some fraction of the direct solar radiation, and a binary variable will no longer be sufficient to characterize the illumination of the spacecraft.

The Earth radiation pressure model (Earth albedo and Earth infrared radiation) incorporated from the GEODYN software included the following subroutines:

- ALBEDO – Calculates the Earth radiation pressure effect on the spacecraft for a spherical model. Calls ALBLOC, ALBANG, and ALBFLX. Calls BWALB and skips the calculations for a spherical model, if the box-wing model is being used instead.

- ALBANG – Calculates the angle between the Earth segment rings and the SBF nadir pointing (+Z) axis.
- ALNRML – Calculates two vectors that are normal to the radial vector and to each other; these are used in the albedo model.
- ALBLOC – Calculates the location of the Earth segments.
- ALBFLX – Calculates the shortwave and longwave radiation flux from each Earth segment.
- TDRSTN – Calculates the transmissivity of the single-access antennae within the TDRSS macro-model based on the solar incidence angle.
- BWALB – Calculates the Earth radiation pressure acceleration on the box-wing model. Calls TDRSTN to include the transmissivity of the single-access antennae in the calculations.

The structure FRC_ALB was created to handle the variables used in the GEODYN Earth radiation pressure model subroutines. All references to variables that previously were handled via common blocks were renamed to “FRC_ALB.<variable name>” within the incorporated subroutines.

The ‘middle-ware’ driver subroutine created for the GEODYN Earth albedo and Earth IR model was named ALBEDO_DRV. ALBEDO_DRV is called by SOLRAD within GTDS, and transfers necessary variables between GTDS common blocks and the structure FRC_ALB. ALBEDO_DRV also calls the subroutines from GEODYN listed above.

Figure 6-4 shows the software design tree for the Earth radiation pressure model incorporated from GEODYN into GTDS:

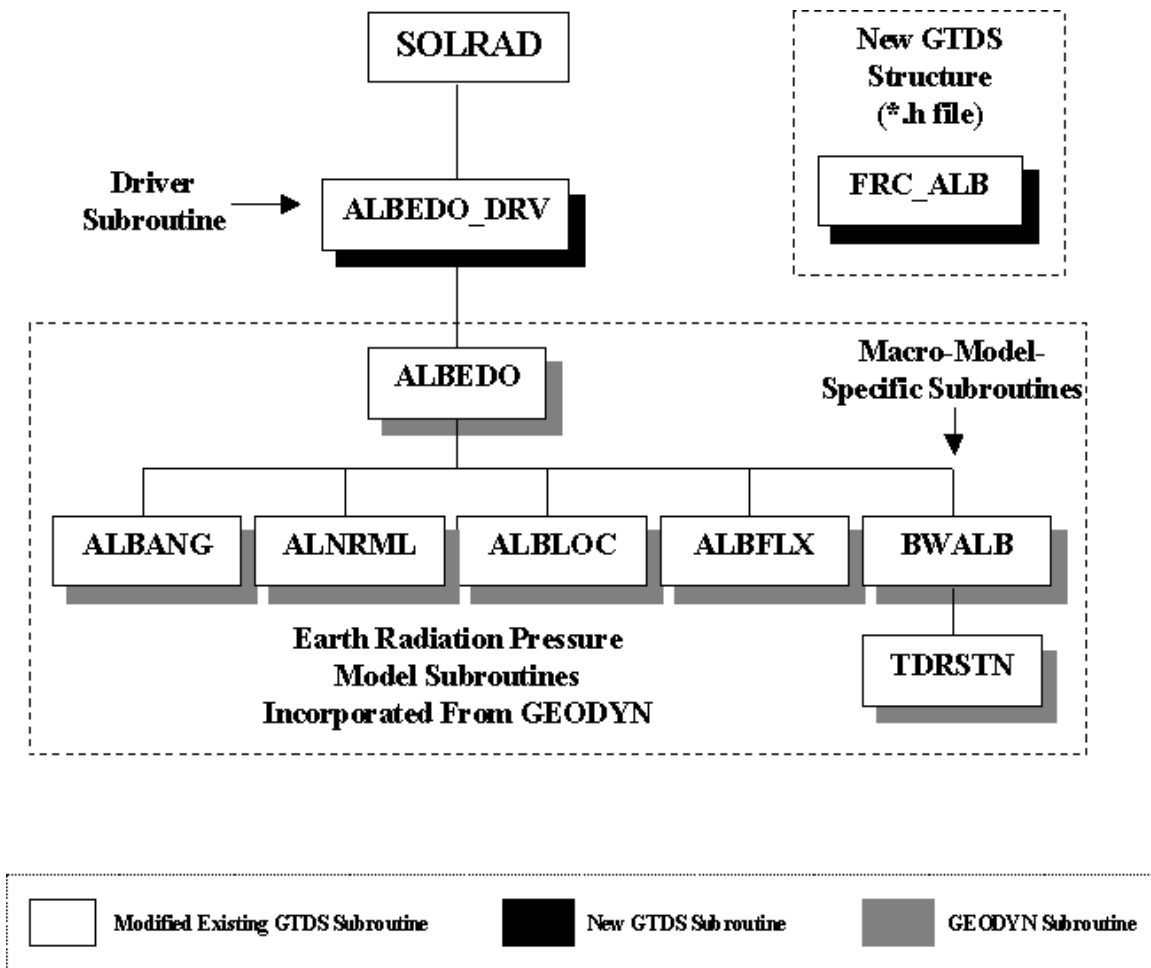


Figure 6-4 – Software Design Tree for Incorporation of GEODYN Earth Radiation Pressure Model (Earth Albedo and Earth IR) Subroutines into GTDS

6.5 Differential Correction Implementation

A number of modifications to several GTDS subroutines were required in order to implement the capability to perform differential correction runs using the improved radiative force models. The desired capability was to be able to solve for various model parameters in addition to the satellite state vector. For the one-panel model, the adjustable parameters include the reflectivity coefficients (σ_a and σ) and panel area of the panel. For the box-wing model, the adjustable parameters include the reflectivity

coefficients (δ and ρ) and area of each plate within the model, as well as a single C_R that scales the entire macro-model. The goal was to implement the differential correction capability in both the numerical (Cowell) orbit generator, as well as in the Semi-analytical Satellite Theory (DSST) orbit generator.

Several of the modifications to the GTDS code were applicable to both the Cowell and DSST orbit generators. These modifications dealt with including the model parameters in the solve-for vector, including the covariances of those parameters in the covariance matrix, and updating the parameter value and covariance at each integration time step. The GTDS subroutines that include such modifications are as follows:

- INTOGN – Modified to support initializing the partial derivative switches associated with the one-panel and box-wing SRP models and to initialize the reflectivity coefficients and variances.
- SOLTAB – Modified to handle including the reflectivity coefficients in the solve-for table.
- PSET – Modified to support resetting the reflectivity coefficients adjusted through the differential correction program from the P array.

The software design tree for the general GTDS Differential Correction program is shown in Figure 6-5:

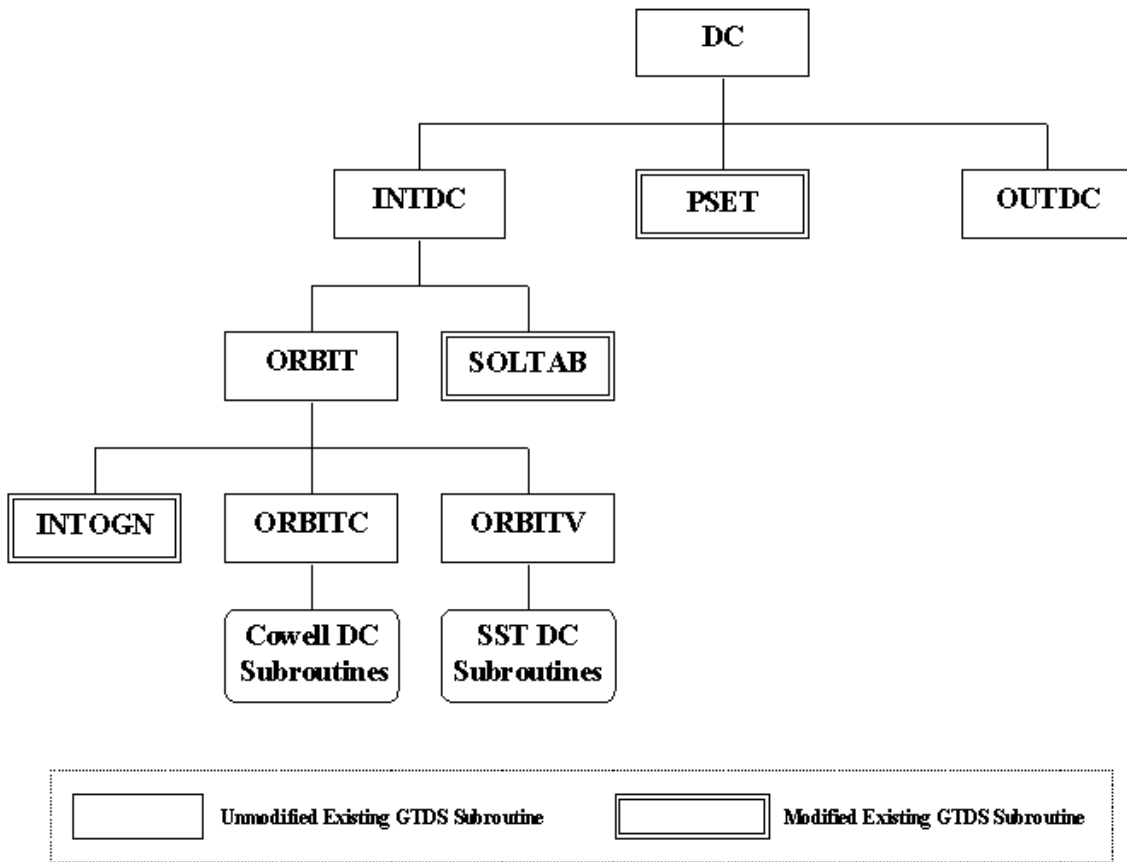


Figure 6-5 – Software Design Tree for GTDS Differential Correction Program

6.5.1 Cowell D.C. Implementation

For the Cowell theory, as discussed in Chapter 4.2, the partial derivatives with respect to the model parameters are calculated using analytical expressions. The subroutines modified are as follows:

- VARFRC – Modified to handle initializing SLRADV correctly and to sum the position partial derivatives correctly when running the one-panel or box-wing SRP models. Also modified with the intent of including the Earth radiation pressure model partials in the future.

- SLRADV – Modified to support calculating the partials with respect to the model parameters for the one-panel and box-wing SRP models. The actual calculation of the partials are done within the force model subroutines below SOLRAD, but the values are transferred to the necessary common block by SLRADV. Also modified to calculate the partial derivatives with respect to position for the new SRP models.

The software design tree for the GTDS Cowell theory differential correction is shown in Figure 6-6:

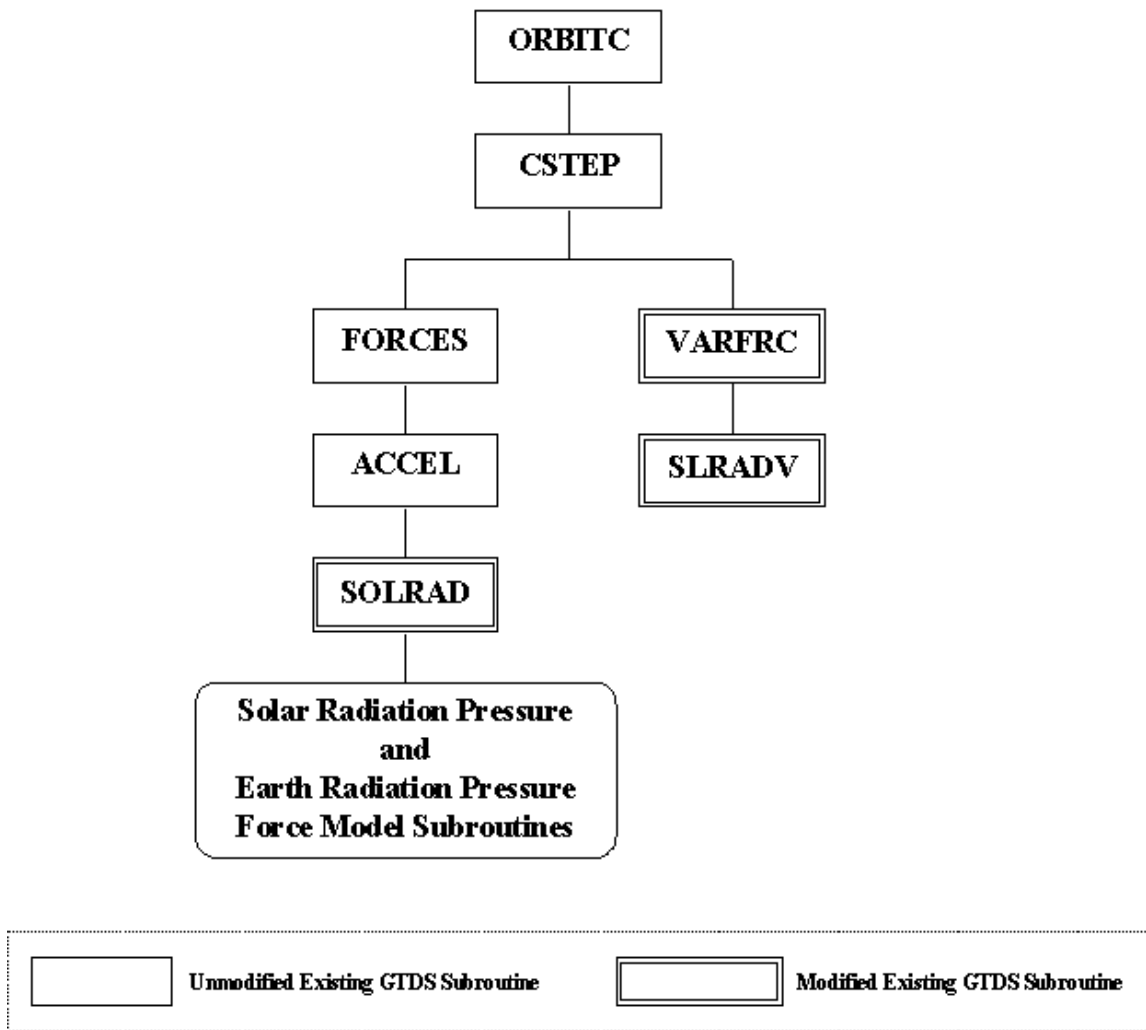


Figure 6-6 – Software Design Tree for GTDS Cowell Theory DC

6.5.2 Semi-analytical Satellite Theory (DSST) D.C. Implementation

For the Semi-analytical Satellite Theory, the partial derivatives with respect to the model parameters can be calculated in several ways: via analytical methods, via numerical quadrature, or via finite-differencing. For this study, as discussed in Chapter 4.3, the partial derivatives calculations were implemented via finite-differencing.

- VARDIF – Modified to support calculation of the one-panel and box-wing SRP reflectivity coefficients by finite differences.
- AVRAGE – Modified to support inclusion of the one-panel and box-wing SRP in the calculation of the element rate partials.

In order to facilitate SST DC, modifications had to be made in the one-panel and box-wing force model subroutines that are implemented below SOLRAD in the software. For the one-panel subroutines, these modifications dealt with the issue of having to use the chain rule to obtain the partial derivatives with respect to σ_a and σ . For the box-wing subroutines, these changes dealt with an issue that was a result of obtaining the partials via finite differencing. This process involved setting the reflectivity terms other than the parameter of interest in the macro-model equal to zero prior to performing the force model calculations. This resulted in an extra term in the $-s$ direction that had to be subtracted in the force model subroutines in order to implement the box-wing model DC correctly.

The software design tree for the GTDS SST differential correction is shown in Figure 6-7:

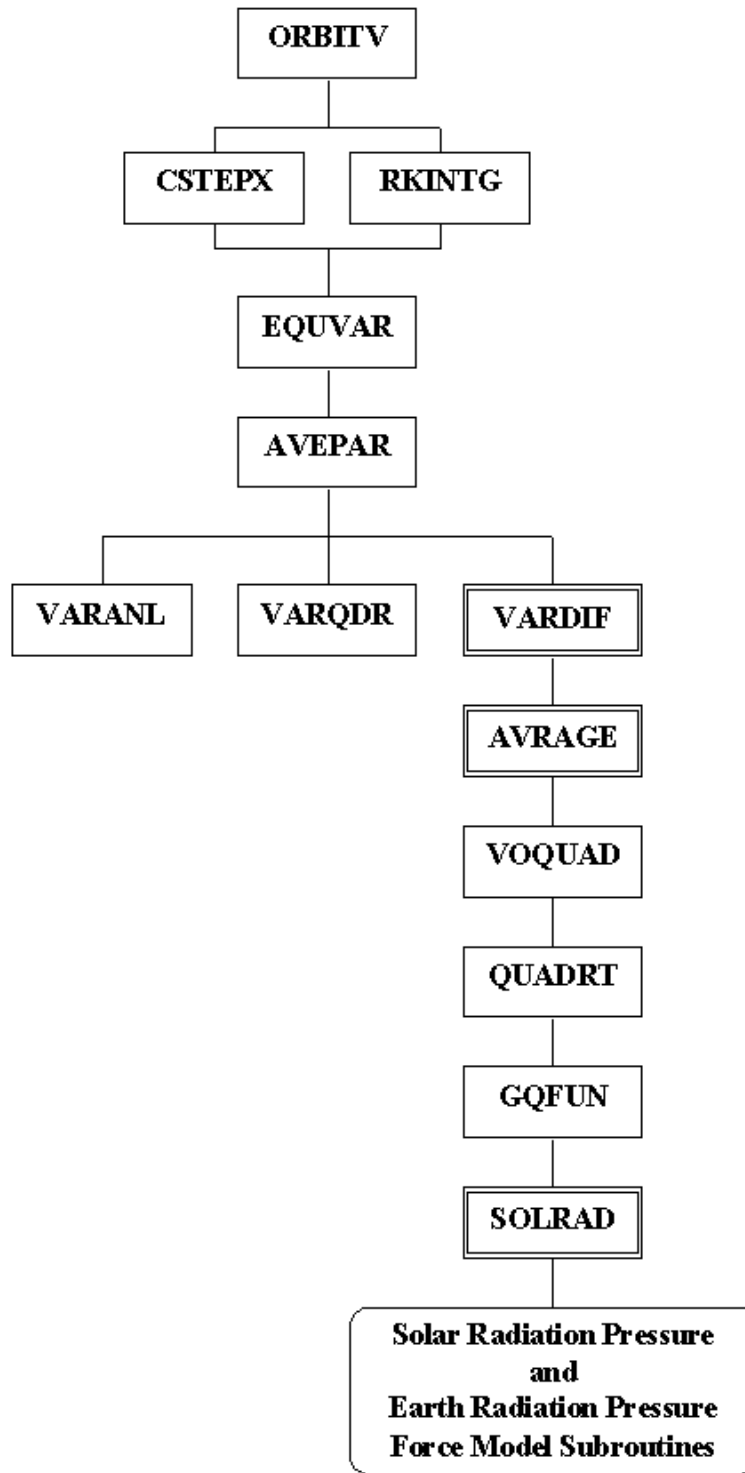


Figure 6-7 – Software Design Tree for GTDS Semi-analytical Satellite Theory DC

6.6 Kalman Filter Implementation

As part of this study, the box-wing model was interfaced with the Extended Semi-analytical Kalman Filter (ESKF) in GTDS. The only solve-for variable implemented at the present time is the single C_R that scales the box-wing model.

Many of the modifications made to GTDS to implement the DSST Differential Correction capability for the box-wing model carried over to the ESKF. These included the modifications to INTOGN and SOLTAB that set up the solve-for variables, as well as the modifications to VARDIF and AVRAGE that calculate the partial derivatives. Modifications were required in three additional GTDS subroutines to support ESKF implementation of the box-wing SRP model:

- COREST – Modified to apply the ESKF update to the box-wing solar radiation pressure model single C_R solve-for and covariance, and to display the correct values in the output file.
- KFUPDT – Modified to update the box-wing solar radiation pressure model single C_R solve-for and covariance, and to display the correct values in the output file.
- SETAPC – Modified to initialize the a priori covariance of the box-wing solar radiation pressure model single C_R solve-for.

It is noted that only the implementation of the box-wing model in the ESKF has been completed at this time. Implementation in the Extended Kalman Filter (EKF), which uses the Cowell theory, still needs to be completed and tested.

6.7 Implementation of the Space-Based Visible Observations Model

In the course of this study, the space-based visible (SBV) observations model was incorporated into R&D GTDS at MIT/Lincoln Laboratory. Dr. Paul Cefola and Mr. Zach Folcik completed the necessary software development and programming.

This section describes the modifications to GTDS that were completed to implement the SBV observations model. It also includes modifications that were completed to correctly implement observations corrections, including light-time corrections, ionospheric refraction corrections, and measurement bias estimation. This section is intended to serve as a reference for possible future implementation of any new space-based sensors, other observations models, or observations corrections. Mr. Zach Folcik graciously provided details on all of the software modification described in this section.

Several block data subroutines were modified to handle variables used by the new SBV observations model:

- EXPDTBD – Added block data elements for the SBV observation types (types 96 and 97)
- FILESD – Modified to include placeholders to process the SBV observations, including placeholders for the space -based observation file (unit 109) and for the space-based position/velocity working file (unit 110)
- DCFLBD – Added storage and equivalence statements for SBV DEC, RA and RHO values. These values allow communication between the subroutine that generate computed observations (OBSTRK) and the subroutine that computes partial derivatives (TRKPRT).

- DSPCONBD – Added DATA statements to populate elements 96 and 97 in arrays. These types help recognize the SBV RA and DEC obs types. This file is used in data simulation. Not all software to simulate space-based observations is implemented.
- SOROMCBD - Added DATA statements to initialize elements 96 and 97 with values like those used for elements 6 and 7. This modification was needed for the default weights for types 96 and 97 to be initialized.
- SWITCHBD – Added comments to explain element 210, which flags which obs model is being used. Also added comments and equivalence statements for items (228,229,230) for the PCE, equinoctial and SBV obs in switchbd.for
- ESTFLGBD – Added comments describing values for the IPCECS, IPCESR.

The existing GTDS subroutines that were modified to incorporate the SBV observations model are as follows:

- SETDM – Modified so that SBV observations are treated as tracking observations.
- OBSWF – Added the SBV observation file indicator, IND(230), in calculating ISUM. Otherwise, the SBV observations would not be used.
- OBS - Modernized code by replacing computed GOTO statement.
- DEFCON – Modified to recognize SBV types 96 and 97 in the ITAB array.
- OBSWT – Modified to handle converting the SBV observations to the sorted working files formatted as required by GTDS.
- OBSTRK – Modified to handle calculating the estimated (computed) SBV observations. Includes the necessary coordinate system conversions from

ECEF to J2000. Calls TRKPRT to calculate the SBV observation partial derivatives. Implemented the SBV light-time correction, which uses J2000 velocity vectors rather than Mean of 1950 velocity vectors. Also added a light time correction to Ground-based optical observations (MTYPES 6, 7, and 8).

- TRKPRT – Added SBV partial derivative functionality to OBSTRK.
- SETDAF – Modified to handle opening the SBV sensor working files. Also modified so that the general ionospheric coefficients file (unit 39) is opened.
- SETDC – Changed the processing of station card zero so that obs types greater than 30 can be processed. Obstat array initialized so that types 96 and 97 are given initial values like those used for types 6 and 7. The limit is now set to 97 to allow use of SBV types 96 and 97. Also modified so that sensor types 11-14 allow bias solves.
- INTDEP – Modified so that simulation of RA,DEC (6,7) obs will default to obs model 1 in IND(210) instead of 2.

Additionally, several new GTDS subroutines had to be created to support the new SBV observations model:

- SBV_RDNUMR – Parses the lines in the new SBV sensor observation file.
- SBV_OBSCRD – Driver for reading the lines from the new SBV sensor observation file.
- SBV_SORT_POS – Sorts the working file used to store the sensor position/velocity vectors.
- SBV_WRITE_POS – Writes records to the working file used to store the sensor position/velocity vectors.

- SBV_READ_POS – Reads the next unread position/velocity record in the space-based sensor position/velocity working file.

[This page intentionally left blank.]

Chapter 7 Simulated Data Results

7.1 Regression Test Results

Incorporation into GTDS of orbit generator functionality has been completed for the DSST Standalone spherical solar pressure model, single-panel solar pressure model, and the GEODYN “Box-wing” macro-model solar pressure model.

Regression testing compared the results from the unmodified version of GTDS to the updated version with the new DSST Standalone spherical model incorporated. 90-day orbit generator runs using the Cowell and Semi-analytical Satellite Theory methods were completed. The orbit used was a “sun-synchronous fixed line of apsides (SSFLA)” orbit that experienced large perturbations due to solar radiation pressure [Ref 78]. The initial osculating orbital elements used for the test are as follows:

Table 7-1 – Initial Orbital Elements for SSFLA Orbit [Ref 78]

Epoch	1 Jan 1997, Midnight (JD 2450449.50)
a	10559.271 km
e	0.345705
i	116.565 deg
ω	270 deg
Ω	280 deg
M	0 deg

The final orbit state vector at the end of the 90-day runs matched exactly, as shown in Table 7-2.

Table 7-2 – Regression Test Results for 90-day DSST Orbit Generator Run

Parameter (end of ephem)	Old GTDS UNIX Value	New GTDS UNIX Value	Δ Old GTDS-New GTDS
X-position	-2328.084487456706	-2328.084487456706	0
Y-position	2688.226161994930	2688.226161994930	0
Z-position	-6009.006408174945	-6009.006408174945	0
X-velocity	8.339152279658741	8.339152279658741	0
Y-velocity	2.068453489745137	2.068453489745137	0
Z-velocity	-1.595342740520495	-1.595342740520495	0

Another regression test of an orbit determination run using the Extended Semi-analytical Kalman Filter (ESKF) [Refs 7, 8] was also done, comparing the unmodified version of GTDS to the updated version with the new spherical model incorporated. The ESKF processed over 8600 observations of the Astra 1K satellite from 27 Nov 2002 through 10 Dec 2002. While in low-earth orbit during its brief lifetime, the Astra 1K satellite’s attitude control system caused a large translational force that was directionally equivalent to solar radiation pressure but three orders of magnitude larger. The results for the final orbital elements, shown in Table 7-3, demonstrate that the updated version is accurate, and also show the sensitivity of the Kalman filter to small changes in the software. We note that the Table 7-3 regression test involves only the orbit propagator, the partial derivatives of the mean element motion and the short periodics, and the estimation algorithms for the spherical solar radiation pressure model.

Table 7-3 – Regression Test Results for ESKF Processing Astra 1K Observations

Element	Old GTDS UNIX Value	New GTDS UNIX Value	Δ Old GTDS-New GTDS
a	6659.532379840033 km	6659.532379839991 km	4.3×10^{-11} km
e	0.1071606293023110	0.1071606293022074	1.036×10^{-13}
i	51.56564988892796 deg	51.56564988892874 deg	7.8×10^{-13} deg
ω	343.3695901693588 deg	343.3695901693569 deg	1.9×10^{-12} deg
Ω	341.0622495437568 deg	341.0622495434934 deg	2.634×10^{-10} deg
M	17.35240145303604 deg	17.35240145334066 deg	3.0462×10^{-10} deg

7.2 Macro-model Acceleration Profiles

In order to gain understanding of the behavior of the macro-models, acceleration profiles were generated. The orbit was propagated forward for one orbital revolution, which corresponds to a one-day time span for a geostationary spacecraft. The propagation was done using the Cowell numerical orbit generator with a 30-second step size. This was done for both the spherical spacecraft model as well as the macro-model. Acceleration profiles were generated to compare the TDRS and GOES macro-models to the spherical model, and were generated for both high and low beta prime angles (which correspond to the solstice and equinox, respectively). To test whether the macro-model was correctly incorporated from GEODYN into GTDS, the GTDS TDRS acceleration profiles were compared to the GEODYN TDRS acceleration profiles generated by Luthcke, et al. [Ref 36].

7.2.1 TDRSS Macro-model Acceleration Profiles

The acceleration profiles for the TDRS macro-model were generated at both $\beta' = 22.5$ degrees, and $\beta' = 0.0$ degrees. The results for the high beta prime case replicate the results obtained by Luthcke, et al. in their study of the TDRS macro-model [Ref 36, pp 360]. Figure 7-1 shows the macro-model acceleration profile for the high beta prime case generated using UNIX GTDS, and Figure 7-2 shows the macro-model acceleration profile generated by Luthcke, et al. using GEODYN. Figure 7-3 shows the macro-model vs. spherical model solar radiation acceleration difference profile generated using UNIX GTDS, and Figure 7-4 shows the macro-model vs. spherical model difference profile generated by Luthcke, et al. using GEODYN. The fact that the GTDS and GEODYN

acceleration profiles match quite well is an encouraging result in that it confirms that the macro-model has been correctly incorporated from GEODYN into GTDS.

The significant features of the TDRS macro-model acceleration profile for the high beta prime angle case are explained by Luthcke, et al.:

“The along-track and radial accelerations are the dominant components. Their variation about the orbit is dominated by the sun-to-spacecraft vector. Radial minimum and maximum accelerations occur at orbit angles of 90 deg and 270 deg respectively where the sun-to-spacecraft vector has no along-track projection. Similarly, along-track minimum and maximum accelerations occur respectively at orbit angles of 0 deg and 180 deg where there is no radial projection of the sun-to-spacecraft vector. The sun-to-spacecraft vector has a component in the direction opposite the orbit normal, and hence, a negative cross-track acceleration is observed which is nearly constant since the cross-track projection does not vary about the orbit.” [Ref 36, pp 360]

Luthcke, et al. also explain the differences between the TDRS macro-model and the cannonball representation of the spacecraft, which are visible in Figures 7-3 & 7-4:

“The small variations ... at 0 deg and 180 deg orbit angle are not seen with the cannonball representation ... They are caused by the changing spacecraft solar projected area as it travels around the orbit. This variation is dominated by the SAA plates. At 0 deg and 180 deg orbit angle the SAA plates are “edge-on” to the sun with their plate normals perpendicular to the sun-to-spacecraft vector, and do not contribute to the accelerations at these orbit locations. The combination of the diminishing SAA plate area and the decreasing SAA transmissivity, as the

spacecraft approaches 0 deg and 180 deg orbit angle, governs these acceleration features ... the cannonball model overestimates the cross-track acceleration and underestimates the radial contribution. This is because the cannonball does not properly model the spacecraft geometry and must utilize the mean spacecraft area and reflectivity giving rise to this “trade-off” in components.” [Ref 36, pp 361]

**TDRS Macro-Model Solar Radiation Acceleration Profile
for 20 June 2003 0:00.00 UT to 21 June 2003 0:00.00 UT (Summer Solstice)**

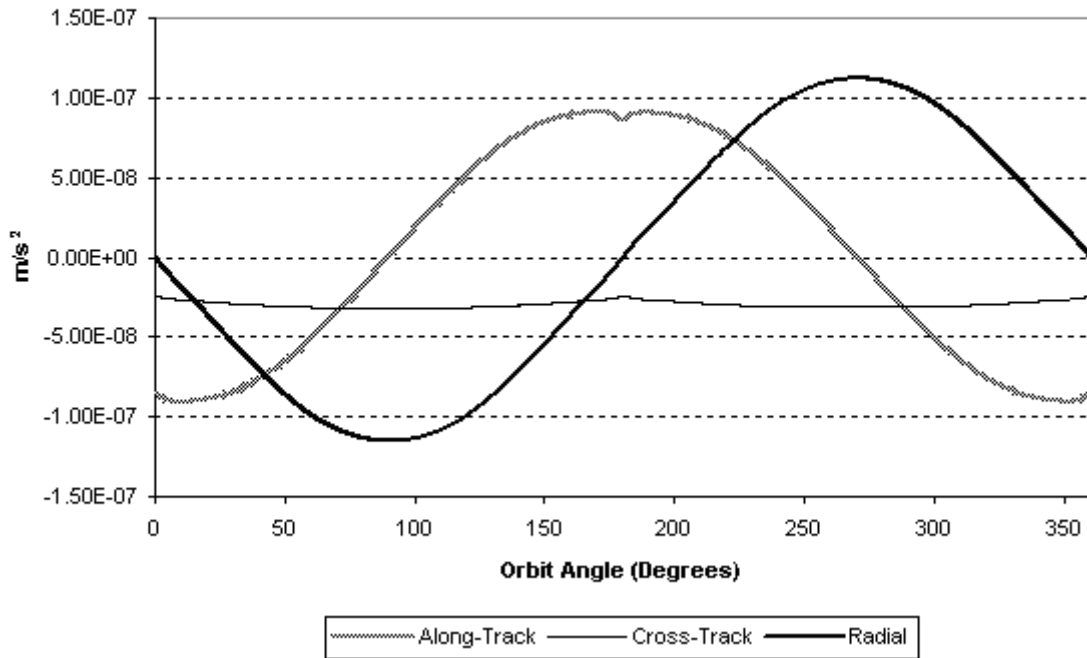
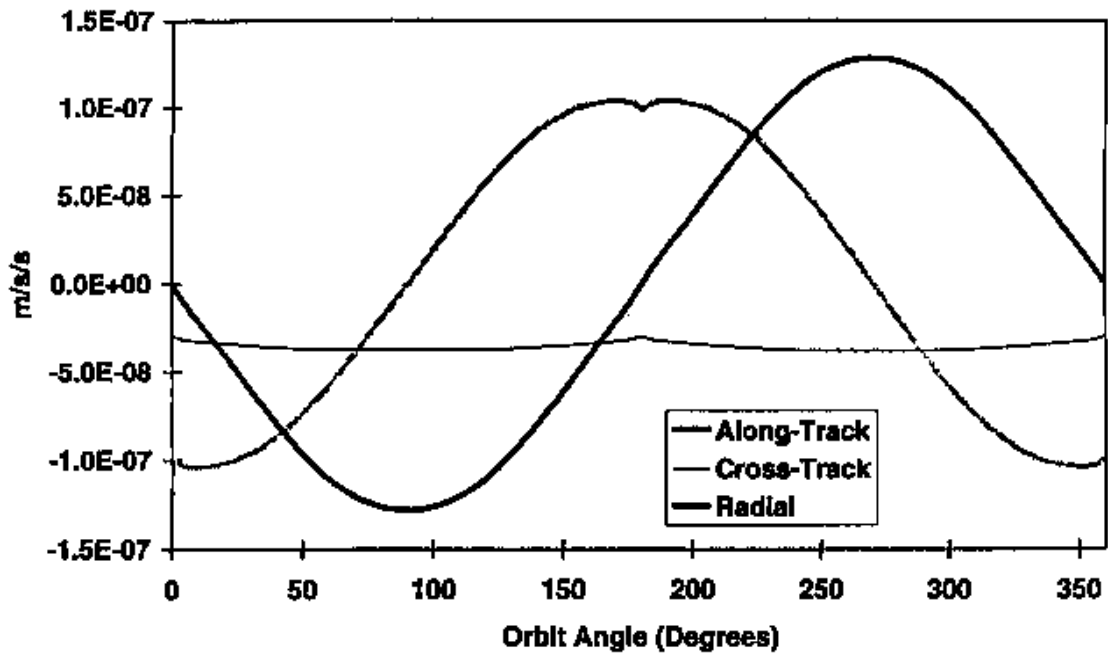


Figure 7-1 – UNIX GTDS TDRS Macro-model Solar Radiation Acceleration Profile at $\beta' = 22.5$



Source – Lutcke, et al.

Figure 7-2 – GEODYN TDRS Solar Radiation Acceleration Difference Profile at $\beta' = 23.4$

**TDRS Macro-Model - Spherical Solar Radiation Acceleration Difference Profile
for 20 June 2003 0:00.00 UT to 21 June 2003 0:00.00 UT (Summer Solstice)**

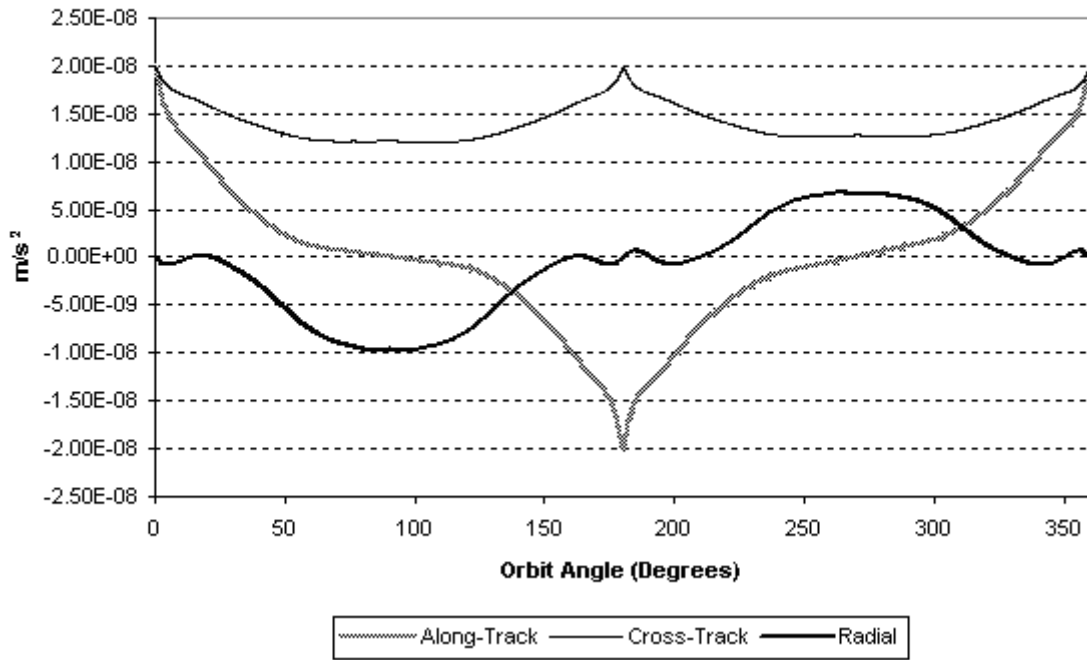
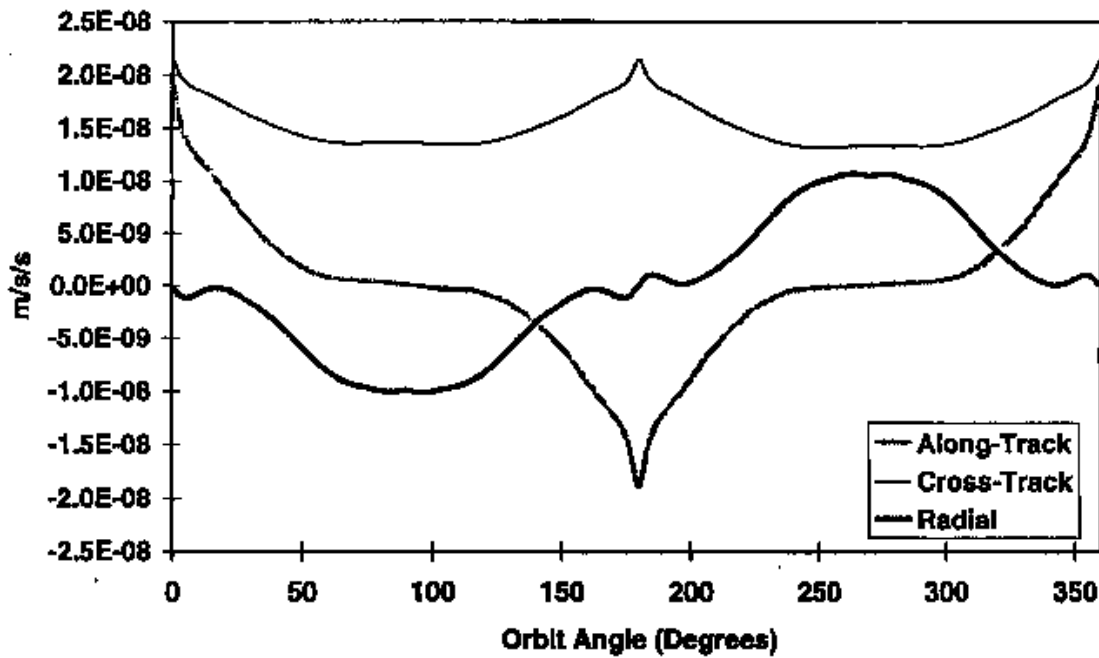


Figure 7-3 – UNIX GTDS TDRS Macro-model - Spherical Acceleration Diff. Profile at $\beta' = 22.5$



Source – Lutcke, et al.

Figure 7-4 – GEODYN TDRS Macro-model - Spherical Acceleration Difference Profile at $\beta' = 23.4$

Luthcke, et al. do not actually publish the GEODYN macro-model acceleration profiles for a low beta prime angle case [Ref 36]. They do explain in words the features they saw in low beta prime cases:

“At β' near 0° , the acceleration profiles remain nearly the same with only a few exceptions: (a) the radial and along-track accelerations slightly increase in amplitude while (b) the cross-track acceleration decreases to zero at $\beta' = 0$, and (c) occultation occurs below $|\beta'| = 8.7^\circ$.” [Ref 36, pp 360]

The same features noted by Luthcke, et al. are seen in the low beta prime angle acceleration profiles generated using UNIX GTDS. Figures 7-5 and 7-6 present the TDRSS macro-model acceleration profile and the macro-model vs. spherical acceleration difference profile, respectively, for the case of a zero-degree beta prime angle. The radial and along-track accelerations show increased amplitude compared to the high beta prime case, and the cross-track acceleration decreases to zero. The occultation (eclipse) is evident from approximately 260-280 degrees orbit angle, and appears as a discrete change to and from zero acceleration due to the use of a cylindrical shadow model in GTDS. These results lend further confidence that the macro-model was successfully implemented from GEODYN into GTDS.

TDRS Macro-Model Solar Radiation Acceleration Profile at $B' = 0.0$ deg

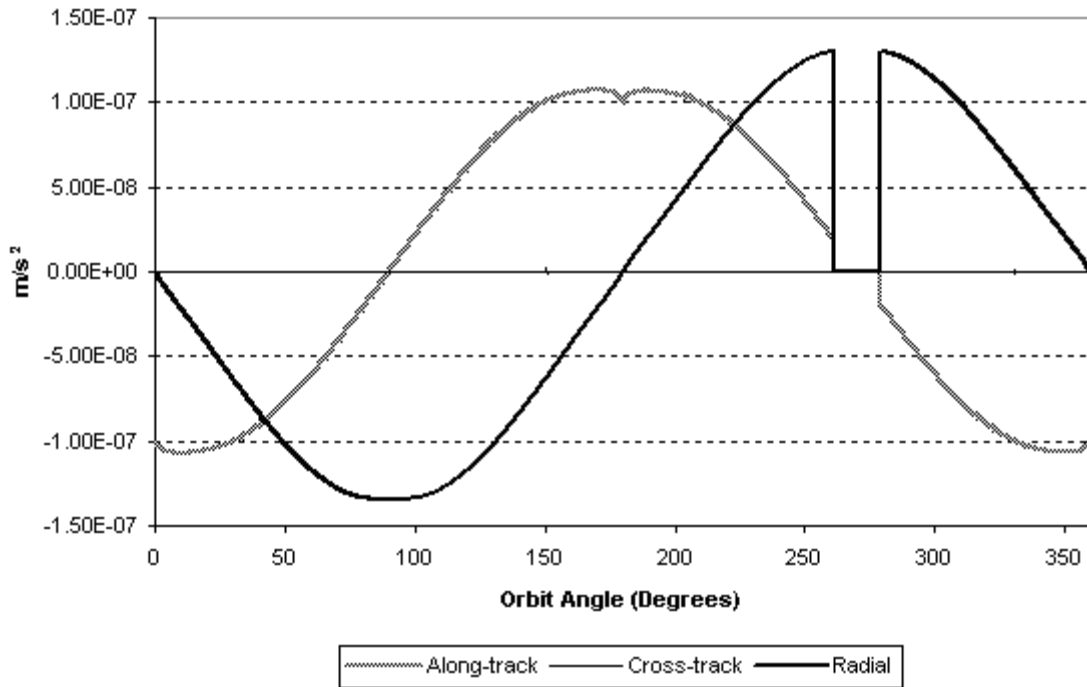


Figure 7-5 – UNIX GTDS TDRS Macro-model Solar Radiation Acceleration Profile for $\beta' = 0^\circ$

TDRS Macro-Model - Spherical Solar Radiation Acceleration Difference Profile at $B' = 0.0$ deg

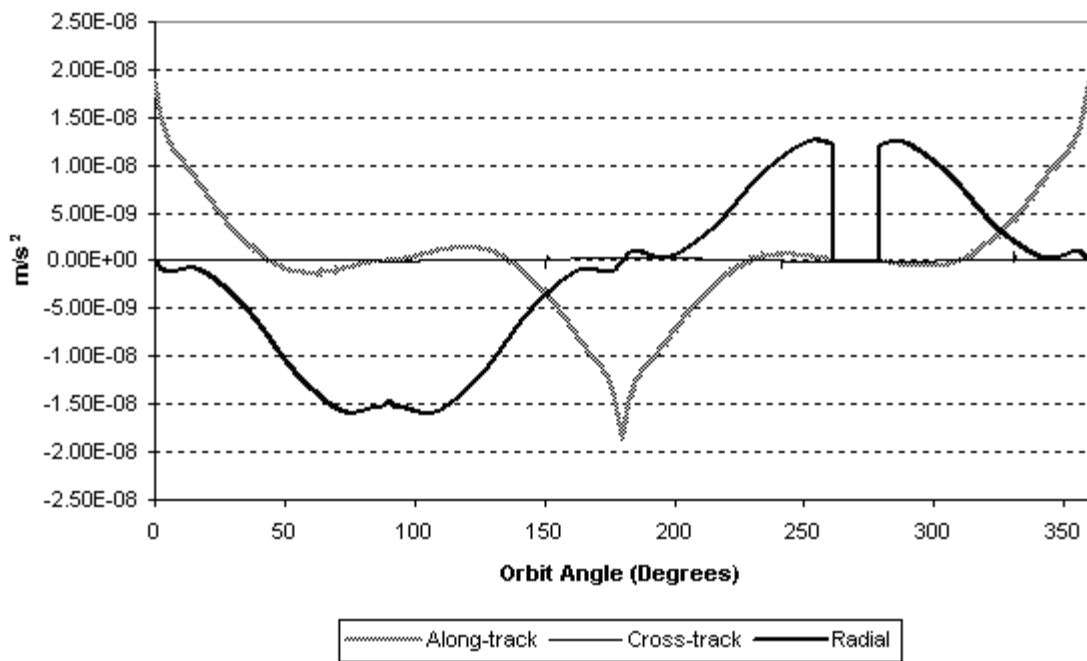


Figure 7-6 – UNIX GTDS TDRS Macro-model - Spherical Acceleration Difference Profile for $\beta' = 0^\circ$

7.2.2 GOES Macro-model Acceleration Profiles

Similarly to the TDRS case, the acceleration profiles for the GOES macro-model were generated at both $\beta' = 22.5$ degrees, and $\beta' = 0.0$ degrees. The GOES macro-model acceleration profile for the high β' case is shown in Figure 7-7. The macro-model vs. spherical model acceleration difference profile for the high β' case is shown in Figure 7-8.

The solar radiation acceleration profiles for the GOES spacecraft do not deviate from the spherical model acceleration profiles as significantly as the ones for the TDRS spacecraft. The reason the GOES spacecraft macro-model behaves similarly to the spherical model is that the GOES spacecraft maintains a more constant geometry projected toward the sun than the TDRS spacecraft. This is because the GOES spacecraft does not have any large nadir-pointing structures, whereas the TDRS spacecraft has the large single-access antennae. Instead, the large structures on the GOES spacecraft present a near-constant projected area to the sun. The solar sail is identical on all sides, and the solar array panels are sun-tracking. Thus, the magnitude of the along-track acceleration at 0 and 180 degrees orbit angle is nearly identical to the magnitude of the radial acceleration at 90 and 270 degrees orbit angle. As a result, the spherical spacecraft model is able to closely model the acceleration on the GOES spacecraft.

The spherical model does overestimate the cross-track acceleration at high beta prime angles. This is caused by the spherical model relying on an average cross-sectional area, as opposed to the true value represented by the macro-model.

**GOES Macro-Model Solar Radiation Acceleration Profile
for 20 June 2003 0:00.00 UT to 21 June 2003 0:00.00 UT (Summer Solstice)**

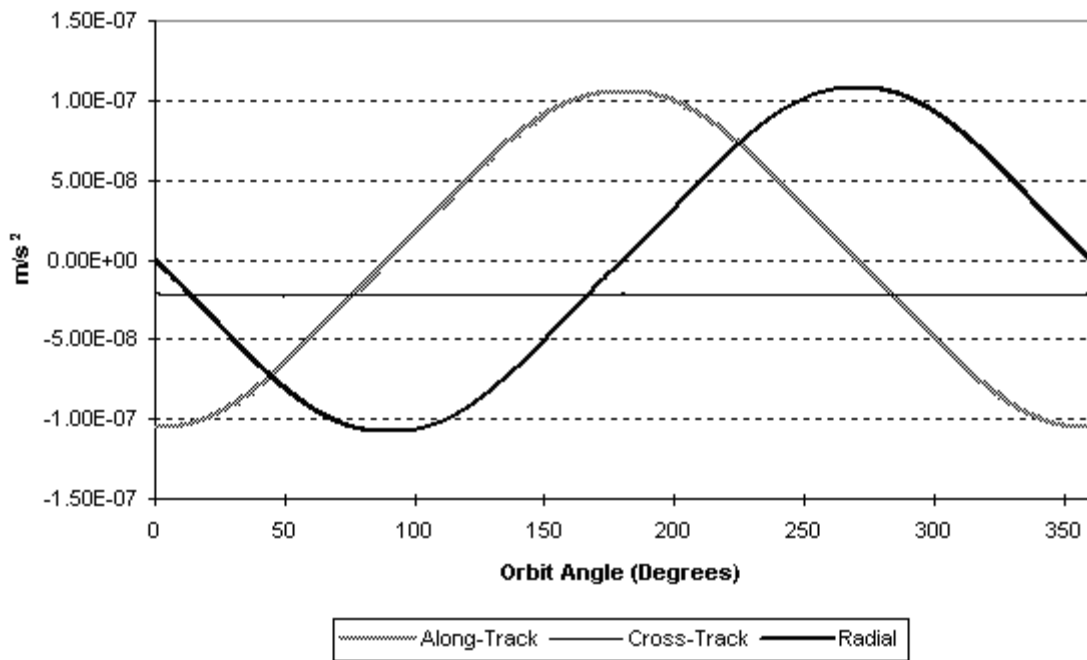


Figure 7-7 – UNIX GTDS GOES Macro-model Solar Radiation Acceleration Profile at $\beta' = 22.5^\circ$

**GOES Macro-Model - Spherical Solar Radiation Acceleration Difference Profile
for 20 June 2003 0:00.00 UT to 21 June 2003 0:00.00 UT (Summer Solstice)**

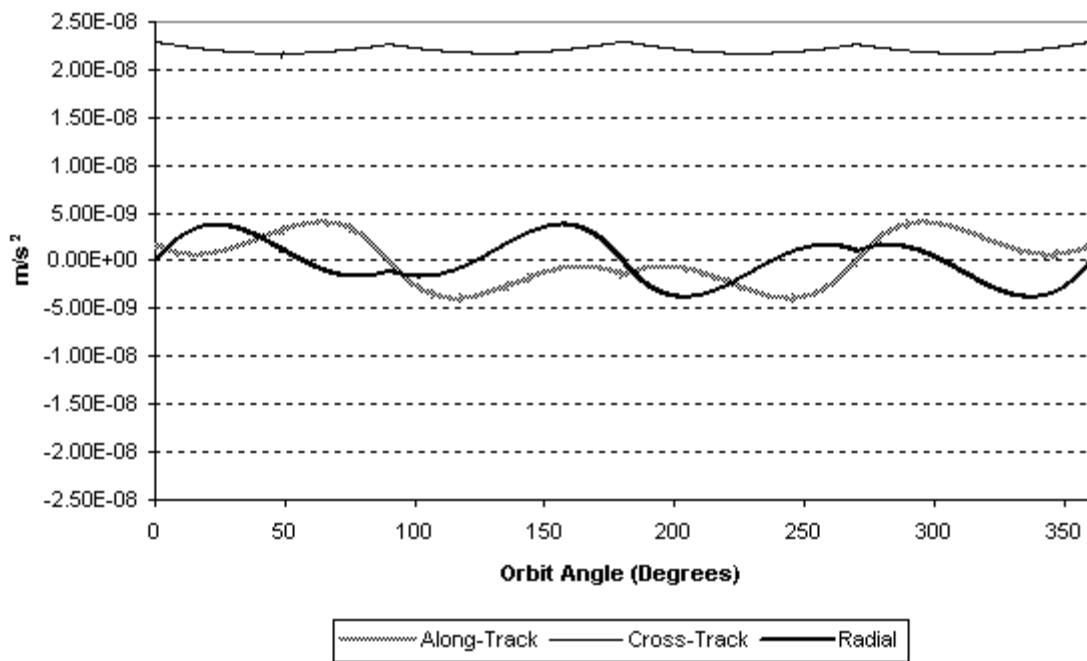


Figure 7-8 – UNIX GTDS GOES Macro-model-Spherical Acceleration Difference Profile at $\beta' = 22.5^\circ$

At low beta prime angles, the cross-track acceleration for the spherical model drops to zero, as expected, due to the fact that there is no cross-track projection of the spacecraft-to-sun vector. The GOES macro-model, on the other hand, exhibits a positive cross-track acceleration. This is caused by the trim tab at the end of the solar panel, which is made of a more highly-reflective material than the rest of the spacecraft. The orientation of the trim tab surface normal vector, due to offset angle between the trim tab and the solar array panels, causes a component of the acceleration on the trim tab to occur in the cross-track direction. This feature is visible in Figures 7-9 and 7-10. Just as with the TDRS macro-model test case, the occultation (eclipse) is evident from approximately 260-280 degrees orbit angle, and appears as a discrete change to and from zero acceleration due to the use of a cylindrical shadow model in GTDS

GOES Macro-Model Solar Radiation Acceleration Profile for $B'=0.0$ deg

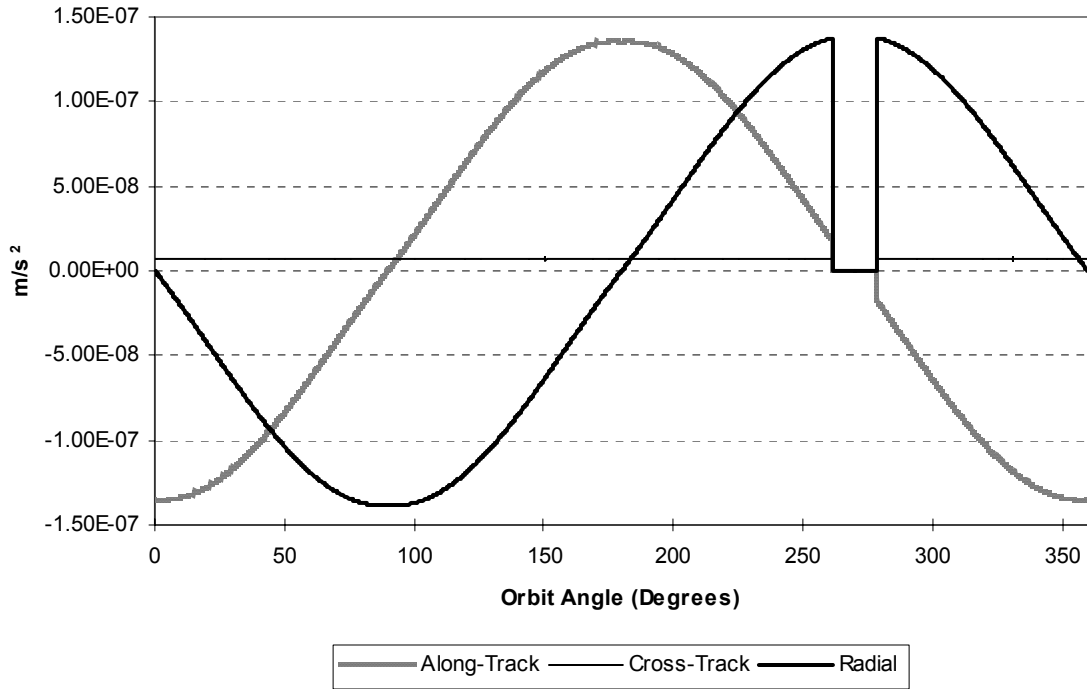


Figure 7-9 – UNIX GTDS GOES Macro-model Solar Radiation Acceleration Profile for $\beta' = 0^\circ$

GOES Macro-Model - Spherical Solar Radiation Acceleration Difference Profile at $B' = 0.0$ deg

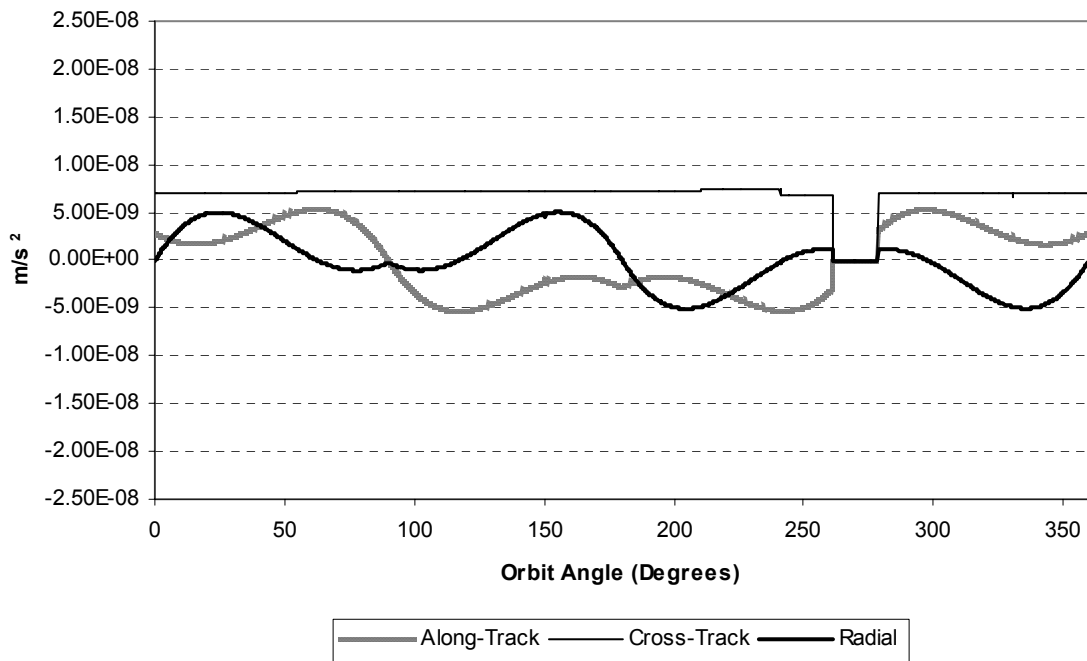


Figure 7-10 – UNIX GTDS GOES Macro-model-Spherical Acceleration Difference Profile for $\beta' = 0^\circ$

7.3 Short-periodic Orbital Element Behavior Testing

In order to further understand and visualize the difference between the different solar radiation pressure models, plots of the osculating Keplerian elements were generated over one orbital revolution. The orbit was propagated forward for one orbital revolution, which corresponds to a one-day time span for a geostationary spacecraft. The propagation was done using the Cowell numerical orbit generator with a 30-second step size. This was done for both the spherical spacecraft model as well as the TDRS macro-model, and was done at both the solstice and the equinox, to see if the time of year had any impact on the behavior of the orbital elements. The difference in the orbital elements between the macro-model case and the spherical model case were plotted.

The differences in the osculating Keplerian elements over one orbital revolution for the summer solstice case are shown in Figures 7-11 – 7-13. The differences are seen to be periodic for most elements, including semimajor axis, inclination, and right ascension of the ascending node. The differences in argument of perigee and true anomaly are seen to sum to zero, meaning that the position of the spacecraft within its orbit is the same for the macro-model and sphere. A secular trend in the difference in eccentricity is evident.

Another feature to note in the short-periodic orbital element plots is that the eclipse region of the orbit is evident in the plots of the difference between the box-wing and spherical models in the equinox case. In the eclipse region, there is zero acceleration on either model, which results in zero element rate difference between them. The eclipse thus shows up as a flat region centered around 0.75 day, which corresponds to the eclipse region seen in the earlier acceleration profiles centered around 270 degrees orbit angle.

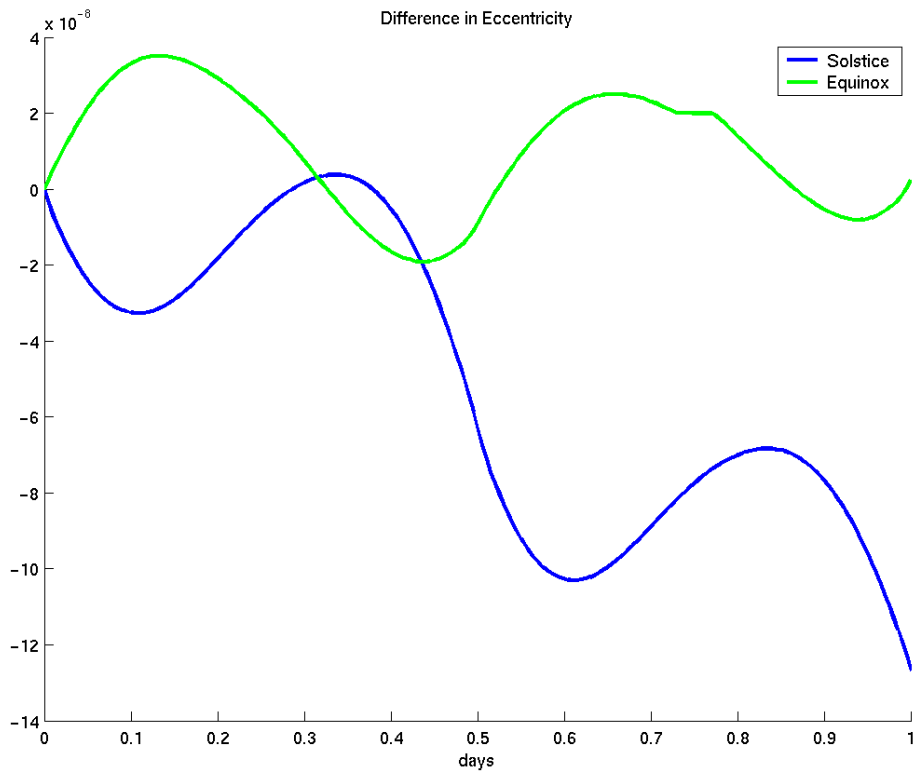
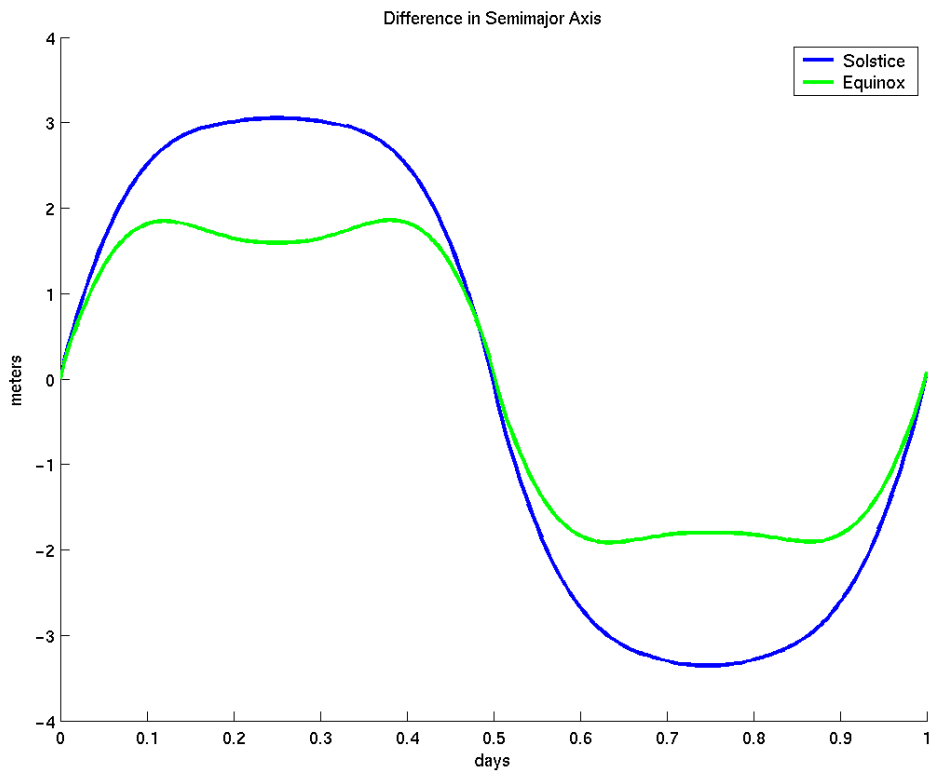


Figure 7-11 – Box-wing – Spherical Difference in a and e

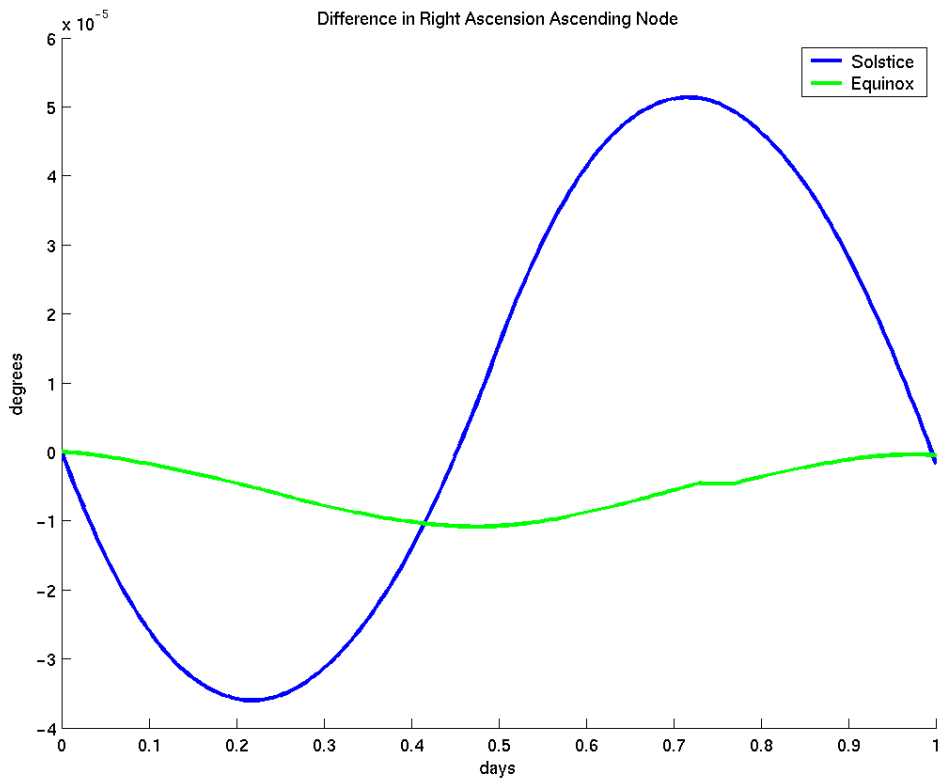
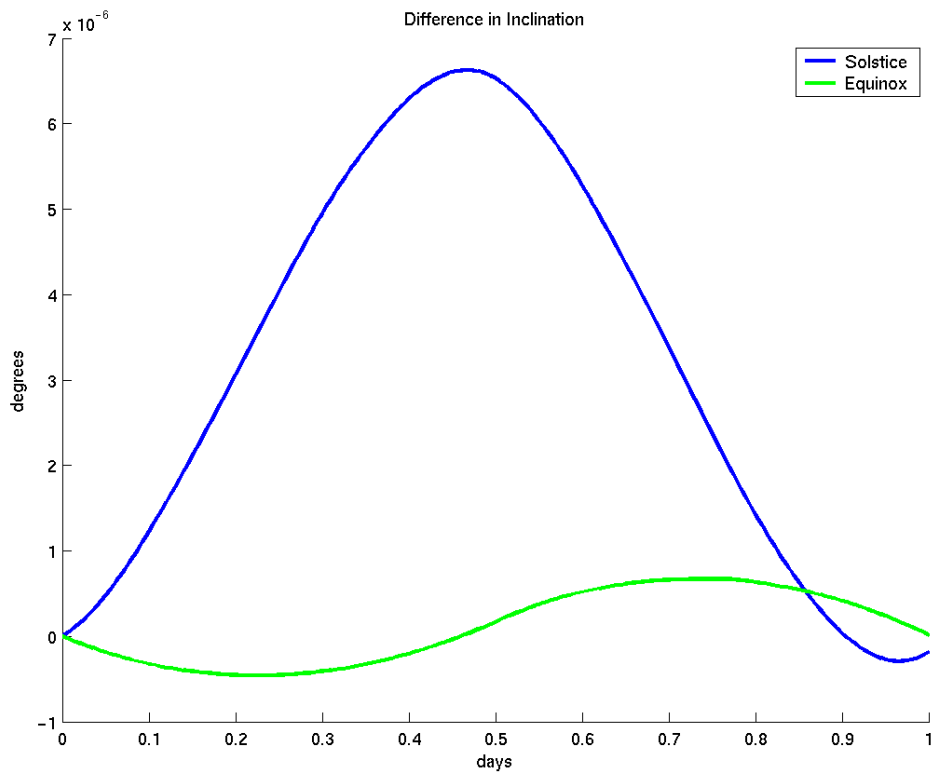


Figure 7-12 – Box-wing – Spherical Difference in i and Ω

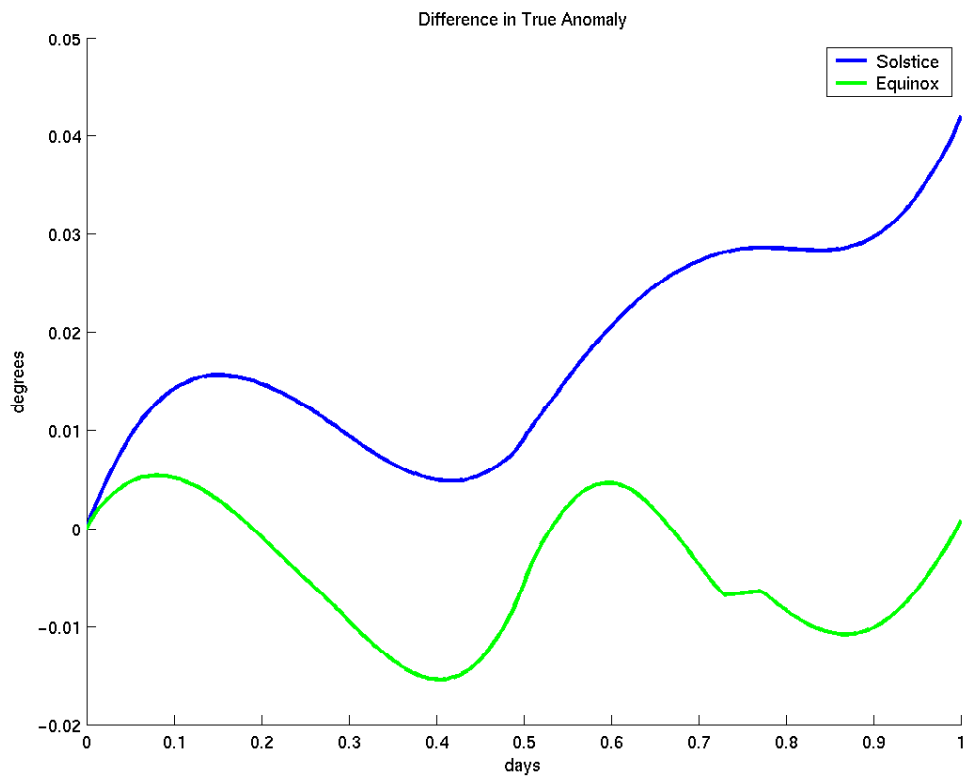
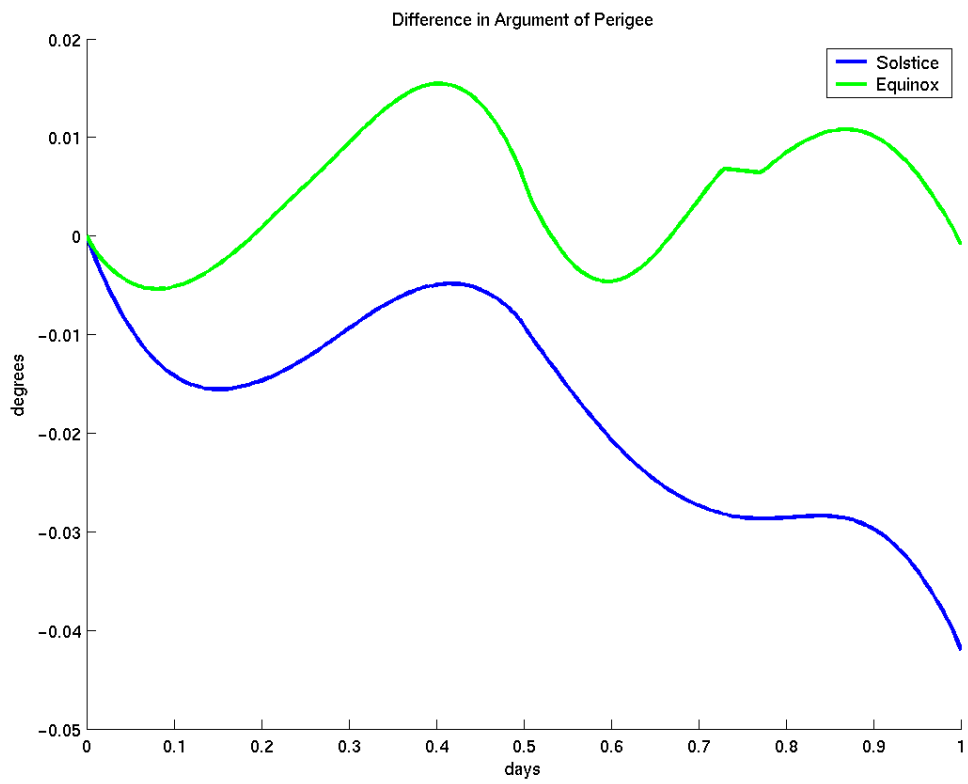


Figure 7-13 – Box-wing – Spherical Difference in ω and v

A complete set of plots, including the actual values of the elements over one orbital revolution, as well as individual plots of the element differences for the solstice and equinox cases, can be found in Appendix A of this thesis.

7.4 Mean Element Evolution Testing

Testing was done to assess the impact of the improved radiative force models on the long-term evolution of orbits. UNIX GTDS has a unique capability in this area due to the precision mean element propagator available via the Semi-analytical Satellite Theory. To take advantage of this unique capability, mean element propagation runs using SST were completed. These runs were done beginning at both the solstice and equinox, and compared the macro-model with an “equivalent” spherical model.

In order to determine the C_R for the “equivalent” spherical model, Cowell PCE runs were completed. The truth orbit was generated using the macro-model. A Differential Correction using the spherical model was then completed, with the orbit state and C_R as the solve-for parameters. The C_R from the converged orbit was taken to be the one corresponding to an “equivalent” spherical model.

7.4.1 One-year Mean Element Propagation Runs

One-year mean element propagation runs were completed using SST. These runs began on each equinox (vernal and autumnal) and solstice (summer and winter) in 2003, and ran until to the corresponding day in 2004, for a total of four propagation runs. The intent of these runs was to examine the long-term impact of the macro-model on the mean element evolution, and to see if that impact is dependent on the time of year.

The one-year runs do not exhibit any notable impact from the macro-model on semimajor axis, p , q , or λ . Differences in h and k are evident in the one-year propagation. The differences appear to be roughly periodic, with a period of approximately one year. This makes sense, as the solar radiation pressure perturbation to h and k is similar to the solar radiation pressure on eccentricity, which is roughly one year periodic.

The largest difference in the mean element rates for k appears in the time periods around the summer and winter solstices. During the time periods near the vernal and autumnal equinoxes, the mean element rates for k appear to be roughly the same between the macro-model and spherical model.

Appendix A of this thesis presents the complete set of plots of the mean-element propagation runs.

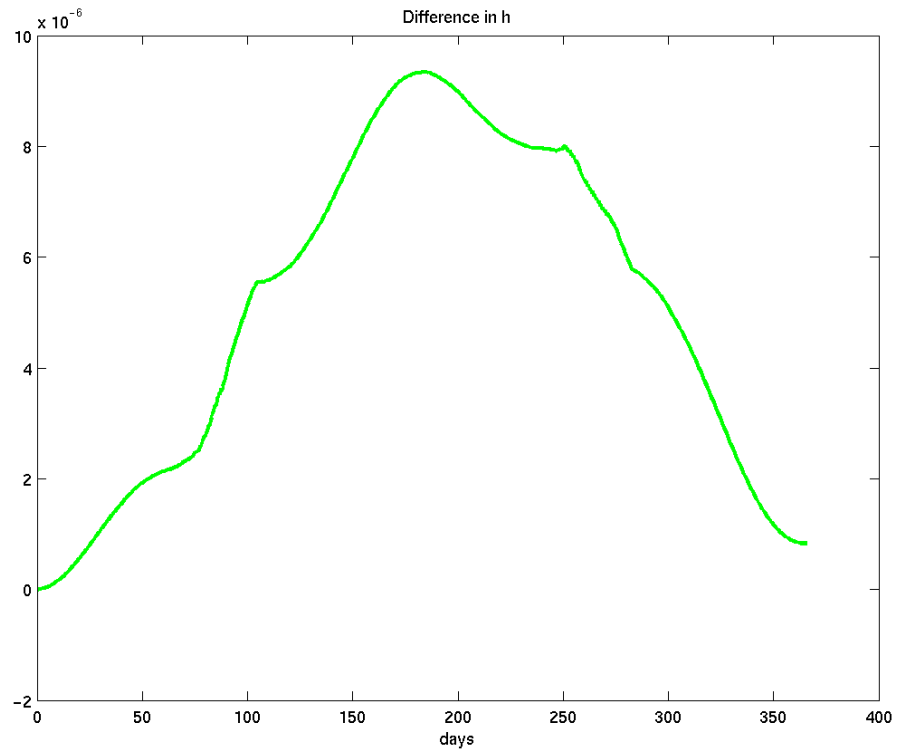


Figure 7-14 – Box-wing – Spherical Difference in h (Jun 03 – Jun 04 Case)

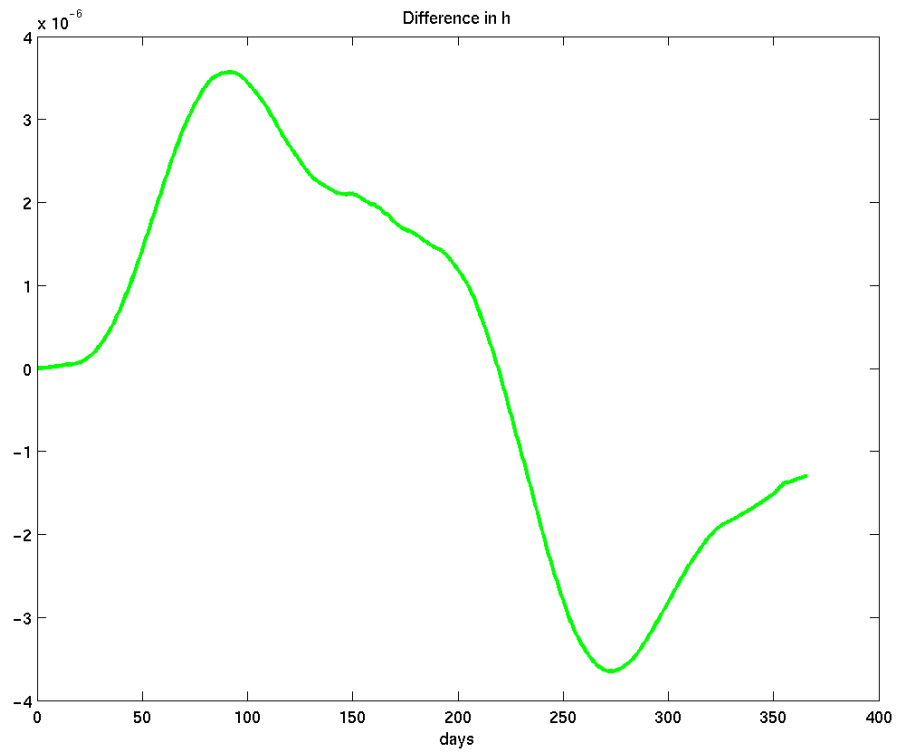


Figure 7-15 – Box-wing – Spherical Difference in h (Sep 03 – Sep 04 Case)

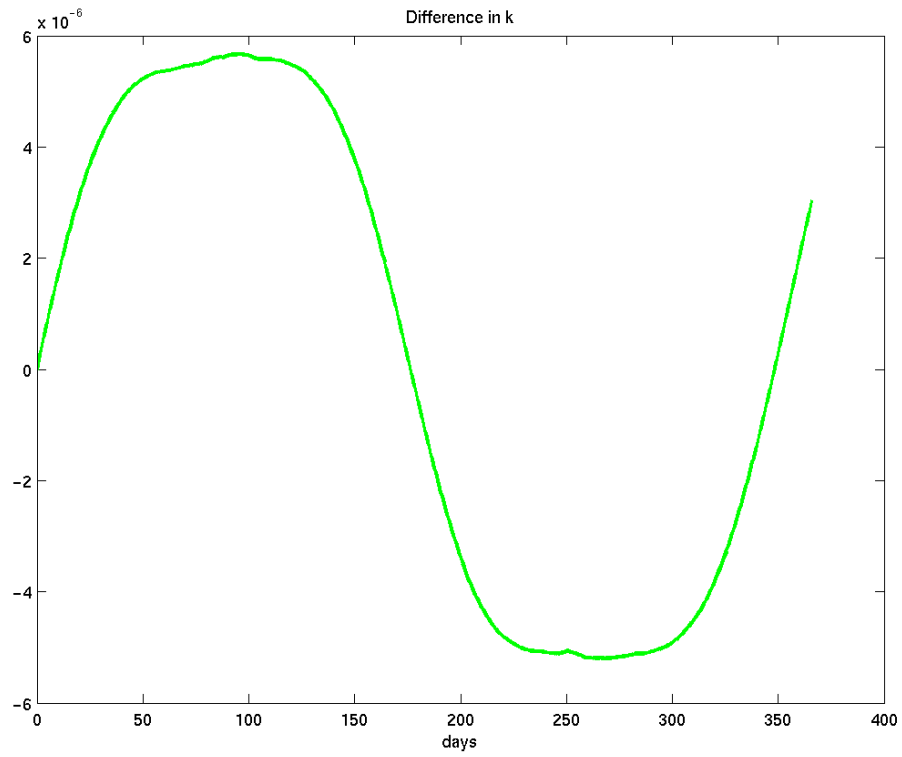


Figure 7-16 – Box-wing – Spherical Difference in k (Jun 03 – Jun 04 Case)

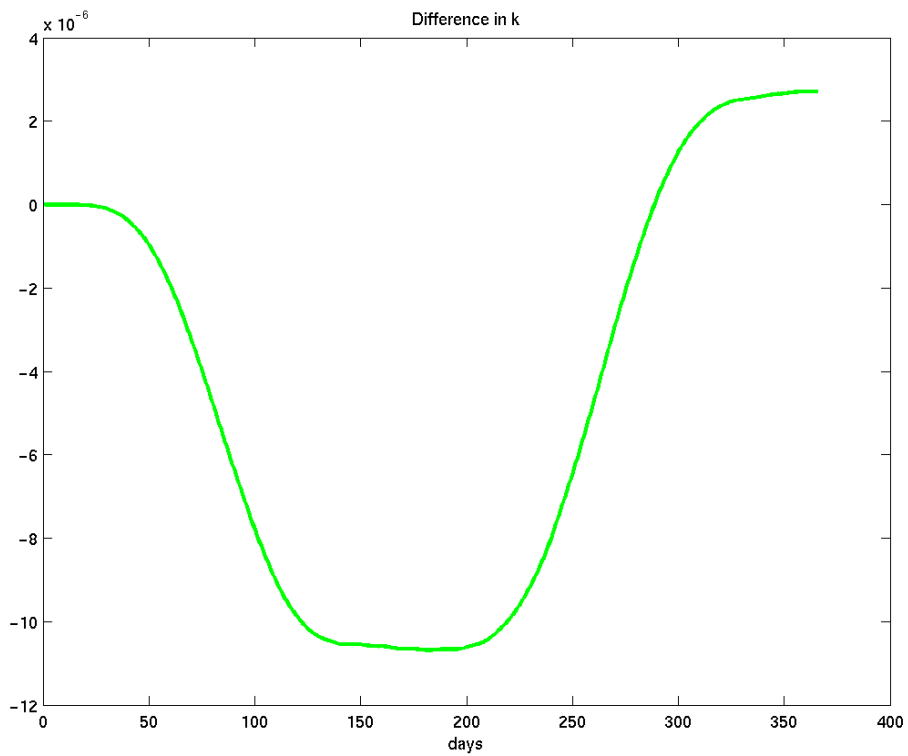


Figure 7-17 – Box-wing – Spherical Difference in k (Sep 03 – Sep 04 Case)

7.4.2 Short-periodic Coefficient Testing

The solar radiation pressure short-periodic coefficients of the sine and cosine terms in the Fourier series expansion were generated using GTDS. The purpose of this testing was to examine the difference between the short periodic coefficients for the macro-model and the short periodic coefficients for the spherical model.

7.5 Single Panel Default Reflectivity Test Results

Testing was also done comparing the single-panel and box-wing models to the spherical model. These tests attempted to replicate the spherical model with the single-panel model as well as the single-panel case of the box-wing model, to determine default values for the pointing offsets and reflectivity values in both models. The default values for the pointing offsets, as expected, turned out to be 0.0 deg, meaning that the surface normal vector of the panel points along the solar incidence vector. The value for the spherical model radiation pressure coefficient, C_R , is 1.2. The values of specular reflectivity (ρ) and diffuse reflectivity (δ) for a single-panel case of the box-wing model that correspond to this C_R are 0.2 and 0.0, respectively. These reflectivity values, expressed using the DSST Standalone one-panel model accommodation coefficient notation, correspond to a percent of radiation absorbed (σ_a) of 0.8, and a percent of reflected radiation diffusely reflected (σ) of 0.0. These results are summarized in Table 7-4.

Table 7-4 – Single Plate Model Default Values (To Replicate Spherical $C_R = 1.2$)

DSST Standalone Single-Panel Model Coefficients	Percent of radiation absorbed, σ_a	0.8
	Percent of reflected radiation diffusely reflected, σ	0.0
Box-wing Model (Single-Panel Case) Reflectivity Coefficients	Specular reflectivity, ρ	0.2
	Diffuse reflectivity, δ	0.0

90-day orbit generator runs using the Cowell and Semi-analytical Satellite Theory methods were completed with both the spherical model and the one-panel model with these defaults, and the results matched exactly. Additionally, the box-wing model was configured to have one panel and to use these default pointing offsets and reflectivity values. As expected, results matched exactly. These orbit generator tests were completed using the SSFLA orbit, which is the sun-synchronous orbit described in Chapter 7-1, as well as using a typical geostationary orbit. The intent was to test different orbit types to which the improved solar radiation pressure models might be applied. These tests demonstrate successful implementation of the orbit propagation functionality using the improved force models.

7.6 Differential Correction Test Results

Incorporation of Differential Correction functionality into GTDS was tested for the DSST Standalone spherical solar pressure model, one-panel solar pressure model, and the GEODYN box-wing model solar pressure model.

For the Semi-analytical Satellite Theory, regression testing was done to ensure that no errors were introduced into the orbit propagator. Results were identical to those discussed earlier for the force model incorporation. Next, GTDS was configured to calculate the partial derivatives of the mean element motion during orbit propagation runs using the various solar pressure models. For the Semi-analytical Satellite Theory, the state transition matrix, or \mathbf{B}_2 matrix, as well as the partial derivatives of the mean element motion with respect to the model parameters, or \mathbf{B}_3 matrix, were printed at each time step in the orbit propagation. The \mathbf{B}_2 matrix at each time step did not depend on which model was used. The \mathbf{B}_3 matrix, however, had a dependence on which model was used. When

the spherical solar pressure model was tested, the \mathbf{B}_3 matrix had one column, representing the partial derivatives of the mean element motion with respect to C_R . When the one-panel solar pressure model was tested, the \mathbf{B}_3 matrix consisted of two columns; these columns represented the partial derivatives of the mean element motion with respect to the two accommodation coefficients, percent of radiation absorbed (σ_a) and percent of reflected radiation diffusely reflected (σ). The box-wing model configured with a single panel had similar results to the one-panel model, with the two columns of the \mathbf{B}_3 matrix representing the partial derivatives of the mean element motion with respect to the diffuse and specular reflectivities. When the box-wing model was tested with more than one panel, the \mathbf{B}_3 matrix consisted of a number of columns equal to the total number of model parameters being solved for. For example, if the box-wing model was configured to have two plates, the \mathbf{B}_3 matrix resulted with four columns.

7.6.1 PCE Runs

The next series of test cases tested the Differential Correction functionality for the three solar pressure models via Precise Conversion of Elements (PCE) runs. First, a 90-day SST mean element orbit propagation run with a one-day time step using the spherical solar pressure model with a C_R of 1.2 was completed, and configured to generate a file of “truth” observation values (position and velocity) for the orbit. Next, a Semi-analytical Satellite Theory Differential Correction run was completed using the spherical solar pressure model, with a perturbed a priori C_R equal to 1.5. Differential Correction runs were completed with the DSST Standalone one-panel model and the box-wing model, configured to replicate the spherical test case. The a priori model parameters were perturbed to correspond to an a priori C_R equal to 1.5.

The DSST PCE runs were completed using both the SSFLA orbit and a typical GEO orbit. For both orbit types, both the single-panel model and box-wing model produced almost identical results to the spherical model. The results from the Semi-analytical Satellite Theory DC runs using the different solar pressure models are summarized in Tables 7-5 and 7-6.

Table 7-5 – DSST Differential Correction Run Results (SSFLA Orbit Case)

DSST DC Test Case	Solar Pressure Model	A Priori Model Parameters	# of Iterations	Final Model Parameters	Final Model Parameter Standard Deviation	Final RMS Position Error (m)
1	Spherical	$C_R = 1.5$	8	$C_R = 1.2$	$\sigma_{C_R} = 0.720D-09$	1.45990098E-03
2	One-panel	$\sigma_a = 0.5$ $\sigma = 0.0$	8	$\sigma_a = 0.8$ $\sigma = 0.0$	$\sigma_{\sigma_a} = 0.720D-09$	1.46159469E-03
3	Box-wing	$\rho = 0.5$ $\delta = 0.0$	8	$\rho = 0.2$ $\delta = 0.0$	$\sigma_\rho = 0.720D-09$	1.46037247E-03

Table 7-6 – DSST Differential Correction Run Results (GEO Orbit Case)

DSST DC Test Case	Solar Pressure Model	A Priori Model Parameters	# of Iterations	Final Model Parameters	Final Model Parameter Standard Deviation	Final RMS Position Error (m)
1	Spherical	$C_R = 1.5$	9	$C_R = 1.2$	$\sigma_{C_R} = 0.365D-07$	4.91247317E-04
2	One-panel	$\sigma_a = 0.5$ $\sigma = 0.0$	9	$\sigma_a = 0.8$ $\sigma = 0.0$	$\sigma_{\sigma_a} = 0.365D-07$	4.91266476E-04
3	Box-wing	$\rho = 0.5$ $\delta = 0.0$	9	$\rho = 0.2$ $\delta = 0.0$	$\sigma_\rho = 0.365D-07$	4.91247643E-04

The same PCE runs were completed using the Cowell Theory. A 30-day Cowell orbit propagation run was completed using the spherical solar pressure model with a C_R of 1.2, and configured to generate the file of “truth” observation values (position and velocity) for the orbit. Next, a Cowell Theory Differential Correction run was completed using the spherical solar pressure model, with a perturbed a priori C_R equal to 1.5. Differential Correction runs were also completed with the DSST Standalone one-panel model and the box-wing model, configured to replicate the spherical test case. The a priori model parameters were perturbed to correspond to an a priori C_R equal to 1.5.

The Cowell PCE runs were completed with both the SSFLA orbit (using a 30-sec integration time step) and a typical GEO orbit (using a 300-sec integration time step). The results from the Cowell Theory DC runs using the different solar pressure models are summarized in Tables 7-7 and 7-8.

For both orbit types, the box-wing model DC converged in the same number of iterations as the spherical model, although the one-panel model DC converged in 11 iterations. It is possible that this difference is due to using the chain rule to calculate the model parameter partial derivatives for the one-panel model.

Additionally, the final RMS position error and parameter standard deviation statistics for both of the improved force models exhibit greater differences from the spherical model statistics in the Cowell DC runs as compared to the DSST DC runs. As expected, the Cowell DC runs required greater computing time compared to the DSST DC runs.

Table 7-7 – Cowell Differential Correction Run Results (SSFLA Orbit Case)

Cowell DC Test Case	Solar Pressure Model	A Priori Model Parameters	# of Iterations	Final Model Parameters	Final Model Parameter Standard Deviation	Final RMS Position Error (m)
1	Spherical	$C_R = 1.5$	7	$C_R = 1.2$	$\sigma_{C_R} = 0.336D-09$	6.34365238E-05
2	One-panel	$\sigma_a = 0.5$ $\sigma = 0.0$	11	$\sigma_a = 0.8$ $\sigma = 0.0$	$\sigma_{\sigma_a} = 0.212D-08$	4.84871301E-04
3	Box-wing	$\rho = 0.5$ $\delta = 0.0$	7	$\rho = 0.2$ $\delta = 0.0$	$\sigma_\rho = 0.943D-09$	1.78499285E-04

Table 7-8 – Cowell Differential Correction Run Results (GEO Orbit Case)

Cowell DC Test Case	Solar Pressure Model	A Priori Model Parameters	# of Iterations	Final Model Parameters	Final Model Parameter Standard Deviation	Final RMS Position Error (m)
1	Spherical	$C_R = 1.5$	5	$C_R = 1.2$	$\sigma_{C_R} = 0.120D-09$	9.46556772E-06
2	One-panel	$\sigma_a = 0.5$ $\sigma = 0.0$	11	$\sigma_a = 0.8$ $\sigma = 0.0$	$\sigma_{\sigma_a} = 0.252D-09$	2.37647944E-05
3	Box-wing	$\rho = 0.5$ $\delta = 0.0$	5	$\rho = 0.2$ $\delta = 0.0$	$\sigma_\rho = 0.233D-09$	1.82885058E-05

7.6.2 DATASIM Runs

The next series of test cases exercised the DATASIM functionality of GTDS with the improved solar radiation pressure models. First, a 20-day Cowell orbit propagation run was completed with a 100-second time step and epoch at the solstice, using the spherical solar pressure model with a C_R of 1.2. Next, the GTDS DATASIM program was configured to generate a file of “truth” observation values for the orbit. The observations were from a simulated network of ground stations, including radar and optical observations, and were simulated every 15 minutes over the propagation span. The observations were simulated without measurement errors. Next, a Cowell Theory Differential Correction (DC) run was completed using the spherical solar pressure model, first with no perturbations to the epoch state, and then with a perturbed epoch semimajor axis and a perturbed a priori C_R equal to 1.5. In both cases, the DC converged to the correct parameters.

A similar DATASIM run was completed using the box-wing solar radiation pressure model. The setup for the DATASIM was the same, with observations simulated for a “network” of ground stations, both radar and optical. Again, no measurement errors were introduced in simulating the observations. A Cowell Theory Differential Correction run was then completed using the box-wing model, first with no perturbations to the

epoch state, and then with a perturbed epoch semimajor axis and a perturbed a priori single C_R equal to 1.5. In all cases, the DC converged to the correct parameters.

The test cases that exercised the DATASIM program gave confidence that the partial derivatives with respect to the single box-wing C_R were implemented correctly in the software. The test cases also showed that the assumption is valid of neglecting the partial derivative of the solar radiation pressure acceleration with respect to position in the \mathbf{A} matrix (see Chapters 4.2 and 4.6).

Example DATASIM input data files are given in Appendix D.3 of this thesis. DATASIM testing has not yet been exercised with the Semi-analytical DC. Additionally, it is expected that DATASIM testing could be very useful in testing both the Extended Kalman Filter (EKF) and Extended Semi-analytical Kalman Filter (ESKF) with the improved radiative force models in GTDS.

Chapter 8 Real Data Processing Results

This chapter includes the results of real data processing. The first group of test cases uses the TDRSS spacecraft macro-model. These include Differential Correction test cases that combine HANDS optical data with SSN data for the TDRS-05 spacecraft. There are also initial real data filter test cases applying the Extended Semi-analytical Kalman Filter (ESKF) to the TDRSS data, for both the HANDS optical data alone as well as the combined data set.

The second group of test cases uses the GOES spacecraft macro-model. These include Differential Correction test cases that combine owner/operator ranging data from NOAA with SSN data for the GOES-10 spacecraft. The ESKF is also applied in initial real data filter test cases to the GOES data, for both the NOAA ranging data alone as well as the combined data set.

8.1 TDRSS Test Cases

8.1.1 SSN with HANDS Optical Data

This set of test cases included SSN observation data as well as very dense, high accuracy optical observations from the High Accuracy Network Determination System (HANDS) telescope. Dr. Chris Sabol of AFRL/AMOS graciously provided these observations for this study. Sabol and his colleagues previously completed GEO orbit determination work, described in Chapter 1.2.3, using these high-accuracy observations and Ops GTDS [Ref 23].

The test cases used observations of the TDRS-05 spacecraft. The fit span used was approximately 10 days long, from 15 December 2003 through 25 December 2003. The fit span was thus roughly centered about the winter solstice.

The SSN observations that were processed included 12 pairs of SBV observations (right ascension and declination). The remainder of the SSN observations included 54 sets of Tradex radar observations (range, range-rate, azimuth, and elevation), and 142 pairs of optical observations (RA and DEC) from various other sensors.

The first set of test cases used only the SSN observations. These observations were processed with both the spherical solar radiation pressure model as well as the TDRS-05 macro-model. The differential correction runs estimated both the orbit state as well as the C_R . These runs were completed using both the Cowell theory and the DSST.

The results do not show a large difference between the performance of the spherical model and the performance of the macro-model. However, the final C_R for the macro-model is very close to 1.0. This is a good indicator that the macro-model for TDRS-05 is reasonably accurate, as it does not require much scaling. There is good consistency in the performance of the DSST as compared to the Cowell Theory. The test cases included SBV observations, and observations corrections and optical sensor biases were applied.

The next set of test cases included the HANDS observations in addition to the SSN observations. The observations that were processed included 1013 sets of optical observations from the HANDS sensor. These observations were originally taken as right ascension and declination pairs, but were pre-processed by Sabol to apply light-time corrections and to convert the observations to azimuth and elevation pairs.

Table 8-1 summarizes the results with the HANDS data included. The high-accuracy data results in significant improvement in the RMS position error for all test cases, as compared to the cases with only SSN data. These runs include SBV observations, observations corrections, and solve for optical sensor biases.

Table 8-1 – TDRS-5 Results, Processing SSN and HANDS Data (DC)

Orbit Generator	SRP Model	# iterations	% obs accepted	Final C_R	Semimajor Axis Std Deviation (cm)	Position Error RMS (m)
Cowell	Spherical	12	90%	1.379154622282465	17.1	221.40723
	Macro-model	12	90%	0.9945671844400008	16.9	219.26747
DSST	Spherical	10	86%	1.379348130513510	12.2	169.21624
	Macro-model	10	86%	0.9916612939523663	12.2	169.38348

The results still do not show a large difference between the performance of the macro-model and the spherical model. However, the RMS position error is quite small for a GEO orbit case, and is significantly improved over the results when only SSN observations were used. This is likely due to the high quality and high density of the HANDS optical data used in the fit. It is noted that most of the observations that were not accepted came from the other sensors. The final C_R for the macro-model is still very close to 1.0, which is a good indicator that the macro-model for TDRS-05 is reasonably accurate and does not require much scaling. An additional note about the results is that Cowell and DSST theories appear to perform comparably.

8.1.2 Kalman Filter Cases Processing TDRSS Data

This set of test cases involved applying the Extended Semi-analytical Kalman Filter (ESKF) [Refs 7, 8] to the HANDS optical data provided by Dr. Chris Sabol and his colleagues at AFRL/AMOS. The test cases used observations of the TDRS-05 spacecraft. The time span used was the same as for the earlier differential correction

cases – approximately 10 days long, from 15 December 2003 through 25 December 2003.

The ESKF was applied first using the spherical solar radiation pressure model, which was a previously-existing capability in GTDS. The mean equinoctial elements and spherical C_R were the solve-for parameters. A semi-analytical differential correction run was completed to obtain the a priori epoch mean elements and C_R for the ESKF.

The ESKF was then applied using the box-wing model for solar radiation pressure. The mean equinoctial elements and the single box-wing C_R were the solve-for parameters. Again, a semi-analytical differential correction run was completed to obtain the a priori epoch mean elements and C_R for the ESKF.

Figures 8-1 and 8-2 show the behavior of the mean elements over the time span using the spherical model, and Figures 8-3 and 8-4 show the behavior of the mean elements over the time span using box-wing model. The mean elements are seen to be well-behaved and smoothly-varying over the fit interval. The mean element motion exhibited in these plots is due to the natural perturbations: tesseral resonance for the semimajor axis, solar radiation pressure for the eccentricity, and lunar-solar point masses for the inclination. The behavior of the mean elements is nearly identical between the spherical and box-wing model.

Figures 8-5 and 8-6 show the azimuth and elevation residuals for the converted HANDS observations using the spherical and box-wing models, respectively. The azimuth residuals are centered about zero mean, with most residuals within ± 4 arcseconds. The elevation residuals are also centered about zero mean, with most

residuals between ± 2 arcseconds. The residuals are very similar between the spherical and box-wing model cases.

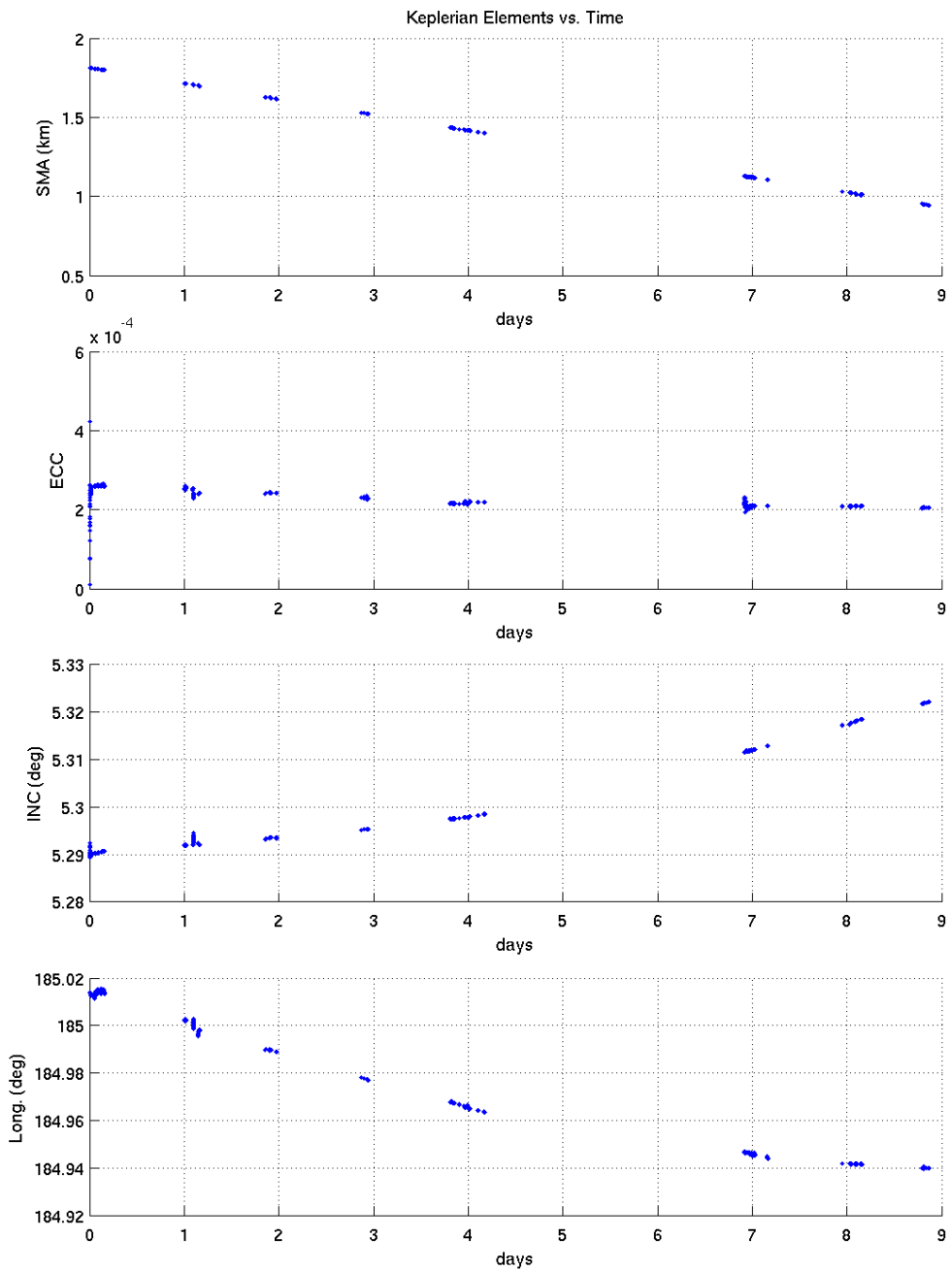


Figure 8-1 – Mean Keplerian Elements vs Time using Only HANDS Data with Spherical Model (ESKF)

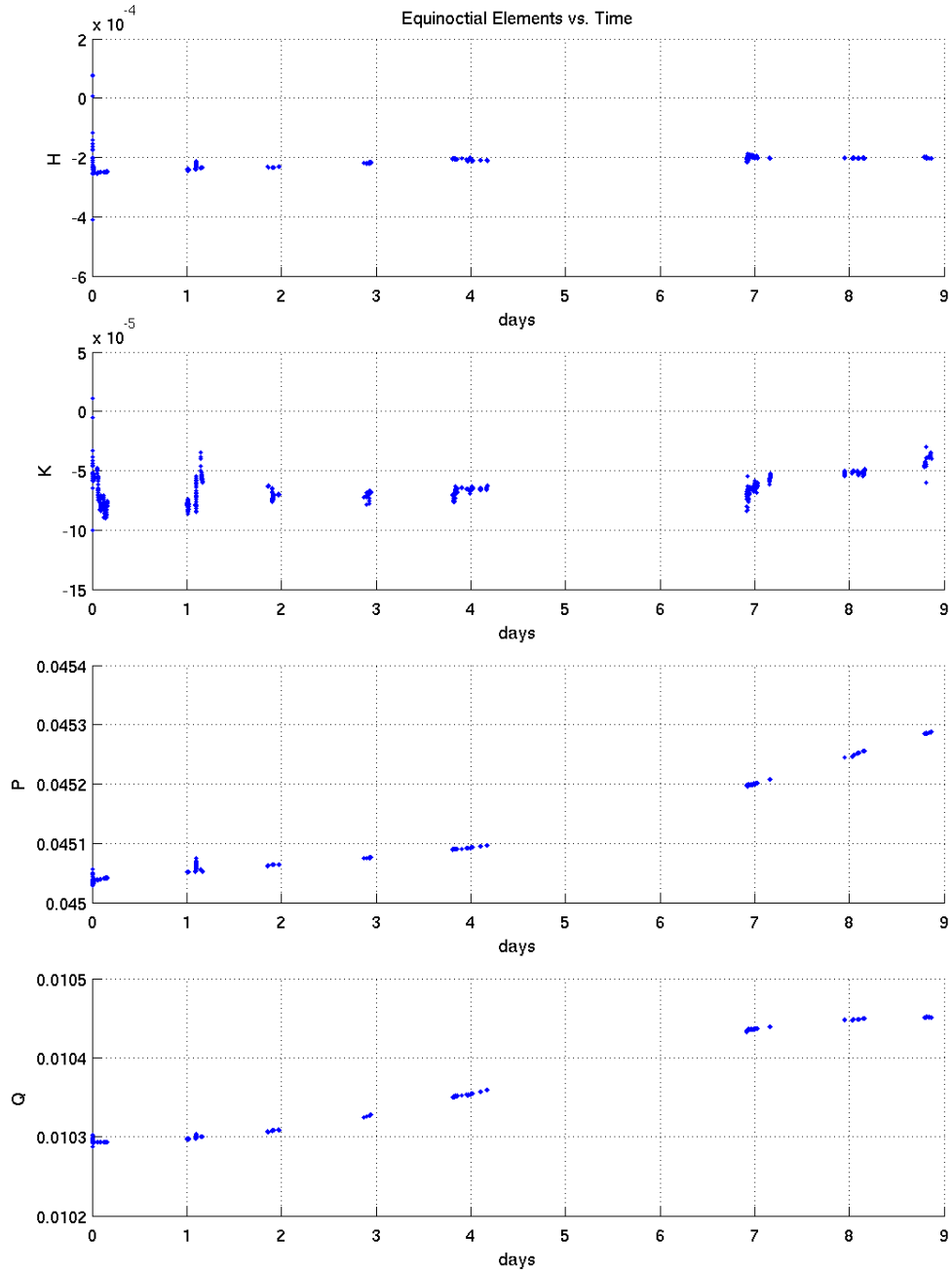


Figure 8-2 – Mean Equinoctial Elements vs Time using Only HANDS Data with Spherical Model (ESKF)

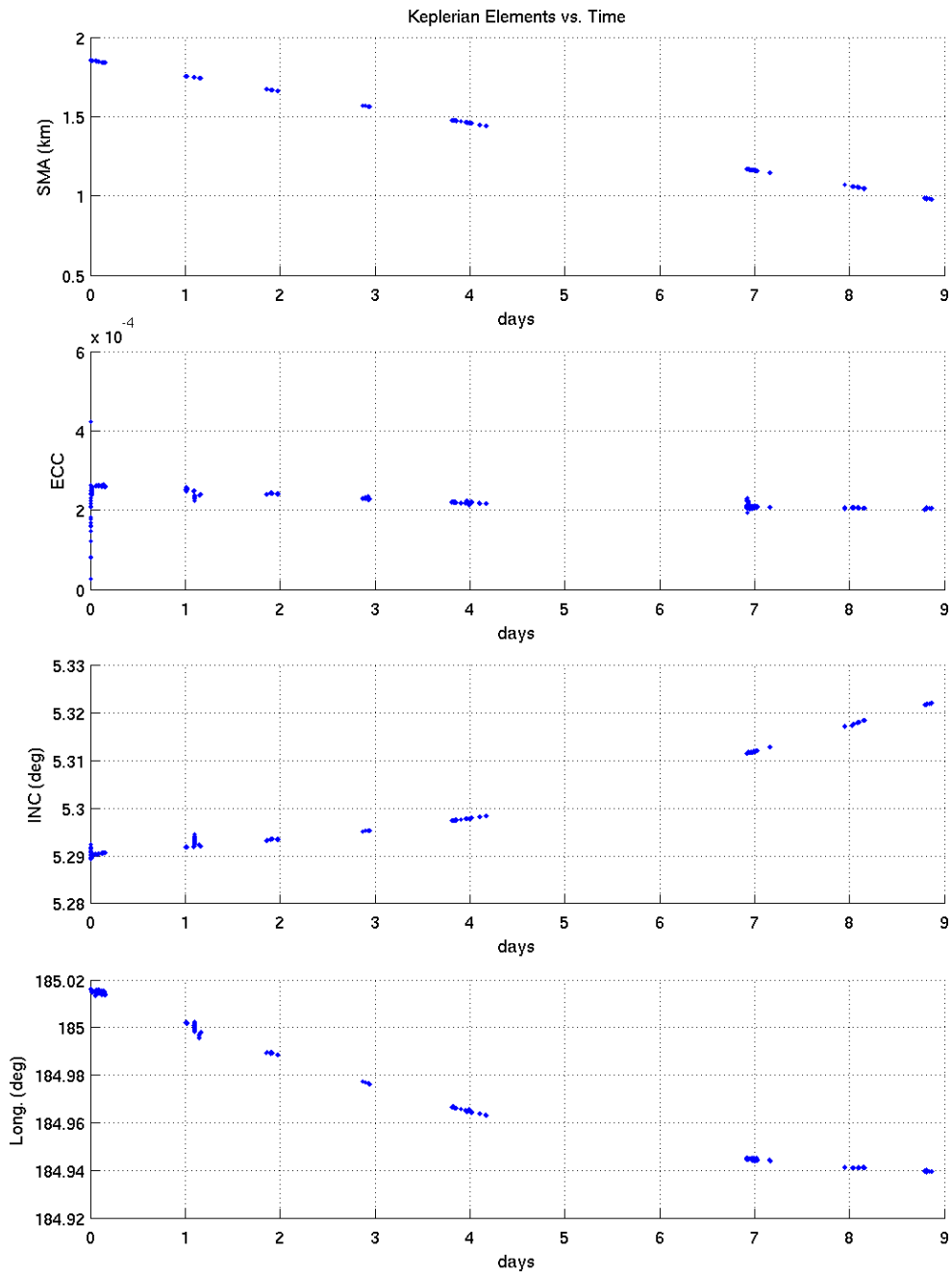


Figure 8-3 – Mean Keplerian Elements vs Time using Only HANDS Data with Box-wing Model (ESKF)

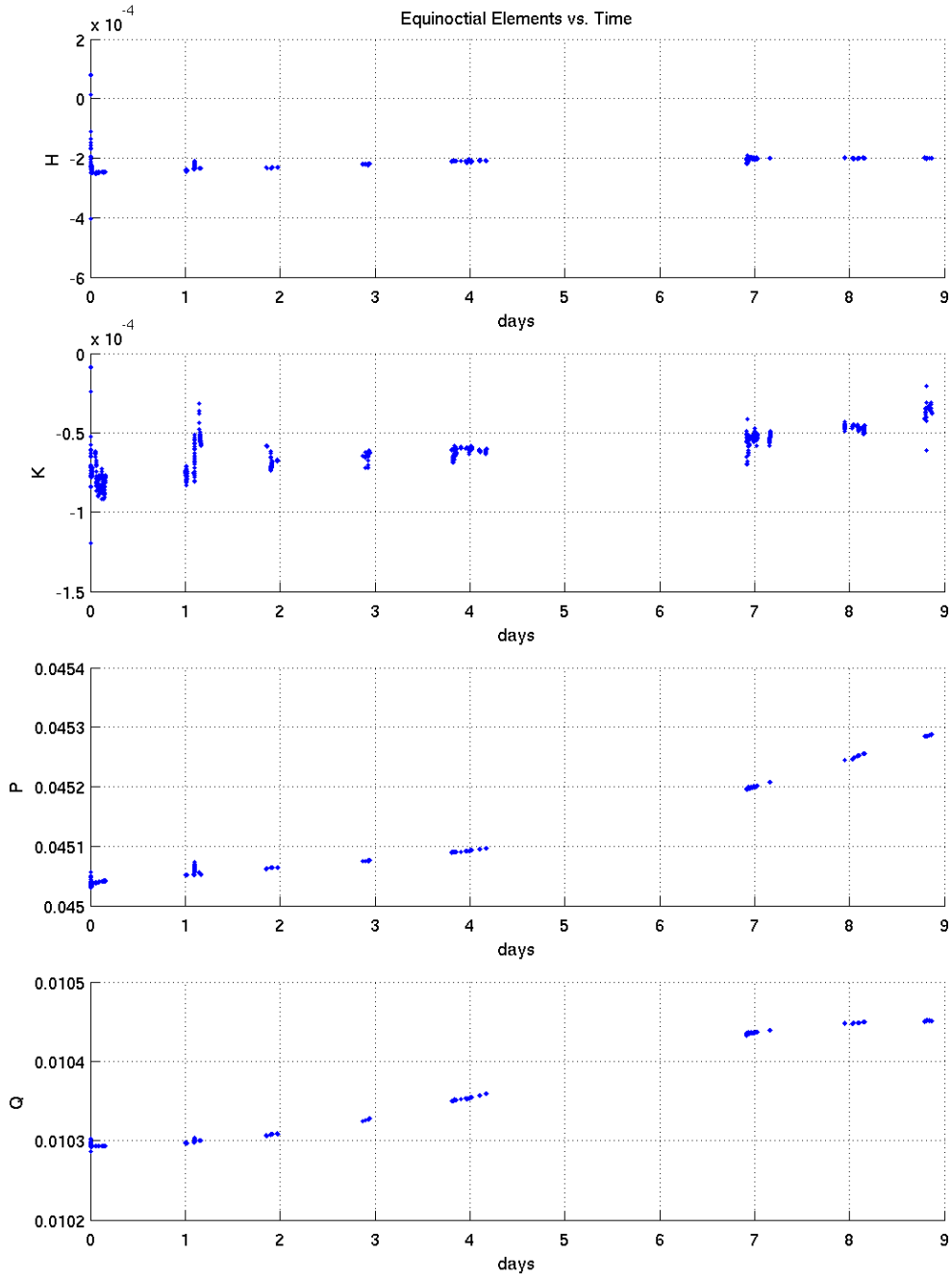


Figure 8-4 – Mean Equinoctial Elements vs Time using Only HANDS Data with Box-wing Model (ESKF)

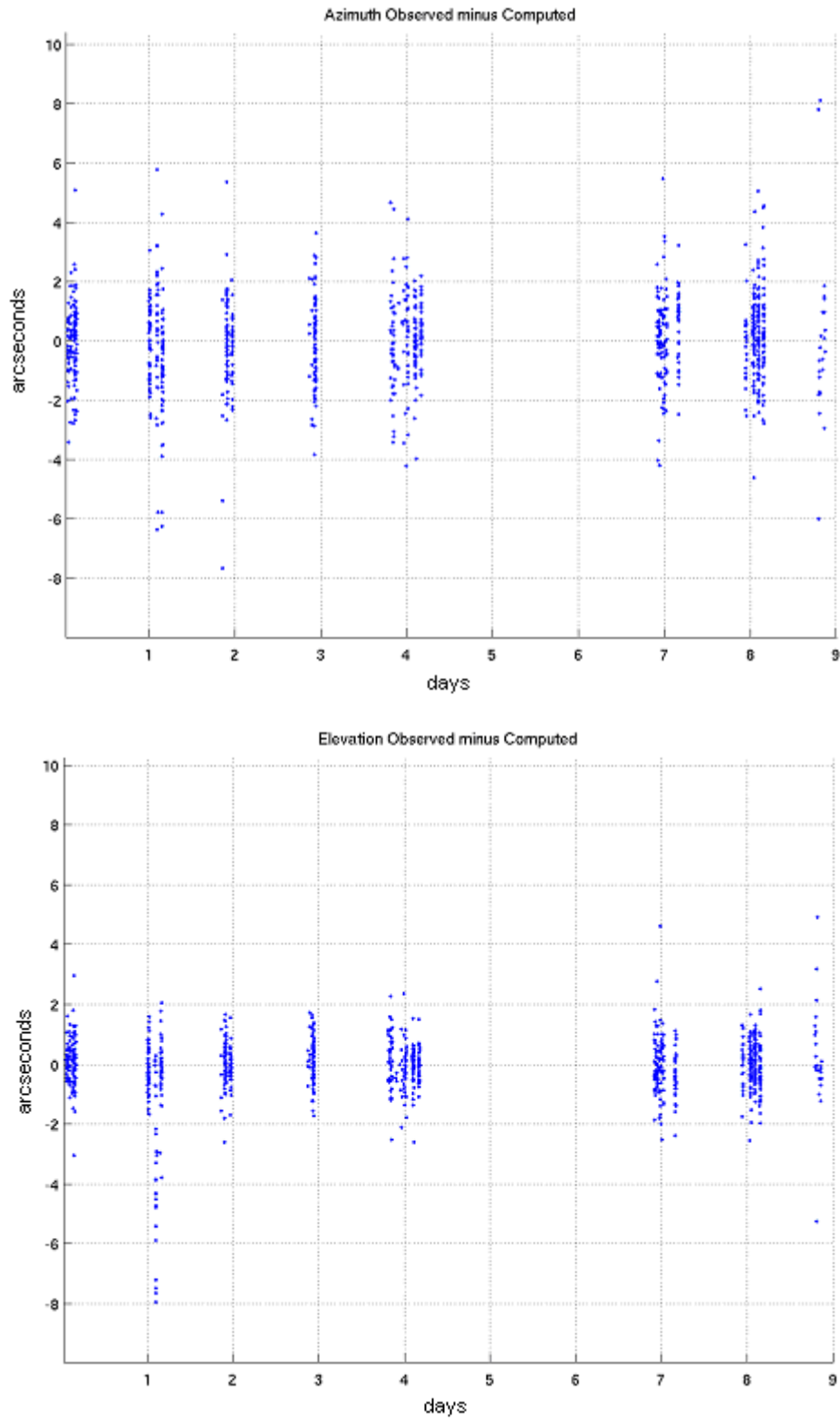


Figure 8-5 – HANDS Azimuth and Elevation Residuals vs Time using Only HANDS Data with Spherical Model (ESKF)

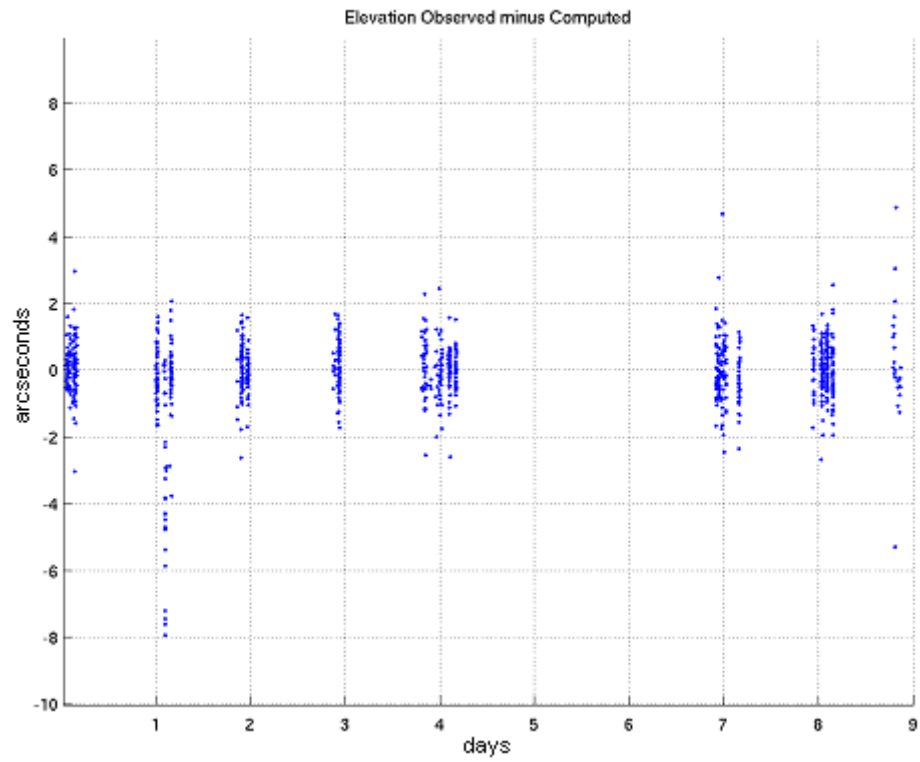
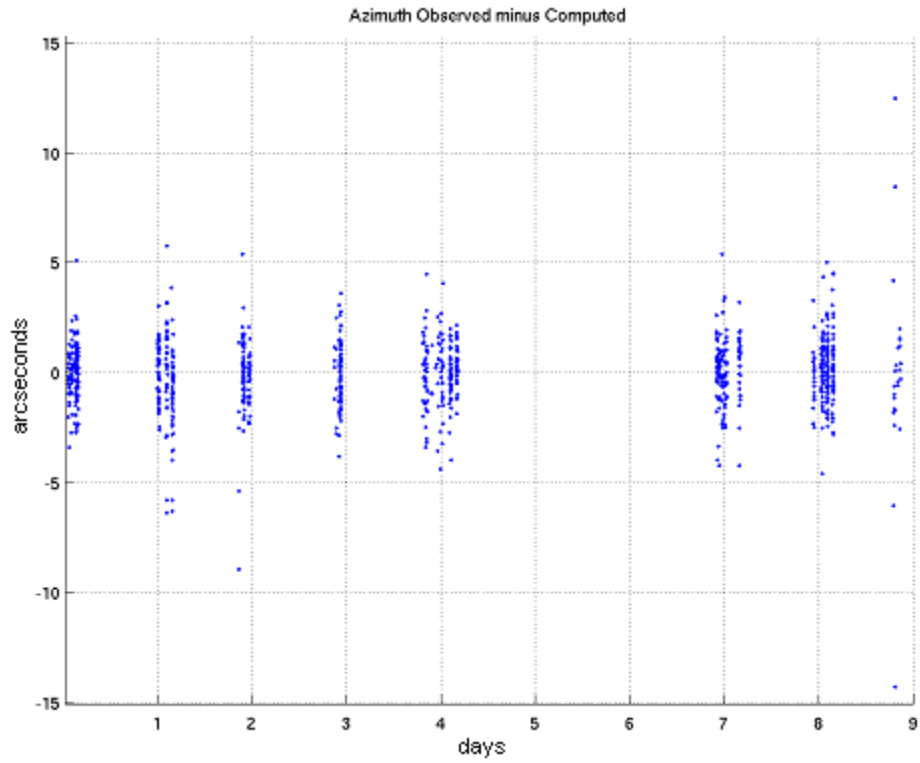


Figure 8-6 – HANDS Azimuth and Elevation Residuals vs Time using Only HANDS Data with Box-wing Model (ESKF)

The ESKF was then applied to a data set that consisted of SSN observations combined with the HANDS optical observations of the TDRS-05 spacecraft. The time span used was the same as for the earlier cases – approximately 10 days long, from 15 December 2003 through 25 December 2003. The test cases were completed with both the spherical and box-wing spacecraft models.

Figures 8-7 and 8-8 show the azimuth and elevation residuals for converted HANDS observations using the spherical and box-wing models, respectively. As before, the residuals are similar between the spherical and box-wing test cases. Compared to the earlier cases that used only the HANDS optical data, the residuals have greater variance and are no longer centered about zero mean. This is especially true near the beginning of the fit interval. It is noteworthy that the HANDS residuals do become tighter toward the end of the fit interval. The difference in HANDS azimuth and elevation residuals from the test cases that used only HANDS data is likely due to the fact that the HANDS sensors were highly-tasked to track TDRS-05 over the fit interval, while the SSN sensors were not.

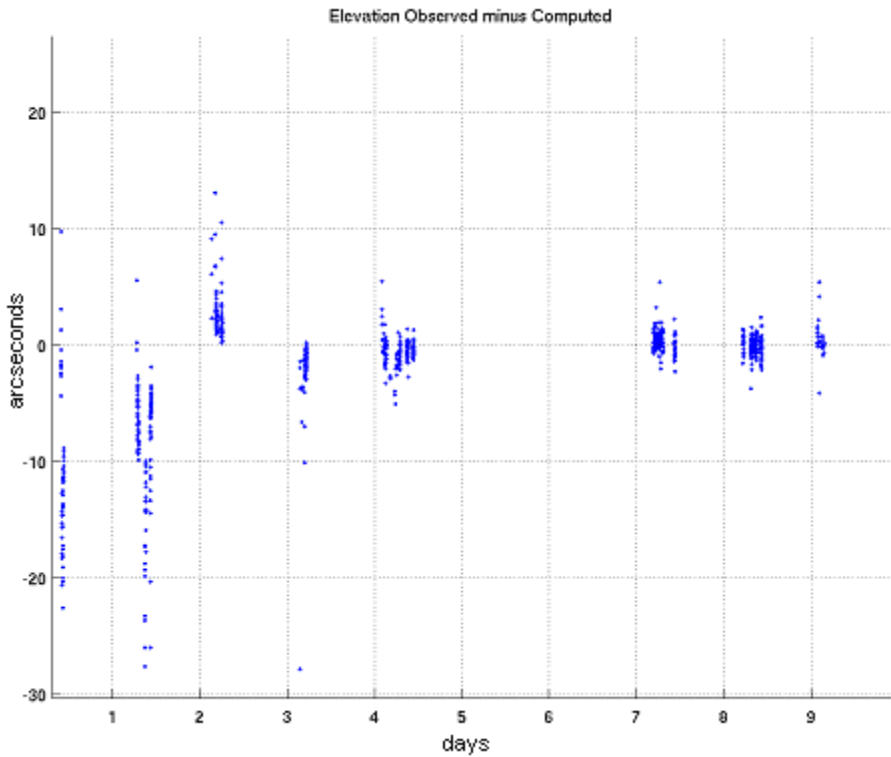
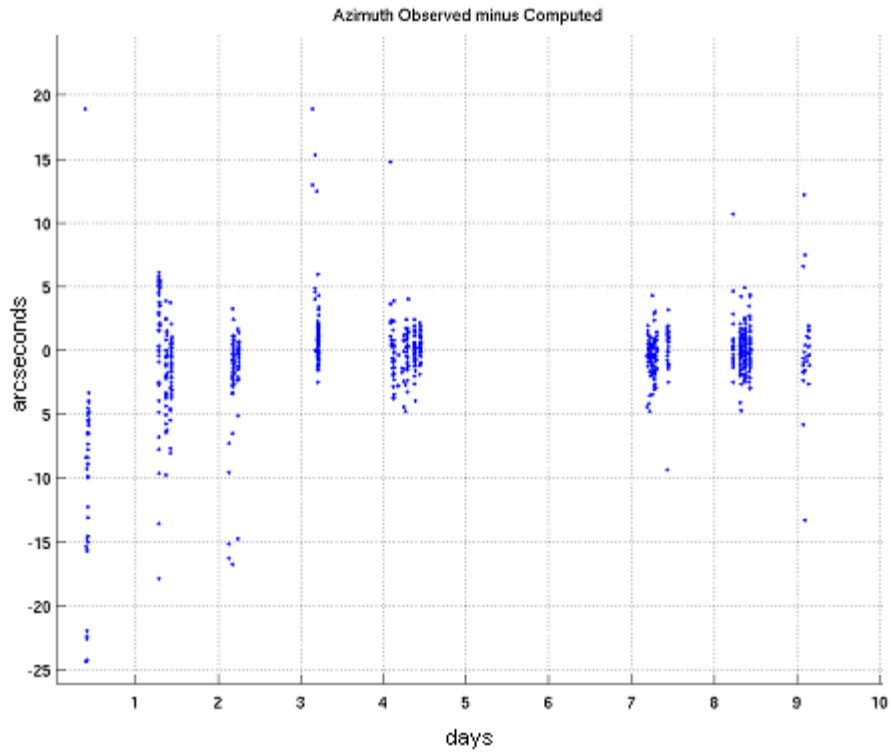


Figure 8-7 – HANDS Azimuth and Elevation Residuals vs Time using SSN and HANDS Data with Spherical Model (ESKF)

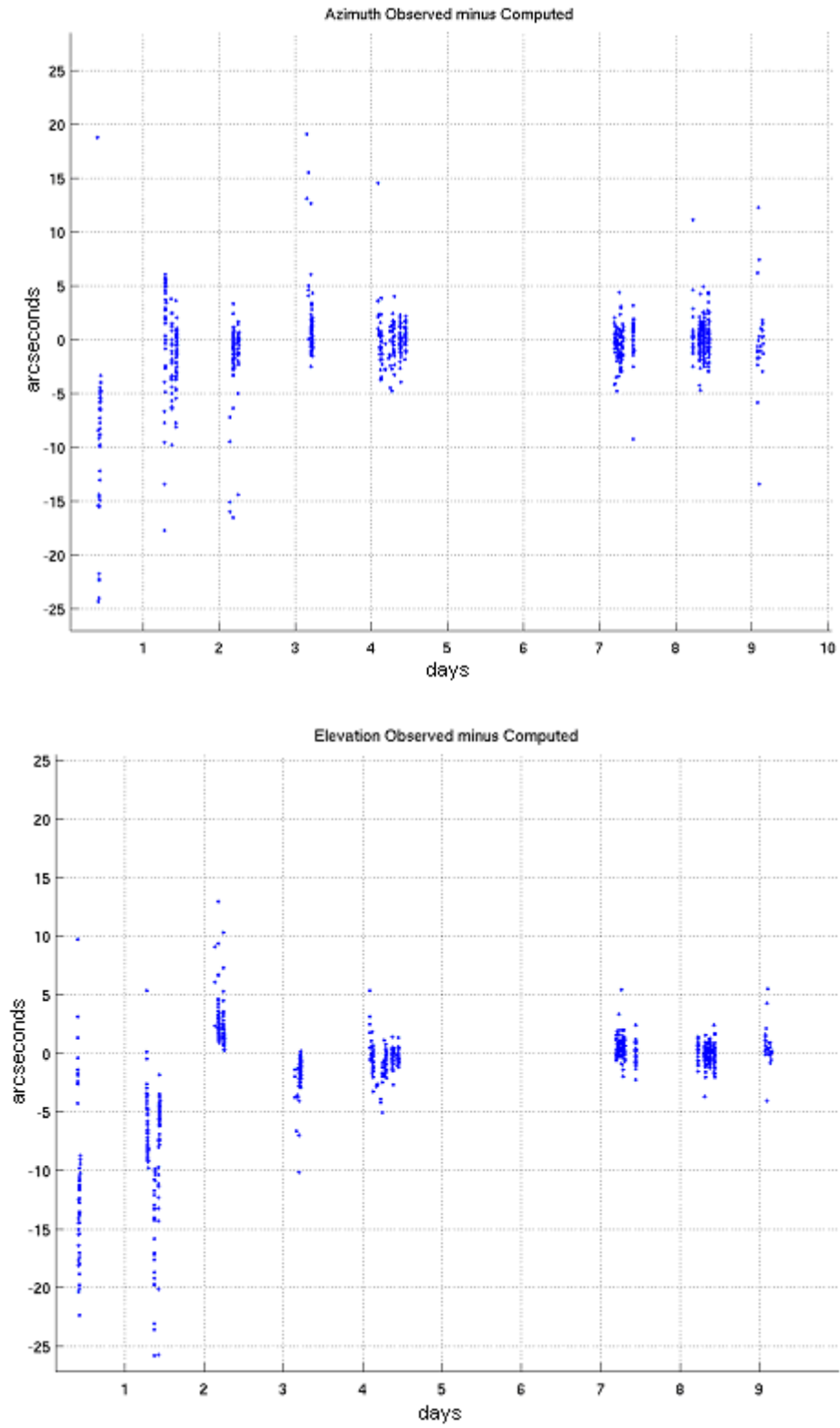


Figure 8-8 – HANDS Azimuth and Elevation Residuals vs Time using SSN and HANDS Data with Box-wing Model (ESKF)

8.2 GOES Test Cases

8.2.1 SSN with NOAA Ranging Data

SSN observations were collected for the GOES-10 spacecraft for the time period of 20 October – 29 November 2003. The data included 894 observations of GOES-10. In addition to the SSN data, GOES owner/operator ranging data were provided by NOAA for the GOES-10 spacecraft. The ranging data came from two stations, designated GOES Station 1 and GOES Station 6, both of which are located near Langley, VA. Both sensors have a reported range sigma of 15 meters, and the ranging measurements were provided with the hardware time delay range bias subtracted out. The ranging measurements covered the time span of 20 October 2003 through 29 November 2003. The available observations for this time span included 894 observations from the Space Surveillance Network, 1706 range observations from GOES Station 1, and 2064 range observations from GOES Station 6.

A preprocessor was built to convert the GOES ranging observations from NOAA format into GTDS format. The combined measurements were then processed using both the spherical spacecraft as well as the GOES macro-model for solar radiation pressure. These runs used the Semi-analytical Satellite Theory for the 40-day fit. The solve-for parameters in these runs included the epoch orbit state as well as a single C_R for both models. The first runs using these data demonstrated a significant improvement in range residuals throughout the fit when the macro-model was used.

However, further review showed that the fit using the macro-model was throwing out most of the GOES Station 1 data. When this was realized, only the combined SSN observations and GOES Station 6 ranging data were reprocessed using both the spherical

and box-wing models. These data were processed using both the DSST and Cowell orbit generators. Figure 8-9 shows the GOES Station 6 range residual in meters using the spherical and box-wing models from the DSST fit. Figure 8-10 shows the range residuals from the Cowell fit. These results are encouraging from the standpoint that the Semi-analytical Satellite Theory and Cowell Theory produce nearly identical results. However, the results are discouraging from the standpoint that the spherical and macro-models produce nearly identical residuals in both cases. The box-wing model does not seem to improve the residuals.

Orbit determination experience with other spacecraft at MIT/LL has shown possible issues that were applicable to the GOES-10 case. The first of these issues is the possibility of maneuvers in the fit span. The two gaps in the GOES Station 6 ranging data were indicative of possible maneuvers during those time spans, as we have seen with similar gaps in other owner/operator range data. The second issue is that a relatively large number of a single source of observations compared to the number of other SSN observations can lead to poor orbit determination performance. Methods used to mitigate this problem include sampling the owner/operator range measurements less frequently, as well as deweighting the range measurements. The third issue is that errors in range bias information can lead to poor orbit determination accuracy. A way to circumvent this issue is to iteratively estimate the range bias in an orbit determination run, and feed back the corrected range bias to a subsequent run.

To address the issue of possible maneuvers, the orbit determination fit span was adjusted to include the time interval between the two gaps. The range residuals outside of this new fit span were larger, which is indicative of the possibility of maneuvers. For

the issue of an overwhelming amount of ranging data compared to SSN observations, a strategy was applied to the GOES Station 6 data of sampling the data once every five measurements. Additionally, the GOES Station 6 observations were deweighted to a sigma of 100 meters. The issue of possible range bias errors was addressed by estimating the GOES Sensor 6 range bias using the spherical spacecraft model. This range bias was then used in subsequent fits for both the spherical and macro-models. All of these runs were completed using the Cowell orbit generator. Figure 8-11 shows the range residuals from these test cases. This plot shows an improvement in residuals with the macro-model over the spherical model.

The next test case applied the same strategies as the previous one, with the exception that a second range bias was estimated with the macro-model. This range bias was then applied to a subsequent differential correction run using the macro-model. Figure 8-12 compares the range residuals from this test case to the test case where the spherical range bias is applied. The macro-model demonstrated significantly improved range residuals compared to the spherical when the respective range biases are applied, and clarified the secular trend in the residuals.

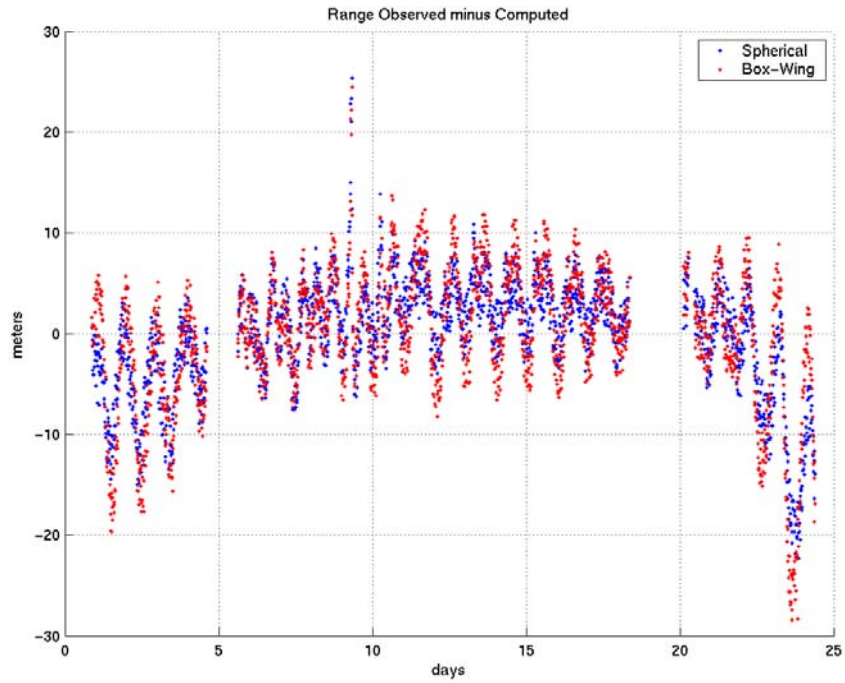


Figure 8-9– GOES Station 6 Range Residuals Using SSN Obs and NOAA Ranging Data – Semi-analytical Satellite Theory Fit (DC)

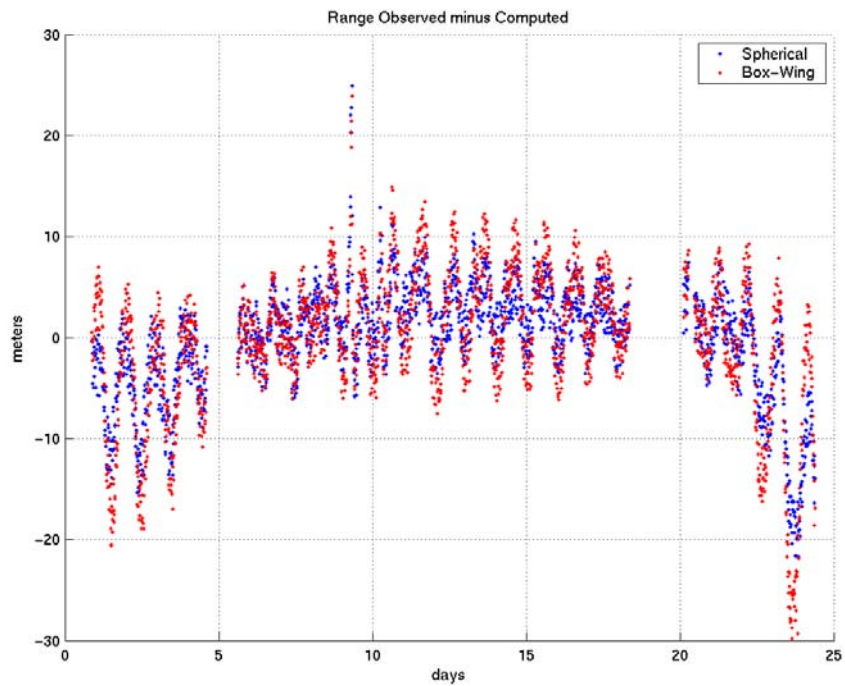


Figure 8-10–GOES Station 6 Range Residuals Using SSN Obs and NOAA Ranging Data – Cowell Theory Fit (DC)

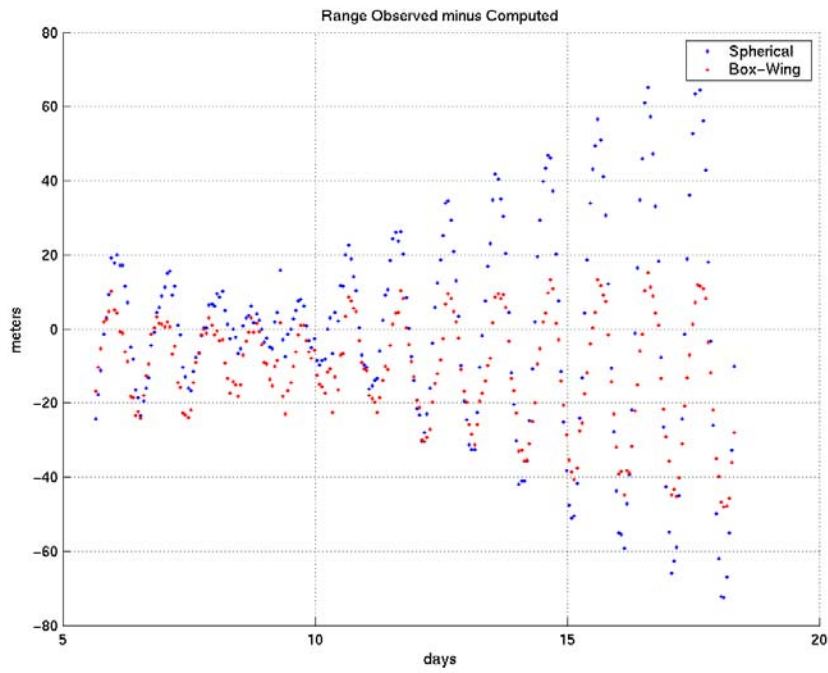


Figure 8-11– GOES Station 6 Range Residuals Using SSN Obs and Thinned/Deweighted NOAA Ranging Data, Spherical Range Bias (DC)

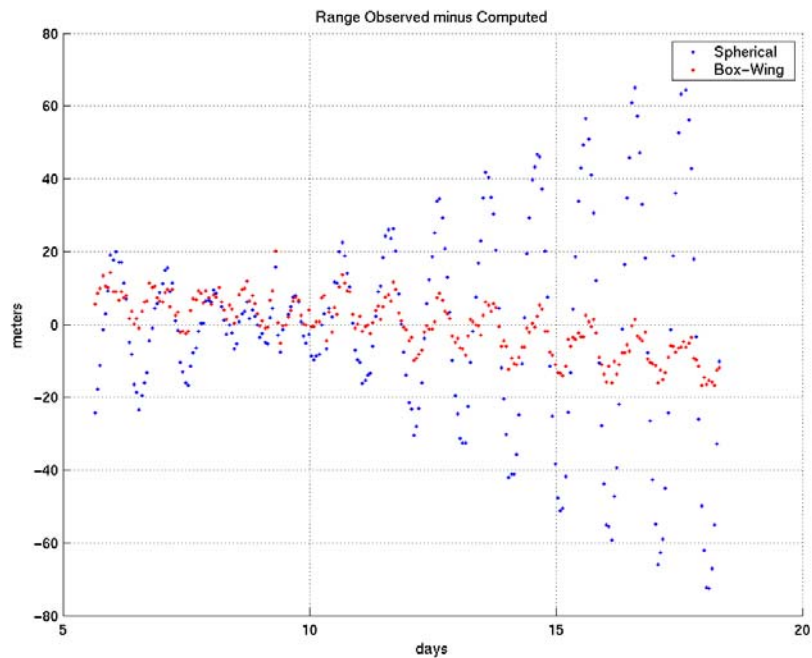


Figure 8-12 – GOES Station 6 Range Residuals Using SSN Obs and Thinned/Deweighted NOAA Ranging Data, Spherical/Macro-model Range Biases (DC)

After completing the test case where the respective range biases were applied to the two models, it was realized that the macro-model was editing out more of the observations than the spherical model. When the same number of observations was edited out of both, the resulting range biases again became nearly identical between the two models. The resulting range biases are shown in Figure 8-13.

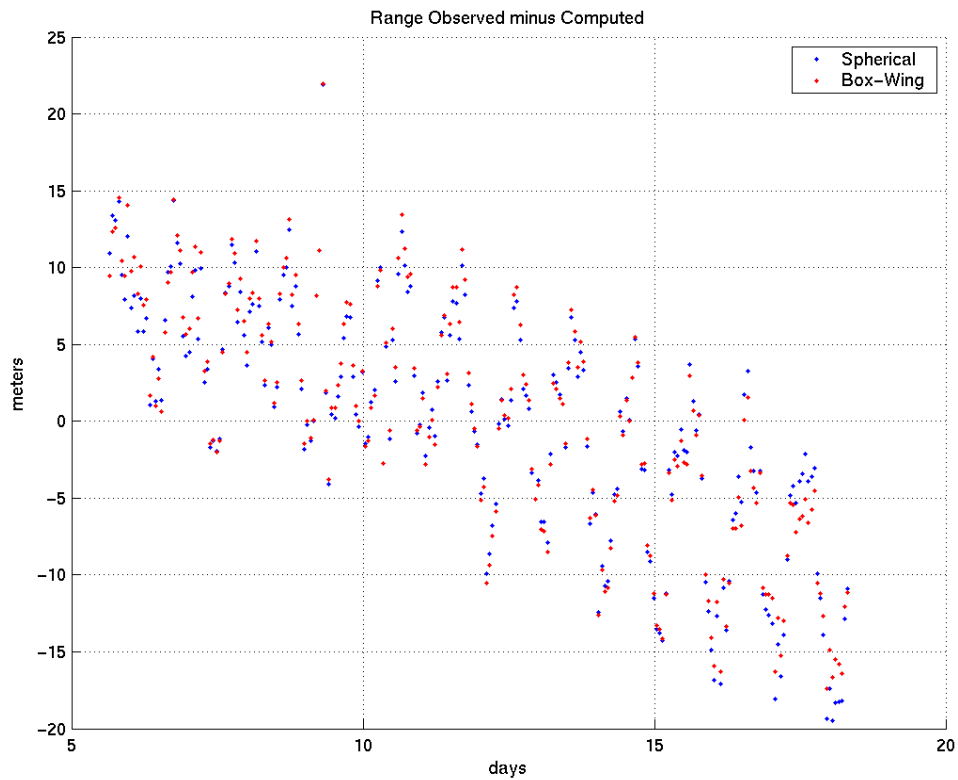


Figure 8-13 - GOES Station 6 Range Residuals Using SSN Obs and Thinned/Deweighted NOAA Ranging Data, Equal % Obs Accepted (DC)

8.2.2 SSN with NOAA Ranging Data and SBV Observation Data

The SBV observations model became available in GTDS in the course of this study. This allowed for processing the GOES-10 test case with SSN, NOAA ranging, and SBV data included. These test cases also gave insight into the observations corrections that should be applied to various observation types.

The first set of test cases compared the results from including the SBV data with the results that did not include the SBV data. A summary of the results is given in Table 8-2. It can be seen that including the SBV data improved the RMS position error metric.

Table 8-2 – GOES-10 Results of Including SBV Observations (DC)

Run Description	SRP Model	% obs accepted	Semimajor Axis Std Deviation (cm)	Weighted RMS	Position Error RMS (m)
No SBV Obs	Spherical	85%	11.2	0.674	7228
	Macro-model	84%	10.4	0.603	6801
SBV Obs Included	Spherical	83%	9.82	0.549	6811
	Macro-model	85%	10.4	0.605	6766

The next set of test cases experimented with various observations corrections, which are discussed in Chapter 2.5.2. The first corrections turned on were the light-time corrections for all sensors, and ionospheric and tropospheric refraction corrections for the radar sites. These corrections resulted in a substantial improvement in orbit accuracy. Finally, optical measurement biases were solved-for and subtracted out with the shorter fit span. In the process of turning on the various observations corrections, an understanding was gained of how they were implemented in GTDS, which then allowed the corrections to be checked to make sure they were correct.

The results of the fits using various observations corrections are summarized in Table 8-3. Again, there is little difference between the macro-model and spherical

model, but applying the various observations corrections gradually produces more accurate orbits. An example input data file for this type of test case that uses the spherical model is shown in Figure D-7.

Table 8-3 – GOES-10 Results of Using Observations Corrections and Biases

Run Description	SRP Model	% obs accepted	Semimajor Axis Std Deviation (cm)	Weighted RMS	Position Error RMS (m)
No Corrections	Spherical	84%	10.5	0.576	6793
	Macro-model	86%	10.5	0.625	6765
Light-time & Refraction Corrections	Spherical	75%	1.21	0.418	1191
	Macro-model	75%	1.23	0.422	1188
Optical Measurement Biases	Spherical	75%	5.64	0.290	888
	Macro-model	78%	6.93	0.357	958

8.2.3 Kalman Filter Cases Processing GOES Data

This set of test cases involved applying the Extended Semi-analytical Kalman Filter (ESKF) to the owner/operator ranging data provided by NOAA. The test cases used observations of the GOES-10 spacecraft. The time span used was approximately 20 days long, from 22 October 2003 through 9 November 2003. The observations processed included all of the NOAA ranging data, which represents approximately one observation every 15 minutes over the fit interval.

The ESKF was applied first using the spherical solar radiation pressure model, which was a previously-existing capability in GTDS. The mean equinoctial elements and spherical C_R were the solve-for parameters. A semi-analytical differential correction run was completed to obtain the a priori epoch mean elements and C_R for the ESKF.

The ESKF was then applied using the box-wing model for solar radiation pressure. This time, the mean equinoctial elements and the single box-wing C_R were the

solve-for parameters. Again, a semi-analytical differential correction run was completed to obtain the a priori epoch mean elements and C_R for the ESKF.

Figures 8-14 and 8-15 show the behavior of the mean elements over the time span using the spherical model, and Figures 8-16 and 8-17 show the behavior of the mean elements over the time span using box-wing model. The mean elements are seen to be well-behaved and smoothly-varying over the fit interval. Similar to the earlier TDRSS ESKF test cases, the mean element motion exhibited is due to the natural perturbations. The behavior of the mean elements is nearly identical between the spherical and box-wing model.

Figures 8-18 and 8-19 show the GOES Station 6 range residuals for the test cases using the spherical and box-wing models, respectively. The range residuals appear to be random noise, centered about zero mean, with most residuals within ± 5 meters. The results are very similar between the spherical and box-wing model cases.

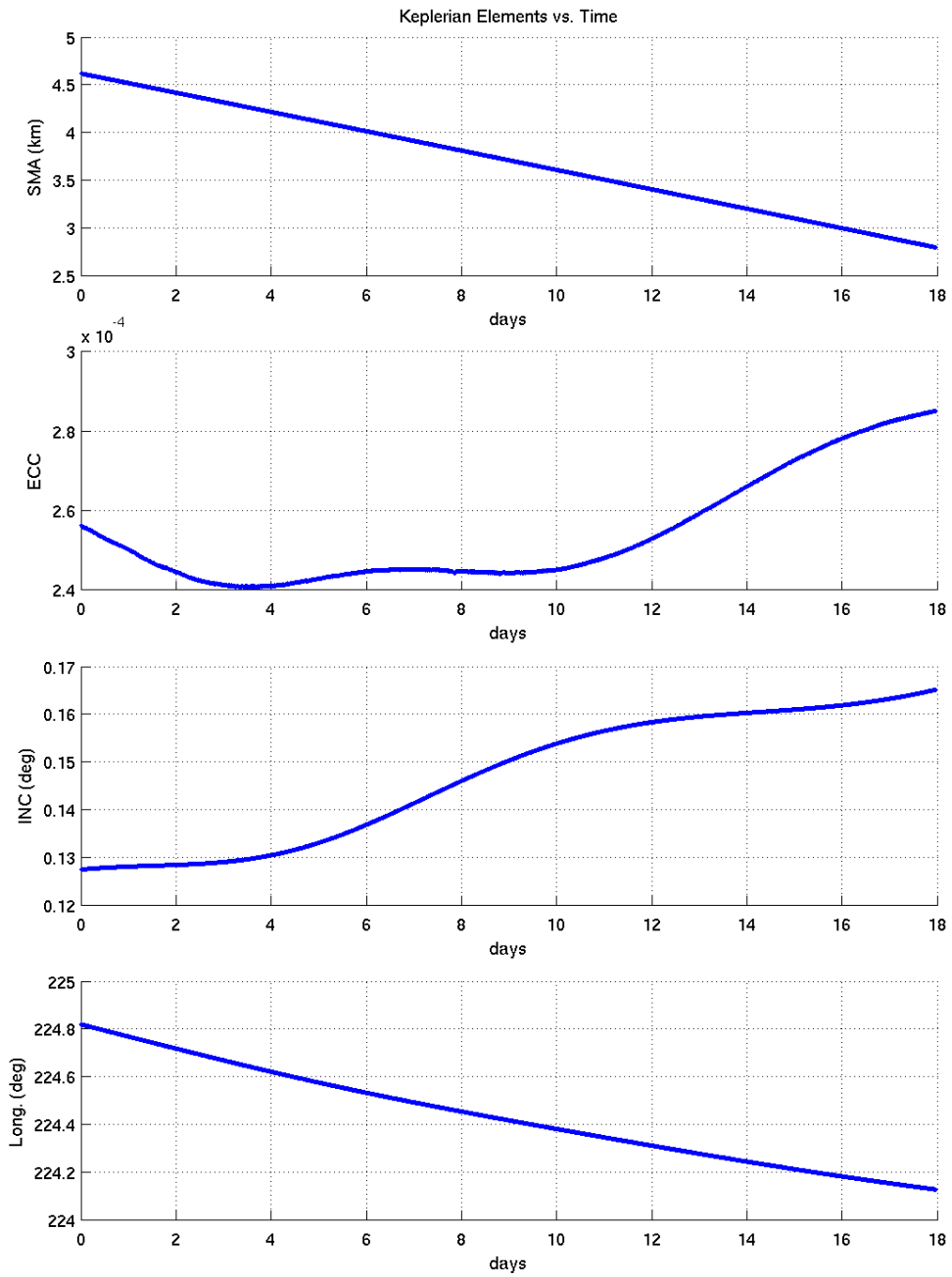


Figure 8-14 – Mean Keplerian Elements vs Time using Only NOAA Ranging Data with Spherical Model (ESKF)

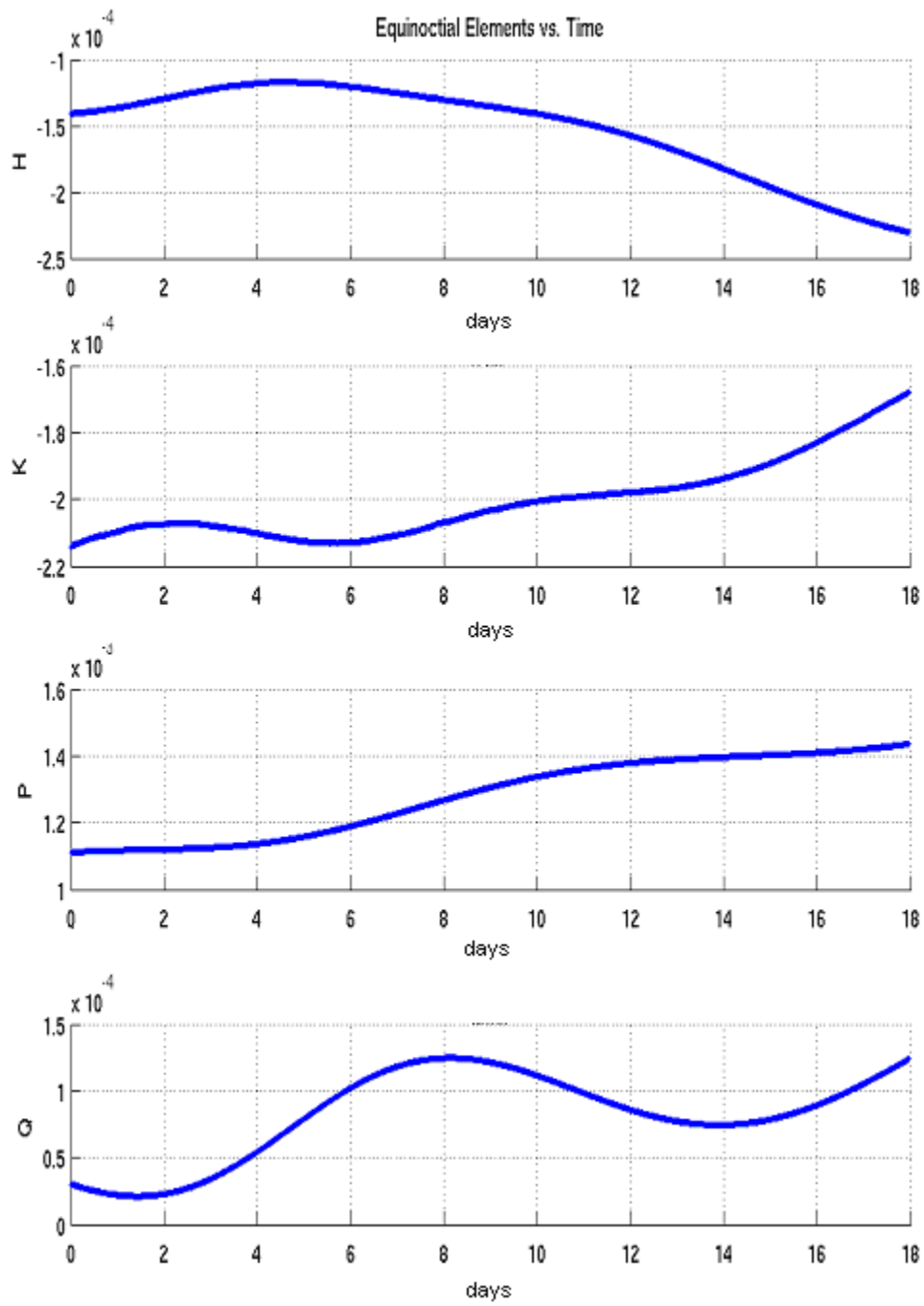


Figure 8-15 – Mean Equinoctial Elements vs Time using Only NOAA Ranging Data with Spherical Model (ESKF)

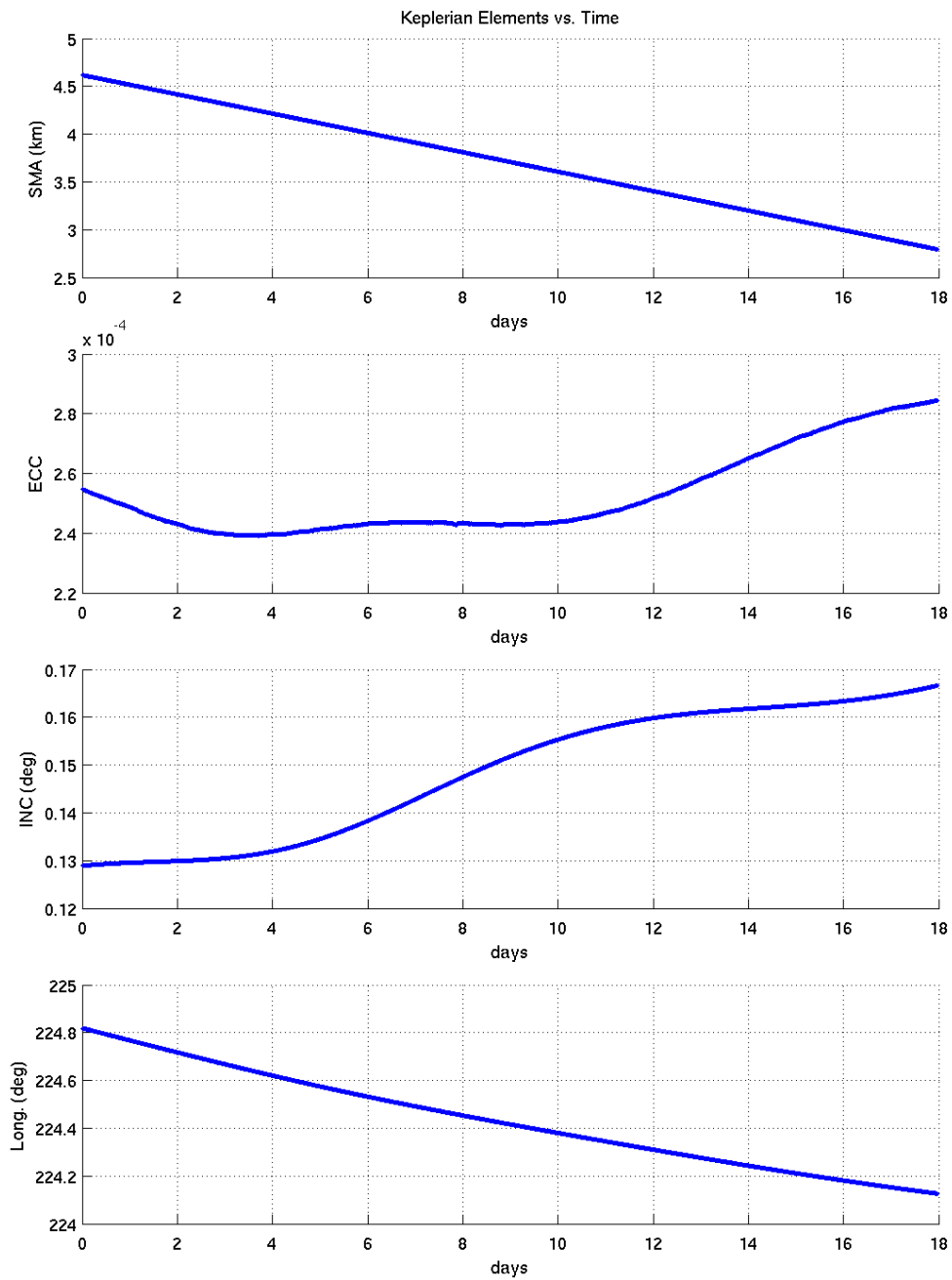


Figure 8-16 – Mean Keplerian Elements vs Time using Only NOAA Ranging Data with Box-wing Model (ESKF)

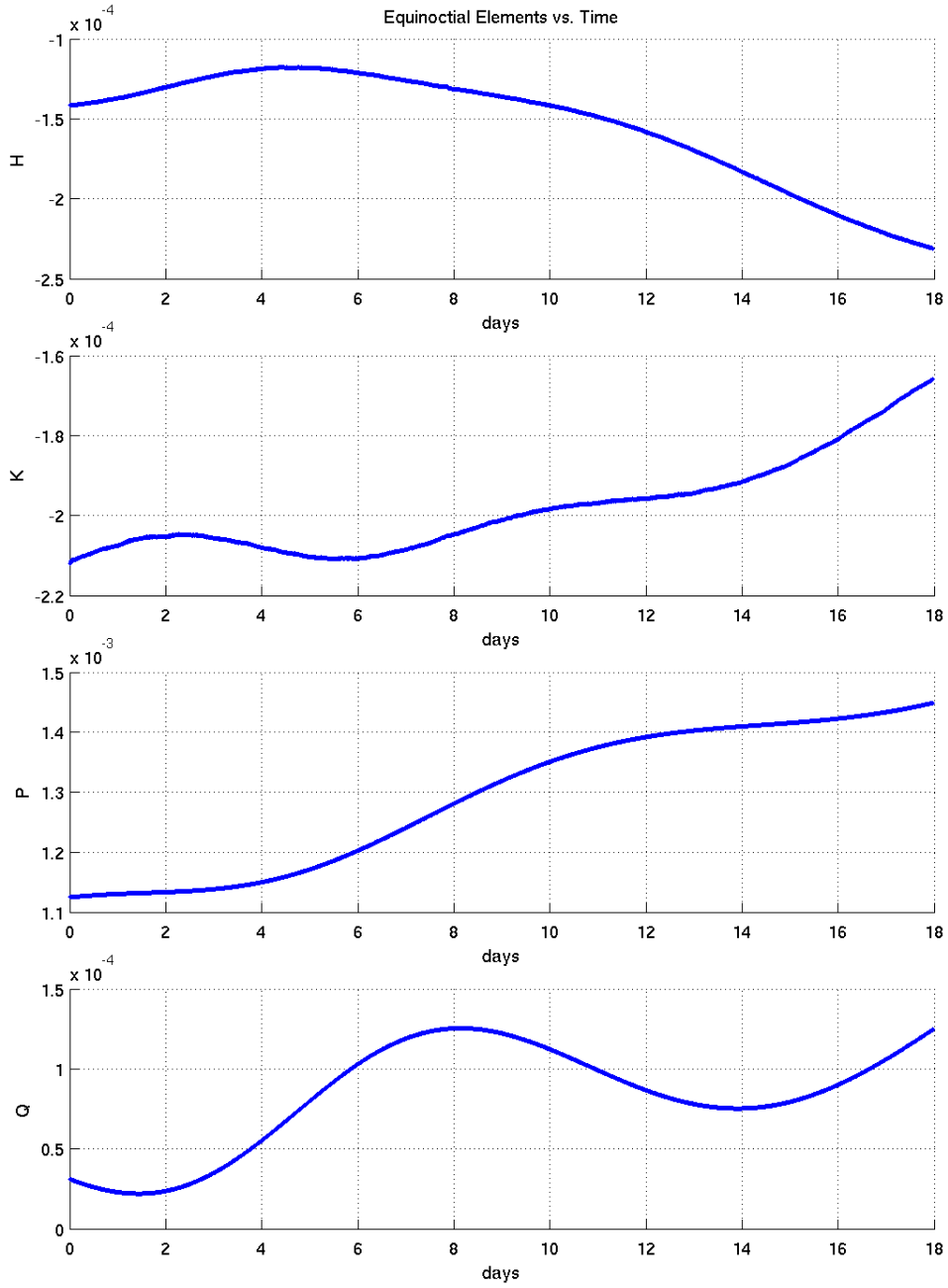


Figure 8-17 – Mean Equinoctial Elements vs Time using Only NOAA Ranging Data with Box-wing Model (ESKF)

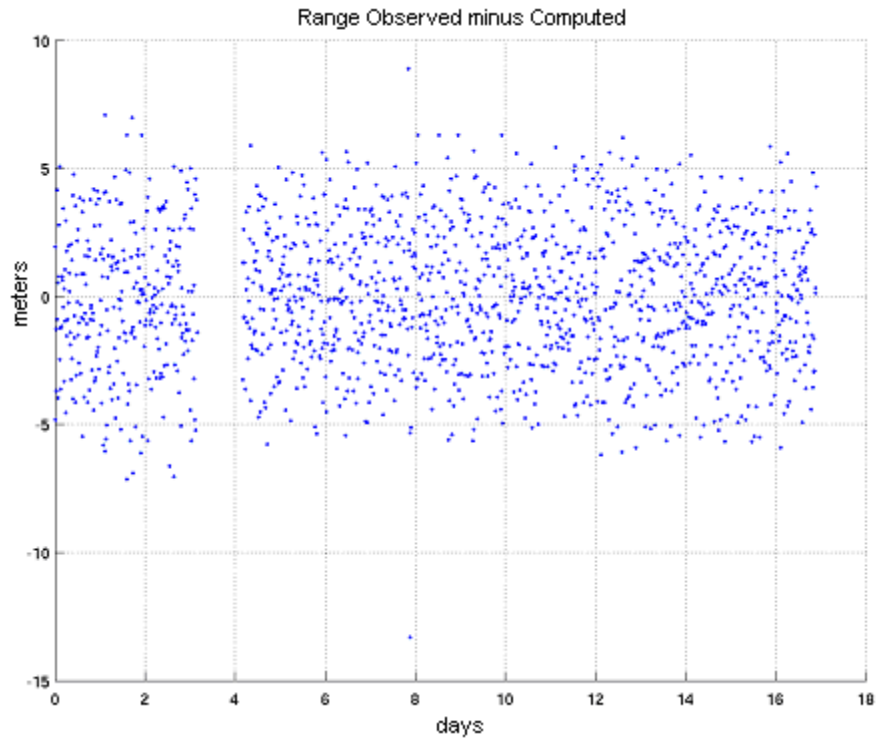


Figure 8-18 – GOES Station 6 Range Residuals vs Time using Only NOAA Ranging Data with Spherical Model (ESKF)

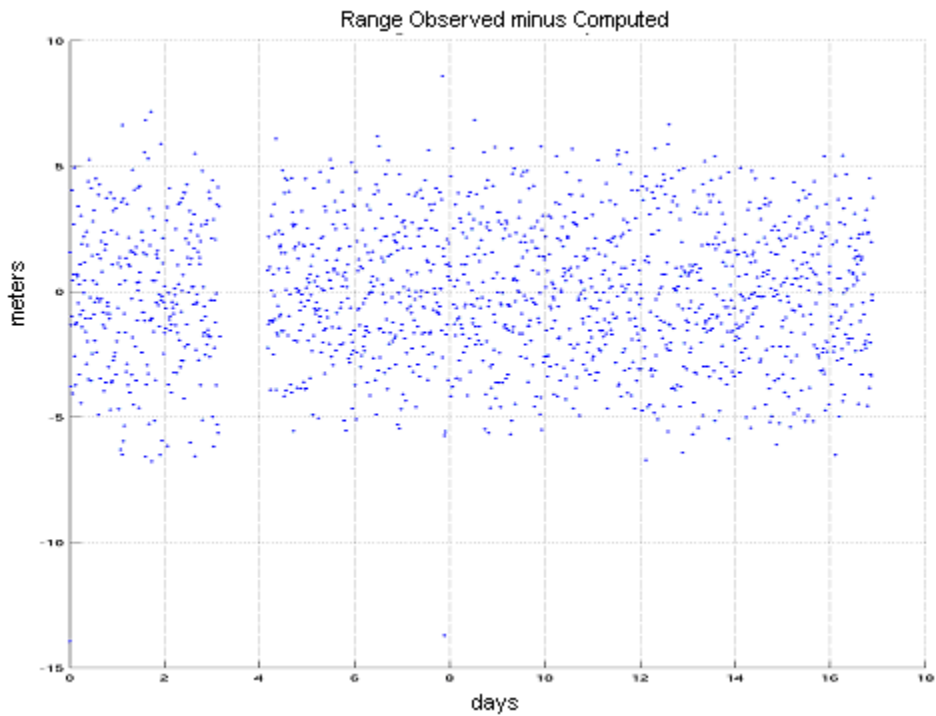


Figure 8-19 – GOES Station 6 Range Residuals vs Time using Only NOAA Ranging Data with Box-wing Model (ESKF)

The ESKF was then applied to a data set that consisted of SSN observations combined with the NOAA ranging observations of the GOES-10 spacecraft. The time span used was the same as for the earlier cases – approximately 20 days long, from 22 October 2003 through 9 November 2003. The test cases were completed with both the spherical and box-wing models.

Figures 8-20 and 8-21 show the behavior of the mean elements over the time span using the spherical model, and Figures 8-22 and 8-23 show the behavior of the mean elements over the time span using the box-wing model. The behavior of the mean elements is nearly identical between the spherical and box-wing model. As compared to the earlier test cases that used only NOAA ranging data, the mean elements are seen to be well-behaved and smoothly-varying for the most part, although there are several discontinuities over the fit interval. These discontinuities tend to occur in regions of the fit interval where there are SSN observation data.

Figures 8-24 and 8-25 show the GOES Station 6 range residuals using the spherical and box-wing models, respectively. As before, the residuals are similar between the spherical and box-wing test cases. Compared to the earlier cases that used only the NOAA ranging data, the residuals are in general still centered about zero mean and vary between ± 5 meters. However, in sections of the fit where there are SSN observations, the GOES Station 6 range residuals grow quite large before converging back to their nominal behavior.

As with the TDRSS filter test cases, the behavior of the mean elements and observation residuals is likely due to the fact that the NOAA sensors were highly-tasked to track GOES-10 over the fit interval, while the SSN sensors were not.

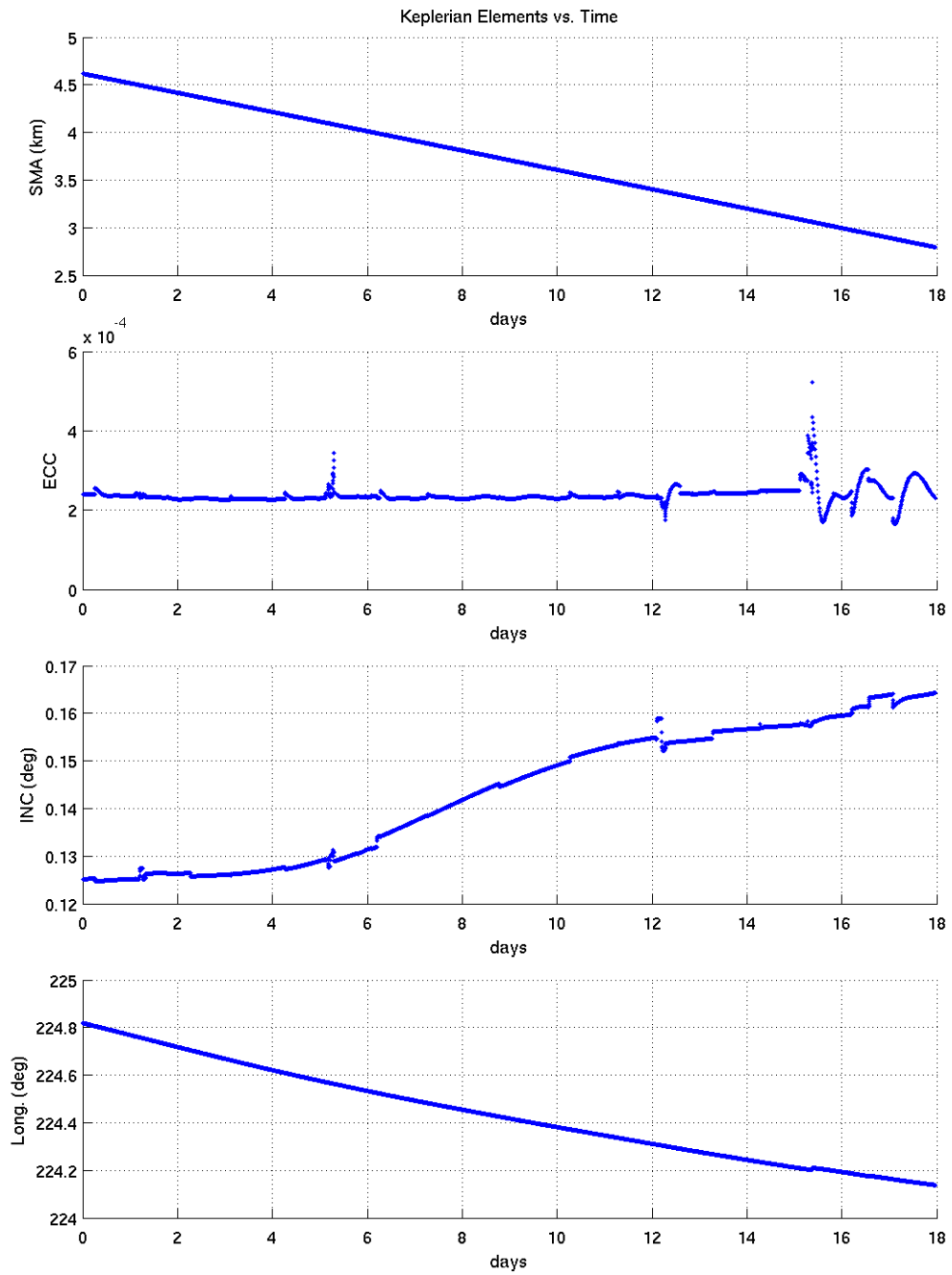


Figure 8-20 – Mean Keplerian Elements vs Time using SSN and NOAA Ranging Data with Spherical Model (ESKF)

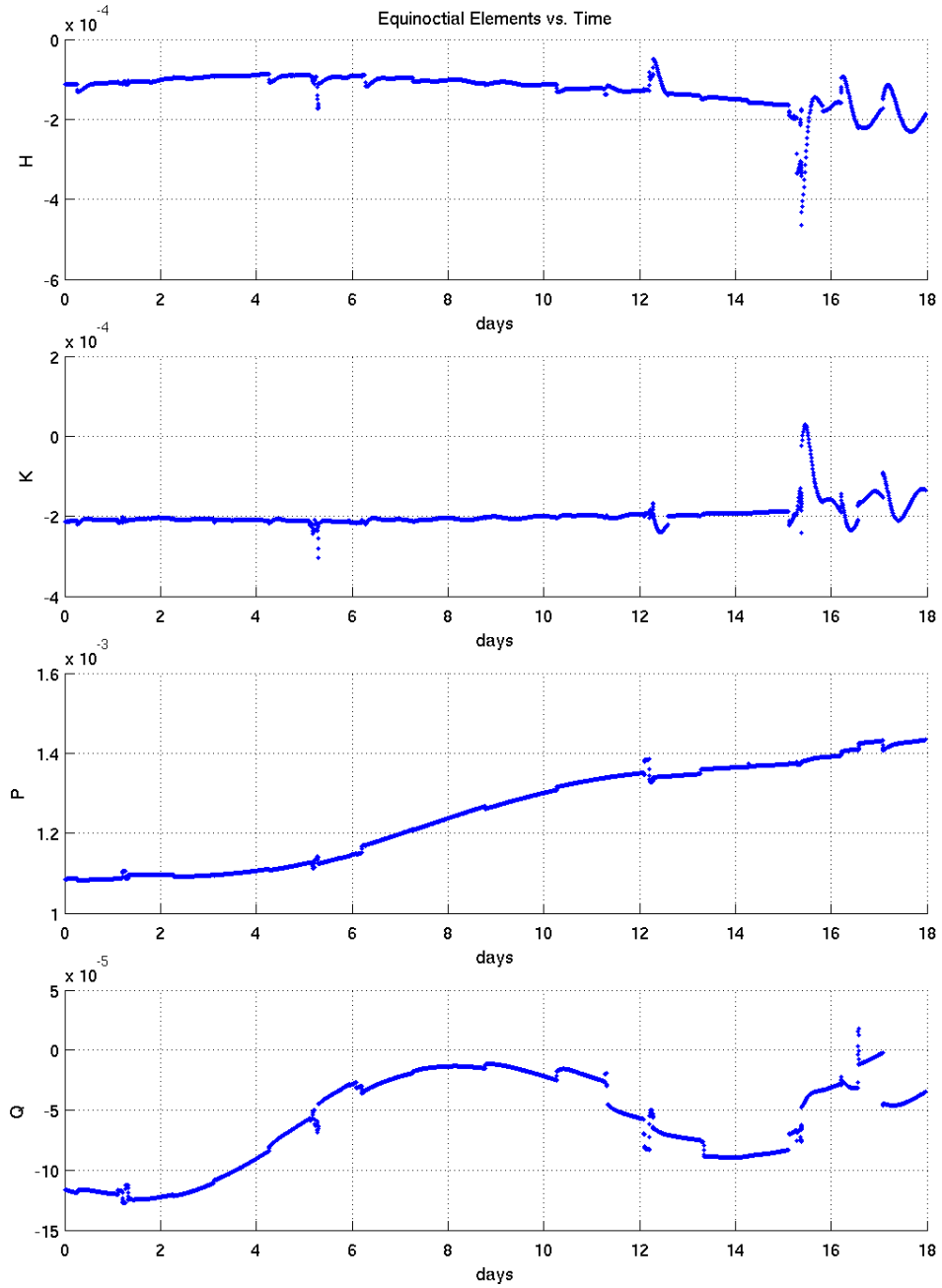


Figure 8-21 – Mean Equinoctial Elements vs Time using SSN and NOAA Ranging Data with Spherical Model (ESKF)

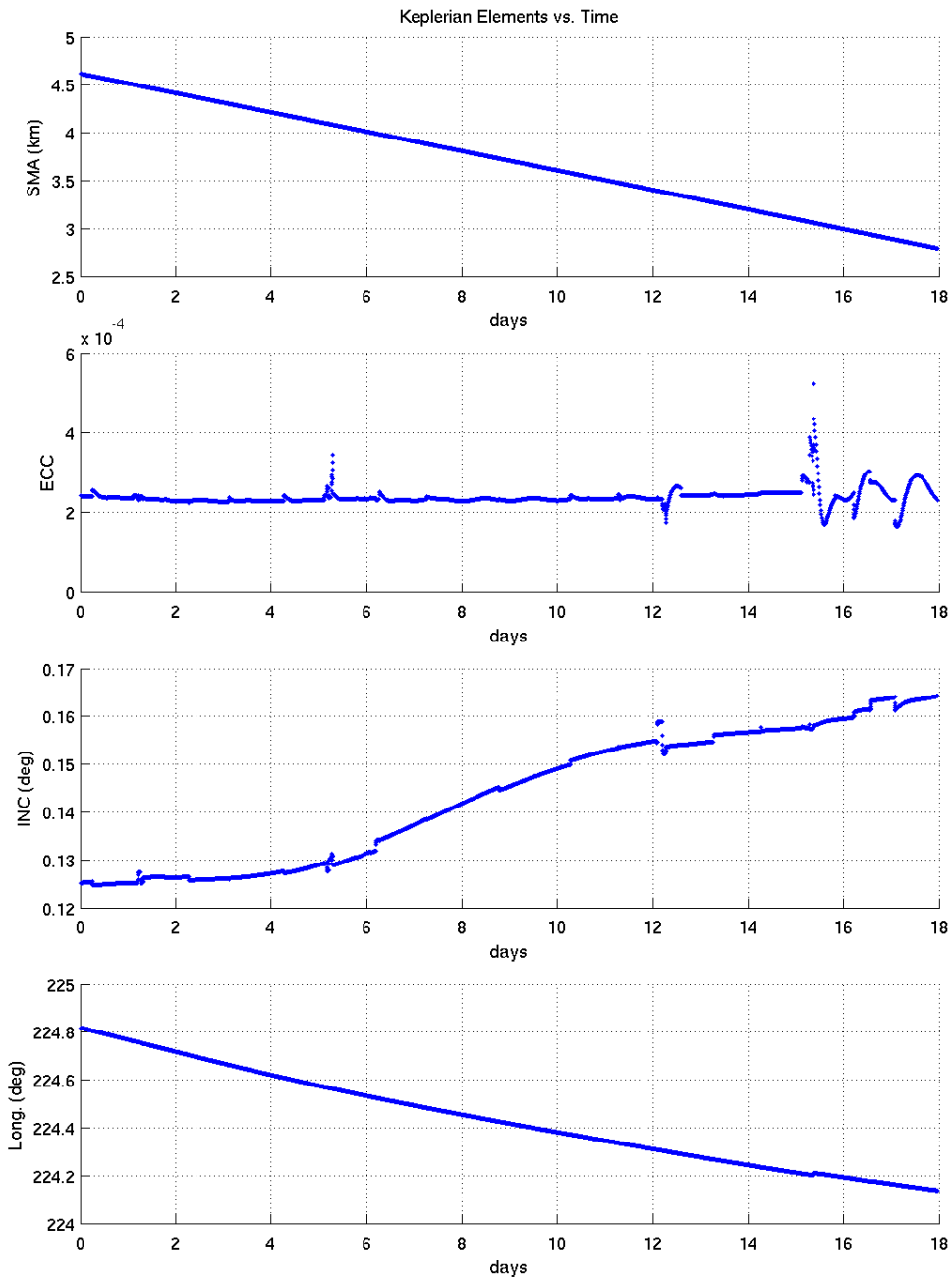


Figure 8-22 – Mean Keplerian Elements vs Time using SSN and NOAA Ranging Data with Box-wing Model (ESKF)

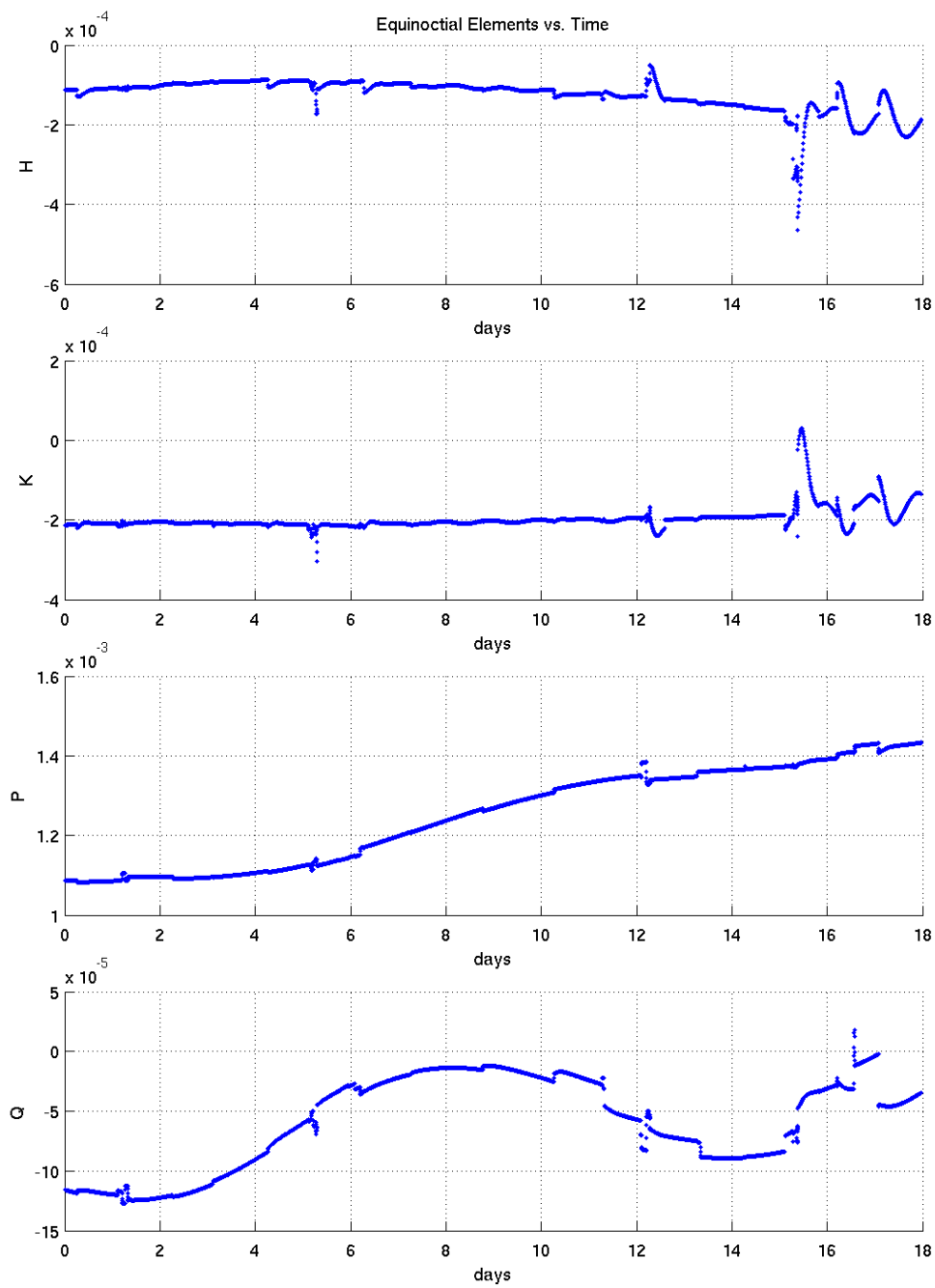


Figure 8-23 – Mean Equinoctial Elements vs Time using SSN and NOAA Ranging Data with Box-wing Model (ESKF)

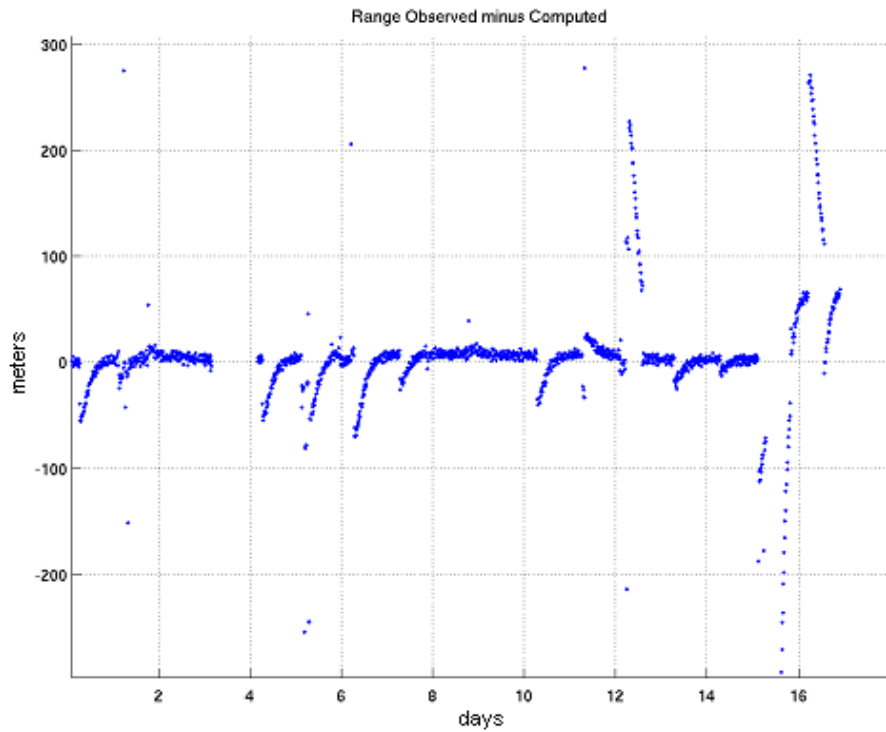


Figure 8-24 – GOES Station 6 Range Residuals vs Time using SSN and NOAA Ranging Data with Spherical Model (ESKF)

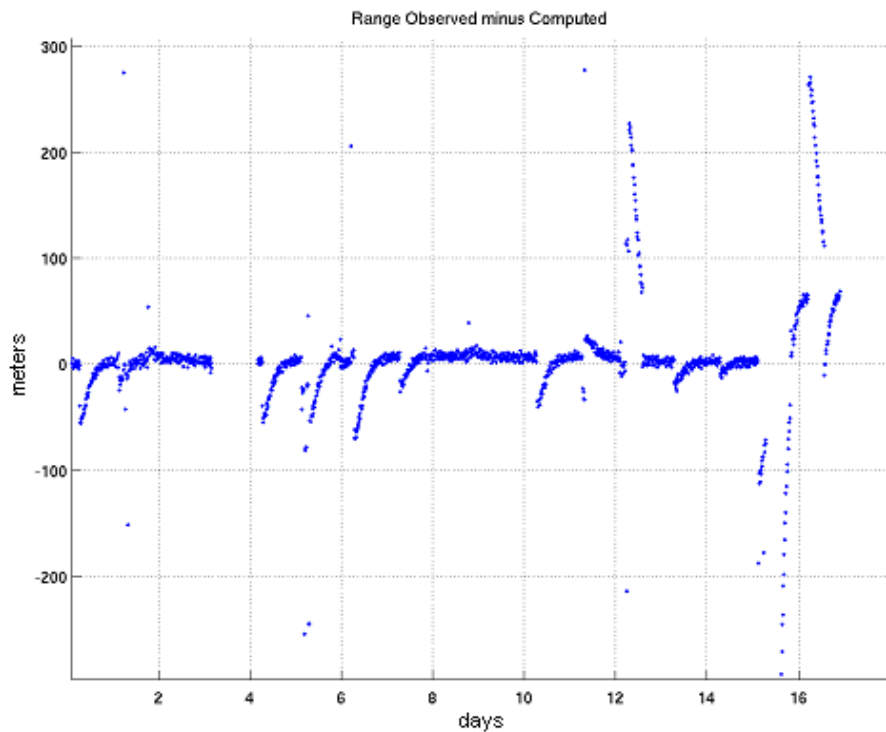


Figure 8-25 – GOES Station 6 Range Residuals vs Time using SSN and NOAA Ranging Data with Box-wing Model (ESKF)

Chapter 9 Conclusions

This thesis was motivated by the need for improved orbit determination for geosynchronous spacecraft. Specifically, this study addressed the issues of the complex geometry and attitude of modern 3-axis stabilized geostationary spacecraft, and began to address the issue of gaining a better understanding the space environment.

9.1 Modeling Enhancements in the Orbit Determination Software

An improved model for solar radiation pressure has been incorporated into the R&D version of GTDS at the MIT/Lincoln Laboratory. This model takes into account the attitude-controlled, geometrically complex nature of spacecraft, and represents the spacecraft as an assembly of flat plates, as opposed to the traditional model that represents the spacecraft as a uniformly-reflecting sphere. This so-called macro-model, or box-wing model, was incorporated from the GEODYN orbit determination system employed by the geodynamics group at the Goddard Space Flight Center.

A separate one-panel model was also incorporated into GTDS from the DSST Standalone orbit propagation system from Draper Laboratory. This model was implemented in order to understand the process of modifying GTDS to include a new solar radiation pressure model.

Additionally, a model of the Earth radiation pressure effects, including Earth albedo and Earth infrared, has been incorporated into GTDS. This model, like the box-wing model, was incorporated from the GEODYN system. The model has the capability

to calculate the force due to Earth radiation pressure for either the spherical model or the box-wing model.

The space-based visible (SBV) observations model was also incorporated into GTDS during the course of this study. Dr. Paul Cefola and Mr. Zach Folcik completed this work at the MIT/Lincoln Laboratory. This model allows GTDS to process observations from the SBV sensor, which gives greater visibility of a number of spacecraft.

All of the enhancements mentioned, including the force models and observation model, are available to both the Cowell and DSST orbit generators in GTDS.

Differential correction capability using the improved solar radiation pressure models has been completed in GTDS, and is available to both the Cowell and DSST orbit generators.

Kalman filtering capability using the box-wing solar radiation pressure model and solving for a single C_R has been implemented in the Extended Semi-analytical Kalman Filter (ESKF), and is thus available to the DSST orbit generator in GTDS.

9.2 Macro-model Analysis

Simulated data testing in this study compared the behavior of the macro-model for solar radiation pressure with the behavior of the traditional spherical model for solar radiation pressure. This testing involved the models of two different geostationary spacecraft (TDRS-05 and GOES I-M) and test cases at different times of the year (solstice and equinox). Several conclusions can be drawn from this testing.

First, the acceleration profiles show that the spherical model cannot properly account for the changing solar projected area of spacecraft. This is especially important

when there are large nadir-pointing structures, such as the single-access antennae on the TDRS spacecraft, whose orientation with respect to the sun changes throughout the orbit. The difference between the spherical and macro-model is not as large for the GOES spacecraft, which has a more constant area projected toward the sun throughout its orbit.

The acceleration profiles also show that the difference between the macro-model and spherical model is greater at the solstice than at the equinox. This is due to the greater sun declination angle (beta prime angle) at solstice, which causes a greater cross-track acceleration that the spherical model overestimates. At the equinox, there is only a small cross-track component of the solar radiation pressure, so the mismodeling by the spherical model is not as much of an issue.

The short-periodic osculating element plots presented in Chapter 7.3 further strengthen these conclusions. These plots show that the difference between the box-wing and spherical model produces a periodic effect in the osculating elements over one orbital revolution, except in the case of the eccentricity, where there is also a secular trend. This trend is greater for the solstice case than the equinox.

The impact of the macro-model on the long-term evolution of orbits was also investigated. This was done by propagating an orbit with DSST for a full year using both the box-wing and the spherical models, using precision mean equinoctial elements. The difference in the mean equinoctial elements between the two was then plotted. As shown in Chapter 7.4, the mean elements that exhibited a difference between the box-wing and spherical model were h and k . This was expected, as these equinoctial elements are the ones related to the eccentricity of the orbit. It is also noteworthy that the differences in h

and k had the greatest rates of change in the times of the year near the solstice, again providing evidence that the macro-model is more important at solstice than at equinox.

9.3 Geosynchronous Orbit Determination

Real observation data were processed in this study for a number of TDRSS spacecraft and a number of GOES spacecraft. The different test cases used different sets of observation data, including SSN observations, HANDS optical observations, NOAA ranging data, and SBV observation data. The test cases are detailed in Chapter 8.

With the observations currently available at the MIT/Lincoln Laboratory, the box-wing model does not exhibit a large improvement over the spherical model in real data processing differential correction runs. This may be due to the fact that the observations available are not of sufficient accuracy to be able to see the improvement given by the macro-model. It could also be due to some other unmodeled effect that is limiting the accuracy of the orbits. One possible idea is to include along-track acceleration as a solve-for parameter to account for unmodeled dynamic effects.

The macro-model was valuable, however, in showing which observations needed to be edited, thinned, or de-weighted. This is most evident in the GOES-10 test cases that included the NOAA ranging data, presented in Chapter 8.2.2. The orbit fits with GOES-10 that used owner/operator ranging data in addition to the SSN observation data initially demonstrated almost identical results between the Semi-analytical and Cowell orbit generators. Unfortunately, they also demonstrated nearly-identical range residuals between the solar radiation pressure models. Due to the overwhelming amount of owner/operator ranging data compared to the amount of SSN observations, techniques were applied to thin and deweight the range data. The station range bias was also

estimated using the spherical model. When this bias was fed back in to the differential correction, an improvement in the ranging residuals was then seen with the macro-model compared to the spherical model. More significant improvement was seen when the box-wing model was used to estimate the station range bias. Additionally, the secular trend in range residuals over the fit span was clarified by the macro-model.

It was later realized that the macro-model was simply doing a better job of editing observations in the DC runs. When the same observations were edited with the spherical model, the orbit accuracy and range residuals once again became nearly identical between the two models. However, the utility of understanding which observations to edit out was a valuable advantage of the box-wing model.

In the course of this study, a better understanding was also gained of the process for determining GEO orbits using GTDS and SSN observations. Insight was gained into what observations corrections need be applied to various observation data types, including light-time corrections, ionospheric and tropospheric refraction corrections, and measurement bias corrections. Additionally, experience with the real data processing has shown which perturbations are important to consider when doing GEO orbit determination. The results are consistent with earlier work by Fonte and Sabol on developing optimal DSST input data files for various orbit types [Ref 79].

The real data processing also showed the importance of high-quality observation data. The TDRS-05 fits that included the HANDS optical data provided by Chris Sabol produced much more accurate orbits than those that used only SSN data. The GOES-10 fits that use NOAA ranging data and SBV data, with the proper observations corrections applied, demonstrated marked improvement over fits that used only SSN data. The

added observability that the owner/operator ranging and SBV data gave significantly improved the accuracy.

Initial real data filter testing using the Extended Semi-analytical Kalman Filter (ESKF) was also completed as part of this study. The ESKF was applied to both the TDRSS and GOES observation data. Similar to earlier differential correction results, there was little difference in the results between the spherical and box-wing models.

The importance of high-quality observations was further strengthened by the initial ESKF testing results. In cases that used only the HANDS optical data for TDRSS or the NOAA ranging data for GOES, the mean elements produced were very well-behaved and smoothly-varying over the fit interval. Additionally, the observation residuals from the sensors were small, with zero mean. In the cases where SSN observations were mixed with the other data sources, the mean elements had more discontinuities, and the observation residuals were not as well-behaved over the fit interval. The changes are likely due to the fact that the SSN sensors were not tasked as heavily to observe the particular spacecraft used in the initial real data ESKF testing.

Additionally, the real data testing showed consistently that the DSST is capable of producing orbits that have comparable accuracy to the Cowell theory. This further validates the usefulness and robustness of the DSST in supporting enhanced force models. It also allows for orbit determination results to be checked between the two theories for accuracy.

Chapter 10 Future Work

This chapter discusses several areas of future research that are related to this study. Some of them deal with gaining a better understanding of the space environment, including improved shadow modeling and modeling thermal re-emission. Other topics deal with extending the application of the macro-model approach in orbit determination research.

10.1 Conical Shadow Model

GTDS currently uses a cylindrical model for the Earth's shadow. This means that there is only an umbra region. Within the umbra region, it is assumed that the spacecraft experiences zero acceleration due to solar radiation pressure. A conical shadow model would include both umbra and penumbra regions. Within the penumbra regions, the spacecraft would experience some percentage of the total solar radiation pressure. Calculating the percentage of total sunlight incident on the spacecraft during penumbra is a complicated problem due to light refracted by the Earth's atmosphere. This effect also makes determining the transitions from sunlight to penumbra and from penumbra to umbra a complex problem. Modeling the space environment with a correct shadow model is thus much more complicated than simply calculating a conical shadow. Hujsak has compiled an excellent survey of technical literature relating to improved shadow modeling [Ref 80]. Vokrouhlicky also has several in-depth papers regarding solar radiation pressure and Earth albedo modeling, focusing on shadow modeling including penumbra transitions [Refs 81 – 84].

10.2 Spacecraft Thermal Imbalance Model

As mentioned in the introduction to this thesis, thermal imbalance causes thermal re-emission from the spacecraft to the ambient space environment, resulting in a disturbing force. Modeling this force requires knowledge of the thermal properties of the spacecraft, including the emissivity of the spacecraft surface materials. One possible solution would be to develop a coupled thermal model with the orbit determination system, though this could prove computationally intensive. An alternative would be to develop a simplified thermal model that captures the critical elements of the spacecraft's thermal behavior that could be used in conjunction with the orbit determination system.

10.3 Earth Radiation Pressure Variational Equations

The Earth radiation pressure model partial derivatives have yet to be implemented in GTDS. This is true for both the spherical and box-wing models.

Additionally, the Earth radiation pressure model could be improved so that it includes the DSST one-panel model. The capability of a one-panel Earth albedo model, coupled with the one-panel aerodynamic force model (see Appendix E), could prove useful in applications to spacecraft in LEO orbit, or space objects entering their decay phase, as Earth radiation pressure effects are greater at lower altitudes.

Extensive testing should also be completed to verify that the Earth albedo and Earth infrared radiation pressure model is correctly implemented into GTDS. This testing could include simulated data test cases such as generating acceleration profiles, and comparing the box-wing model to the spherical model.

10.4 Attitude Estimation

The attitude of the spacecraft in orbit affects the orientation of the macro-model with respect to the sun. It would be insightful to study the effect of misalignments in the spacecraft attitude on the effect of solar radiation pressure. Additionally, it would prove useful to have precise knowledge of the attitude of spacecraft when trying to perform precision orbit determination. The idea is that with better knowledge of the attitude, we could gain better knowledge of the radiative forces. One option that has been looked at is possibly estimating the attitude using optical observations. The intent would be to develop a coupled attitude and orbit determination system.

10.5 Kalman Filter Implementation

The capability to include the box-wing model in the Extended Semi-analytical Kalman Filter (ESKF) with a single C_R solve-for has been completed, and initial real data testing has been completed. Further testing of the ESKF, as well as implementation and testing of the Extended Kalman Filter (EKF), which uses the Cowell theory, needs to be completed. Implementing the one-panel model, as well as implementing solar radiation pressure solve-for parameters other than the single C_R , also has yet to be completed. As mentioned in Chapter 1, filters and smoothers are essential to deal with the numerous discrete events that arise in GEO orbit determination. These events include station-keeping maneuver detection, and station-keeping using electric propulsion. Future real data filter test cases could include spacecraft that use electric propulsion that have frequent owner/operator observation data available.

10.6 SOLVE Mathematics

The reflectivity values used in constructing the spacecraft macro-models used in this study were determined from a priori data based on materials properties. The true thermo-optical properties of the spacecraft in orbit are impossible to determine exactly, and can vary due to a number of factors. Because of this, it would be very useful to be able to include the reflectivity values of various plates in the macro-model as solve-for parameters. Unfortunately, there are observability issues when trying to estimate certain combinations of reflectivity coefficients, such as trying to estimate the specular and diffuse reflectivities of a single plate at the same time [Ref 36].

One possible way to solve this problem is to combine data from multiple spacecraft with similar optical properties, or data from multiple orbit arcs of the same spacecraft. A tool that could be used for this is the SOLVE mathematics package, developed at Hughes STX for NASA/GSFC [Ref 85]. Implementing the SOLVE functionality would allow for inclusion of constraints on the reflectivity coefficients to physically realistic values. The macro-models could then be “tuned” based on the observation data.

10.7 Macro-model Development for Other Spacecraft

The macro-model approach better models the radiative forces acting on spacecraft than the spherical model. Macro-models could be developed for other spacecraft of interest. The approach would be especially useful for spacecraft with large structures that present a changing projected area to the sun throughout their orbit (i.e. the nadir-pointing

single-access antennae on TDRSS). The spherical model is unable to account for the variation in the spacecraft area throughout the orbit.

The macro-model approach could be applied to spacecraft in various orbit regimes. The macro-model for solar radiation pressure would have the most impact for spacecraft with a large semimajor axis, including GEO spacecraft, where direct solar radiation pressure is a significant perturbation. An example of a candidate spacecraft is the SIRIUS spacecraft, in a long-period high-eccentricity orbit. The macro-model approach for Earth radiation pressure would have the most impact for satellites with a smaller semimajor axis, including LEO spacecraft, where the effect of Earth radiation pressure is greater. The macro-model approach could also be implemented for atmospheric effects (drag and lift) for LEO spacecraft. An example of a candidate LEO spacecraft is the IRIDIUM spacecraft.

[This page intentionally left blank.]

Appendix A Element Propagation Results

A.1 Short-periodic Element Results

This section presents complete plots of the Cowell propagation runs over one orbital revolution. These plots compare the osculating Keplerian elements between the TDRS macro-model and the spherical spacecraft model.

Figures A-1 – A-3 show the differences in the osculating elements between the TDRS macro-model and spherical model for the summer solstice test case.

Figures A-4 – A-6 show the differences in the osculating elements between the TDRS macro-model and spherical model for the autumnal equinox test case.

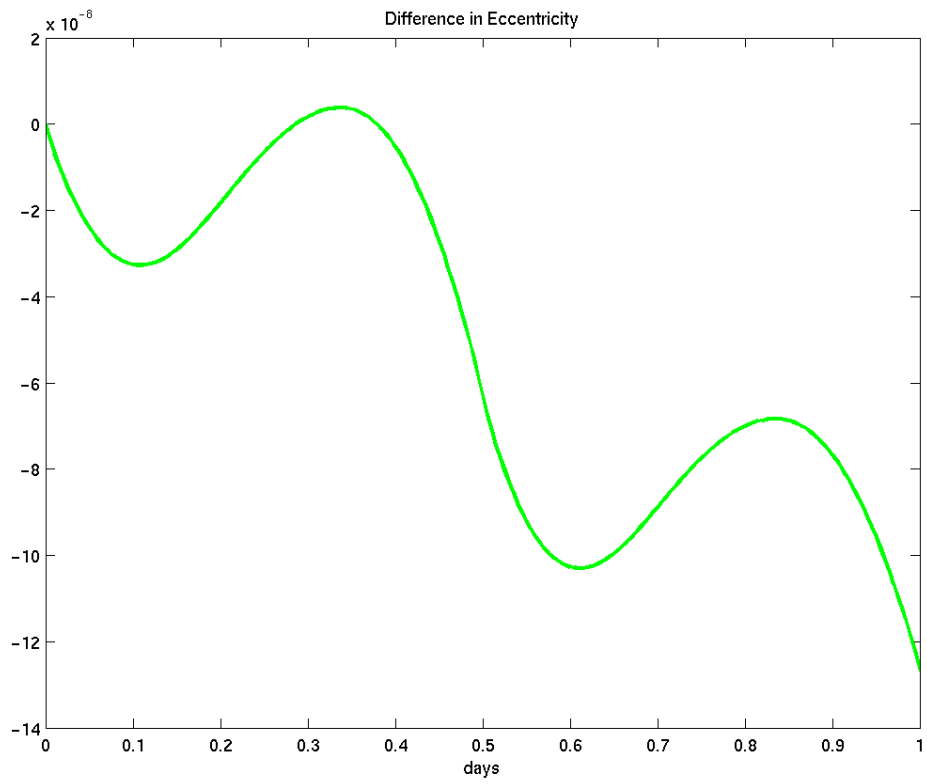
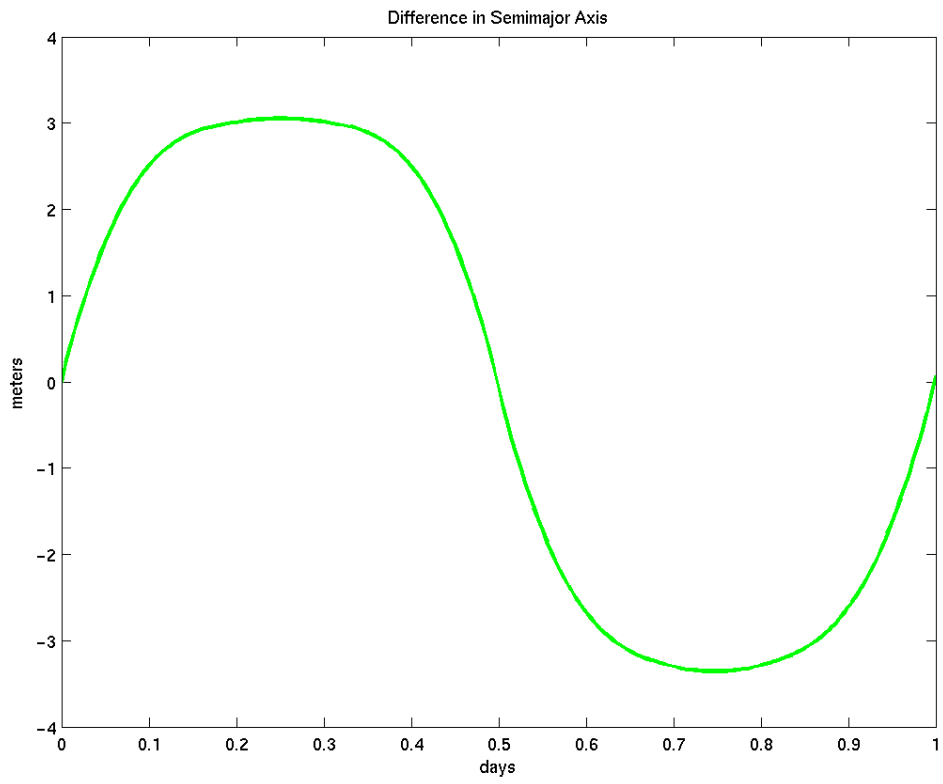


Figure A-1 – Box-wing – Spherical Difference in a and e (Summer Solstice Case)

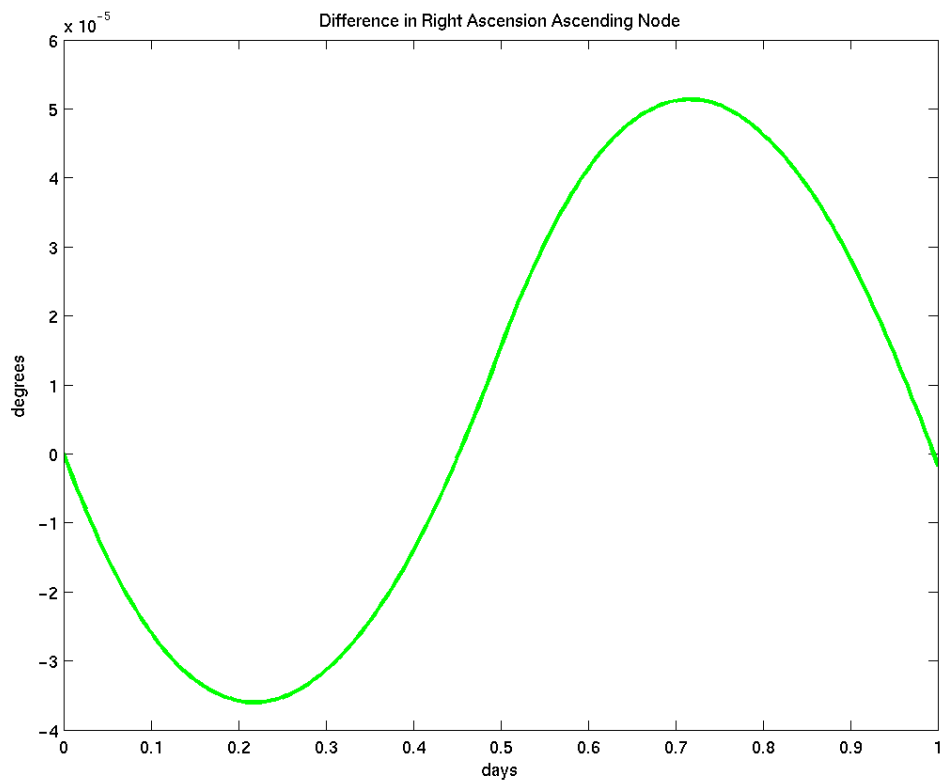
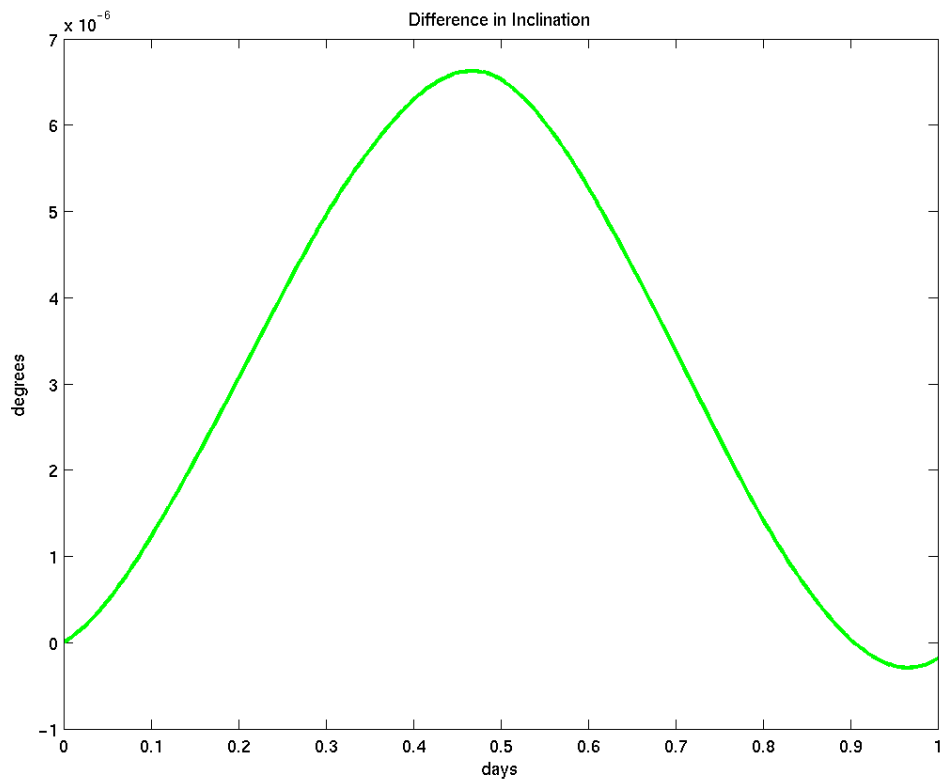


Figure A-2 – Box-wing – Spherical Difference in i and Ω (Summer Solstice Case)

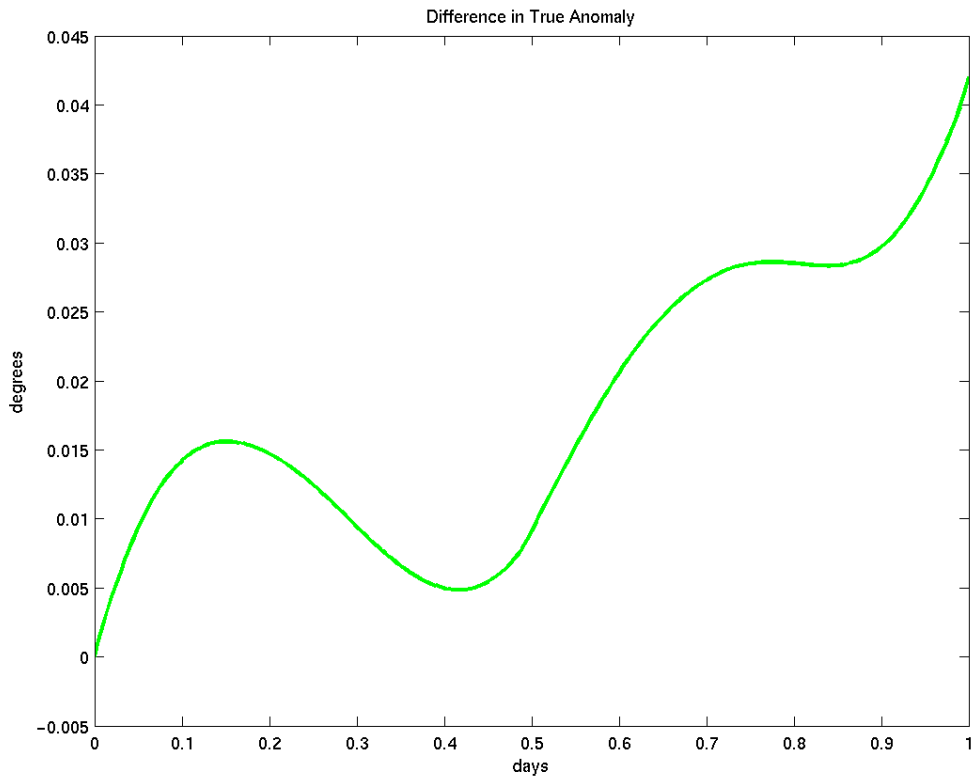
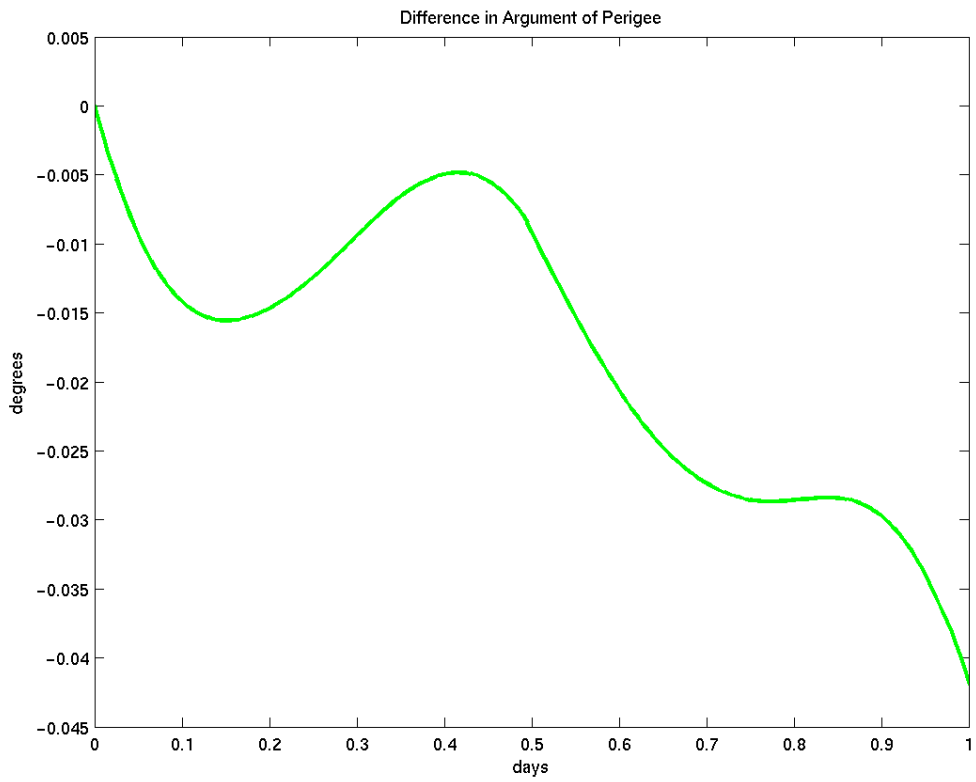


Figure A-3 – Box-wing – Spherical Difference in ω and v (Summer Solstice Case)

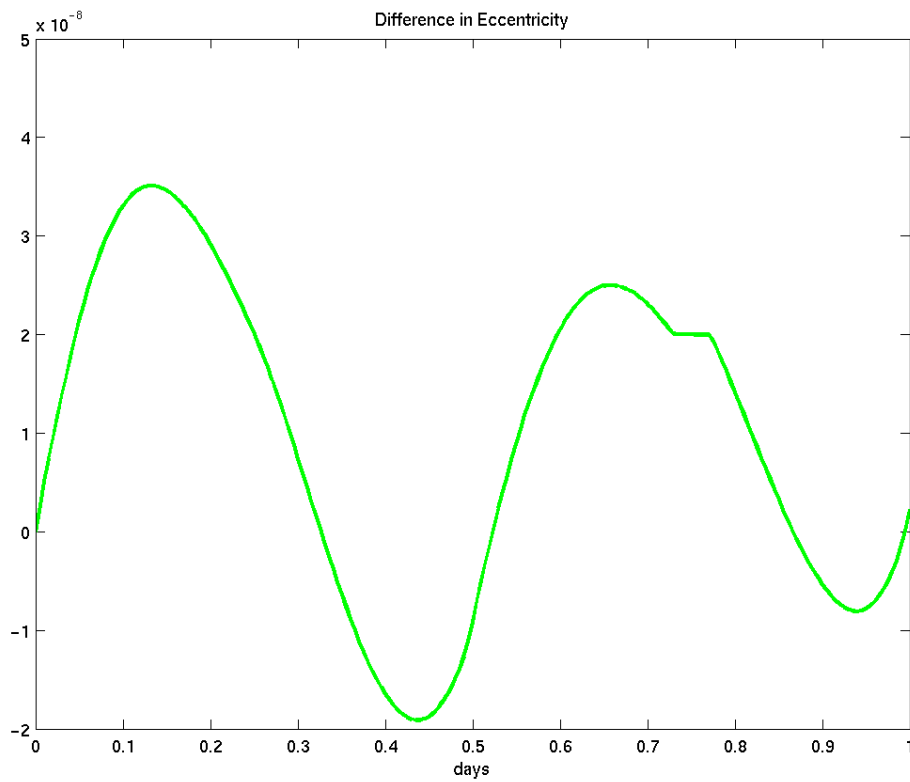
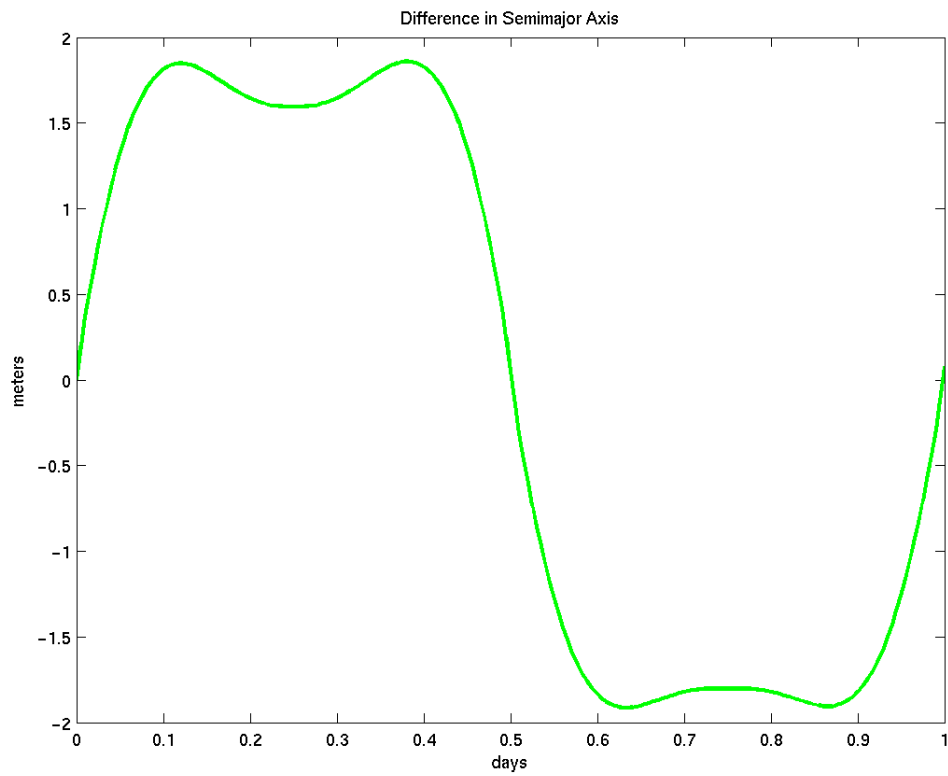


Figure A-4 – Box-wing – Spherical Difference in a and e (Autumnal Equinox Case)

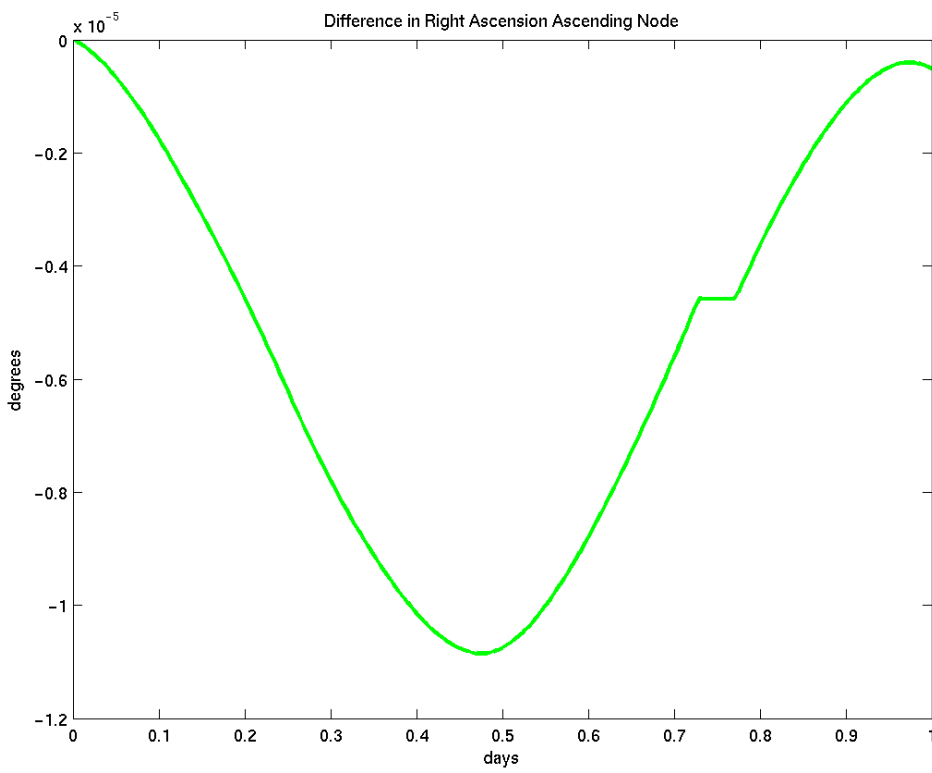
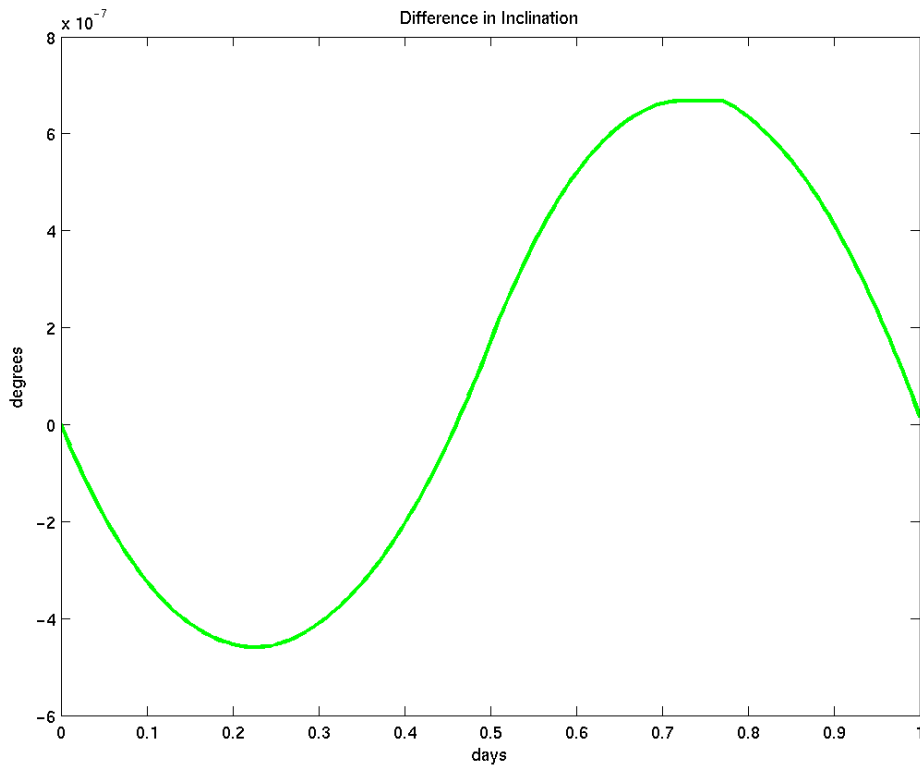


Figure A-5 – Box-wing – Spherical Difference in i and Ω (Autumnal Equinox Case)

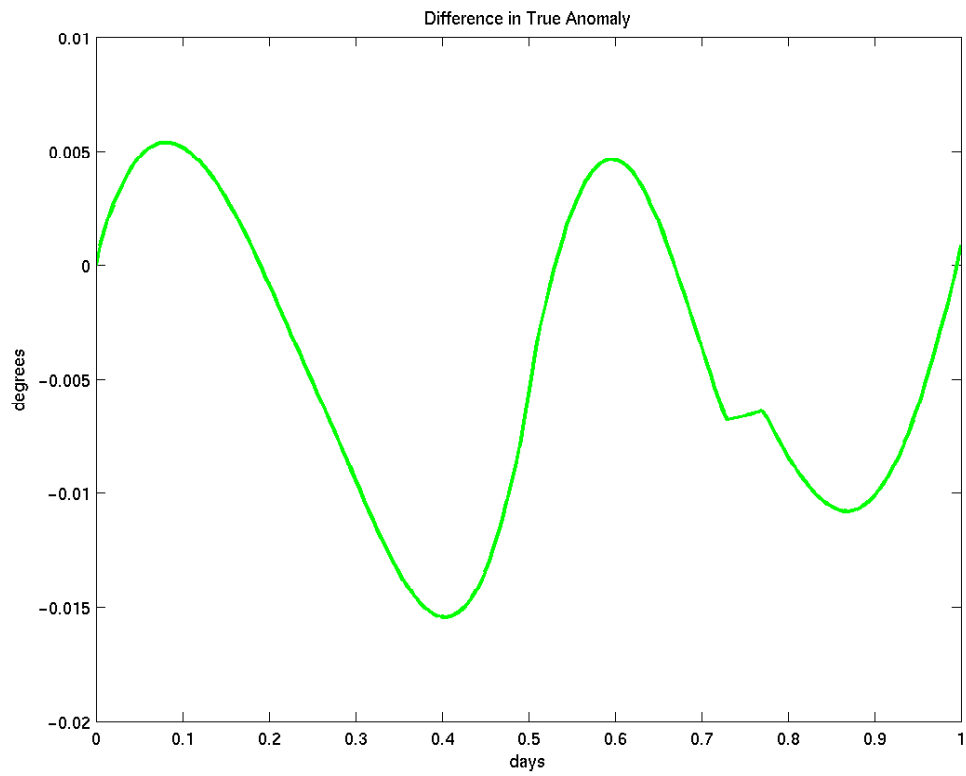
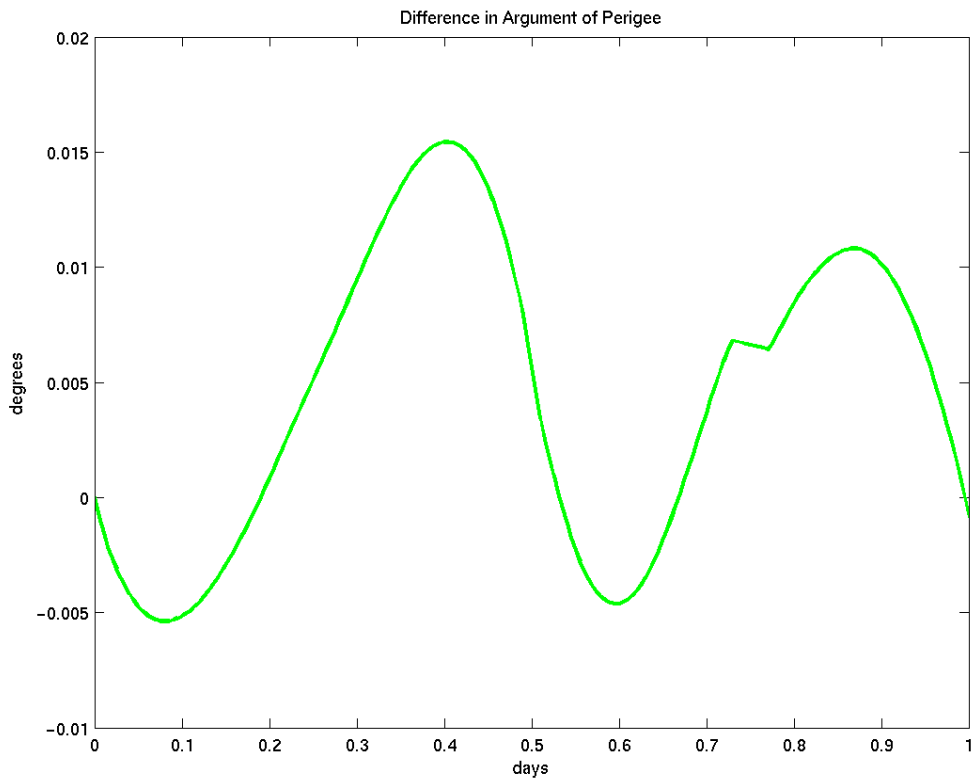


Figure A-6 – Box-wing – Spherical Difference in ω and v (Autumnal Equinox Case)

A.2 One Year Mean Element Propagation

This Appendix contains the complete set of plots of the mean equinoctial element behavior using the box-wing and spherical models. The elements are propagated using DSST for one year.

A.2.1 March 2003 – March 2004 (Vernal Equinox)

Figures A-7 – A-9 show plots of the mean elements from March 2003 – March 2004, beginning at approximately the Vernal Equinox.

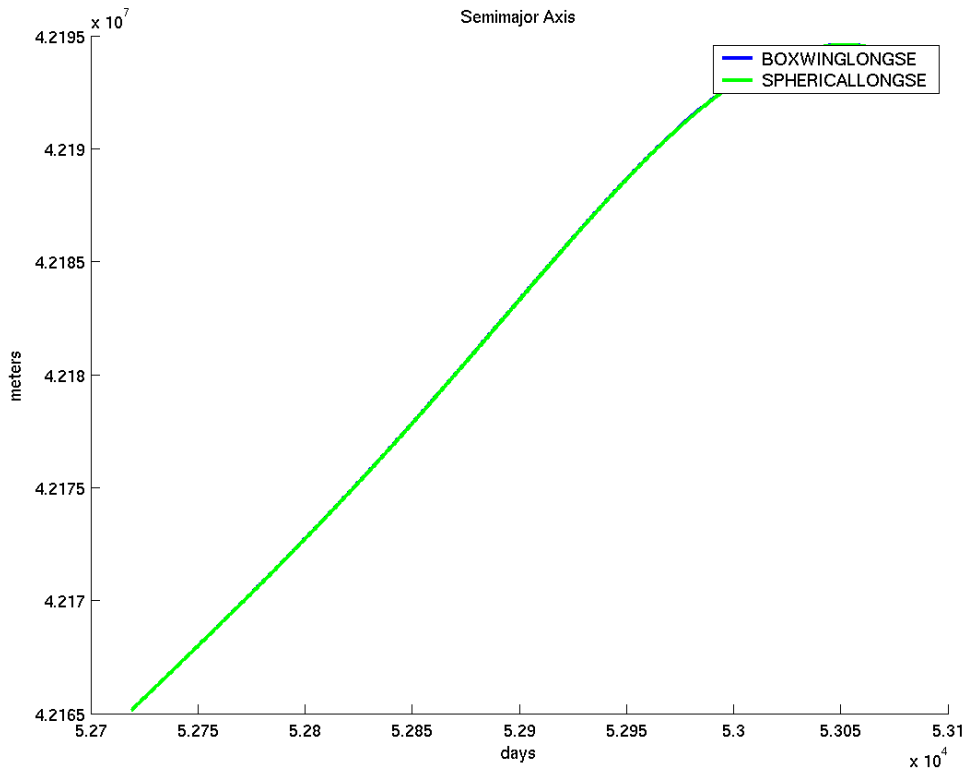


Figure A-7 – One-year Mean Element Plot of a (Vernal Equinox)

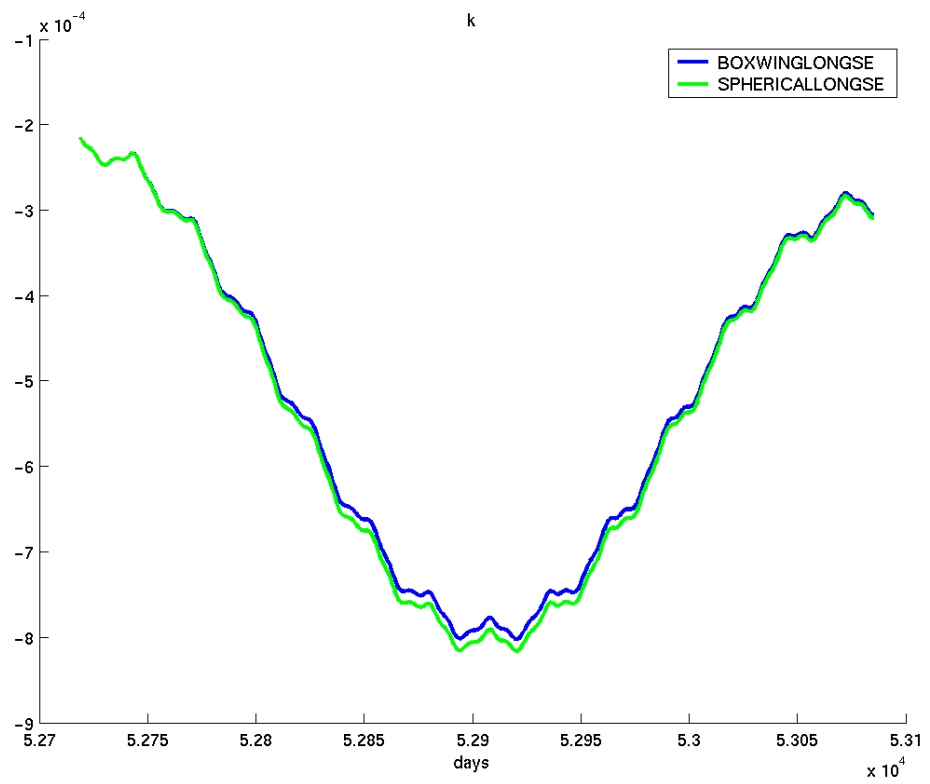
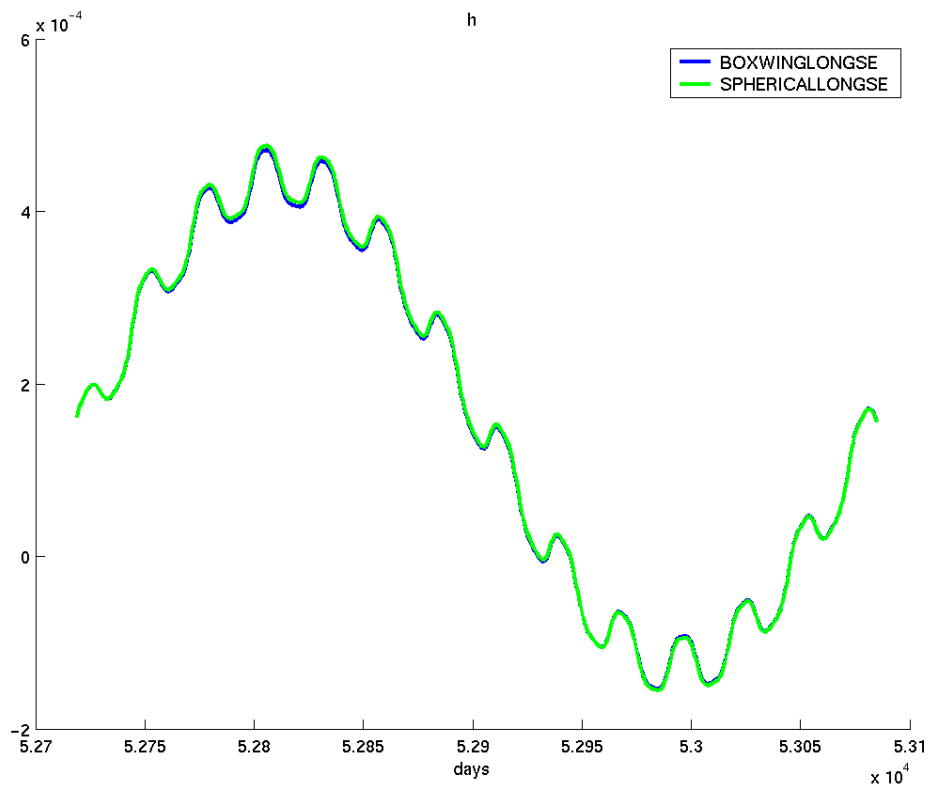


Figure A-8 – One-year Mean Element Plots of h and k (Vernal Equinox)

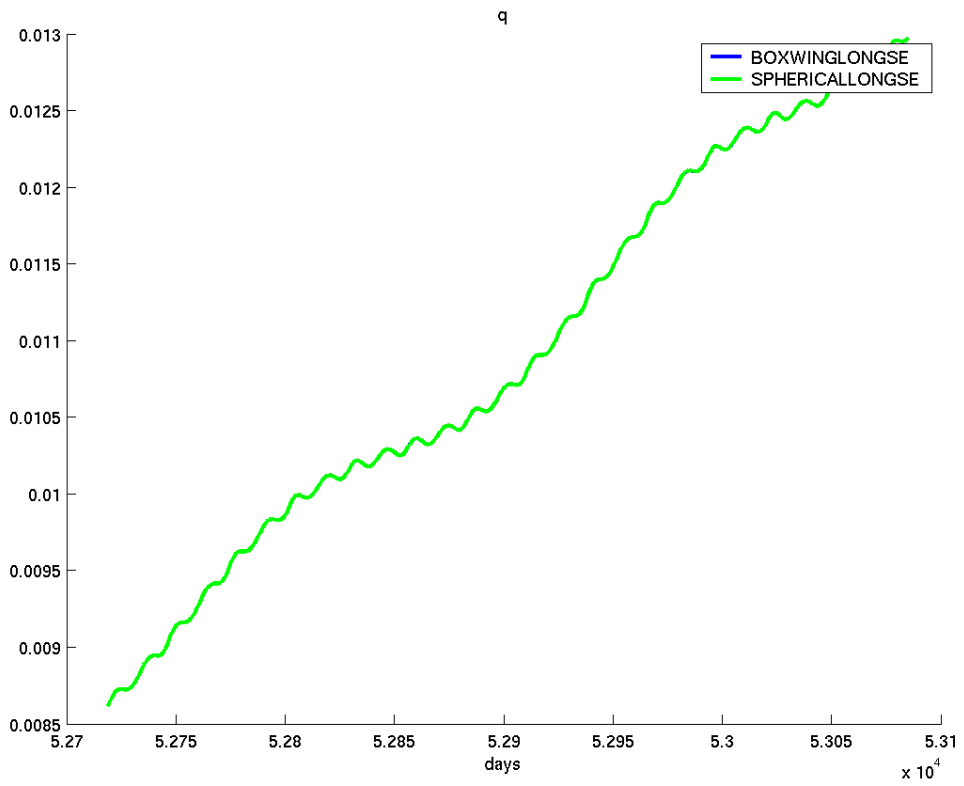
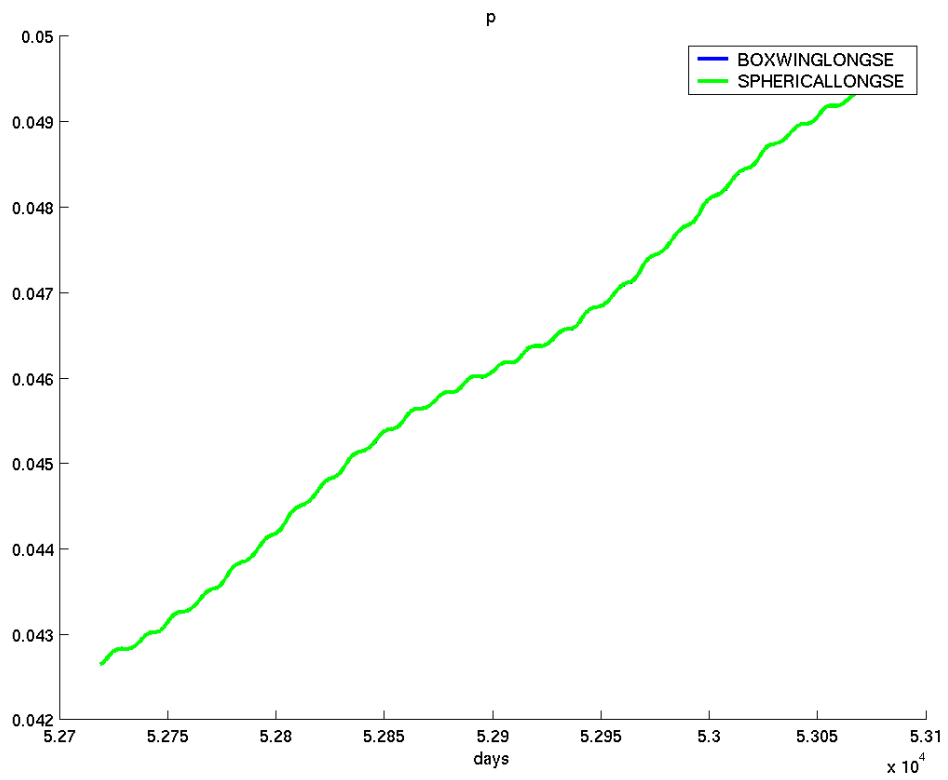


Figure A-9 – One-year Mean Element Plots of p and q (Vernal Equinox)

A.2.2 June 2003 – June 2004 (Summer Solstice)

Figures A-10 – A-12 show plots of the mean elements from June 2003 – June 2004, beginning at approximately the Summer Solstice.

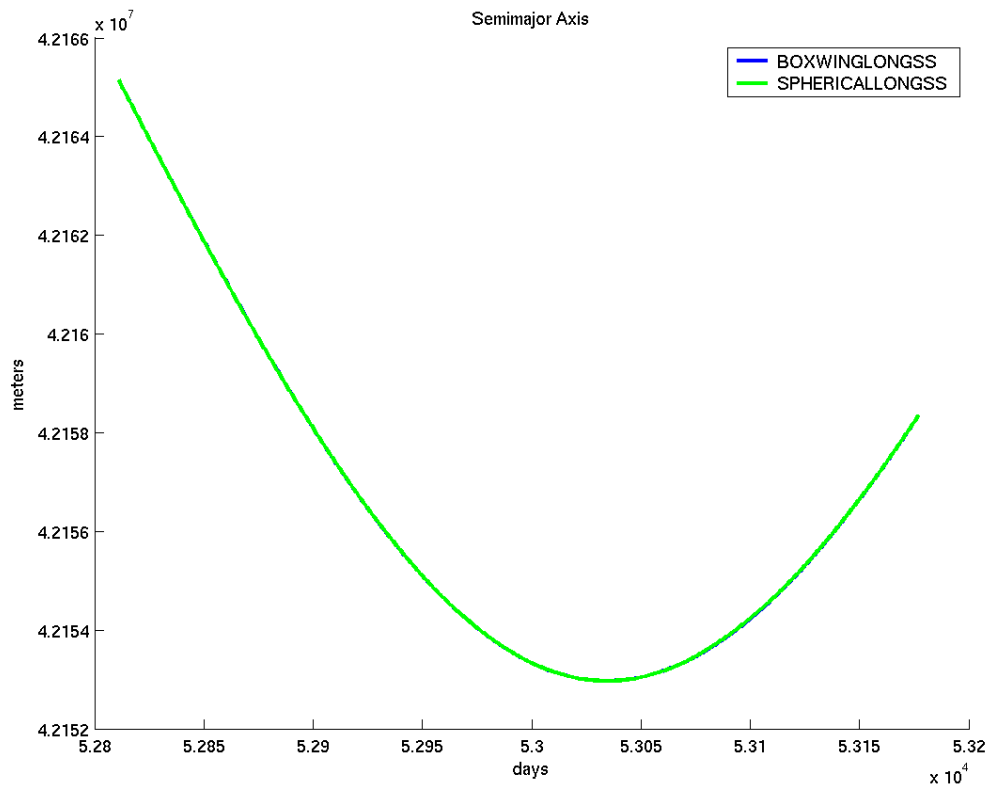


Figure A-10 – One-year Mean Element Plot of a (Summer Solstice)

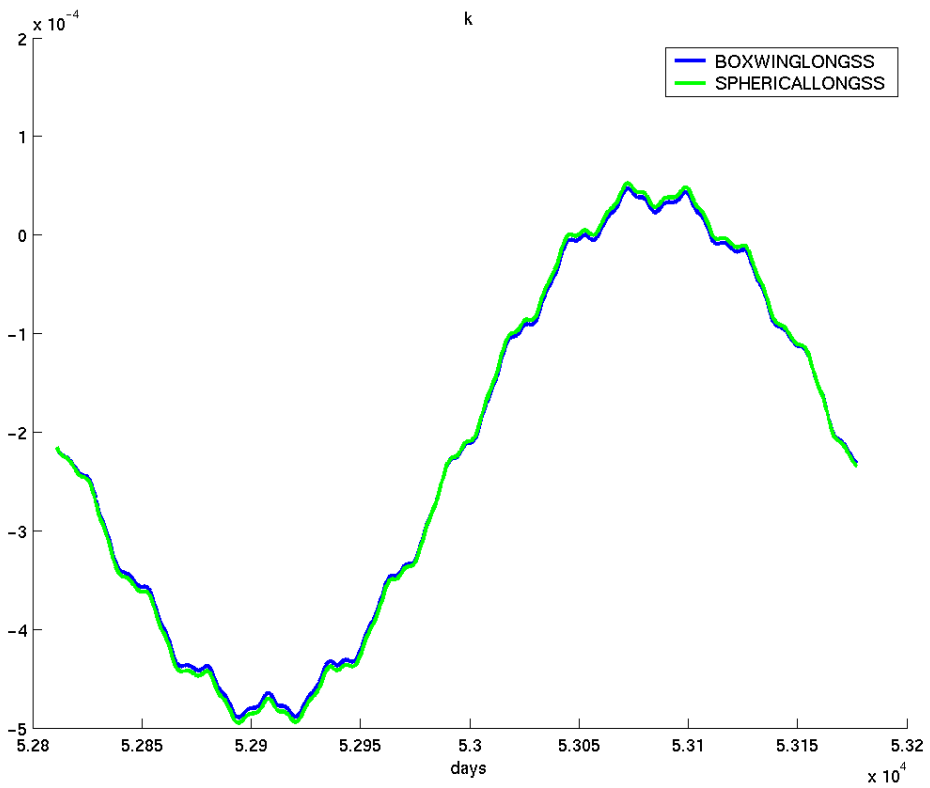
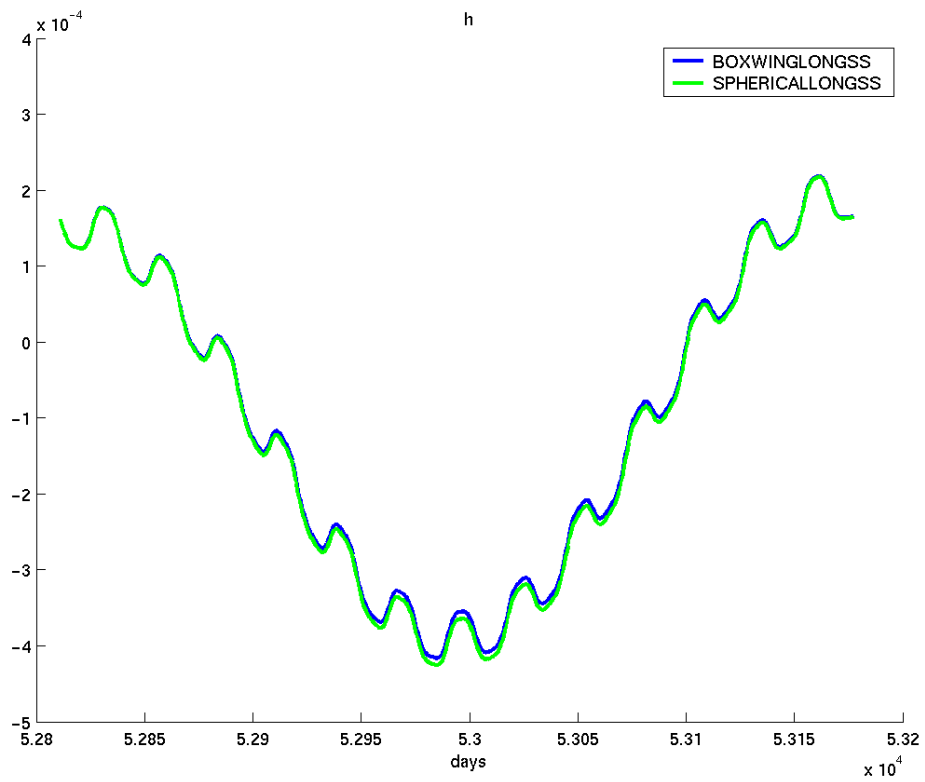


Figure A-11 – One-year Mean Element Plots of h and k (Summer Solstice)

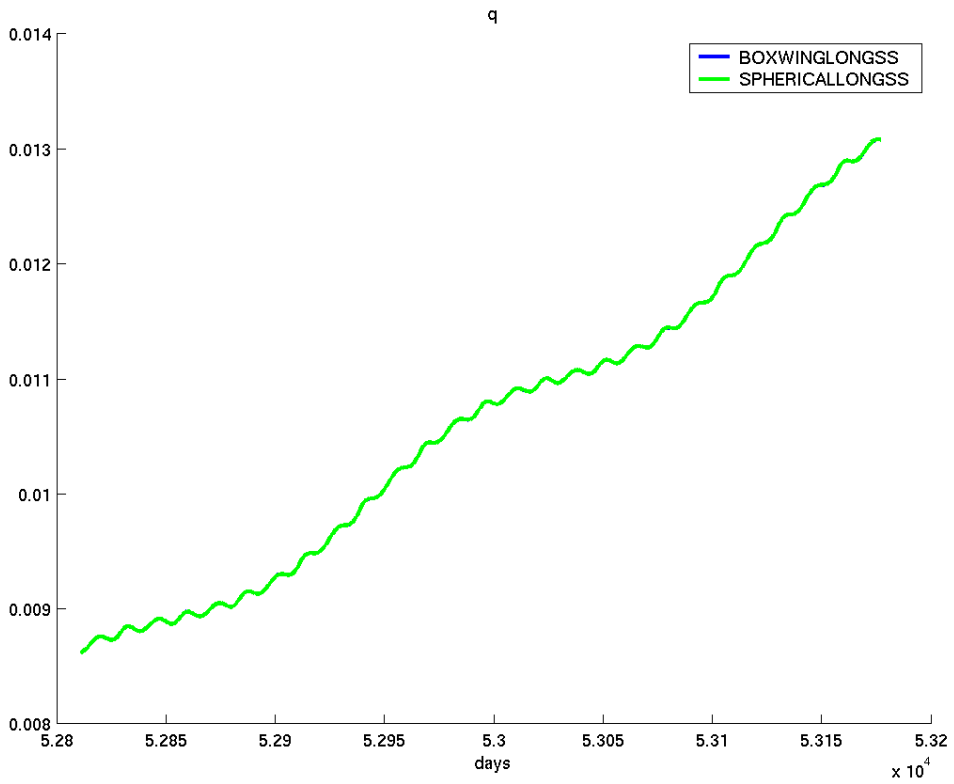
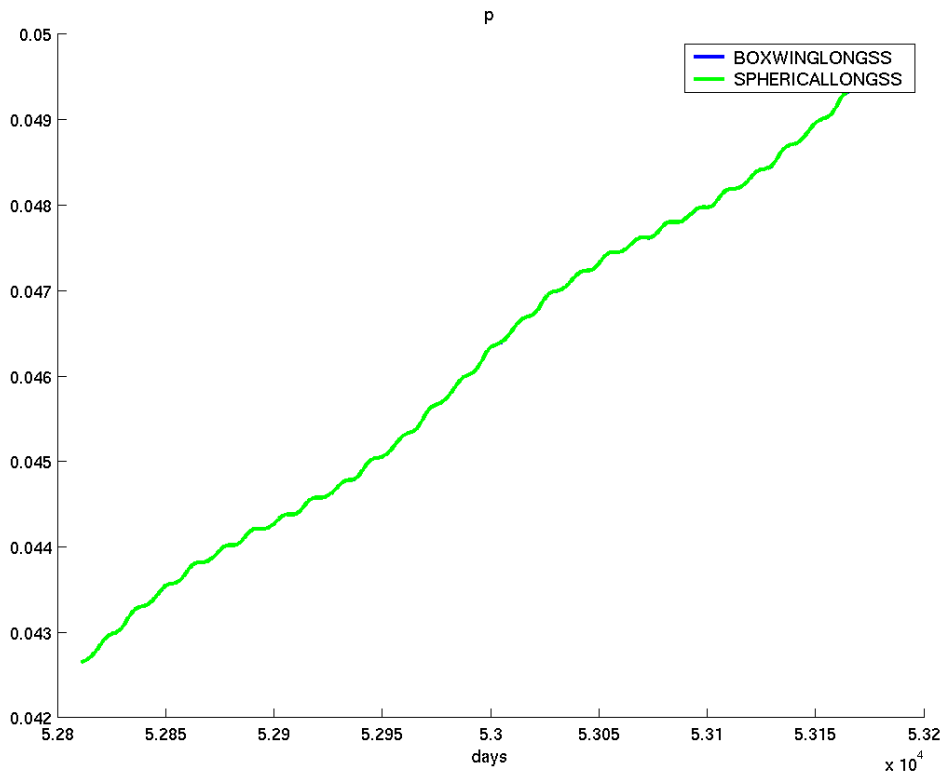


Figure A-12 – One-year Mean Element Plots of p and q (Summer Solstice)

[This page intentionally left blank.]

Appendix B Description of Modified/New GTDS Subroutines

This Appendix includes details about all of the GTDS subroutines modified, all of the new GTDS subroutines created, and all subroutines incorporated from external code as part of this project. It also includes details about the Concurrent Versions System (CVS) [Ref 40] used to control the GTDS software development environment at MIT/Lincoln Laboratory.

B.1 GTDS Subroutines for Improved Force Models

Table B-1 is a summary of the GTDS subroutines relevant to the improved radiative force model and improved aerodynamic force model improvements to GTDS. All subroutines are *.for subroutines unless otherwise indicated.

Table B-1 - Summary of Improved Force Model GTDS Subroutines

Modified Existing GTDS Subroutines:			
SETORB	SETOG1	SOLRAD	AERO
ACCEL	GQFUN	INTOGN	SOLTAB
PSET	VARFRC	SLRADV	VARDIF
AVRAGE	COREST	KFUPDT	SETAPC
New GTDS Subroutines and Include Modules:			
SOLPREBD	ALBPRED	SOLSFR_DRV	SOLPNL_DRV
BWSOLR_DRV	ALBEDO_DRV	DRGPNL_DRV	GOESAT
MAG	FRC_BW.h	FRC_ALB.h	FRC_DRG.h
Incorporated DSST Standalone Subroutines and Include Modules:			
SUNFLX	SOLSFR	ORIENT_PANEL	
SOLPNLQNT	SOLPNL	FRC_PNL.h	
PANEL.h			
Incorporated GEODYN Subroutines:			
TDRSAT	TDRSTN	BWSOLR	
ALBEDO	ALBANG	ALNRML	
ALBLOC	ALBFLX	BWALB	

B.1.1 Existing GTDS Subroutines Modified

- SETORB – Modified to handle the initial processing of the new keywords. The total number of keywords was increased, and the keyword names were entered in this subroutine.
- SETOG1 – Modified to handle the detailed processing of the new input keywords.
- SOLRAD – Modified to include more modern programming style (IMPLICIT NONE, use of structures and INCLUDE statements, etc), and to call the driver subroutines for the improved radiative force models.
- AERO – Modified to include the one-panel aerodynamic force model.
- ACCEL – Modified to properly call SOLRAD when using the Earth radiation pressure model.
- GQFUN – Modified to properly call SOLRAD when using the Earth radiation pressure model.
- INTOGN – Modified to support initializing the partial derivative switches associated with the one-panel and box-wing SRP models and to initialize the reflectivity coefficients and variances.
- SOLTAB – Modified to handle including the reflectivity coefficients in the solve-for table.
- PSET – Modified to support resetting the reflectivity coefficients adjusted through the differential correction program from the P array.
- VARFRC – Modified to handle initializing SLRADV correctly and to sum the position partial derivatives correctly when running the one-panel or box-wing

SRP models. Also modified with the intent of including the Earth radiation pressure model partials in the future.

- SLRADV – Modified to support calculating the partials with respect to the model parameters for the one-panel and box-wing SRP models. The actual calculation of the partials are done within the force model subroutines below SOLRAD, but the values are transferred to the necessary common block by SLRADV. Also modified to calculate the partial derivatives with respect to position for the new SRP models.
- VARDIF – Modified to support calculation of the one-panel and box-wing SRP reflectivity coefficients by finite differences. Also supports calculation of the one-panel lift/drag coefficients by finite differences.
- AVRAGE – Modified to support inclusion of the one-panel and box-wing SRP and the one-panel lift/drag in the calculation of the element rate partials.
- COREST – Modified to apply the ESKF update to the box-wing solar radiation pressure model single C_R solve-for and covariance, and to display the correct values in the output file.
- KFUPDT – Modified to update the box-wing solar radiation pressure model single C_R solve-for and covariance, and to display the correct values in the output file.
- SETAPC – Modified to initialize the a priori covariance of the box-wing solar radiation pressure model single C_R solve-for.

B.1.2 New GTDS Subroutines Created

- SOLPREBD – Block data subroutine that creates the SOLPRE common block, which handles variables used by the improved solar radiation pressure models.
- ALBPRED – Block data subroutine that creates the ALBPRED common block, which handles variables used by the new Earth radiation pressure model.
- SOLSFR_DRV – Driver subroutine for the spherical SRP model.
- SOLPNL_DRV – Driver subroutine for the one-panel SRP model.
- BWSOLR_DRV – Driver subroutine for the box-wing SRP model.
- ALBEDO_DRV – Driver subroutine for the Earth radiation pressure model.
- DRGPNL_DRV – Driver subroutine for the one-panel drag/lift model.
- GOESAT – Rotates the plate unit normal vectors from the spacecraft body-fixed (SBF) coordinate frame to the inertial frame for the GOES macro-model. This subroutine was based on the subroutine TDRSAT, and modified for the GOES spacecraft.
- MAG – Function that calculates the magnitude of a vector with three components. The function is called by several of the subroutines incorporated from the DSST Standalone and GEODYN.
- FRC_BW – Include module created to handle variables for the box-wing model subroutines incorporated from the GEODYN system.
- FRC_ALB – Include module created to handle variables for the Earth radiation pressure model subroutines incorporated from the GEODYN system.

- FRC_DRG – Include module created to handle variables for the one-panel aerodynamic force model.

B.1.3 Subroutines Incorporated from the DSST Standalone Orbit Propagator

- SUNFLX – Calculates the solar radiation flux at the spacecraft’s position.
- SOLSFR – Calculates the acceleration on a uniformly-reflecting spherical spacecraft due to solar radiation pressure.
- ORIENT_PANEL – Calculates the orientation of the flat panel with a given angular offset from the spacecraft-to-sun vector.
- SOLPNLQNT – Calculates the cross-sectional area of the flat panel projected toward the sun.
- SOLPNL – Calculates the solar radiation pressure acceleration on the one-panel model. Calls ORIENT_PANEL and SOLPNLQNT.
- FRC_PNL – Include module that handles variables for the subroutines incorporated from the DSST Standalone. Renamed from FRC to FRC_PNL to avoid confusion with the existing GTDS common block FRC.
- PANEL – Include module that handles variables for the one-panel model subroutines incorporated from the DSST Standalone.
- ORIENT_PANEL_DRG – Calculates the orientation of the flat panel with a given angular offset from the relative velocity vector.
- DRGPNLQNT – Calculates the cross-sectional area of the flat panel projected toward the relative velocity vector.
- DRGPNL – Calculates the aerodynamic acceleration on the one-panel model. Calls ORIENT_PANEL_DRG and DRGPNLQNT.

B.1.4 Subroutines Incorporated from the GEODYN Orbit Determination System

- TDRSAT – Rotates the plate unit normal vectors from the spacecraft body-fixed (SBF) coordinate frame to the inertial frame for the TDRSS macro-model.
- TDRSTN – Calculates the transmissivity of the single-access antennae within the TDRSS macro-model based on the solar incidence angle.
- BWSOLR – Calculates the solar radiation pressure acceleration on the box-wing model. Calls TDRSTN to include the transmissivity of the single-access antennae in the calculations.
- ALBEDO – Calculates the Earth radiation pressure effect on the spacecraft for a spherical model. Calls ALBLOC, ALBANG, and ALBFLX. Calls BWALB and skips the calculations for a spherical model, if the box-wing model is being used instead.
- ALBANG – Calculates the angle between the Earth segment rings and the SBF nadir pointing (+Z) axis.
- ALNRML – Calculates two vectors that are normal to the radial vector and to each other; these are used in the albedo model.
- ALBLOC – Calculates the location of the Earth segments.
- ALBFLX – Calculates the shortwave and longwave radiation flux from each Earth segment.
- BWALB – Calculates the Earth radiation pressure acceleration on the box-wing model. Calls TDRSTN to include the transmissivity of the single-access antennae in the calculations.

B.2 GTDS Subroutines for SBV Observations Model

Table B-2 is a summary of the GTDS subroutines relevant to the space-based visible (SBV) observations model improvements to GTDS.

Table B-2 - Summary of SBV Obs Model GTDS Subroutines

Modified Existing GTDS Subroutines:			
EXPDTBD	FILESBD	DCFLBD	DSPCONBD
SOROMCBD	SWITCHBD	ESTFLGBD	SETDM
OBSWF	OBS	DEFCON	OBSWT
OBSTRK	TRKPRT	SETDAF	SETDC
INTDEP			
New GTDS Subroutines:			
SBV_RDNUMR	SBV_OBSCRD	SBV_SORT_POS	
SBV_READ_POS		SBV_WRITE_POS	

B.2.1 Existing GTDS Subroutines Modified

- EXPDTBD – Added block data elements for the SBV observation types (types 96 and 97)
- FILESBD – Modified to include placeholders to process the SBV observations, including placeholders for the space -based observation file (unit 109) and for the space-based position/velocity working file (unit 110)
- DCFLBD – Added storage and equivalence statements for SBV DEC, RA and RHO values. These values allow communication between the subroutine that generate computed observations (OBSTRK) and the subroutine that computes partial derivatives (TRKPRT).
- DSPCONBD – Added DATA statements to populate elements 96 and 97 in arrays. These types help recognize the SBV RA and DEC obs types. This file is used in data simulation. Not all software to simulate space-based observations is implemented.

- SOROMCBD - Added DATA statements to initialize elements 96 and 97 with values like those used for elements 6 and 7. This modification was needed for the default weights for types 96 and 97 to be initialized.
- SWITCHBD – Added comments to explain element 210, which flags which obs model is being used. Also added comments and equivalence statements for items (228,229,230) for the PCE, equinoctial and SBV obs in switchbd.for
- ESTFLGBD – Added comments describing values for the IPCECS, IPCESR.
- SETDM – Modified so that SBV observations are treated as tracking observations.
- OBSWF – Added the SBV observation file indicator, IND(230), in calculating ISUM. Otherwise, the SBV observations would not be used.
- OBS - Modernized code by replacing computed GOTO statement.
- DEFCON – Modified to recognize SBV types 96 and 97 in the ITAB array.
- OBSWT – Modified to handle converting the SBV observations to the sorted working files formatted as required by GTDS.
- OBSTRK – Modified to handle calculating the estimated (computed) SBV observations. Includes the necessary coordinate system conversions from ECEF to J2000. Calls TRKPRT to calculate the SBV observation partial derivatives. Implemented the SBV light-time correction, which uses J2000 velocity vectors rather than Mean of 1950 velocity vectors. Also added a light time correction to Ground-based optical observations (MTYPES 6, 7, and 8).
- TRKPRT – Added SBV partial derivative functionality to OBSTRK.

- SETDAF – Modified to handle opening the SBV sensor working files. Also modified so that the general ionospheric coefficients file (unit 39) is opened.
- SETDC – Changed the processing of station card zero so that obs types greater than 30 can be processed. Obstat array initialized so that types 96 and 97 are given initial values like those used for types 6 and 7. The limit is now set to 97 to allow use of SBV types 96 and 97. Also modified so that sensor types 11-14 allow bias solves.
- INTDEP – Modified so that simulation of RA,DEC (6,7) obs will default to obs model 1 in IND(210) instead of 2.

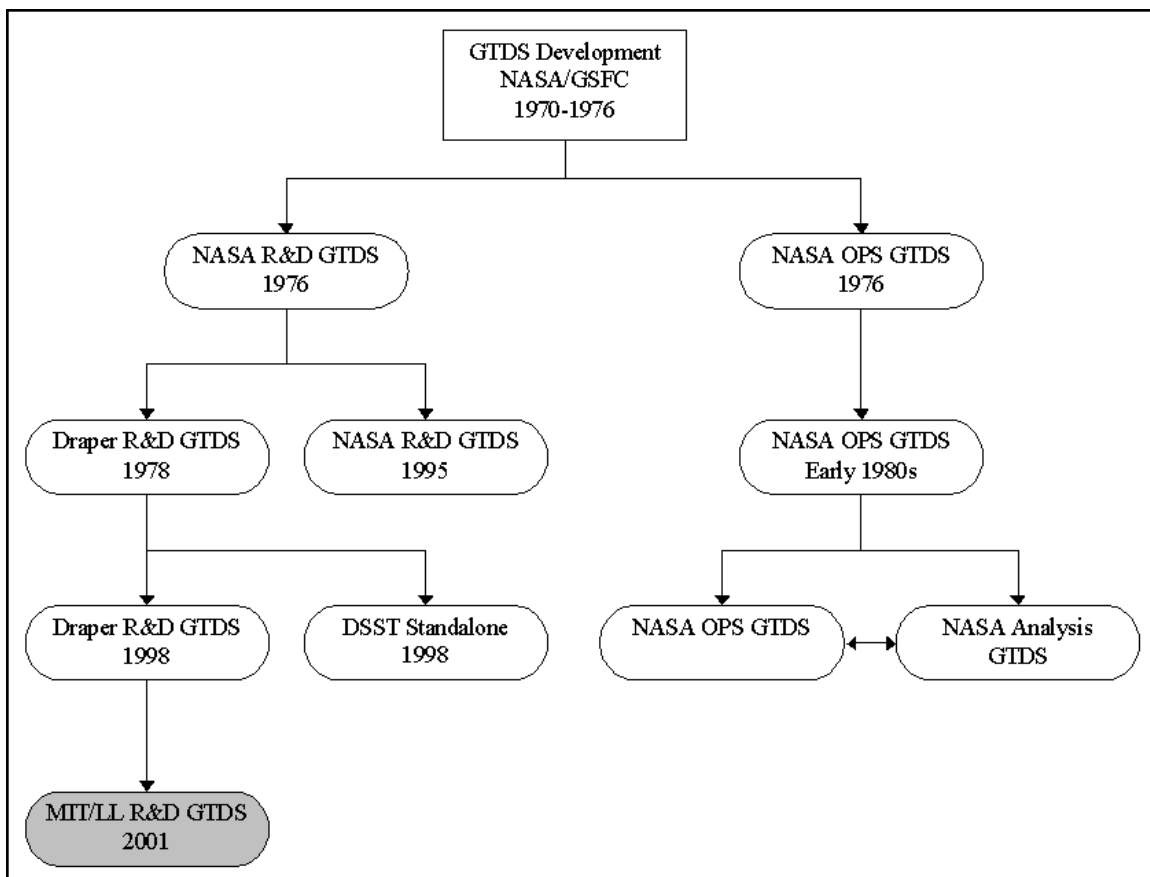
B.2.2 New GTDS Subroutines Created

- SBV_RDNUMR – Parses the lines in the new SBV sensor observation file.
- SBV_OBSCRD – Driver for reading the lines from the new SBV sensor observation file.
- SBV_SORT_POS – Sorts the working file used to store the sensor position/velocity vectors.
- SBV_WRITE_POS – Writes records to the working file used to store the sensor position/velocity vectors.
- SBV_READ_POS – Reads the next unread position/velocity record in the space-based sensor position/velocity working file.

B.3 GTDS Developmental History

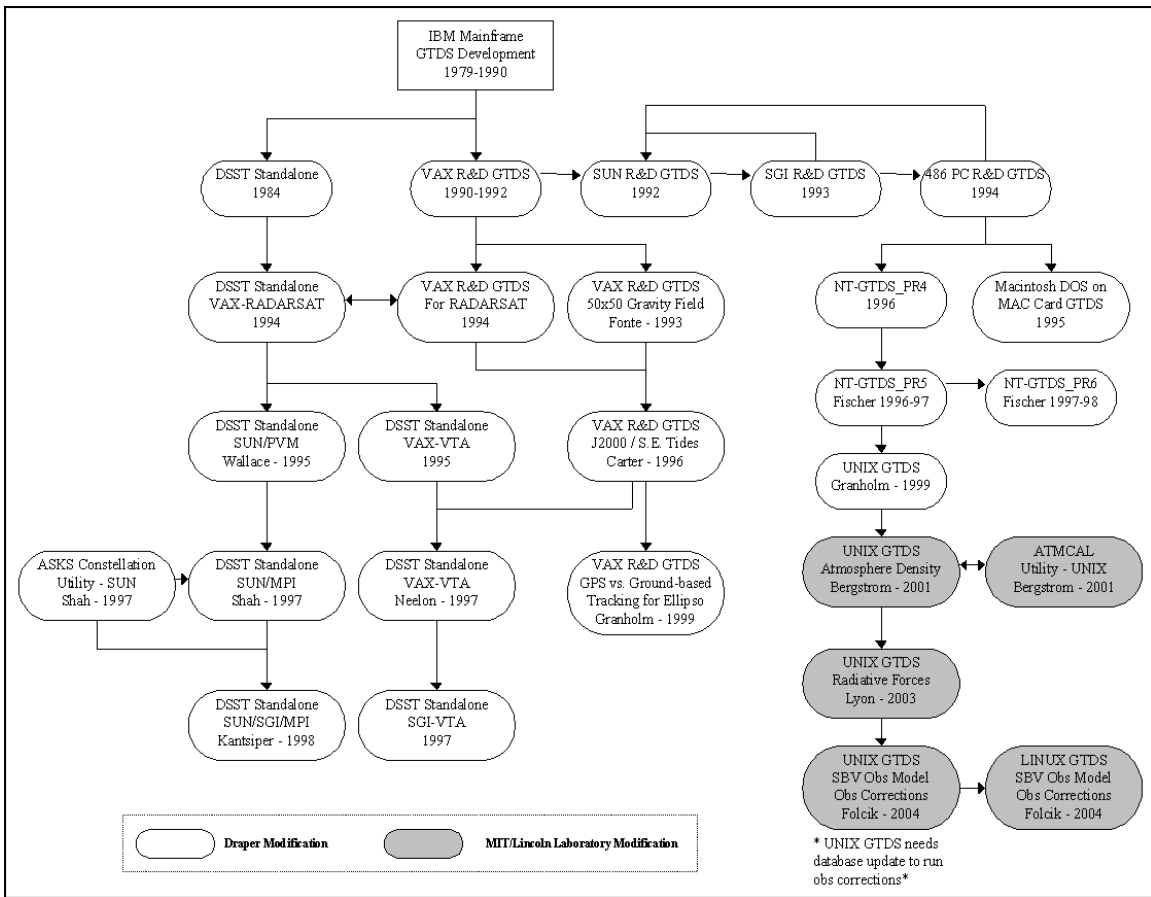
Figure B-1 shows the initial developmental history of the Goddard Trajectory Determination System (GTDS), as documented in Jack Fischer's 1998 MIT SM thesis

[Ref 53]. Initial development took place at NASA/GSFC in the early 1970s, followed by evolution into two primary separate versions: the operational and R&D versions. The R&D version was transferred to the Draper Laboratory by NASA/GSFC in 1978 to support a project for the U.S. Air Force Space Division, and has been extensively modified at the Draper over the past 25 years. The R&D version came to the MIT/Lincoln Laboratory in 2001 to support Sarah Bergstrom’s work on atmospheric density corrections [Ref 71].



Source – Jack Fischer’s MIT SM Thesis [Ref 53]

Figure B-1 – GTDS Initial Developmental History Diagram



Source – Jack Fischer’s MIT SM Thesis [Ref 53]

Figure B-2 – Draper and MIT/LL R&D GTDS Developmental History

Figure B-2 shows the developmental history of R&D GTDS at Draper Laboratory, as documented in Jack Fischer’s 1998 MIT SM thesis [Ref 53]. It also shows the developmental history of GTDS at the MIT/Lincoln Laboratory. Of note are the multiple platforms on which versions of GTDS have been developed, including the IBM Mainframe, VAX, Sun Workstation, Macintosh, PC, UNIX, and LINUX environments. Test cases by Rick Metzinger [Ref 74] have demonstrated that the various versions yield nearly identical results for the basic GTDS functions, and these test cases have been used to validate the system when it has been ported to new environments. Different functional capabilities have been implemented on the various platforms, and

effort is necessary to consolidate all of the various versions and capabilities into a single cross-platform version. At the MIT/Lincoln Laboratory, there currently exist UNIX and LINUX versions of R&D GTDS, which have evolved from the Draper Laboratory PC version of R&D GTDS.

B.4 Concurrent Versions System (CVS) at MIT/LL

Files included in CVS are stored in repositories. The files in the repositories are never modified directly, but instead are checked in and out using CVS commands [Ref 40]. The files under CVS are stored with a revision number and corresponding comments. These comments are input by the user when the file is checked into the repository. It is possible to view comments, track changes, and revert to old versions of files. CVS is also able to merge changes made by multiple users, as it compares files line-by-line when updating.

The CVS repositories at the MIT/Lincoln Laboratory are used to control the source code for R&D GTDS and are stored on the SGI-UNIX computer 'pisces'. They are accessible via both the SGI-UNIX and LINUX environments at the MIT/Lincoln Laboratory. Enhancements made to GTDS at MIT/LL that are committed to the CVS repository are thus available to either version of the system. George Granholm's MIT SM thesis [Ref 70] and the CVS webpage [Ref 40] have details about the various CVS commands, and are good resources for actually using CVS.

Appendix C GTDS Input Keyword Descriptions

This appendix contains detailed usage descriptions for all of the GTDS input keywords that were created as part of this study. These keywords are used to set options and parameters for the improved radiative force models implemented into GTDS, including the new solar radiation pressure models (the DSST one-panel model and the macro-model from GEODYN), as well as the Earth albedo/IR model from GEODYN. A summary of the new GTDS input keywords may be found in Chapter 6.2.3 of this thesis.

The following table is a repeat of Table 6-1, giving a concise summary and classification of the new GTDS input keywords.

General Solar Radiation Pressure Keyword:	
SOLRADMD	
One-panel Model (Alternate Parameterization) Keywords:	
Force Model Keywords	Differential Correction Keywords
SRPPANOF SRPPANRE	SRPPANSL SRPAPGSP
Box-wing Model (Macro-model) Keywords:	
Force Model Keywords	Differential Correction Keywords
SRPBWNUM SRPBWNRM SRPBWREF	SRPBWSLV SRPAPGBW
General Earth Radiation Pressure Keyword:	
ALBEDOMD	

(10 Jan 2003)
(rev. 20 Oct 2003)

SOLRADMD
(OGOPT)

SOLRADMD

- Card format: (A8, 3I3, 3G21.14)
- Applicable Programs: (EPHEM, DC, FILTER)
- Detailed Format:

<u>Columns</u>	<u>Format</u>	<u>Description</u>
1-8	A8	SOLRADMD - KEYWORD to set the particular solar radiation pressure model
9-11	I3	Solar radiation pressure model: <ul style="list-style-type: none">= 1, GTDS spherical spacecraft model (this is the model that was available in the MIT community 1978 till 2003) [default]= 2, reserved for the GTDS cylindrical spacecraft model with solar panels (not currently available for solar radiation pressure – Jan 2003)= 3, reserved for the GTDS cylindrical spacecraft model without solar panels (not currently available for solar radiation pressure – Jan 2003)= 4, DSST Standalone One-panel Model – this model treats the spacecraft as a single flat plate considering specular and diffuse reflected radiation (this model was implemented in the DSST Standalone in CY 2000 and is described in an AAS Pre-print given at the Quebec City meeting in August 2001)= 5, GEODYN Box-wing Model – This model represents the spacecraft as a combination of flat plates; the radiative forces acting on each plate are computed and vector summed to produce the overall acceleration of the spacecraft center of mass= 6, GEODYN GPS ROCK4 Model – this gives the GEODYN implementation of the Global Positioning System (GPS) Rockwell 4 solar radiation pressure. It is

anticipated that this model will be used in real data testing of the enhanced solar radiation pressure options implemented in GTDS (not currently available)

12-14	I3	GEODYN Box-wing Database Options
		= 1, Single-panel Model oriented toward the sun. (This case replicates the DSST Standalone One-panel model provided by Dr. Ron Proulx with no pointing offset)
		= 2, Two-plate Model, with Plate 1 sun-pointing, and Plate 2 nadir-pointing. (This case is the model suggested by Dr. Ken Chan, "Feasibility Study of Using a Two-plate Model to Approximate the Tracking and Data Relay Satellite", NASA Contract No. NAS-25139, 31 August 1979)
		= 3, TDRS. (This case is the one used by Luthcke et. al., "Enhanced Radiative Force Modeling of the Tracking and Data Relay Satellites", 1997)
		= 4, GOES.
		= 5, LORAL Geosynchronous s/c (not currently available)
15-17	I3	Not Used
18-80	3G21.14	Not Used

(10 Jan 2003)

SRPPANOF
(OGOPT)

SRPPANOF

- Card format: (A8, 3I3, 3G21.14)
- Applicable Programs: (EPHEM, DC, FILTER)
- Detailed Format:

<u>Columns</u>	<u>Format</u>	<u>Description</u>
1-8	A8	SRPPANOF - KEYWORD to set the Solar Radiation Pressure pointing offsets for the "one-panel" spacecraft model
9-11	I3	Not Used
12-14	I3	Not Used
15-17	I3	Not Used
18-38	G21.14	Rotation angle $d\theta$ offset from nominal (sun-pointing) in inertial reference frame
39-59	G21.14	Rotation angle $d\phi$ offset from nominal (sun-pointing) in inertial reference frame
60-80	G21.14	Not Used

(10 Jan 2003)

SRPPANRE
(OGOPT)

SRPPANRE

- Card format: (A8, 3I3, 3G21.14)
- Applicable Programs: (EPHEM, DC, FILTER)
- Detailed Format:

<u>Columns</u>	<u>Format</u>	<u>Description</u>
1-8	A8	SRPPANRE - KEYWORD to set the Solar Radiation Pressure reflectivity coefficients for the "one-panel" spacecraft model
9-11	I3	Not Used
12-14	I3	Not Used
15-17	I3	Not Used
18-38	G21.14	Percent of incident radiation absorbed ($0 \leq \sigma_a \leq 1$)
39-59	G21.14	Percent of reflected radiation diffusely reflected ($0 \leq \sigma \leq 1$)
60-80	G21.14	Not Used

(28 May 2003)

SRPPANSL
(OGOPT)

SRPPANSL

- Card format: (A8, 3I3, 3G21.14)
- Applicable Programs: (EPHEM, DC, FILTER)
- Detailed Format:

<u>Columns</u>	<u>Format</u>	<u>Description</u>
1-8	A8	SRPPANSL - KEYWORD to set the solve-for parameters for the "one-panel" solar radiation pressure model (σ_a , σ , and/or panel area)
9-11	I3	= 0, neither the percent of incident radiation absorbed (σ_a) nor the percent of reflected radiation diffusely reflected (σ) is a solve-for or consider parameter with the one-panel solar radiation pressure model = 1, solve for the percent of incident radiation absorbed (σ_a) only with the one-panel solar radiation pressure model = 2, solve for the percent of reflected radiation diffusely reflected (σ) only with the one-panel solar radiation pressure model = 3, solve for both the percent of incident radiation absorbed (σ_a) and the percent of reflected radiation diffusely reflected (σ) with the one-panel solar radiation pressure model
12-14	I3	= 0, the panel area is not a solve-for or consider parameter with the one-panel solar radiation pressure model = 1, solve for the panel area with the one-panel solar radiation pressure model
15-17	I3	Not Used

18-38	G21.14	Percent of incident radiation absorbed (σ_a) standard deviation
39-59	G21.14	Percent of reflected radiation diffusely reflected (σ) standard deviation
60-80	G21.14	Panel area standard deviation

(04 June 2003)

SSTAPGSP
(OGOPT)

SSTAPGSP

- Card format: (A8, 3I3, 3G21.14)
- Applicable Programs: (EPHEM, DC, FILTER)
- Detailed Format:

<u>Columns</u>	<u>Format</u>	<u>Description</u>
1-8	A8	SSTAPGSP - KEYWORD to include "one-panel" model solar radiation pressure in the element rate partial derivatives
9-11	I3	Include flat panel percent of incident radiation absorbed (σ_a) in the element rate partials = 0, no = 1, finite differences
12-14	I3	Include flat panel percent of reflected radiation diffusely reflected (σ) in the element rate partials = 0, no = 1, finite differences
15-17	I3	Not Used
18-38	G21.14	Not Used
39-59	G21.14	Not Used
60-80	G21.14	Not Used

(13 Jan 2003)

SRPBWNUM
(OGOPT)

SRPBWNUM

- Card format: (A8, 3I3, 3G21.14)
- Applicable Programs: (EPHEM, DC, FILTER)
- Detailed Format:

<u>Columns</u>	<u>Format</u>	<u>Description</u>
1-8	A8	SRPBWNUM - KEYWORD to set the number of plates to be used in the GEODYN Box-wing solar radiation pressure model
9-11	I3	Number of plates to be used for the GEODYN Box Wing solar radiation pressure model. (EX: TDRSS model uses 24 plates.)
12-14	I3	Number of plates that are moveable with respect to the spacecraft body fixed (SBF) coordinate frame. (EX: TDRSS model has 2 sun-tracking solar panels (modeled by 4 flat plates) that are moveable with respect to the SBF coordinate frame.)
15-17	I3	Not Used
18-80	3G21.14	Not Used

(13 Jan 2003)

SRPBWNRM
(OGOPT)

SRPBWNRM

- Card format: (A8, I3, 3G21.14)
- Applicable Programs: (EPHEM, DC, FILTER)
- Detailed Format:

<u>Columns</u>	<u>Format</u>	<u>Description</u>
1-8	A8	SRPBWNRM - KEYWORD to set the normal vectors for each plate in the Spacecraft Body-Fixed (SBF) coordinate frame for the GEODYN Box-wing spacecraft model
9-11	I3	Panel number
12-14	I3	Not Used
15-17	I3	Not Used
18-38	G21.14	Plate unit normal vector X component
39-59	G21.14	Plate unit normal vector Y component
60-80	G21.14	Plate unit normal vector Z component

(13 Jan 2003)

SRPBWREF
(OGOPT)

SRPBWREF

- Card format: (A8, 3I3, 3G21.14)
- Applicable Programs: (EPHEM, DC, FILTER)
- Detailed Format:

<u>Columns</u>	<u>Format</u>	<u>Description</u>
1-8	A8	SRPBWREF - KEYWORD to set the diffuse reflectivity, specular reflectivity, and area for each plate in the GEODYN Box Wing spacecraft model
9-11	I3	Plate number
12-14	I3	Not Used
15-17	I3	Not Used
18-38	G21.14	Plate diffuse reflectivity, δ , percentage of total incoming radiation
39-59	G21.14	Plate specular reflectivity, ρ , percentage of total incoming radiation
60-80	G21.14	Plate area

(28 May 2003)
 (rev Jan 2004)

SRPBWSLV
 (OGOPT)

SRPBWSLV

- Card format: (A8, 3I3, 3G21.14)
- Applicable Programs: (EPHEM, DC, FILTER)
- Detailed Format:

Columns	Format	Description
1-8	A8	SRPBWSLV - KEYWORD to set the solve-for parameters for the GEODYN Box-wing radiative force model. (Diffuse reflectivity, specular reflectivity, and area for each plate)
9-11	I3	= 1 – 50, Panel number = 0, Solve for a single C_R to scale the entire box-wing model
12-14	I3	= 0, neither the diffuse reflectivity nor specular reflectivity is a solve-for or consider parameter with the GEODYN box-wing radiative force model = 1, solve for diffuse reflectivity only with the GEODYN box-wing radiative force model = 2, solve for specular reflectivity only with the GEODYN box-wing radiative force model = 3, solve for both diffuse reflectivity and specular reflectivity with the GEODYN box-wing radiative force model
15-17	I3	= 0, the panel area is not a solve-for or consider parameter with the GEODYN box-wing radiative force model = 1, solve for the panel area with the GEODYN box-wing radiative force model
18-38	G21.14	Plate diffuse reflectivity coefficient standard deviation -or- Single C_R standard deviation

39-59	G21.14	Plate specular reflectivity coefficient standard deviation -or- Single C_R a priori value [default = 1.0]
60-80	G21.14	Plate area standard deviation

(04 June 2003)

SSTAPGBW
(OGOPT)

SSTAPGBW

- Card format: (A8, I3, 3G21.14)
- Applicable Programs: (EPHEM, DC, FILTER)
- Detailed Format:

<u>Columns</u>	<u>Format</u>	<u>Description</u>
1-8	A8	SSTAPGBW - KEYWORD to include "box-wing" model solar radiation pressure in the element rate partial derivatives
9-11	I3	Plate number
12-14	I3	Include plate diffuse reflectivity in the element rate partials = 0, no = 1, finite differences
15-17	I3	Include plate specular reflectivity in the element rate partials = 0, no = 1, finite differences
18-38	G21.14	Not Used
39-59	G21.14	Not Used
60-80	G21.14	Not Used

(24 Nov 2003)

ALBEDOMD
(OGOPT)

ALBEDOMD

- Card format: (A8, 3I3, 3G21.14)
- Applicable Programs: (EPHEM, DC, FILTER)
- Detailed Format:

<u>Columns</u>	<u>Format</u>	<u>Description</u>
1-8	A8	ALBEDOMD - KEYWORD to set the Albedo/Earth IR Radiation Pressure model options.
9-11	I3	Albedo/Earth IR Radiation Pressure Switch: = 0, Do not compute acceleration due to Albedo/Earth IR Radiation Pressure [default] = 1, Compute acceleration due to Albedo/Earth IR Radiation Pressure
12-14	I3	Number of Earth segment rings surrounding the central cap to be used in calculating Albedo and Earth IR radiation pressure [default = 2]
15-17	I3	Not Used
18-80	3G21.14	Not Used

[This page intentionally left blank.]

Appendix D Example GTDS Input Data Files

This Appendix contains example GTDS input data files that make use of the improved radiative force models, as well as the SBV observations model. These are intended to assist future researchers in utilizing the new models, in replicating the results of this thesis, and in future development of GTDS.

D.1 EPHEM Runs

The input data files in this section are used for ephemeris generation runs using the various solar radiation pressure models. The solar radiation pressure model keywords are placed in the OGOPT section of the data file.

Figure D-1 shows the input data file for an EPHEM run using the Cowell theory, the ELLIPSO Borealis orbit, and the traditional spherical solar radiation pressure model.

CONTROL	EPHEM				BOREALIS	1000701
EPOCH			970101.0	0.0		
ELEMENT1	3	2	1	10559.271	0.345705	116.565
ELEMENT2				280.0	270.0	0.0
OUTPUT	6	2	1	970401.0	0.0	86400.
ORBTYP	2	1	1	30.0		
OGOPT						
POTFIELD	1	4				
MAXDEGEQ	1			8		
MAXORDEQ	1			8		
SOLRAD	1			1		
SOLRADMD	1					
SCPARAM				2.D-6	100.0	
END						
FIN						

Figure D-1 - EPHEM Input Data File with Spherical Model

Figure D-2 shows the input data file for an EPHEM run using the DSST, the ELLIPSO Borealis orbit, and the one-panel solar radiation pressure model. This is done using the SOLRADMD, SRPPANOF, and SRPPANRE keywords..

```

CONTROL   EPHEM                                     BOREALIS   1000701
EPOCH                970101.0                      0.0
ELEMENT1  3  6  1  10472.201                       0.32652     116.583
ELEMENT2                280.0                      270.0       0.0
OUTPUT    6  2  1  970401.0                       0.0         86400.
ORBTYPE   5  1  1  43200.0                       1.0
OGOPT
SPSHPER   1
POTFIELD  1  4
MAXDEGEQ  1          8
MAXORDEQ  1          8
SOLRAD    1          1
SOLRADMD  4
SRPPANOF          0.0                      0.0
SRPPANRE          0.8                      0.0
SCPARAM          2.D-6                    100.0
AVERAGE    2                      24.0
END
FIN

```

Figure D-2 – EPHEM Input Data File with One-panel Model

Figure D-3 shows an input data file for an EPHEM run using Cowell theory, the ELLIPSO Borealis orbit, and the macro-model configured with a single panel. This is done using the SOLRADMD, SRPBWNUM, SRPBWNRM, and SRPBWREF keywords.

```

CONTROL   EPHEM                                     BOREALIS   1000701
EPOCH                970101.0                      0.0
ELEMENT1  3  2  1  10559.271                       0.345705    116.565
ELEMENT2                280.0                      270.0       0.0
OUTPUT    6  2  1  970401.0                       0.0         86400.
ORBTYPE   2  1  1  30.0
OGOPT
POTFIELD  1  4
MAXDEGEQ  1          8
MAXORDEQ  1          8
SOLRAD    1          1
SOLRADMD  5  1
SRPBWNUM  1  0
SRPBWNRM  1          1.0                      0.0         0.0
SRPBWREF  1          0.0                      0.2         2.D-6
SCPARAM          2.D-6                    100.0
END
FIN

```

Figure D-3 – EPHEM Input Data File with Macro-model (Single-Panel Case)

Figure D-4 shows an input data file for an EPHEM run using Cowell theory, the ELLIPSO Borealis orbit, the spherical solar radiation pressure model, and the albedo model. This is done using the SOLRADMD and ALBEDOMD keywords.

CONTROL	EPHEM				BOREALIS	1000701
EPOCH			970101.0	0.0		
ELEMENT1	3	2	1	10559.271	0.345705	116.565
ELEMENT2				280.0	270.0	0.0
OUTPUT	6	2	1	970401.0	0.0	86400.
ORBTYP	2	1	1	30.0		
OGOPT						
POTFIELD	1	4				
MAXDEGEQ	1			8		
MAXORDEQ	1			8		
SOLRAD	1			1		
SOLRADMD	1					
ALBEDOMD	1	2				
SCPARAM				2.D-6	100.0	
END						
FIN						

Figure D-4 - EPHEM Input Data File with Albedo Model

D.2 PCE Runs

The input data files in this section are used for Precise Conversion of Elements (PCE) runs using the various solar radiation pressure models. The solar radiation pressure model keywords are placed in the OGOPT section of the data file.

Figure D-5 shows the input data file for a test case that replicates the spherical model with the box-wing model configured as a single panel. This is the “default” reflectivity value type of test case described in Chapter 7-5. This run uses a typical GEO orbit, and a “truth” C_R of 1.2.

Figure D-6 shows the input data file for a test case using the 2-plate macro-model (one plate sun-tracking, one plate nadir-pointing), and a typical GEO orbit, with the initial reflectivity coefficients in the DC perturbed from the truth values. The DC solves for one reflectivity coefficient on each of the plates.

```

CONTROL   EPHEM                               GEO           1000001
EPOCH                                1030519.0      000000.000000
ELEMENT1  3  6  1  4.2166321655290E+04  2.8832701510676E-04  2.2774491539699E-02
ELEMENT2                                3.1135474343889E+02  1.1354633483489E+02  5.2593199972834E+01
OUTPUT    1  2  1  1030819.0          0.0            86400.0
ORBTYPE   5  1  1  43200.0          1.0
OGOPT
OUTOPT    1                                1030519000001.000  1030819000000.000  86400.00
POTFIELD  1  4
SPSHPER   1
MAXDEGEQ  1                                8.0
MAXORDEQ  1                                8.0
NCBODY    1  2  3
SOLRAD    1                                1.0
SOLRADMD  1
SCPARAM   2.D-6                            100.0
END
FIN
CONTROL   DC                               GEO           1000001
EPOCH                                1030519.0      000000.000000
ELEMENT1  3  6  1  4.2166321655290E+04  2.8832701510676E-04  2.2774491539699E-02
ELEMENT2                                3.1135474343889E+02  1.1354633483489E+02  5.2593199972834E+01
OBSINPUT  15                            1030519000000.000  1030819000000.000
ORBTYPE   5  1  1  43200.0          1.0
DMOPT
OBSDEV    21 22 23 100.0          100.0          100.0
OBSDEV    24 25 26 10.0          10.0            10.0
END
DCOPT
CONVERG   30  3  0.0001
EDIT      3  10.0
PRINTOUT  1  4  10.0
END
OGOPT
POTFIELD  1  4
MAXDEGEQ  1                                8.0
MAXORDEQ  1                                8.0
NCBODY    1  2  3
SOLRAD    1                                1.0
SOLRADMD  5  1
SRPBWNUM  1  0
SRPBWNRM  1                                1.0          0.0          0.0
SRPBWREF  1                                0.0          0.5          2.D-6
SRPBWSLV  1  2
SSTAPGBW  1  0  1
SCPARAM   2.D-6                            100.0
SPGRVFRC  1  1  1  3.0          1.0          3.0
SPTESSLC  6  6  4  2.0          -10.0         10.0
SSTESTFL  1  2  0  0.0
SSTAPGFL  1  0  0  0.0          0.0          1.0
STATEPAR  3  1
STATETAB  1  2  3  4.0          5.0          6.0
END
FIN

```

Figure D-5 – PCE Input Data File for “Default” Reflectivity Test Case

```

CONTROL   EPHEM                               GEO           1000001
EPOCH                                1030519.0      000000.000000
ELEMENT1  3  6  1  4.2166321655290E+04  2.8832701510676E-04  2.2774491539699E-02
ELEMENT2                                3.1135474343889E+02  1.1354633483489E+02  5.2593199972834E+01
OUTPUT    1  2  1  1030819.0          0.0            86400.0

```

```

ORBTYPE 5 1 1 43200.0 1.0
OGOPT
OUTOPT 1 1030519000001.000 1030819000000.000 86400.00
POTFIELD 1 4
SPSHPER 1
MAXDEGEQ 1 8.0
MAXORDEQ 1 8.0
NCBODY 1 2 3
SOLRAD 1 1.0
SOLRADMD 5 2
SRPBWNUM 2 1
SRPBWNRM 1 1.0 0.0 0.0
SRPBWREF 1 0.2 0.4 2.D-6
SRPBWNRM 2 0.0 0.0 1.0
SRPBWREF 2 0.6 0.4 2.D-6
SCPARAM 2.D-6 100.0
END
FIN
CONTROL DC GEO 1000001
EPOCH 1030519.0 000000.000000
ELEMENT1 3 6 1 4.2166321655290E+04 2.8832701510676E-04 2.2774491539699E-02
ELEMENT2 3.1135474343889E+02 1.1354633483489E+02 5.2593199972834E+01
OBSINPUT 15 1030519000000.000 1030819000000.000
ORBTYPE 5 1 1 43200.0 1.0
DMOPT
OBSDEV 21 22 23 100.0 100.0 100.0
OBSDEV 24 25 26 10.0 10.0 10.0
END
DCOPT
CONVERG 30 3 0.0001
EDIT 3 10.0
PRINTOUT 1 4 10.0
END
OGOPT
POTFIELD 1 4
MAXDEGEQ 1 8.0
MAXORDEQ 1 8.0
NCBODY 1 2 3
SOLRAD 1 1.0
SOLRADMD 5 2
SRPBWNUM 2 1
SRPBWNRM 1 1.0 0.0 0.0
SRPBWREF 1 0.2 0.5 2.D-6
SRPBWNRM 2 0.0 0.0 0.1
SRPBWREF 2 0.5 0.4 2.D-6
SRPBWSLV 1 2
SSTAPGBW 1 0 1
SRPBWSLV 2 1
SSTAPGBW 2 1 0
SCPARAM 2.D-6 100.0
SPGRVFRC 1 1 1 3.0 1.0 3.0
SPTESSLC 6 6 4 2.0 -10.0 10.0
SSTESTFL 1 2 0 0.0
SSTAPGFL 1 0 0 0.0 0.0 1.0
STATEPAR 3 1
STATETAB 1 2 3 4.0 5.0 6.0
END
FIN

```

Figure D-6 – PCE Input Data File with 2-plate Macro-model Test Case

D.3 DATASIM Runs

The input data files in this section are examples of those used for Data Simulation (DATASIM) runs using the various solar radiation pressure models. The solar radiation pressure model keywords are placed in the OGOPT section of the data files.

Figure D-7 shows the input data file that generates the “truth” orbit and observations for a test case that exercises the DATASIM program. The “CONTROL EPHEM” section of the data file generates an orbit using the Cowell theory and the TDRS-05 macro-model. The “CONTROL DATASIM” section of the data file simulates the observations using a “network” of ground stations, including radar and optical sites. The observations are simulated every 15 minutes over the propagation time span, and are simulated with no measurement errors.

Figure D-8 shows the input data file that processes the simulated observations using the Cowell Differential Correction algorithm. The TDRS-05 macro-model is used. The epoch semimajor axis is perturbed from the “truth” value by 1 km, and the single box-wing C_R is perturbed to 1.2 from its “truth” value of 1.0.

```

CONTROL   EPHEM                                     SATSAT 1
EPOCH      1031022.0                                000000.000000
ELEMENT1   1  2  1+4.21684241326894E+04+2.33191365580421E-04+1.54175713009508E-01
ELEMENT2   +2.65316474744120E+02+2.98022277606990E+02+5.21362920098702E+01
OUTPUT     1  2  1  1031109.0000                    000000.0000                    3600.0
ORBTYPE    2  1  1  100.0
OGOPT
SOLRAD     1      1.0
SOLRADMD   5  3
SRPBWNUM   24  4
SRPBWNRM   1      0.0                        0.0                        1.0
SRPBWREF   1      0.6                        0.15                       18.8574099D-6
SRPBWNRM   2      0.0                        0.0                        -1.0
SRPBWREF   2      0.6                        0.15                       18.8574099D-6
SRPBWNRM   3      0.0                        0.0                        1.0
SRPBWREF   3      0.6                        0.15                       18.8574099D-6
SRPBWNRM   4      0.0                        0.0                        -1.0
SRPBWREF   4      0.6                        0.15                       18.8574099D-6
SRPBWNRM   5      0.0                        0.0                        1.0
SRPBWREF   5      0.24482383119439              0.0736                    11.34271D-6
SRPBWNRM   6      0.0                        0.0                        -1.0
SRPBWREF   6      0.32965200271756                    0.0527                    10.76055D-6

```

SRPBWNRM	7	0.0	1.0	0.0
SRPBWREF	7	0.030847108402777	0.3391	1.449D-6
SRPBWNRM	8	0.866	0.5	0.0
SRPBWREF	8	0.2013	0.2468815012552	1.412D-6
SRPBWNRM	9	0.866	-0.5	0.0
SRPBWREF	9	0.019461061203629	0.2119	1.449D-6
SRPBWNRM	10	0.0	0.0	-1.0
SRPBWREF	10	0.3094673382933	0.2268	1.449D-6
SRPBWNRM	11	-0.866	-0.5	0.0
SRPBWREF	11	0.1789	0.12361622710403	1.45D-6
SRPBWNRM	12	-0.866	0.5	0.0
SRPBWREF	12	0.13695431202326	0.2232	1.449D-6
SRPBWNRM	13	0.0	1.0	0.0
SRPBWREF	13	0.095746628585072	0.04	1.11771D-6
SRPBWNRM	14	1.0	0.0	0.0
SRPBWREF	14	0.095746628585072	0.04	1.11771D-6
SRPBWNRM	15	0.0	-1.0	0.0
SRPBWREF	15	0.095746628585072	0.04	1.11771D-6
SRPBWNRM	16	-1.0	0.0	0.0
SRPBWREF	16	0.095746628585072	0.04	1.11771D-6
SRPBWNRM	17	0.0	1.0	0.0
SRPBWREF	17	0.095746628585072	0.04	1.11771D-6
SRPBWNRM	18	1.0	0.0	0.0
SRPBWREF	18	0.095746628585072	0.04	1.11771D-6
SRPBWNRM	19	0.0	-1.0	0.0
SRPBWREF	19	0.095746628585072	0.04	1.11771D-6
SRPBWNRM	20	-1.0	0.0	0.0
SRPBWREF	20	0.095746628585072	0.04	1.11771D-6
SRPBWNRM	21	1.	0.	0.
SRPBWREF	21	0.636	0.0375	14.7553D-6
SRPBWNRM	22	-1.	0.	0.
SRPBWREF	22	0.112	0.028	14.7553D-6
SRPBWNRM	23	1.	0.	0.
SRPBWREF	23	0.636	0.0375	14.7553D-6
SRPBWNRM	24	-1.	0.	0.
SRPBWREF	24	0.112	0.028	14.7553D-6
SCPARAM		2.D-4	2200.0	
POTFIELD	1 4			
MAXDEGEQ	1	8.0		
MAXORDEQ	1	8.0		
NCBODY	1 2 3			
OUTOPT	0 2 1	103102200000.0000	103110900000.0000	60.00
END				
FIN				
CONTROL	DATASIM			SATSAT 1
DMOPT				
/MILQ	1 0369 3	125.68676	423702.7668	2883032.7722
/EGLQ	1 0399 3	36.4885164	303420.8593581	2734707.10912
/ALTQ	1 0334 3	62.700	92413.0781	1672856.9910
/CGAC	1 0211 13	1512.224725	334902.1756	2532023.4600
/GOFQ	1 0934 3	-17.4	375644.016	2843217.016
END				
DCOPT				
DSPEA1	2 0	1031022.0	000000.0	900.0
DSPEA2	20 1 0	1031109.0	000000.0	
DSPEA3	2 1 0			
/MILQ	001004005	10.0	10.0	10.0
/MILQ	009	5.0		
/EGLQ	001004005	10.0	10.0	10.0
/EGLQ	009	10.0		
/ALTQ	001004005	8.0	10.8	10.8
/ALTQ	009	500.0		
/CGAC	006007	10.8	10.8	
/GOFQ	001004005	10.0	10.8	10.8
ELLMODEL	1	6378.137	298.257224	
/MILQ	200001			
/EGLQ	200001			
/ALTQ	200001			
/CGAC	200001			
/MGAC	200001			
/DGAC	200001			

```

/GOFQ 200001
/MILQ 700000000 900.0 1641600.0 5.0
/EGLQ 700000000 900.0 1641600.0 5.0
/ALTQ 700000000 900.0 1641600.0 5.0
/CGAC 700000000 900.0 1641600.0 5.0
/GOFQ 700000000 900.0 1641600.0 5.0
TRACKELV 3 5.0
TRACKELV 2 10.0
END
FIN

```

Figure D-7 – Cowell DATASIM Input Data File using TDRS-05 Macro-model

```

CONTROL DC SATSAT 1
EPOCH 1031022.0 000000.000000
ELEMENT1 1 2 1+4.21674241326894E+04+2.33191365580421E-04+1.54175713009508E-01
ELEMENT2 +2.65316474744120E+02+2.98022277606990E+02+5.21362920098702E+01
OBSINPUT 1 1031022000000.000 1031109000000.000
ORBTYPE 2 1 1 100.0000
DMOPT
/MILQ 1 0369 3 125.68676 423702.7668 2883032.7722
/EGLQ 1 0399 3 36.4885164 303420.8593581 2734707.10912
/ALTQ 1 0334 3 62.700 92413.0781 1672856.9910
/CGAC 1 0211 13 1512.224725 334902.1756 2532023.4600
/MGAC 1 0231 13 3059.664806 204228.9800 2034431.9812
/DGAC 1 0241 13 -62.249331 -072441.8054069 0722707.41416
/GOFQ 1 0934 3 -17.4 375644.016 2843217.016
END
DCOPT
EDIT 3 3.000000
TRACKELV 3 3.0
TRACKELV 13 3.0
/MILQ 001004005 10.0 18.0 18.0
/EGLQ 001004005 39.0 68.0 68.0
/ALTQ 001004005 8.0 28.8 28.8
/CGAC 006007 10.8 10.8
/MGAC 006007 10.8 10.8
/DGAC 006007 10.8 10.8
/GOFQ 001 10.0
PRINTOUT 1 4 10.0
ELLMODEL 1 6378.137 298.257224
END
OGOPT
POTFIELD 1 4
MAXDEGEQ 1 8.0
MAXORDEQ 1 8.0
NCBODY 1 2 3
STATEPAR 1 1
STATETAB 1 2 3 4.0 5.0 6.0
SOLRAD 1 1.0
SOLRADMD 5 3
SRPBWNUM 24 4
SRPBWNRM 1 0.0 0.0 1.0
SRPBWREF 1 0.6 0.15 18.8574099D-6
SRPBWNRM 2 0.0 0.0 -1.0
SRPBWREF 2 0.6 0.15 18.8574099D-6
SRPBWNRM 3 0.0 0.0 1.0
SRPBWREF 3 0.6 0.15 18.8574099D-6
SRPBWNRM 4 0.0 0.0 -1.0
SRPBWREF 4 0.6 0.15 18.8574099D-6
SRPBWNRM 5 0.0 0.0 1.0
SRPBWREF 5 0.24482383119439 0.0736 11.34271D-6
SRPBWNRM 6 0.0 0.0 -1.0
SRPBWREF 6 0.32965200271756 0.0527 10.76055D-6
SRPBWNRM 7 0.0 1.0 0.0
SRPBWREF 7 0.030847108402777 0.3391 1.449D-6
SRPBWNRM 8 0.866 0.5 0.0
SRPBWREF 8 0.2013 0.2468815012552 1.412D-6
SRPBWNRM 9 0.866 -0.5 0.0
SRPBWREF 9 0.019461061203629 0.2119 1.449D-6

```

SRPBWNRM	10	0.0	0.0	-1.0
SRPBWREF	10	0.3094673382933	0.2268	1.449D-6
SRPBWNRM	11	-0.866	-0.5	0.0
SRPBWREF	11	0.1789	0.12361622710403	1.45D-6
SRPBWNRM	12	-0.866	0.5	0.0
SRPBWREF	12	0.13695431202326	0.2232	1.449D-6
SRPBWNRM	13	0.0	1.0	0.0
SRPBWREF	13	0.095746628585072	0.04	1.11771D-6
SRPBWNRM	14	1.0	0.0	0.0
SRPBWREF	14	0.095746628585072	0.04	1.11771D-6
SRPBWNRM	15	0.0	-1.0	0.0
SRPBWREF	15	0.095746628585072	0.04	1.11771D-6
SRPBWNRM	16	-1.0	0.0	0.0
SRPBWREF	16	0.095746628585072	0.04	1.11771D-6
SRPBWNRM	17	0.0	1.0	0.0
SRPBWREF	17	0.095746628585072	0.04	1.11771D-6
SRPBWNRM	18	1.0	0.0	0.0
SRPBWREF	18	0.095746628585072	0.04	1.11771D-6
SRPBWNRM	19	0.0	-1.0	0.0
SRPBWREF	19	0.095746628585072	0.04	1.11771D-6
SRPBWNRM	20	-1.0	0.0	0.0
SRPBWREF	20	0.095746628585072	0.04	1.11771D-6
SRPBWNRM	21	1.	0.	0.
SRPBWREF	21	0.636	0.0375	14.7553D-6
SRPBWNRM	22	-1.	0.	0.
SRPBWREF	22	0.112	0.028	14.7553D-6
SRPBWNRM	23	1.	0.	0.
SRPBWREF	23	0.636	0.0375	14.7553D-6
SRPBWNRM	24	-1.	0.	0.
SRPBWREF	24	0.112	0.028	14.7553D-6
SCPARAM		2.D-4	2200.0	
SRPBWSLV	0		1.2	
END				
FIN				

Figure D-8 – Cowell DC Input Data File for DATASIM Case using TDRS-05 Macro-model

D.4 Real Data DC Runs

The input data files in this section are used for Differential Correction (DC) runs using real observation data and the various solar radiation pressure models. The solar radiation pressure model keywords are placed in the OGOPT section of the data file. These runs also use the SBV observations model. The relevant SBV control keywords are included in the DCOPT and DMOPT sections of the data file.

Figure D-9 shows the input data file for a test case that uses the DSST, the spherical solar radiation pressure model, and the GOES-10 test case. The observation data for this run includes SSN data, owner/operator ranging data, and SBV data. The spherical C_R is included as a solve-for parameter using the SOLRDPAR keyword. Additionally, observations corrections included in this run include light-time corrections, ionospheric and tropospheric refraction corrections, measurement bias corrections for the optical sensors, and measurement bias corrections for the owner-operator ranging station. The DC is followed by an EPHEM run that covers the fit span.

```

CONTROL   DC                               SATSAT-0   0024786
EPOCH                    1031020.0          120000.000
ELEMENT1  1  6  1+4.21618142278187E+04+4.408000000000000E-04+1.650000000000000E-01
ELEMENT2  0                    +2.728000000000000E+02+3.031480000000000E+02+2.180870000000000E+02
OBSINPUT  5                    1031020120000.000  1031109120000.000
OBSINPUT 35                   1031020120000.000  1031109120000.000
ORBTYPE   5  1  1  43200.0000          1.0
DMOPT
WORKIONO  1  1          1031020          1031109
/MILQ     1 0369  3    125.68676          423702.7668          2883032.7722
/GOFQ     1 0934  3     -17.4            375644.016           2843217.016
/MGCC     1 0233 13   3059.764843          204230.7116          2034433.1944
/CGAC     1 0211 13   1512.224725          334902.1756          2532023.4600
/MGBC     1 0232 13   3059.664806          204228.9836          2034433.0972
/CGBC     1 0212 13   1512.204725          334902.1756          2532025.1700
/TDXQ     1 0335  3     59.93106          092355.6808          1672856.3159
/CGCC     1 0213 13   1512.214710          334901.3836          2532024.9612
/GOAQ     1 0933  3     -17.96            375645.1572          2843222.40412
/MGAC     1 0231 13   3059.664806          204228.9800          2034431.9812
/SBVC     1 0504 13     0.0              0.0                  0.0
END
DCOPT
CONVERG   30  3          0.00001
EDIT      3              3.0
TRACKELV  3              1.0
TRACKELV 13              3.0

```

```

OBSCORR 1 1 0 2122
/MILQ 001004005 15.0 18.0 18.0
/MILQ 009 5.0
/MILQ 6 001001 2.0 2.0
/GOFQ 001 15.0
/GOFQ 5 001001 0.0
/GOFQ 6 001001
/MGCC 006007 10.8 10.8
/MGCC 5 006001 0.0
/MGCC 5 007001 0.0
/CGAC 006007 10.8 10.8
/CGAC 5 006001 0.0
/MGBC 006007 10.8 10.8
/MGBC 5 007001 0.0
/CGBC 006007 10.8 10.8
/CGBC 5 006001 0.0
/CGBC 5 007001 0.0
/TDXQ 001004005 50.0 61.0 61.0
/TDXQ 009 500.0
/TDXQ 6 001001 2.0 2.0
/CGCC 006007 10.8 10.8
/GOAQ 001 15.0
/GOAQ 5 001001 0.0
/GOAQ 6 001001
/MGAC 006007 10.8 10.8
/SBVC 096097 7.0 7.0
/SBVC 5 096001 0.0
/SBVC 5 097001 0.0
PRINTOUT 1 4 10.0
ELLMODEL 1 6378.137 298.257224
END
OGOPT
POTFIELD 1 5
SPGRVFR 1 3 3 2.0 1.0 3.0
SSTESTFL 1 2 0 0.0
SSTAPGFL 1 0 0 0.0 0.0 1.0
SPNUMGRV 7 1 8 2.0 2.0 3600.0
SPSRP 1 7 1 6.0 2.0 1.0
MAXDEGEQ 1 8.0
MAXORDEQ 1 8.0
POLAR 1 1.0
NCBODY 1 2 3
STATEPAR 3 1
STATETAB 1 2 3 4.0 5.0 6.0
SCPARAM +3.640300000000000E-05+8.683900000000000E+02
SOLRAD 1 1.0
SOLRDPAR 1 1.0
END
FIN
CONTROL EPHEM OUTPUT SATSAT-0 0024786
OUTPUT 1 2 1 1031109.0 120000.000 43200.0000
ORBTYPE 5 1 1 43200.0000 1.0
OGOPT
OUTOPT 1 1031020120000.000 1031109120000.000 600.0000
POTFIELD 1 5
MAXDEGEQ 1 8.0
MAXORDEQ 1 8.0
POLAR 1 1.0
NCBODY 1 2 3
SPGRVFR 1 3 3 2.0 1.0 3.0
SSTESTFL 1 2 0 0.0
SSTAPGFL 1 0 0 0.0 0.0 1.0
SPNUMGRV 7 1 8 2.0 2.0 3600.0
SPSRP 1 7 1 6.0 2.0 1.0
SCPARAM +3.640300000000000E-05+8.683900000000000E+02
SOLRAD 1 1.0
SOLRDPAR 1 1.0
END
FIN

```

Figure D-9 – Real Data Input Data File for GOES-10 using Spherical Model

Figure D-10 shows an input data file for a test case that uses the DSST, the TDRS-05 macro-model, and the TDRS-05 test case. The observation data for this run includes SSN data, HANDS optical data (provided by Chris Sabol), and SBV data. A single C_R that scales the macro-model is included as a solve-for parameter. The DC is followed by an EPHEM run that covers the fit span.

```

CONTROL  DC
EPOCH          1031215.0          000000.000          SATSAT-0  0021639
ELEMENT1  1  6  1+4.21666632200000E+04+2.80606431900000E-04+5.28966114500000E+00
ELEMENT2  0          +7.71237211400000E+01+1.79752378200000E+02+1.13896087200000E+01
OBSINPUT  5          1031215000000.000  1040109000000.000
OBSINPUT 35         1031215000000.000  1040109000000.000
ORBTYPE   5  1  1  43200.0000  1.0
DMOPT
WORKIONO  1  1  1031215          1040109
/HNCQ    1  0997  3  101.78          204447.4013          2033404.6188
/TDXQ    1  0335  3  59.93106          092355.6808          1672856.3159
/MGBC    1  0232  13  3059.664806          204228.9836          2034433.0972
/MGAC    1  0231  13  3059.664806          204228.9800          2034431.9812
/AMRC    1  0970  13  3066.014852          204231.1004          2034432.8344
/MGCC    1  0233  13  3059.764843          204230.7116          2034433.1944
/CGBC    1  0212  13  1512.204725          334902.1756          2532025.1700
/SBVC    1  0504  13  0.0          0.0          0.0
END
DCOPT
CONVERG  30  3  0.00001
EDIT      3  3.0
TRACKELV  3  1.0
TRACKELV 13  3.0
/HNCQ    004005  10.8          10.8
/TDXQ    001004005  50.0          0.0          0.0
/TDXQ    009  500.0
/MGBC    006007  10.8          10.8
/MGAC    006007  10.8          10.8
/AMRC    006007  10.8          10.8
/MGCC    006007  10.8          10.8
/CGBC    006007  10.8          10.8
/SBVC    096097  7.0          7.0
PRINTOUT  1  4  10.0
ELLMODEL  1  6378.137          298.257224
END
OGOPT
POTFIELD  1  5
SPGRVFRC  1  1  1  2.0          1.0          1.0
SSTESTFL  1  2  0  0.0
SSTAPGFL  1  0  0  0.0          0.0          1.0
SPNUMGRV  7  1  10  2.0          2.0          3600.0
SPSRP     1  7  1  6.0          2.0          1.0
SPTESSLC  6  6  4  2.0          -8.0          8.0
SPZONALS  8  5  11
SPJ2MDLY  4  4  5  2.0
SPMDAILY  8  8  5
MAXDEGEQ  1          12.0
MAXORDEQ  1          12.0
POLAR     1          1.0
NCBODY    1  2  3
STATEPAR  3  1
STATETAB  1  2  3  4.0          5.0          6.0
SCPARAM   +4.00000000000000E-05+1.71276170000000E+03

```

SOLRAD	1		1.0			
SOLRADMD	5	3				
SRPBWNUM	24	4				
SRPBWNRM	1		0.0	0.0	1.0	
SRPBWREF	1		0.6	0.15	18.8574099D-6	
SRPBWNRM	2		0.0	0.0	-1.0	
SRPBWREF	2		0.6	0.15	18.8574099D-6	
SRPBWNRM	3		0.0	0.0	1.0	
SRPBWREF	3		0.6	0.15	18.8574099D-6	
SRPBWNRM	4		0.0	0.0	-1.0	
SRPBWREF	4		0.6	0.15	18.8574099D-6	
SRPBWNRM	5		0.0	0.0	1.0	
SRPBWREF	5		0.24482383119439	0.0736	11.34271D-6	
SRPBWNRM	6		0.0	0.0	-1.0	
SRPBWREF	6		0.32965200271756	0.0527	10.76055D-6	
SRPBWNRM	7		0.0	1.0	0.0	
SRPBWREF	7		0.030847108402777	0.3391	1.449D-6	
SRPBWNRM	8		0.866	0.5	0.0	
SRPBWREF	8		0.2013	0.2468815012552	1.412D-6	
SRPBWNRM	9		0.866	-0.5	0.0	
SRPBWREF	9		0.019461061203629	0.2119	1.449D-6	
SRPBWNRM	10		0.0	0.0	-1.0	
SRPBWREF	10		0.3094673382933	0.2268	1.449D-6	
SRPBWNRM	11		-0.866	-0.5	0.0	
SRPBWREF	11		0.1789	0.12361622710403	1.45D-6	
SRPBWNRM	12		-0.866	0.5	0.0	
SRPBWREF	12		0.13695431202326	0.2232	1.449D-6	
SRPBWNRM	13		0.0	1.0	0.0	
SRPBWREF	13		0.095746628585072	0.04	1.11771D-6	
SRPBWNRM	14		1.0	0.0	0.0	
SRPBWREF	14		0.095746628585072	0.04	1.11771D-6	
SRPBWNRM	15		0.0	-1.0	0.0	
SRPBWREF	15		0.095746628585072	0.04	1.11771D-6	
SRPBWNRM	16		-1.0	0.0	0.0	
SRPBWREF	16		0.095746628585072	0.04	1.11771D-6	
SRPBWNRM	17		0.0	1.0	0.0	
SRPBWREF	17		0.095746628585072	0.04	1.11771D-6	
SRPBWNRM	18		1.0	0.0	0.0	
SRPBWREF	18		0.095746628585072	0.04	1.11771D-6	
SRPBWNRM	19		0.0	-1.0	0.0	
SRPBWREF	19		0.095746628585072	0.04	1.11771D-6	
SRPBWNRM	20		-1.0	0.0	0.0	
SRPBWREF	20		0.095746628585072	0.04	1.11771D-6	
SRPBWNRM	21		1.	0.	0.	
SRPBWREF	21		0.636	0.0375	14.7553D-6	
SRPBWNRM	22		-1.	0.	0.	
SRPBWREF	22		0.112	0.028	14.7553D-6	
SRPBWNRM	23		1.	0.	0.	
SRPBWREF	23		0.636	0.0375	14.7553D-6	
SRPBWNRM	24		-1.	0.	0.	
SRPBWREF	24		0.112	0.028	14.7553D-6	
SRPBWSLV	0	1	1			
END						
FIN						
CONTROL	EPHEM			OUTPUT	SATSAT-0 0021639	
OUTPUT	1	2	1	1040109.0	000000.000	43200.0000
ORBTYP	5	1	1	43200.0000	1.0	
OGOFT						
OUTOPT	1			1031215000000.000	1040109000000.000	600.0000
POTFIELD	1	5				
MAXDEGEQ	1			12.0		
MAXORDEQ	1			12.0		
POLAR	1			1.0		
NCBODY	1	2	3			
SPGRVFRC	1	1	1	2.0	1.0	1.0
SSTESTFL	1	2	0	0.0		
SSTAPGFL	1	0	0	0.0	0.0	1.0
SPNUMGRV	7	1	10	2.0	2.0	3600.0
SPSRP	1	7	1	6.0	2.0	1.0
SPTESLCL	6	6	4	2.0	-8.0	8.0
SPZONALS	8	5	11			

```

SPJ2MDLY 4 4 5 2.0
SPMDAILY 8 8 5
SPOUTPUT 2 2 2 1.0
SCPARAM +4.000000000000000E-05+1.712761700000000E+03
SOLRAD 1 1.0
SOLRADMD 5 3
SRPBWNUM 24 4
SRPBWNRM 1 0.0 0.0 1.0
SRPBWREF 1 0.6 0.15 18.8574099D-6
SRPBWNRM 2 0.0 0.0 -1.0
SRPBWREF 2 0.6 0.15 18.8574099D-6
SRPBWNRM 3 0.0 0.0 1.0
SRPBWREF 3 0.6 0.15 18.8574099D-6
SRPBWNRM 4 0.0 0.0 -1.0
SRPBWREF 4 0.6 0.15 18.8574099D-6
SRPBWNRM 5 0.0 0.0 1.0
SRPBWREF 5 0.24482383119439 0.0736 11.34271D-6
SRPBWNRM 6 0.0 0.0 -1.0
SRPBWREF 6 0.32965200271756 0.0527 10.76055D-6
SRPBWNRM 7 0.0 1.0 0.0
SRPBWREF 7 0.030847108402777 0.3391 1.449D-6
SRPBWNRM 8 0.866 0.5 0.0
SRPBWREF 8 0.2013 0.2468815012552 1.412D-6
SRPBWNRM 9 0.866 -0.5 0.0
SRPBWREF 9 0.019461061203629 0.2119 1.449D-6
SRPBWNRM 10 0.0 0.0 -1.0
SRPBWREF 10 0.3094673382933 0.2268 1.449D-6
SRPBWNRM 11 -0.866 -0.5 0.0
SRPBWREF 11 0.1789 0.12361622710403 1.45D-6
SRPBWNRM 12 -0.866 0.5 0.0
SRPBWREF 12 0.13695431202326 0.2232 1.449D-6
SRPBWNRM 13 0.0 1.0 0.0
SRPBWREF 13 0.095746628585072 0.04 1.11771D-6
SRPBWNRM 14 1.0 0.0 0.0
SRPBWREF 14 0.095746628585072 0.04 1.11771D-6
SRPBWNRM 15 0.0 -1.0 0.0
SRPBWREF 15 0.095746628585072 0.04 1.11771D-6
SRPBWNRM 16 -1.0 0.0 0.0
SRPBWREF 16 0.095746628585072 0.04 1.11771D-6
SRPBWNRM 17 0.0 1.0 0.0
SRPBWREF 17 0.095746628585072 0.04 1.11771D-6
SRPBWNRM 18 1.0 0.0 0.0
SRPBWREF 18 0.095746628585072 0.04 1.11771D-6
SRPBWNRM 19 0.0 -1.0 0.0
SRPBWREF 19 0.095746628585072 0.04 1.11771D-6
SRPBWNRM 20 -1.0 0.0 0.0
SRPBWREF 20 0.095746628585072 0.04 1.11771D-6
SRPBWNRM 21 1.0 0.0 0.0
SRPBWREF 21 0.636 0.0375 14.7553D-6
SRPBWNRM 22 -1.0 0.0 0.0
SRPBWREF 22 0.112 0.028 14.7553D-6
SRPBWNRM 23 1.0 0.0 0.0
SRPBWREF 23 0.636 0.0375 14.7553D-6
SRPBWNRM 24 -1.0 0.0 0.0
SRPBWREF 24 0.112 0.028 14.7553D-6
SRPBWSLV 0 1 1
END
FIN

```

Figure D-10 – Real Data Input Data File for TDRS-05 using Macro-model

D.5 Real Data ESKF Runs

The input data files in this section are used for Extended Semi-analytical Kalman Filter (ESKF) runs using real observation data and the various solar radiation pressure

models. The solar radiation pressure model keywords are placed in the OGOPT section of the data file.

Figure D-11 shows the input data file for a test case that uses the ESKF, the spherical solar radiation pressure model, and the GOES-10 test case. The observation data for this run includes owner/operator ranging data only. The spherical C_R is included as a solve-for parameter using the SOLRDPAR keyword. It is also noted that it is important to specify an a priori covariance for C_R in the third real field of the SOLRDPAR keyword in the filter subdeck. The data file includes a Semi-analytical DC to obtain the a priori epoch mean elements and C_R , followed by the ESKF run.

```

CONTROL   DC                               SATSAT-0   0024786
EPOCH                    1031022.0          000000.000000
ELEMENT1 11 6 1+4.21684241326894E+04+2.33191365580421E-04+1.54175713009508E-01
ELEMENT2                    +2.65316474744120E+02+2.98022277606990E+02+5.21362920098702E+01
OBSINPUT  5                    1031022000000.0000  1031109000000.0000
ORBTYPE   5 1 1 43200.0000                    1.0
DMOPT
/GOFQ     1 0934 3 -17.4                      375644.016          2843217.016
/GOAQ     1 0933 3 -17.96                     375645.1572        2843222.40412
END
DCOPT
EDIT      3          3.000000
CONVERG   30 3      0.00001
TRACKELV  3          3.0
TRACKELV 13          3.0
/GOFQ     001          10.0
/GOAQ     001          10.0
PRINTOUT  1          4      10.0
ELLMODEL  1          6378.137          298.257224
END
OGOPT
POTFIELD  1 5
POLAR     1          1.0
MAXDEGEQ  1          8.0
MAXORDEQ  1          8.0
NCBODY    1 2 3
STATEPAR  3 1
STATETAB  1 2 3 4.0          5.0          6.0
SCPARAM   +1.0000000000000000E-06+1.0000000000000000E+03
SOLRAD    1          1.0
SOLRADMD  1
SOLRDPAR  1          1.0
SPGRVFRC  1 1 1 2.0          1.0          1.0
SSTESTFL  1 2 0 0.0
SSTAPGFL  1 0 0 0.0          0.0          1.0
SPNUMGRV  7 1 10 2.0          2.0          3600.0
SPSRP     1 7 1 6.0          2.0          1.0
SPTESSLC  6 6 4 2.0          -8.0          8.0
SPZONALS  8 5 11
SPJ2MDLY  4 4 5 2.0
SPMDAILY  8 8 5
END
FIN
CONTROL   FILTER                               OUTPUT          SATSAT-0   0024786

```

```

OBSINPUT 5          103102200000.0000  103110900000.0000
ORBTYPE  5  1  1  43200.0000          1.0
DMOPT
/GOFQ   1  0934  3  -17.4              375644.016          2843217.016
/GOAQ   1  0933  3  -17.96             375645.1572          2843222.40412
END
DCOPT
EDIT           3          10.000000
TRACKELV  3          3.0
TRACKELV 13          3.0
/GOFQ   001          10.0
/GOAQ   001          10.0
PRINTOUT  1          4          10.0
ELLMODEL  1          6378.137          298.257224
END
OGOPT
POTFIELD  1  5
POLAR     1          1.0
MAXDEGEQ  1          8.0
MAXORDEQ  1          8.0
NCBODY    1  2  3
STATEPAR  3  1
STATETAB  1  2  3  4.0              5.0              6.0
SCPARAM           +1.000000000000000E-06+1.000000000000000E+03
SOLRAD    1          1.0
SOLRADMD  1
SOLRDPAR  1          1.0
SPGRVFRC  1  1  1  2.0              1.0              1.0
SSTESTFL  1  2  0  0.0
SSTAPGFL  1  0  0  0.0              0.0              1.0
SPNUMGRV  7  1 10  2.0              2.0              3600.0
SPSRP     1  7  1  6.0              2.0              1.0
SPTESSLC  6  6  4  2.0              -8.0             8.0
SPZONALS  8  5 11
SPJ2MDLY  4  4  5  2.0
SPMDAILY  8  8  5
COVARNC   11 12 13  1.0E-4          0.0              0.0
COVARNC   14 15 16  0.0              0.0              0.0
COVARNC   22 23 24  1.0E-4          0.0              0.0
COVARNC   25 26 33  0.0              0.0              1.0E-4
COVARNC   34 35 36  0.0              0.0              0.0
COVARNC   44 45 46  1.0E-6          0.0              0.0
COVARNC   55 56 66  1.0E-6          0.0              1.0E-6
END
FILOPT
FILTER    2  1          1.0              0.0
INPUT     1
DYNOISE           1.0E-8
SPNOISE   11 12 13  1.0E-09          0.0              0.0
SPNOISE   14 15 16  0.0              0.0              0.0
SPNOISE   22 23 24  1.0E-10          0.0              0.0
SPNOISE   25 26 33  0.0              0.0              1.0E-10
SPNOISE   34 35 36  0.0              0.0              0.0
SPNOISE   44 45 46  1.0E-11          0.0              0.0
SPNOISE   55 56 66  1.0E-11          0.0              1.0E-12
COVHSTRY  1  1  4
ESKFCNTL  1  1  1
ESKFOUT   1  1  1  6.0
END
FIN

```

Figure D-11 – Real Data ESKF Input Data File for GOES-10 using Spherical Model

Figure D-12 shows the input data file for a test case that uses the ESKF, the box-wing solar radiation pressure model, and the TDRS-05 test case. The observation data for this run includes HANDS optical data only. The single box-wing C_R is included as a solve-for parameter using the SRPBWSLV keyword with a 0 in the first integer field. It is also noted that it is important to specify an a priori covariance for C_R in the first real field of the SRPBWSLV keyword in the filter subdeck. Additionally, the a priori value for the box-wing C_R is input using the second real field of the SRPBWSLV keyword in the filter subdeck. The data file includes a Semi-analytical DC to obtain the a priori epoch mean elements and C_R , followed by the ESKF run.

```

CONTROL   DC                               SATSAT-0   0021639
EPOCH                    1031214.0           164760.000000
ELEMENT1  1  6  1+4.21669321664237E+04+2.69878035537712E-04+5.28898913035578E+00
ELEMENT2                    +7.71228255992724E+01+1.73765339222226E+02+2.69084947859471E+02
OBSINPUT  5                    1031214164760.0000  1031225000000.0000
ORBTYPE   5  1  1  43200.0000                1.0
DMOPT
/HNCQ     1  0997  3   101.78                204447.4013          2033404.6188
END
DCOPT
EDIT      3           3.000000
CONVERG   30  3           0.00001
TRACKELV  3           3.0
TRACKELV  13          3.0
/HNCQ     004005      10.8                  10.8
PRINTOUT  1           4   10.0
ELLMODEL  1           6378.137              298.257224
END
OGOPT
POTFIELD  1  5
POLAR     1           1.0
MAXDEGEQ  1           8.0
MAXORDEQ  1           8.0
NCBODY    1  2  3
STATEPAR  3  1
STATETAB  1  2  3  4.0                5.0                6.0
SCPARAM   +1.0000000000000000E-06+1.0000000000000000E+03
SOLRAD    1           1.0
SOLRADMD  5  3
SRPBWNUM  24  4
SRPBWNRM  1           0.0                0.0                1.0
SRPBWREF  1           0.6                0.15              18.8574099D-6
SRPBWNRM  2           0.0                0.0                -1.0
SRPBWREF  2           0.6                0.15              18.8574099D-6
SRPBWNRM  3           0.0                0.0                1.0
SRPBWREF  3           0.6                0.15              18.8574099D-6
SRPBWNRM  4           0.0                0.0                -1.0
SRPBWREF  4           0.6                0.15              18.8574099D-6
SRPBWNRM  5           0.0                0.0                1.0
SRPBWREF  5           0.24482383119439  0.0736            11.34271D-6
SRPBWNRM  6           0.0                0.0                -1.0
SRPBWREF  6           0.32965200271756  0.0527            10.76055D-6
SRPBWNRM  7           0.0                1.0                0.0
SRPBWREF  7           0.030847108402777  0.3391            1.449D-6

```

SRPBWNRM	8	0.866	0.5	0.0
SRPBWREF	8	0.2013	0.2468815012552	1.412D-6
SRPBWNRM	9	0.866	-0.5	0.0
SRPBWREF	9	0.019461061203629	0.2119	1.449D-6
SRPBWNRM	10	0.0	0.0	-1.0
SRPBWREF	10	0.3094673382933	0.2268	1.449D-6
SRPBWNRM	11	-0.866	-0.5	0.0
SRPBWREF	11	0.1789	0.12361622710403	1.45D-6
SRPBWNRM	12	-0.866	0.5	0.0
SRPBWREF	12	0.13695431202326	0.2232	1.449D-6
SRPBWNRM	13	0.0	1.0	0.0
SRPBWREF	13	0.095746628585072	0.04	1.11771D-6
SRPBWNRM	14	1.0	0.0	0.0
SRPBWREF	14	0.095746628585072	0.04	1.11771D-6
SRPBWNRM	15	0.0	-1.0	0.0
SRPBWREF	15	0.095746628585072	0.04	1.11771D-6
SRPBWNRM	16	-1.0	0.0	0.0
SRPBWREF	16	0.095746628585072	0.04	1.11771D-6
SRPBWNRM	17	0.0	1.0	0.0
SRPBWREF	17	0.095746628585072	0.04	1.11771D-6
SRPBWNRM	18	1.0	0.0	0.0
SRPBWREF	18	0.095746628585072	0.04	1.11771D-6
SRPBWNRM	19	0.0	-1.0	0.0
SRPBWREF	19	0.095746628585072	0.04	1.11771D-6
SRPBWNRM	20	-1.0	0.0	0.0
SRPBWREF	20	0.095746628585072	0.04	1.11771D-6
SRPBWNRM	21	1.	0.	0.
SRPBWREF	21	0.636	0.0375	14.7553D-6
SRPBWNRM	22	-1.	0.	0.
SRPBWREF	22	0.112	0.028	14.7553D-6
SRPBWNRM	23	1.	0.	0.
SRPBWREF	23	0.636	0.0375	14.7553D-6
SRPBWNRM	24	-1.	0.	0.
SRPBWREF	24	0.112	0.028	14.7553D-6
SRPBWSLV	0	1	1	
SPGRVFRC	1	1	1	2.0
SSTESTFL	1	2	0	0.0
SSTAPGFL	1	0	0	0.0
SPNUMGRV	7	1	10	2.0
SPSRP	1	7	1	6.0
SPTESLCL	6	6	4	2.0
SPZONALS	8	5	11	
SPJ2MDLY	4	4	5	2.0
SPMDAILY	8	8	5	
END				
FIN				
CONTROL	FILTER		OUTPUT	SATSAT-0 0021639
OBSINPUT	5	1031214164760.0000	1031225000000.0000	
ORBTYP	5 1 1	43200.0000	1.0	
DMOPT				
/HNCQ	1 0997 3	101.78	204447.4013	2033404.6188
END				
DCOPT				
EDIT	3	10.000000		
TRACKELV	3	3.0		
TRACKELV	13	3.0		
/HNCQ	004005	10.8	10.8	
PRINTOUT	1 4	10.0		
ELLMODEL	1	6378.137	298.257224	
END				
OGOPT				
POTFIELD	1 5			
POLAR	1	1.0		
MAXDEGEQ	1	8.0		
MAXORDEQ	1	8.0		
NCBODY	1 2 3			
STATEPAR	3 1			
STATETAB	1 2 3	4.0	5.0	6.0
SCPAM		+1.0000000000000000E-06	+1.0000000000000000E+03	
SOLRAD	1	1.0		
SOLRADMD	5 3			

SRPBWNRM	24	4			
SRPBWREF	1		0.0	0.0	1.0
SRPBWREF	1		0.6	0.15	18.8574099D-6
SRPBWREF	2		0.0	0.0	-1.0
SRPBWREF	2		0.6	0.15	18.8574099D-6
SRPBWREF	3		0.0	0.0	1.0
SRPBWREF	3		0.6	0.15	18.8574099D-6
SRPBWREF	4		0.0	0.0	-1.0
SRPBWREF	4		0.6	0.15	18.8574099D-6
SRPBWREF	5		0.0	0.0	1.0
SRPBWREF	5		0.24482383119439	0.0736	11.34271D-6
SRPBWREF	6		0.0	0.0	-1.0
SRPBWREF	6		0.32965200271756	0.0527	10.76055D-6
SRPBWREF	7		0.0	1.0	0.0
SRPBWREF	7		0.030847108402777	0.3391	1.449D-6
SRPBWREF	8		0.866	0.5	0.0
SRPBWREF	8		0.2013	0.2468815012552	1.412D-6
SRPBWREF	9		0.866	-0.5	0.0
SRPBWREF	9		0.019461061203629	0.2119	1.449D-6
SRPBWREF	10		0.0	0.0	-1.0
SRPBWREF	10		0.3094673382933	0.2268	1.449D-6
SRPBWREF	11		-0.866	-0.5	0.0
SRPBWREF	11		0.1789	0.12361622710403	1.45D-6
SRPBWREF	12		-0.866	0.5	0.0
SRPBWREF	12		0.13695431202326	0.2232	1.449D-6
SRPBWREF	13		0.0	1.0	0.0
SRPBWREF	13		0.095746628585072	0.04	1.11771D-6
SRPBWREF	14		1.0	0.0	0.0
SRPBWREF	14		0.095746628585072	0.04	1.11771D-6
SRPBWREF	15		0.0	-1.0	0.0
SRPBWREF	15		0.095746628585072	0.04	1.11771D-6
SRPBWREF	16		-1.0	0.0	0.0
SRPBWREF	16		0.095746628585072	0.04	1.11771D-6
SRPBWREF	17		0.0	1.0	0.0
SRPBWREF	17		0.095746628585072	0.04	1.11771D-6
SRPBWREF	18		1.0	0.0	0.0
SRPBWREF	18		0.095746628585072	0.04	1.11771D-6
SRPBWREF	19		0.0	-1.0	0.0
SRPBWREF	19		0.095746628585072	0.04	1.11771D-6
SRPBWREF	20		-1.0	0.0	0.0
SRPBWREF	20		0.095746628585072	0.04	1.11771D-6
SRPBWREF	21		1.0	0.0	0.0
SRPBWREF	21		0.636	0.0375	14.7553D-6
SRPBWREF	22		-1.0	0.0	0.0
SRPBWREF	22		0.112	0.028	14.7553D-6
SRPBWREF	23		1.0	0.0	0.0
SRPBWREF	23		0.636	0.0375	14.7553D-6
SRPBWREF	24		-1.0	0.0	0.0
SRPBWREF	24		0.112	0.028	14.7553D-6
SRPBWSLV	0	1	1	0.57851261982E+00	
SPGRVFRC	1	1	1	2.0	1.0
SSTESTFL	1	2	0	0.0	
SSTAPGFL	1	0	0	0.0	1.0
SPNUMGRV	7	1	10	2.0	3600.0
SPSRP	1	7	1	6.0	1.0
SPTESLCL	6	6	4	2.0	-8.0
SPZONALS	8	5	11		
SPJ2MDLY	4	4	5	2.0	
SPMDAILY	8	8	5		
COVARNCL	11	12	13	1.0E-4	0.0
COVARNCL	14	15	16	0.0	0.0
COVARNCL	22	23	24	1.0E-4	0.0
COVARNCL	25	26	33	0.0	0.0
COVARNCL	34	35	36	0.0	1.0E-4
COVARNCL	44	45	46	1.0E-6	0.0
COVARNCL	55	56	66	1.0E-6	0.0
COVARNCL	55	56	66	1.0E-6	1.0E-6
END					
FILOPT					
FILTER	2	1	1.0	172800.0	
INPUT	1				
DYNOISE			1.0E-8		

```
SPNOISE 11 12 13 1.0E-12 0.0 0.0
SPNOISE 14 15 16 0.0 0.0 0.0
SPNOISE 22 23 24 1.0E-13 0.0 0.0
SPNOISE 25 26 33 0.0 0.0 1.0E-13
SPNOISE 34 35 36 0.0 0.0 0.0
SPNOISE 44 45 46 1.0E-14 0.0 0.0
SPNOISE 55 56 66 1.0E-14 0.0 1.0E-15
COVHSTRY 1 1 4
ESKFCNTL 1 1 1
ESKFOUT 1 1 1 6.0
END
FIN
```

Figure D-12 – Real Data ESKF Input Data File for TDRS-05 using Macro-model

Appendix E One-panel Aerodynamic Force Model

E.1 Introduction

This appendix gives details about a one-panel model for aerodynamic force (lift and drag) acting on a space object. This work was undertaken as a side study to the main thesis work. It was motivated by the Space Shuttle Columbia accident that occurred in early February 2003 [Ref 41]. Specifically, this work contributed to the analysis of the fragment that separated from the Shuttle on Day 2 of the flight and later re-entered [Ref 41]. The fragment was tracked by SSN radars. However, the motion of the fragment could not be correctly modeled using the traditional spherical spacecraft model for drag.

The one-panel model for lift and drag is related to the one-panel model for solar radiation pressure. In fact, as part of the PowerSail project, Ron Proulx' one-panel model took into account both solar radiation pressure and atmospheric effects [Ref 28]. His work and implementation of the model in the DSST Standalone software were consulted as a starting point in the implementation of the model into UNIX GTDS [Ref 28]. Also, Jack Fisher's 1998 MIT SM thesis included work on implementing a Simplified Lift Model (SLM) into NT GTDS [Ref 53]. The SLM was used to analyze the decay of Molniya rocket body orbits [Ref 53]. Fischer's work was consulted in implementing the one-panel aerodynamic force model.

The one-panel aerodynamic force model was implemented into GTDS during April and May 2003. The software integration was a helpful experience in the later implementation of the Differential Correction capability for the solar pressure models.

E.2 Mathematical Specification

The equation for the aerodynamic force acting on a flat plate, in terms of the normal and tangential accommodation coefficients of the plate, is as follows [Refs 28, 29]:

$$\mathbf{F} = -\rho V_{rel}^2 A \cos \alpha \left[(2 - \sigma_n - \sigma_t) \cos(\alpha) \hat{\mathbf{n}} + \sigma_t \hat{\mathbf{v}}_{rel} \right] \quad (\text{E.1})$$

where:

- \mathbf{F} = force due to solar radiation pressure on the flat plate, N
- ρ = atmospheric density
- V_{rel} = relative velocity
- A = surface area of the flat plate
- α = angle between surface normal and relative velocity vector (incidence angle)
- σ_n = normal accommodation coefficient
- σ_t = tangential accommodation coefficient
- $\hat{\mathbf{v}}_{rel}$ = unit vector in the direction of relative velocity
- $\hat{\mathbf{n}}$ = surface normal vector

We wish to express the above equation in terms of the coefficients of lift and drag, as defined by the following equations [Ref 53]:

$$C_L = \frac{L}{\frac{1}{2} \rho V_{rel}^2 A'} \quad (\text{E.2a})$$

$$C_D = \frac{D}{\frac{1}{2} \rho V_{rel}^2 A'} \quad (\text{E.2b})$$

where:

- C_L = coefficient of lift
- C_D = coefficient of drag
- ρ = atmospheric density
- V_{rel} = relative velocity
- A' = projected area of the flat plate ($A \cos(\alpha)$)
- L = magnitude of the aerodynamic force in the lift direction (the direction perpendicular to drag)
- D = magnitude of the aerodynamic force in the drag direction (the direction opposite V_{rel})

To do this, we draw a picture of the flat plate:

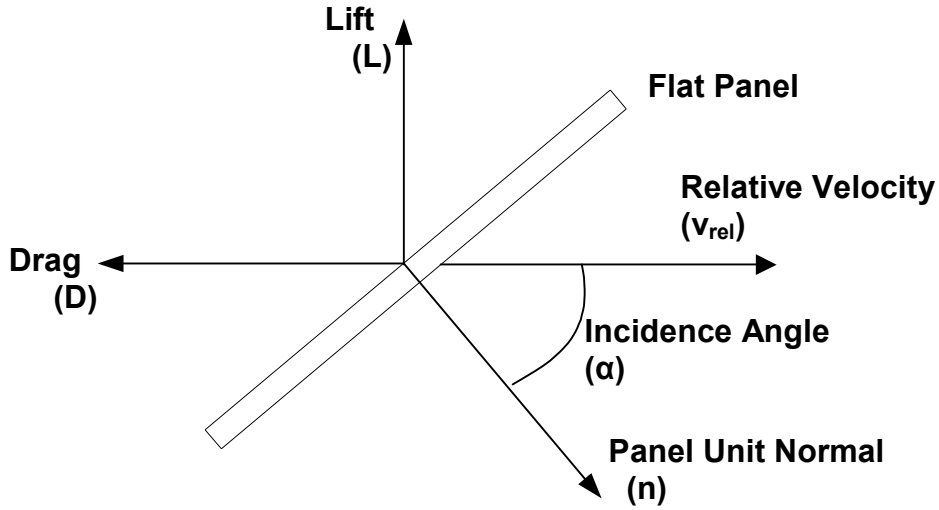


Figure E-1 – Flat Plate Aerodynamic Force Model

From Eq (E.1), we define the components of the force in the direction of the surface normal and relative velocity vectors as:

$$\mathbf{f}_n = -\rho V_{rel}^2 A \cos^2(\alpha)(2 - \sigma_n - \sigma_t) \hat{\mathbf{n}} \quad (\text{E.3a})$$

$$\mathbf{f}_{v_{rel}} = -\rho V_{rel}^2 A \cos(\alpha) \sigma_t \hat{\mathbf{v}}_{rel} \quad (\text{E.3b})$$

From Figure E-1, it can be seen that the lift and drag forces in terms of the force components in the direction of the surface normal and relative velocity are:

$$\mathbf{L} = [|\mathbf{f}_n| \sin(\alpha)] \hat{\mathbf{L}} \quad (\text{E.4a})$$

$$\mathbf{D} = [|\mathbf{f}_{v_{rel}}| + |\mathbf{f}_n| \cos(\alpha)] \hat{\mathbf{D}} \quad (\text{E.4b})$$

Plugging in the values for \mathbf{f}_n and $\mathbf{f}_{v_{rel}}$:

$$\mathbf{L} = -\rho V_{rel}^2 A \cos^2(\alpha) \sin(\alpha)(2 - \sigma_n - \sigma_t) \hat{\mathbf{L}} \quad (\text{E.5a})$$

$$\mathbf{D} = -\rho V_{rel}^2 A \cos(\alpha) [\sigma_t + \cos^2(\alpha)(2 - \sigma_n - \sigma_t)] \hat{\mathbf{D}} \quad (\text{E.5b})$$

Plugging these values into Eqs (E-2) yields the following expressions for the coefficient of drag and coefficient of lift in terms of the normal and tangential accommodation coefficients and incidence angle:

$$C_L = 2 \cos(\alpha) \sin(\alpha) (2 - \sigma_n - \sigma_t) \quad (\text{E.6a})$$

$$C_D = 2[\sigma_t + \cos^2(\alpha)(2 - \sigma_n - \sigma_t)] \quad (\text{E.6b})$$

Solving these equations for the normal and tangential accommodation coefficients yields:

$$\sigma_n = \frac{1}{2} \left[\left(\frac{\cos(\alpha)}{\sin(\alpha)} - \frac{1}{\cos(\alpha) \sin(\alpha)} \right) C_L - C_D \right] + 2 \quad (\text{E.7a})$$

$$\sigma_t = \frac{1}{2} \left(C_D - \frac{\cos(\alpha)}{\sin(\alpha)} C_L \right) \quad (\text{E.7b})$$

Plugging these expressions into Eq (E.1) yields:

$$\mathbf{F} = -\frac{1}{2} \rho V_{rel}^2 A \left[\frac{\cos(\alpha)}{\sin(\alpha)} C_L \hat{\mathbf{n}} + \left(\cos(\alpha) C_D - \frac{\cos^2(\alpha)}{\sin(\alpha)} C_L \right) \hat{\mathbf{v}}_{rel} \right] \quad (\text{E.8})$$

It is noted that an incidence angle of 0 degrees produces an infinite result; however, at 0 degrees incidence angle, there is no lift force, so C_L is by definition 0. In this case, the equation for aerodynamic forces reduces to the equation for drag on a uniformly-reflecting sphere:

$$\mathbf{F} = -\frac{1}{2} \rho V_{rel}^2 A C_D \hat{\mathbf{v}}_{rel} \quad (\text{E.9})$$

E.3 Software Development

E.3.1 Force Model Implementation

The software development for the one-panel aerodynamic force model was implemented in a similar fashion as the one-panel solar pressure model. The actual drag force model calculations in GTDS are handled in the subroutine AERO. As such, we modified AERO to include the one-panel model.

The subroutines incorporated from the DSST Standalone were modified so that the input force model parameters in GTDS included the spacecraft lift and drag coefficients, instead of the normal and tangential accommodation coefficients that were included in the DSST Standalone. The one-panel aerodynamic force model incorporated from the DSST Standalone includes three subroutines:

- ORIENT_PANEL_DRG – Calculates the orientation of the flat panel with a given angular offset from the relative velocity vector.
- DRGPNLQNT – Calculates the cross-sectional area of the flat panel projected toward the relative velocity vector.
- DRGPNL – Calculates the aerodynamic acceleration on the one-panel model. Calls ORIENT_PANEL_DRG and DRGPNLQNT.

Similarly to the DSST Standalone solar radiation pressure model subroutines, the aerodynamic force model subroutines referenced the structure FRC to store common variables. As mentioned earlier, to avoid confusion with the GTDS common block FRC, the structure from the DSST Standalone was renamed FRC_PNL for incorporation into GTDS, and all references to the structure FRC were renamed to FRC_PNL within the incorporated subroutines. The one-panel model subroutines also use the structure

PANEL to store variables related to the orientation of the panel with respect to the relative velocity vector.

The ‘middle-ware’ driver subroutine created for the DSST one-panel model was named DRGPNL_DRV. DRGPNL_DRV is called by AERO within GTDS, and in turn calls the subroutines from the DSST Standalone listed above.

The software design tree for the one-panel aerodynamic force model incorporated from the DSST Standalone into GTDS is shown in Figure E-2.

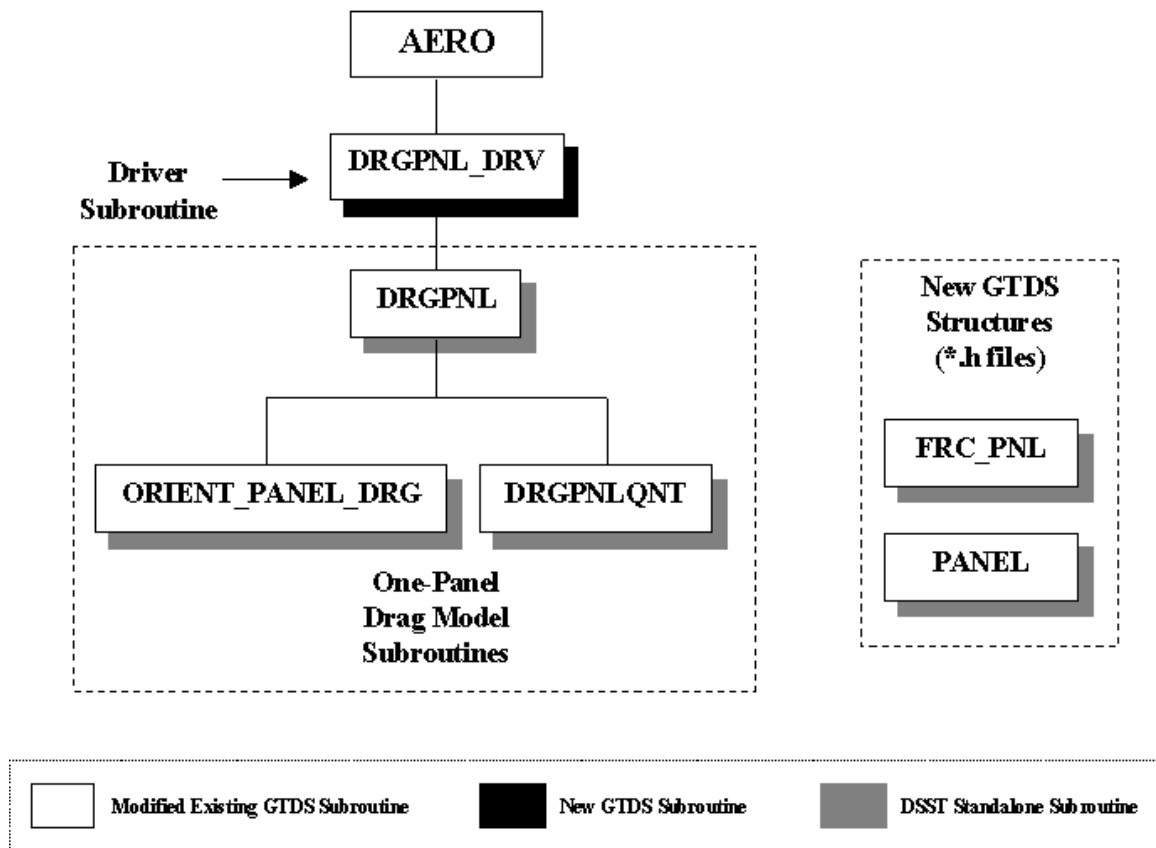


Figure E-2 – Software Design Tree for Incorporation of DSST Standalone One-panel Drag Model Subroutines into GTDS

To handle the input variables for the aerodynamic force modeling, a new common block, DRGPAN, was created. The subroutines SETORB and SETOG1 were modified to handle the input processing.

E.3.2 Differential Correction Implementation

We also implemented the capability to calculate the partial derivatives of the spacecraft acceleration with respect to the spacecraft lift and drag coefficients, as well as the capability to solve for them as solve-for parameters, in differential correction and filtering applications. The Differential Correction capability was only implemented for the Semi-analytical Satellite Theory (DSST), and was not implemented for the Cowell orbit generator. The partial derivatives calculations were implemented via finite-differencing.

The following subroutines were modified to implement the Differential Correction capability with the one-panel aerodynamic force model:

- INTOGN – Modified to support initializing the partial derivative switches associated with the one-panel aerodynamic force model and to initialize the lift and drag coefficients and variances.
- SOLTAB – Modified to handle including the lift and drag coefficients in the solve-for table.
- PSET – Modified to support resetting the lift and drag coefficients adjusted through the differential correction program from the P array.
- VARDIF – Modified to support calculation of the one-panel lift/drag coefficients by finite differences.
- AVRAGE – Modified to support inclusion of the one-panel aerodynamic force model in the calculation of the element rate partials.

The design tree for the one-panel aerodynamic force model differential correction software is shown in Figure E-3.

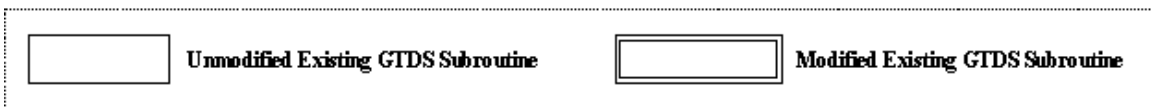
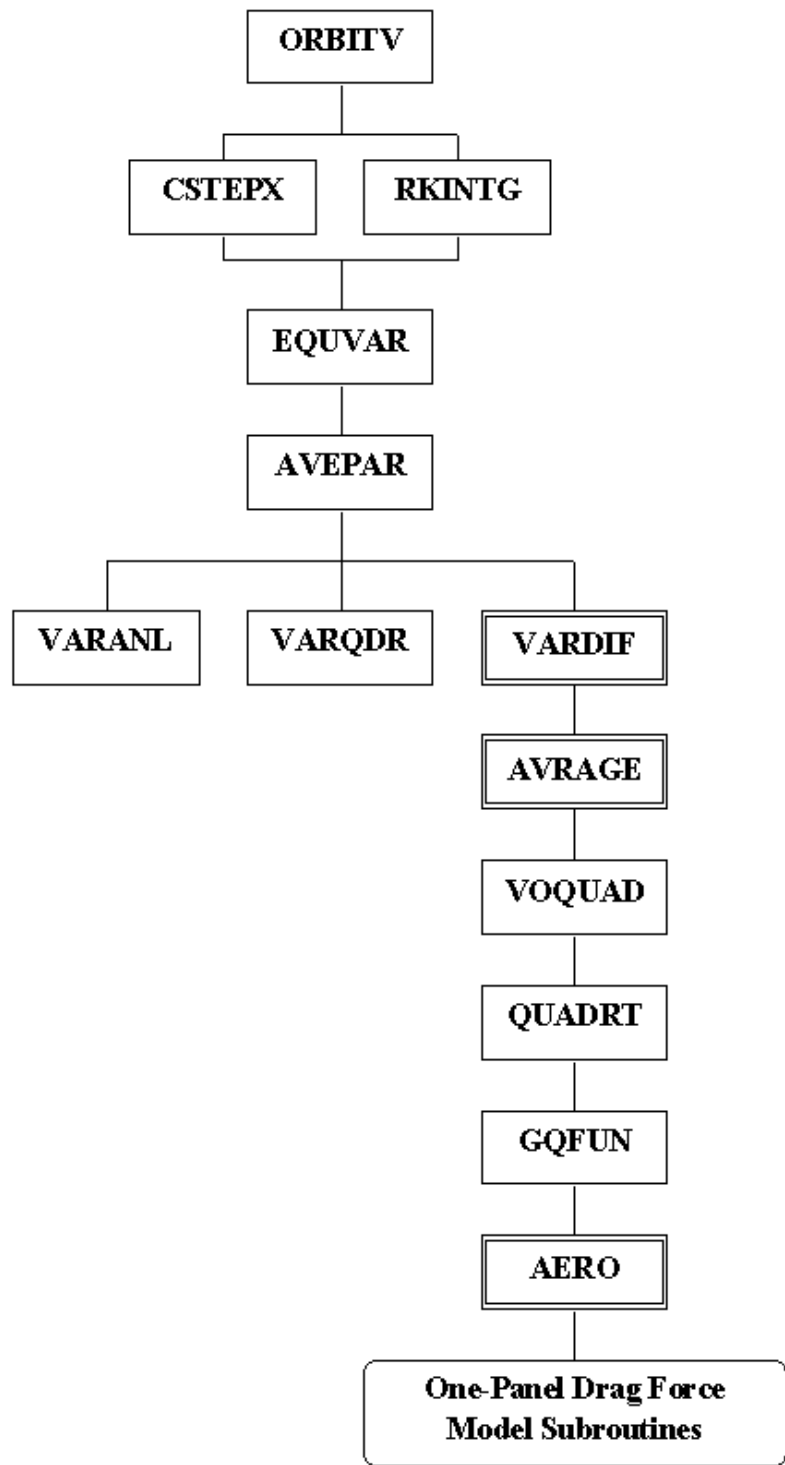


Figure E-3 – Software Design Tree for GTDS One-panel Drag Model DSST DC

E.4 Simulated Data Results

The simulated data testing completed with the one-panel aerodynamic force model was similar to the DSST differential correction simulated data testing completed with the improved radiative force models described in Chapter 7.6. For the Semi-analytical Satellite Theory, regression testing was done to ensure that no errors were introduced into the orbit propagator.

Next, GTDS was configured to calculate the partial derivatives of the mean element motion during orbit propagation runs using the spherical drag model and the one-panel aerodynamic force model. For the Semi-analytical Satellite Theory, the state transition matrix, or \mathbf{B}_2 matrix, as well as the partial derivatives of the mean element motion with respect to the model parameters, or \mathbf{B}_3 matrix, were printed at each time step in the orbit propagation. The \mathbf{B}_2 matrix at each time step did not depend on which model was used. The \mathbf{B}_3 matrix, however, had a dependence on which model was used. When the spherical drag model was tested, the \mathbf{B}_3 matrix had one column, representing the partial derivatives of the mean element motion with respect to C_D . When the one-panel drag/lift model was tested, the \mathbf{B}_3 matrix consisted of two columns; these columns represented the partial derivatives of the mean element motion with respect to the drag and lift coefficients.

The final simulated data test cases with the one-panel aerodynamic force model included PCE runs.

E.5 Real Data Processing Results

The one-panel aerodynamic force model was used to process radar observations of the Day 2 fragment that separated from the Space Shuttle in January 2003. The one-panel model was able to model the motion of the fragment as it decayed more closely to the actual observations than the traditional spherical drag model.

Figure E-4 shows plots of the semimajor axis and eccentricity over the three days that the fragment decayed. Each of the short signals represent the behavior of the orbital element in separate DC runs followed by short predicts with EPHEM runs, using the observation data from each of the three days. The long signal shows the behavior of the orbital element using the spherical model, and propagating forward with an EPHEM run. As can be seen, the spherical model matches the observation data reasonably well in the semimajor axis, but matches poorly with the eccentricity.

Figure E-5 shows a similar set of plots with the one-panel model. The short signals are the same ones shown in Figure E-4. The long signal shows the behavior of the orbital element using the one-panel model, and propagating forward with an EPHEM run. The one-panel model is seen to match the observation data reasonably well in both semimajor axis and eccentricity.

As mentioned earlier, the one-panel model was able to model the motion of the fragment as it decayed more closely to the actual observations than the traditional spherical drag model. This insight was useful in the investigation to characterize the size and shape of the Day 2 fragment.

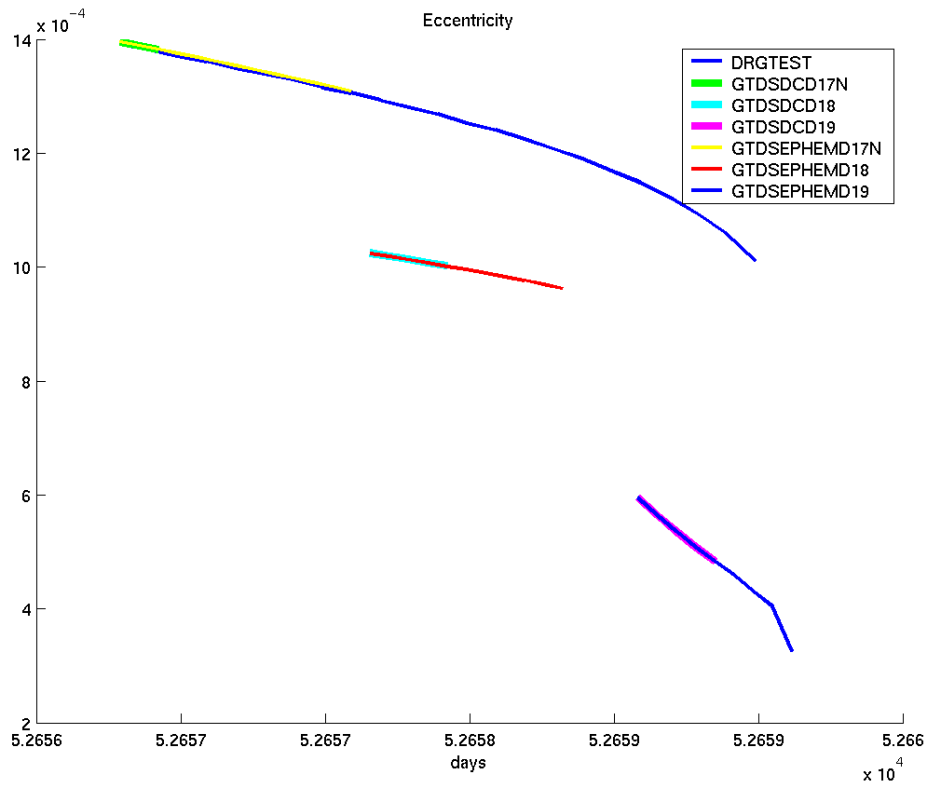
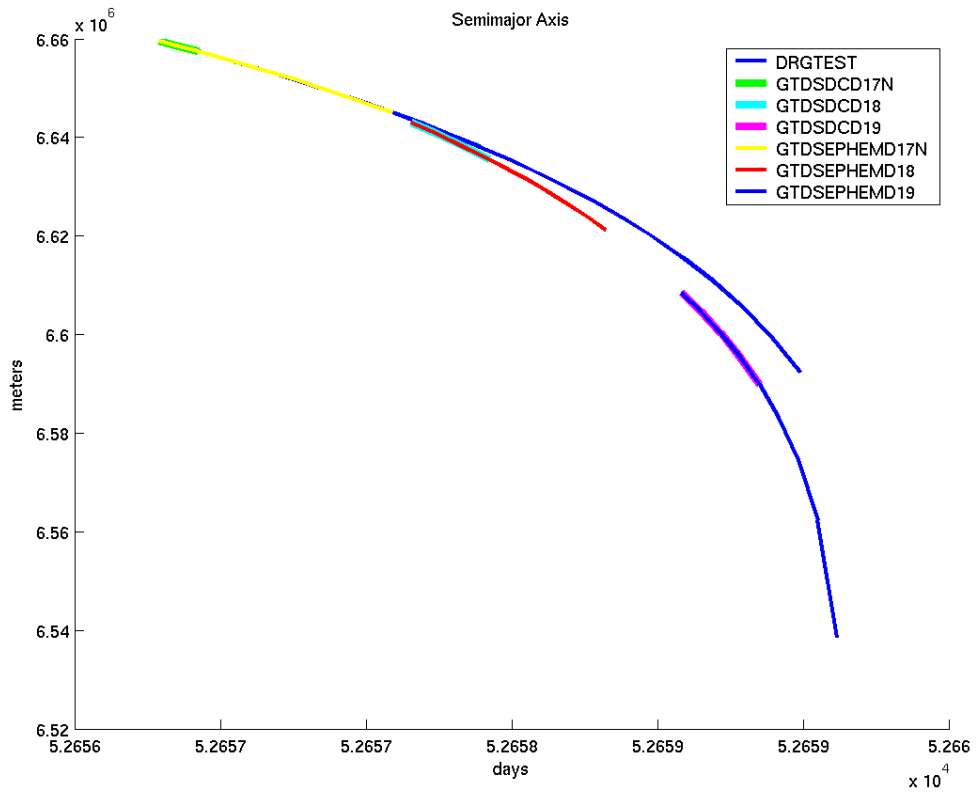


Figure E-4 – Semimajor Axis and Eccentricity Behavior Using the Spherical Model

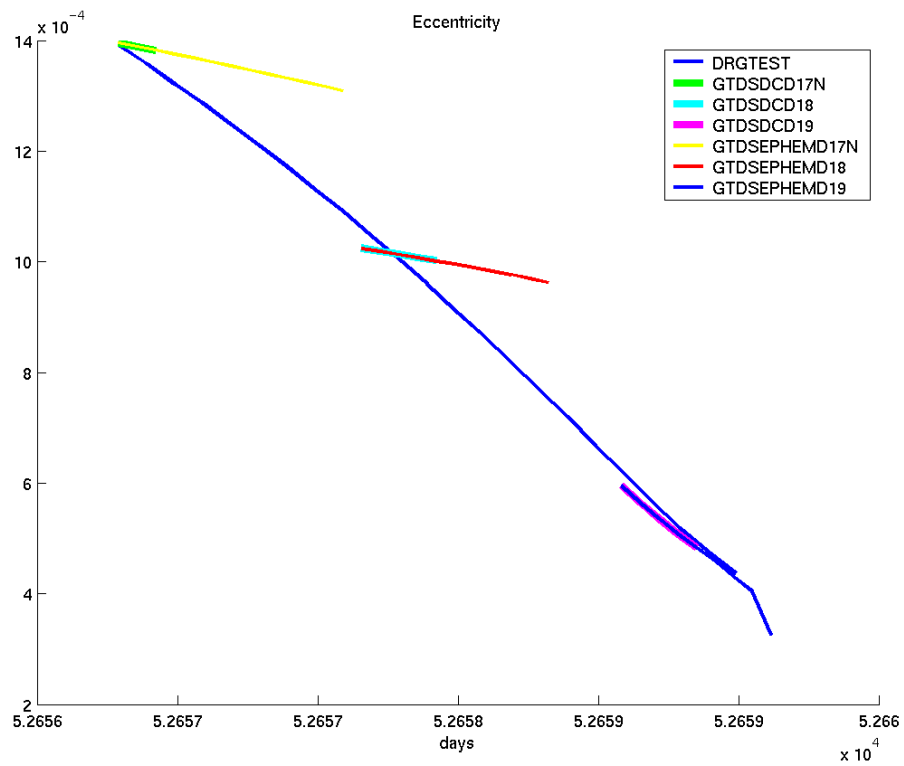
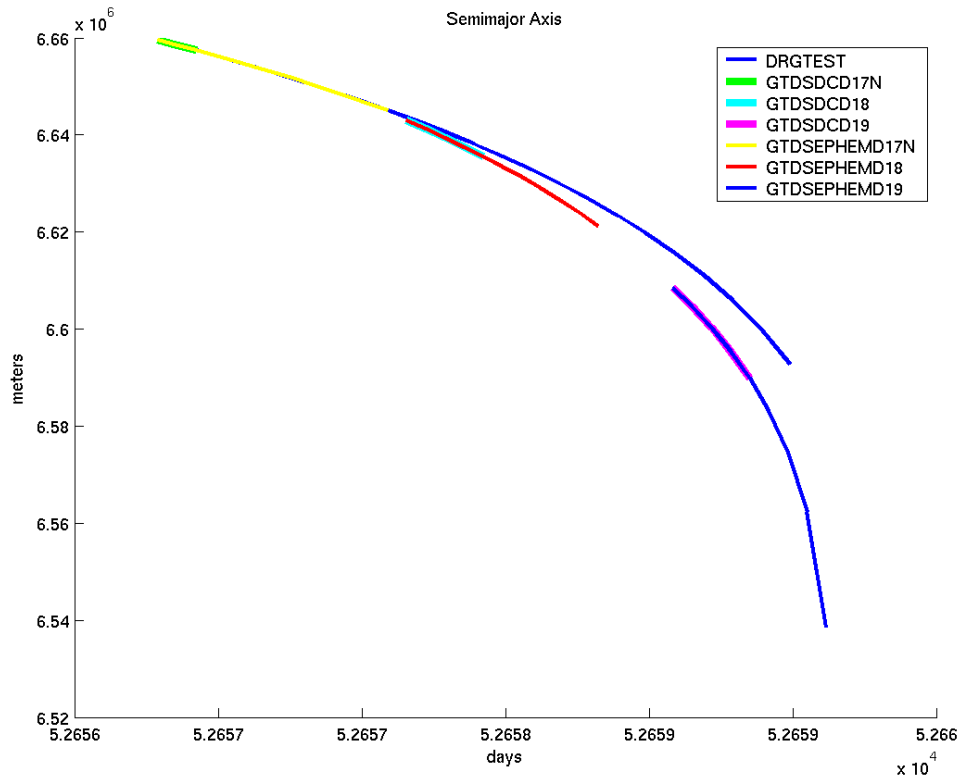


Figure E-5 – Semimajor Axis and Eccentricity Behavior Using the One-panel Model

References

1. Rumsfeld, Donald H., et al. "Report of the Commission to Assess United States National Security Space Management and Organization." Pursuant to Public Law 106-65. January 11, 2001. Available at <http://www.space.gov/docs/fullreport.pdf>.
2. Yurasov, Vasily S., Vadim G. Vygon, and Viktor D. Shargorodskiy. "Classification and Identification of Geostationary Space Objects by Using Coordinate and Photometric Observations." Fourth US/Russian Space Surveillance Workshop, US Naval Observatory, Washington, DC, October 23-27, 2000, pp 117-146
3. Kelso, T.S, Center for Space Standards and Innovation, Analytical Graphics, Inc. Private e-mail communication. March 5, 2004.
4. Futron Corporation. GEO Commercial Satellite Bus Operations: A Comparative Analysis. August 13, 2003. Available at <http://www.futron.com>.
5. Anzel, B. "Stationkeeping the Hughes HS 702 Satellite with Xenon Ion Propulsion System." IAF-98-A.1.09. The 49th International Astronautical Congress, Sept 28 – Oct 2, 1998, Melbourne, Australia.
6. Goebel, D. M., M. Martinez-Lavin, T. A. Bond, and A. M. King, "Performance of XIPS Electric Propulsion in On-orbit Station Keeping of the Boeing 702 Spacecraft." AIAA 2002-4348. The 38th AIAA/ASME/SAE/ASEE Joint Propulsion Conference, July 7 - 10 2002, Indianapolis, Indiana.
7. Taylor, Stephen P. Semianalytical Satellite Theory and Sequential Estimation. SM Thesis, Department of Mechanical Engineering, MIT, September 1981.
8. Wagner, Elaine A. Application of the Extended Semianalytical Kalman Filter to Synchronous Orbits. SM Thesis, Department of Aeronautics and Astronautics, MIT, June 1983.
9. Herklotz, Robert L. Incorporation of Cross-Link Range Measurements in the Orbit Determination Process to Increase Satellite Constellation Autonomy. Ph.D. Thesis, Department of Aeronautics and Astronautics, MIT, December 1987.
10. Vallado, David A. Fundamentals of Astrodynamics and Applications. The McGraw-Hill Companies, Inc., 1997 (1st edition), pp 651-658.
11. Wertz, James R. (ed.) Spacecraft Attitude Determination and Control. Computer Sciences Corporation. D. Reidel Publishing Company, Boston, 1978. pp 71-98, 129-132, 570-573.
12. Møller, C. The Theory of Relativity. Second Edition. Clarendon Press, Oxford, 1972.
13. Antreasian, Peter Garo. Precision Radiation Force Modeling for the TOPEX/Poseidon Mission. PhD Thesis, Department of Aerospace Engineering Sciences, University of Colorado, Boulder, 1992.

14. Amundsen, Ruth M. "Some Useful Innovations with TRAYSIS and SINDA-85." Fifth Annual Thermal and Fluids Analysis Workshop, NASA Lewis Research Center and The Ohio Aerospace Institute, August 16-20, 1993.
15. Sharma, Jayant, Grant H. Stokes, Curt von Braun, George Zollinger, and Andrew J. Wiseman. "Toward Operational Space-Based Space Surveillance." *MIT Lincoln Laboratory Journal*, Vol. 13, No. 2, 2002, pp 309-334.
16. Gaposchkin, E. Michael, Curt von Braun, and Jayant Sharma. "Space-Based Surveillance with the Space-Based Visible." *AIAA Journal of Guidance, Control, and Dynamics*, Vol. 23, No. 1, January-February 2000, pp 148-152.
17. Stone, Melvin L., and Gerald P. Banner. "Radars for the Detection and Tracking of Ballistic Missiles, Satellites, and Planets." *MIT Lincoln Laboratory Journal*, Vol. 12, No. 2, 2000, pp 217-244.
18. Sabol, Chris A. A Role For Improved Angular Observations in Geosynchronous Orbit Determination. PhD Thesis, Department of Aerospace Engineering Sciences, University of Colorado, Boulder, 1998.
19. Kelso, T.S. "Space Surveillance." *Satellite Times*, 4, No. 1, September/October 1997, pp 68-69. Available at <http://www.celestrak.com>.
20. Seago, John H., Mark A. Davis, Anne E. Reed, Paul W. Schumacher, Jr., and Edward D. Lydick. "Navy Calibration of the US Space Surveillance Network Using Satellite Laser Ranging." Fourth US/Russian Space Surveillance Workshop, US Naval Observatory, Washington, DC, October 23-27, 2000, pp 187-204.
21. Abbot, R.I., R. Clouser, E.W. Evans, J. Sharma, R. Sridharan, and L.E. Thornton. "Close Geostationary Satellite Encounter Analysis: 1997-2001." 2002 AAS/AIAA Space Flight Mechanics Meeting, San Antonio, Texas, January 2002.
22. Gaposchkin, E. Michael, Mark T. Lane, and Rick I. Abbot. "Reduction and Analysis of MSX Surveillance Data." AAS 95-234. *Spaceflight Mechanics 1995*. Advances in the Astronautical Sciences, Vol 89, Part II, pp 1691-1709
23. Sabol, Chris, Tom Kelecyc, and Michael Murai. "Geosynchronous Orbit Determination Using the High Accuracy Network Determination System (HANDS)." AAS 04-216. 14th AAS/AIAA Space Flight Mechanics Meeting, Maui, Hawaii, February 2004.
24. Sabol, Chris, K.K. Luu, et al. "Recent Developments of the Raven Small Telescope Program." AAS 02-131. 2002 AAS/AIAA Space Flight Mechanics Meeting, San Antonio, Texas, January 2002.
25. Sabol, Chris and R. Culp. "Improved Angular Observations in Geosynchronous OD." *AIAA Journal of Guidance, Control, and Dynamics*, Vol. 24, No. 1, January-February 2001, pp 123-130.
26. Khutorovsky, Zakhary N. "Monitoring of GEO Satellites in Russian Space Surveillance Center." Proceedings of the Third US/Russian Space Surveillance Workshop, US Naval Observatory, Washington, DC, USA, October 20 -23, 1998, pp 281 – 310

27. Donath, Th., V. Martinot, P. Ameline, T. Schildknecht, and R. Walker. "A European Space Surveillance Study." IAC-03-IAA.5.1.01. 54th International Astronautical Congress of the International Astronautical Federation, the International Academy of Astronautics, and the International Institute of Space Law, 29 September – 3 October 2003, Bremen, Germany.
28. Proulx, Ronald, Paul Cefola, and Kim Luu. "The Role of Short-periodic Motion in Formation Flying of Satellites with Large Differential Area to Mass Ratio." AAS 01-454. 2001 AAS/AIAA Astrodynamics Specialist Conference, Quebec City, Quebec, Canada, 30 July – 2 August 2001.
29. Hughes, Peter C. Spacecraft Attitude Dynamics. John Wiley & Sons, 1986, pp 260-264.
30. Chan, F.K. "Feasibility Study of Using a Two-plate Model to Approximate the TDRSS Solar Pressure Effects." NASA/GSFC Flight Mechanics/Estimation Theory Symposium, October 21-22, 1980.
31. Chan, F.K. "A General Method for Computing the Total Solar Radiation Force on Complex Spacecraft Structures." NASA/GSFC Flight Mechanics/Estimation Theory Symposium, October 27-28, 1981.
32. Pechenick, Kay R. *Solar Radiation Pressure on Satellites and Other Effects*. The General Electric Company, 1983. Copy received 8 Mar 2004 from Dr. Paul Cefola.
33. Pechenick, Kay and Richard Hujsak. *TDRS Solar Pressure Model for Filtering*. Applied Technology Associates, Inc., Delaware. December 11, 1987. Copy received 8 Mar 2004 from Dr. Paul Cefola.
34. Marshall, J.A., S.B. Luthcke, P.G. Antreasian, and G.W. Rosborough. *Modeling Radiation Forces Acting on TOPEX/Poseidon for Precision Orbit Determination*. NASA Technical Memorandum 104564. NASA Goddard Space Flight Center, Greenbelt, MD. June 1992.
35. Luthcke, S.B. and J.A. Marshall. *Nonconservative Force Model Parameter Estimation Strategy for TOPEX/Poseidon Precision Orbit Determination*. NASA Technical Memorandum 104575. NASA Goddard Space Flight Center, Greenbelt, MD. November 1992.
36. Luthcke, S.B., J.A. Marshall, S.C. Rowton, K.E. Rachlin, C.M. Cox, and R.G. Williamson. "Enhanced Radiative Force Modeling of the Tracking and Data Relay Satellites." *The Journal of the Astronautical Sciences*, Vol. 45, No. 3, July-September 1997, pp 349-370.
37. Harvie, Edwin J. NOAA GOES Flight Ops Team. Personal correspondence. January, 2004.
38. DeGumbia, Jonathan D., and Yo-Kung J. Tsui. "Solar Torque Compensation Determination System for the GOES I-M Series Weather Satellites." AAS 98-374. *Advances in the Aeronautical Sciences*, Vol. 100, Pt. 2, 1998, pp 905-916.
39. Harvie, Edwin J. *SOLARSXI.FOR*. FORTRAN program that models the GOES solar torque. February 27, 1996. Revised September 27, 2001.

40. Price, Derek, The Concurrent Versions System, computer software, 2001. Available at <http://www.cvshome.org>.
41. Gehman, Harold W., Jr., et al. "Columbia Accident Investigation Board Report Volume I," Columbia Accident Investigation Board. August 2003. Available at http://www.caib.us/news/report/pdf/vol1/full/caib_report_volume1.pdf.
42. Battin, Richard H. An Introduction to the Mathematics and Methods of Astrodynamics, Revised Edition. AIAA Education Series, Reston, VA, 1999.
43. Montenbruck, Oliver and Eberhard Gill. Satellite Orbits – Models, Methods, and Applications. Springer, Berlin, 2001.
44. Smart, W.M. Celestial Mechanics. Longmans, Green and Co. Inc., New York, 1953.
45. McClain, W. D., "A Recursively Formulated First-Order Semianalytic Artificial Satellite Theory Based on the Generalized Method of Averaging," Volume 1, Computer Sciences Corporation CSC/TR-77/6010, 1977 (an updated version of this document is available from W. D. McClain).
46. Wright, J. R. "Variation of Parameters for Definitive Geocentric Orbits." AIAA 92-4361. AIAA/AAS Astrodynamics Conference, Hilton Head Island, SC, 10-12 Aug. 1992.
47. Sellers, Jerry J. et al. Understanding Space: An Introduction to Astronautics. McGraw-Hill, Inc. New York, 1994.
48. *Goddard Trajectory Determination System (GTDS) Mathematical Theory*. NASA Operational GTDS Mathematical Specification. Rev. 1. Ed. Computer Sciences Corporation and NASA Goddard Space Flight Center. Contract NAS 5-31500, Task 213, July 1989.
49. Carter, Scott Shannon. Precision Orbit Determination from GPS Receiver Navigation Solutions. SM Thesis, Department of Aeronautics and Astronautics, MIT, June 1996.
50. Seago, John H. and David A. Vallado. "Coordinate Frames of the U.S. Space Object Catalogs." AIAA 2000-4025. AIAA/AAS Astrodynamics Specialist Conference, Denver, Colorado, August 2000.
51. Gordon, Gary D. and Morgan, Walter L. Principles of Communications Satellites. John Wiley & Sons, New York. 1993. pp 331-335.
52. Berry, Matt and Liam Healy. "A Variable-step Double-integration Multi-step Integrator." AAS 04-238. 14th AAS/AIAA Space Flight Mechanics Meeting, Maui, Hawaii, February 2004.
53. Fischer, Jack David. The Evolution of Highly Eccentric Orbits. SM Thesis, Department of Aeronautics and Astronautics, MIT, June 1998.
54. Lodato, M.W. and J.B. Frazer. *An Introduction to the Brouwer Theory*. Project no. 496.2, The Mitre Corporation, Bedford, MA. 25 January 1965. Copy received March 2004 from Dr. Paul Cefola.
55. Brouwer, Dirk. "Solution of the Problem of Artificial Satellite Theory Without Drag." *The Astronomical Journal*, 64, No. 1274, pp 378-397. October 27, 1959.

56. Deprit, André and Arnold Rom. "The Main Problem of Artificial Satellite Theory for Small and Moderate Eccentricities." *Celestial Mechanics*, Volume 2, No 2, July 1970, pp 166-206.
57. Early, L. W., "A Portable Orbit Generator Using Semianalytical Satellite Theory", AIAA Paper 86-2164-CP, AIAA/AAS Astrodynamics Conference, Williamsburg, VA, August 1986.
58. Cefola, Paul J., and Vasiliy Yurasov, "Optical Measurements Processing Technology on Geostationary Satellite." Proceedings of the Third US/Russian Space Surveillance Workshop, US Naval Observatory, Washington, DC, USA, October 20 -23, 1998, pp 311 – 338.
59. Thomas, G. B., Calculus and Analytic Geometry, Addison-Wesley, Third Edition, 1960.
60. Milani, Andrea, Nobili, Anna Maria, and Farinella, Paolo. *Dipartimento di Matematica, Universita di Pisa*. "Non-gravitational Perturbations and Satellite Geodesy." pp 48-76.
61. Kubo-oka, Toshihiro, and Sengoku, Arata. "Solar Radiation Pressure Model for the Relay Satellite of SELENE." *Earth Planets Space*, 51, 1999, pp 979-986.
62. Knocke, P.C., Ries, J.C., and Tapley, B.D. *Center for Space Research, The University of Texas at Austin, Austin, Texas*. "Earth Radiation Pressure Effects on Satellites." Proceedings of the AIAA/AAS Astrodynamics Conference, Minneapolis, MN, August 1988. pp 577-587.
63. Wyatt, Stanley P. "The Effect of Terrestrial Radiation Pressure on Satellite Orbits." Dynamics of Satellites Symposium, IUTAM, 18-30 May 1962, Paris. Ed. M. Roy, Academic Press, New York, 1963, pp 180-196.
64. Lochry, Robert R. The Perturbative Effects of Diffuse Radiation From the Earth and Moon on Close Satellites. PhD Thesis, Engineering, University of California, Los Angeles. 1966.
65. Green, Andrew J., Orbit Determination and Prediction Processes for Low Altitude Satellites, PhD Thesis, Department of Aeronautics and Astronautics, MIT, December 1979.
66. The Tracking and Data Relay Satellite Project Webpage. Code 454. NASA Goddard Spaceflight Center. Available <http://tdrs.gsfc.nasa.gov/Tdrsproject/>.
67. NOAASIS Satellite Information Gateway Webpage. Available <http://noaasis.noaa.gov/NOAASIS/ml/gateway.html>.
68. GOES I-M Data Book. Revision 1. National Aeronautics and Space Administration, Goddard Space Flight Center, Greenbelt, MD. 31 August, 1996.
69. Wong, Mike. Space Systems/Loral. GOES I-M Data Package and Drawings. November 2003.

70. Granholm, George R., Near-Real Time Atmospheric Density Model Correction Using Space Catalog Data, SM Thesis, Department Of Aeronautics And Astronautics, MIT, June 2000.
71. Bergstrom, Sarah E., An Algorithm for Reducing Atmospheric Density Model Errors Using Satellite Observation Data in Real-Time, SM Thesis, Department of Aeronautics and Astronautics, MIT, June 2002.
72. Fonte, Daniel J. Implementing a 50 x 50 Gravity Field Model in an Orbit Determination System. SM Thesis, Department of Aeronautics and Astronautics, MIT, June 1993.
73. Cefola, P. J., Yurasov, V. S., Folcik, Z. J., Phelps, E. B., Proulx, R. J., and Nazarenko, A. I., "Comparison of the DSST and the USM Semi-analytical Orbit Propagators", AAS pre-print 03-236, presented at the AAS/AIAA Spaceflight Mechanics Meeting, Ponce, Puerto Rico, February 2003.
74. Metzinger, R.W., Validation of the Workstation Version of R&D GTDS. Charles Stark Draper Laboratory: February 1993. Copy available through Dr. Rick Metzinger, (617)-258-2912.
75. Neelon, J. G., Paul J. Cefola, and Ronald J. Proulx, "Current Development Of The Draper Semianalytical Satellite Theory Standalone Orbit Propagator Package", AAS pre-print 97-731, presented at the AAS/AIAA Astrodynamics Specialist Conference, Sun Valley, ID, August 1997.
76. Herriges, Darrell L., NORAD General Perturbation Theories: An Independent Analysis, Master of Science Thesis, CSDL-T-972, submitted to the Department of Aeronautics and Astronautics, Massachusetts Institute of Technology, Cambridge, Massachusetts, January 1988.
77. Cefola, P.J., Fonte, D.J., and Shah, N. "The Inclusion of the Naval Space Command Satellite Theory PPT2 in the R&D GTDS Orbit Determination System." Presented at the 2002 AAS/AIAA Space Flight Mechanics Meeting, Austin, Texas, February 1996.
78. Sabol, Chris, Draim, John, and Cefola, Paul J. "Refinement of a Sun-Synchronous, Critically Inclined Orbit for the ELLIPSO Personal Communication System." The Journal of the Astronautical Sciences, Vol. 44, No. 4, October-December 1996, pp 467-489.
79. Fonte, Capt Daniel J., and Chris Sabol. "Optimal DSST Input Decks for Various Orbit Types," PL-TR-95-1072. Final Report, Phillips Laboratory. June 1995.
80. Hujsak, R.S., "Solar Pressure." Proceedings of the Artificial Satellite Theory Workshop, U.S. Naval Observatory, 8-9 November, 1993, pp 54-72.
81. Vokrouhlicky, D., P. Farinella, and F. Mignard. "Solar radiation pressure perturbations for Earth satellites, I. A complete theory including penumbra transitions." Astronomy and Astrophysics. 280, 295-312, 1993.
82. Vokrouhlicky, D., P. Farinella, and F. Mignard. "Solar radiation pressure perturbations for Earth satellites, II. An approximate method to model penumbra

- transitions and their long-term orbital effects on LAGEOS.” Astronomy and Astrophysics. 285, 333-343, 1994.
83. Vokrouhlicky, D., P. Farinella, and F. Mignard. “Solar radiation pressure perturbations for Earth satellites, III. Global atmospheric phenomena and the albedo effect.” Astronomy and Astrophysics. 290, 324-334, 1994.
84. Vokrouhlicky, D., P. Farinella, and F. Mignard. “Solar radiation pressure perturbations for Earth satellites, IV. Effects of the Earth’s polar flattening on the shadow structure and the penumbra transitions.” Astronomy and Astrophysics. 307, 635-644, 1996.
85. Ullman, Richard E. SOLVE Program Mathematical Formulation – June 2003. Hughes STX Corporation, Lanham, MD, for NASA GSFC, Greenbelt, MD. June 2003.